

Dissertation

submitted to the

Combined Faculty of Mathematics, Engineering and Natural Sciences

of

Heidelberg University, Germany

for the degree of

Doctor of Natural Sciences

Put forward by

Adrian Lukas Braemer

born in: Heidelberg, Germany

Oral examination: 14.11.2024

QUANTUM DYNAMICS OF DISORDERED MANY-BODY SPIN SYSTEMS

Effects of Spatial Disorder in a Dipolar, Frozen Gas and
Influence of Spatial Inhomogeneity in Periodically Driven Systems

Referees: Prof. Dr. Martin Gärttner
Prof. Dr. Tilman Enss

A B S T R A C T

In this thesis, we study the thermalization properties in both closed and periodically driven systems subject to spatial inhomogeneities.

In Part 1, we focus on long-range Heisenberg spin models of spatially disordered spins which can be realized experimentally by current state-of-the-art platforms. We find numerically that the disordered couplings induced by the randomly positioned spins can lead to a many-body localized regime. Using perturbative arguments based on the real-space renormalization group, we demonstrate that the emergent quasi-conserved quantities arise from pairs of strongly interacting spins decoupling from their environment. Predictions from the resulting effective model of pairs are compared to real experimental data from a Rydberg quantum simulator for validation and are found to be highly accurate.

In Part 2, we shift our focus to periodically driven systems which are known to exhibit long-lived (meta-)stable states under certain conditions. Specifically, we consider an ordered Ising chain subject to a driving field of varying strength across different parts of the chain. We demonstrate that a configuration where the driving field has the same strength for all spins except one can dramatically prolong time-crystalline signatures. We link this behavior to the presence of approximate conservation laws stabilized by the spatial inhomogeneity. Additionally, we present preliminary results on the possibility to create a time crystal by driving the pair model derived in the first part.

Z U S A M M E N F A S S U N G

In dieser Arbeit untersuchen wir die Thermalisierungseigenschaften sowohl in isolierten als auch in periodisch getriebenen Quantensystemen mit räumlichen Inhomogenitäten.

Im ersten Teil konzentrieren wir uns auf Heisenberg-Spin-Modelle von räumlich ungeordneten Spins mit langreichweitigen Wechselwirkungen, wie sie in derzeitigen Experimenten realisiert werden können. Numerische Untersuchungen zeigen, dass durch die ungeordneten Kopplungen, die durch die zufällig positionierten Spins induziert werden, Vielteilchen-Lokalisierung auftreten kann. Mithilfe perturbativer Argumente der Realraum-Renormierungsgruppe zeigen wir, dass die entstehenden quasi-erhaltenen Größen aus Paaren stark wechselwirkender Spins bestehen. Daraus resultiert ein effektives Modell von Paaren dessen Vorhersagen sich sehr präzise mit experimentellen Daten eines Rydberg-Quantensimulators decken.

Im zweiten Teil dieser Arbeit fokussieren wir uns auf periodisch getriebene Systeme. Diese können unter bestimmten Bedingungen von Unordnung stabilisierte, langlebige Zustände aufweisen. Konkret betrachten wir eine geordnete Ising-Kette, die einem zeitlich periodischen Feld ausgesetzt ist. Wir zeigen, dass in diesem System die Lebensdauer der zeitkristallinen Signaturen sehr empfindlich auf räumlich lokale Abweichungen des Antriebs ist. Diesen Effekt führen wir auf Quasi-Erhaltungsgrößen zurück, die durch die Abweichungen im Feld stabilisiert werden. Zusätzlich präsentieren wir vorläufige Resultate zur Frage ob das Paarmodell aus dem ersten Teil unter Treiben auch eine Zeitkristall-Phase ermöglichen kann.

PUBLICATIONS

This thesis is based on the following manuscripts and publications:

- [A] **A. Braemer**, T. Franz, M. Weidemüller, and M. Gärtnner, “Pair localization in dipolar systems with tunable positional disorder,” *Physical Review B* **106**, 134212 (2022).
- [B] **A. Braemer**, J. Vahedi, and M. Gärtnner, “Cluster truncated Wigner approximation for bond-disordered Heisenberg spin models,” *Physical Review B* **110**, 054204 (2024).
- [C] T. Franz*, S. Geier*, C. Hainaut, **A. Braemer**, N. Thaicharoen, M. Hornung, E. Braun, M. Gärtnner, G. Zürn, and M. Weidemüller, “Observation of anisotropy-independent magnetization dynamics in spatially disordered Heisenberg spin systems,” *Physical Review Research* **6**, 033131 (2024).
- [D] T. Franz, S. Geier, A. Braemer, C. Hainaut, A. Signoles, N. Thaicharoen, A. Tebben, A. Salzinger, M. Gärtnner, G. Zürn, and M. Weidemüller, *Emergent pair localization in a many-body quantum spin system*, ArXiv preprint, Feb. 2024.
- [E] N. Euler*, **A. Braemer***, L. Benn, and M. Gärtnner, “Metronome spin stabilizes time-crystalline dynamics,” *Physical Review B* **109**, 224301 (2024).

The author also contributed to the following publications:

- [F] S. Geier, **A. Braemer**, E. Braun, M. Müllenbach, T. Franz, M. Gärtnner, G. Zürn, and M. Weidemüller, “Time-reversal in a dipolar quantum many-body spin system,” *Physical Review Research* **6**, 033197 (2024).
- [G] M. Müllenbach*, S. Geier*, **A. Braemer**, T. Franz, G. Zürn, M. Weidemüller, and M. Gärtnner, *Detecting operator spreading in Rydberg quantum simulators*, In preparation.
- [H] M. Erpelding*, **A. Braemer***, and M. Gärtnner, *Symmetries of the disorder-averaged time evolution*, In preparation.

*These authors contributed equally.

CONTENTS

I Introduction

II Pair localization in spatially disordered Heisenberg spin models

1	Concepts: Thermalization and absence thereof in closed quantum systems	9
1.1	Thermalization in closed quantum systems	9
1.2	Many-body localization	13
1.2.1	LIOM picture	13
1.2.2	MBL in long-range, bond-disordered systems	14
1.3	Using cold Rydberg gases to probe thermalization	16
2	Pair localization transition	19
3	Efficient time evolution of pair localized systems	31
4	Evidence of pair localization in the dynamics of Rydberg spins	47
4.1	Anisotropy-independent relaxation dynamics	47
4.2	Emergent pair localization	60
4.2.1	Origin of the cusp-like signature	74
5	Conclusion	79

III Periodically driven quantum systems with spatial inhomogeneity

6	Concepts: Periodically driven systems and time crystals	83
6.1	Introduction to Floquet systems	83
6.2	Thermalization in Floquet systems	84
6.3	Time crystals	85
7	Stabilization by spatial variation of the drive	87
8	Outlook: Can pairs stabilize time crystalline dynamics?	99
8.1	Time crystal protocol with pairs	99
8.2	Discussion	103
9	Conclusion	105

IV Summary

Bibliography	111
Acknowledgments	121

LIST OF FIGURES

Figure 1	Schematic of the thermalization process of a classical latte.	3
Figure 1.1	Gas in box. (a) Initially all particles are confined to the left. (b) At a later time the gas has spread evenly throughout the box.	10
Figure 1.2	Comparison thermalizing and non-thermalizing system using a long-range Heisenberg model (cf. Equation 1.13) where $\Delta = 0.4, \alpha = 3$ and $h = 0$. The spins are randomly positioned as seen in (a). (b) shows the eigenstate expectation values for the observable $2S_z^{(10)}$. (c) shows the eigenstate occupation numbers (binned into 100 bins) w.r.t. the domain-wall state, where the left 7 spins are $ \downarrow\rangle$ and the other 6 are $ \uparrow\rangle$. The shaded region indicates the mean energy and its variance. The time traces of this operator and initial state are shown in (d). Also shown are the respective prediction by the diagonal and microcanonical ensembles.	12
Figure 1.3	Real-space structure of a couple of eigenstates of the XXZ chain with random on-site potentials (cf. Equation 1.11) in the single excitation sector with $W = 15$. The exponential tails are clearly visible.	14
Figure 1.4	Schematic overview of the experimental features. (a) Spins are randomly distributed in space and feature power-law interactions and can evolve under different Heisenberg Hamiltonians. Depending on the choice of states, the experiment can realize XX (b), XXZ (c) and Ising (d) models. Taken from [C].	16
Figure 1.5	Example configurations (top row) and corresponding nearest-neighbor distance distributions (bottom row) for high density/weak disorder (left column), intermediate density/disorder (middle column) and low density/strong disorder (right column).	17
Figure 4.1	Steady-state magnetization curves of the two-component model using the same color scheme as Fig. 2 (d) and (e) of [D]. Parameters, α and d correspond to (a) Fig. 2 (b) Fig. 4. The inset shows a zoom around $\Omega = 0$ to highlight the qualitative difference between the curves.	76
Figure 4.2	Comparison of the two-component model (dashed lines) with another model where the constituents' magnetization is given by a Lorentzian (solid lines). (a) steady-state magnetization of the constituent. (b) predictions of both model for $\alpha = d = 3$ [same parameters as Figure 4.1(a)].	77

Figure 8.1 Preliminary experimental results on time-crystalline signatures in a spatially disordered XX model. a) sketches the experimental sequence. Then experimental results for perfect rotation (b), short interaction times and imperfect rotation (c) and longer interaction times with imperfect rotation (d) follow. Left column depict the magnetization's time trace, while right column shows the Fourier transform of the signal. e) Then plots the normalized Fourier weight at $\nu = 0.5$ versus rotational deviation ϵ . Taken with permission from Ref. [160] 100

Figure 8.2 Preliminary result of the pair model applied to the time crystal protocol for $d = \alpha$, $\epsilon = 2\%$ and $\tau = 10J_{med}$. (a) shows the distribution of the pair couplings as given by Equation 4.10. The yellow shaded area indicates the region where the approximation is applied. The gray, dashed, line indicates where $\bar{J} = 1$ and thus phase wrapping sets in. (b) Resulting distribution if the couplings contained in the yellow area of panel (a) are phase wrapped. The gray, dotted, line is a guide to the eye and marks a uniform distribution. (c) Compares the time traces resulting from averaging exact pair dynamics (gray), averaging the approximated pair dynamics and (blue) and the approximate analytical average (yellow dashed). 102

Figure 9.1 Localization exemplified by a macchiato. 109

NOTATION

We will work with natural units $\hbar = k_B = c = 1$. Furthermore, we will denote matrices and operators as uppercase letters O , vectors using arrows \vec{o} and scalars as lowercase letters o . In special instances, we will use a calligraphic font, such as \mathcal{H} to denote Hilbert spaces. All other notation is explained at the first point of occurrence.

Part I
INTRODUCTION

INTRODUCTION

When pouring some milk into a cup of coffee, one can watch as it distributes itself throughout the cup rather quickly until a homogeneous mixture is reached (cf. Figure 1). Or, as a physicist might say, the system evolves to *thermal equilibrium*. The reason for this thermalization process can be stated statistically: There are just many more possible configurations where milk and coffee particles are mixed than ones where they are spatially separated, i.e. most microstates are *typical*. Assuming the dynamics explore many different configurations¹, we will thus find the system in a typical microstate most of the time. Zooming out and taking a macroscopic point of view, the system appears to be in equilibrium. To emphasize: Although there is still on-going dynamics on the microscopic level, the macroscopic state appears to be stationary simply because most microstates exhibit similar macroscopic features. Importantly, this apparent equilibrium state can be described using only a few *macroscopic quantities*, such as the average temperature and the ratio of milk to coffee. Knowledge of this handful of values allows to compute all other properties of the system simply by averaging over all compatible microscopic configurations without having to know the precise dynamics. Strikingly, most classical systems show thermalization: From small, simple ones like coffee in a cup, over more complex ones such as fridges and engines even up to stellar objects like black holes. This underpins the great predictive power of *statistical mechanics*.

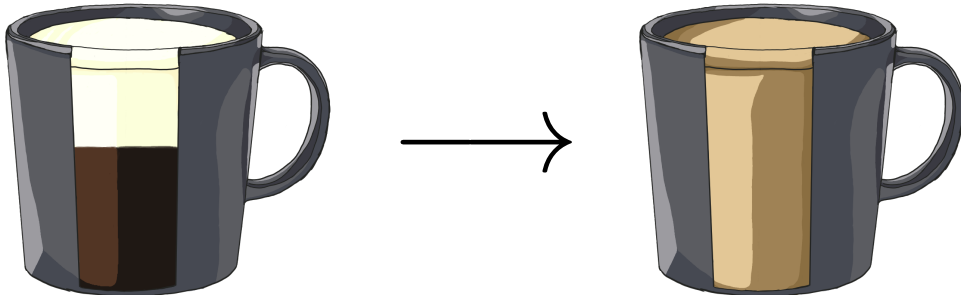


Figure 1: Schematic of the thermalization process of a classical latte.

In the quantum realm, the situation turns out to be similar for many cases. For example, even isolated quantum systems initialized in a pure state are oftentimes found to thermalize rapidly. This means they reach a state where observables are consistent with a thermal description depending only on few parameters. This is quite surprising considering the time evolution dictated by the Schrödinger equation preserves the purity and additionally thermal states are usually highly mixed (i.e. a statistical mixture of many pure states). Thus, an initially pure quantum state can never come close to a thermal state in state space. This conundrum can be alleviated by restricting to *local observables*, i.e. observables that extract information from only a small subsystem such as the magnetization of a single spin. Then the measurement process effectively averages over the state of the rest of the system which is equivalent to performing a measurement on a mixed state. If most of the states one averages over have the same local expectation value, then this explains

¹ More precisely, the dynamics needs to be *ergodic*.

the observed thermalization. This assumption is now known as *eigenstate thermalization hypothesis* (ETH) [1–3] and is conceptually similar to the *typicality* of microstates in classical systems. From a dynamical perspective, the consequences of ETH and thus the mechanism behind quantum thermalization, can be stated more intuitively: Consider some quantum spin system initialized in a product state, such that each spin has a well defined magnetization and there is no entanglement among spins. Letting the system evolve for some time, the interactions will cause entanglement to form and thus the initially local information about the initial state of each spin will be distributed throughout the whole system - hidden in the complicated correlations between all spins and utterly inaccessible to small scale measurements. In fact, the stronger the entanglement between subsystem and rest, the more the subsystem appears to be mixed. Thus, the *rapid buildup of entanglement* is the main driver behind thermalization of local observables in closed quantum systems.

If interactions are the main reason behind the build-up of entanglement and thus thermalization, should not every non-integrable quantum system thermalize? The story is not as simple as that! In his seminal 1958 paper [4], Anderson showed that for a single excitation hopping in a lattice with random on-site potentials, all motion, and thus thermalization, arrests *completely* if the randomness of said potentials is sufficiently strong. This phenomenon, now dubbed Anderson localization, started a new branch of research on models subject to *static randomness*. These kinds of systems arise naturally in many different contexts such as cold atomic gases [5, 6], color centers in diamond [7, 8] or generally systems with impurities [9, 10]. A few years after Anderson's paper, localization was generalized to interacting many-body systems under the name *many-body localization* (MBL) [11–14]. Conceptually, in an MBL system, the disorder causes local energy mismatches of such severity that the transport of physical quantities (e.g. magnetization) is (almost) completely prohibited [15–17]. Even though the system appears to be fully interacting at first glance, the strong disorder causes it to fracture into small pieces, called local integrals of motion (LIOMs), that cannot exchange information. Such a system of course *never thermalizes*, therefore no thermal description can ever be applied! Fortunately, one can still describe the state of the system rather easily if the structure of those LIOMs constituting the system is known. Thus, the concept of MBL can also be a practical tool to understand the dynamics of strongly disordered quantum systems.

The existence of MBL was demonstrated numerically in a large variety of systems with tens of spins/sites in a huge number of studies (e.g. [18–22]) and also experimentally [5, 23–25]. However, its existence in the *thermodynamic limit*, i.e. infinitely large systems, is currently hotly debated [26–29]. The reason for the absence of MBL in large systems is seen in the so-called *avalanche instability* of MBL [27, 30–32]. This mechanism is rooted in the observation that a thermal region can thermalize neighboring LIOMs which results in a larger thermal region. Thus, a small thermal inclusion in an otherwise localized system can grow slowly and cause thermalization of the whole. Large enough systems will always feature some statistically *rare regions* of low disorder that then seed a thermalization avalanche. For systems featuring long-range interactions, which are of particular relevance in this thesis, there exists even more direct arguments based on *counting resonances* that rules out MBL whenever the interaction decays slower than a power-law with exponent twice the spatial dimension [33–36].

However, thermalization achieved through either mechanism, avalanche thermalization or resonance proliferation, appears to slowdown exponentially with the system's size [29, 37, 38]. Thus, the question whether these truly prohibit localization in infinitely large systems is still considered open. Independently of the theoretical debate, it is unclear how relevant

the resulting thermalization timescales are for experiments [39]. In fact in Chapter 4, we show evidence that MBL can still be applied to describe the dynamics of an experiment featuring power-law interactions with an exponent equal to the spatial dimension despite MBL being ruled out in that parameter range. Of course the experiment can only probe finite times and thus cannot rule out thermalization at later times. Nonetheless, MBL proves to be a useful concept for understanding the observed phenomena.

Notably, most systems used for studying avalanche thermalization or counting resonances feature random on-site potentials, whereas the experiment realizes a bond-disordered model, i.e. its main source of randomness lies within the interactions between the spins. Thus, aforementioned arguments might not apply readily to this kind of system. Usually, bond-disordered models are tackled using real-space renormalization group (RSRG) techniques, which iteratively identify and eliminate the strongest coupling of the system [40–43]. Traditionally, RSRG has been applied to models with nearest neighbor interactions to derive properties of the groundstate (e.g. [44–46]) but was recently generalized to study excited states as well [47]. Even more recently it has also been applied to long-range systems [48–52]. All of these works use exact numerics to benchmark their results and thus comparison is limited to small systems.

Given this background, we explore localization phenomena in Part II using a model that can be realized naturally in a Rydberg quantum simulator. This opens up the possibility for benchmarking the theoretical results with much larger systems than accessible via numerics. Concretely, we consider a bond-disordered Heisenberg spin model where the disorder arises from power-law interaction between randomly positioned spins. After a brief review of the relevant context in Chapter 1, we start the analysis of this model in Chapter 2 by performing a numerical study in one spatial dimension across disorder strength. We find a clear crossover from a thermalizing into a localized regime at sufficiently strong disorder and apply RSRG to derive the locally (quasi-)conserved quantities, which consist of pairs of strongly interacting spins. In the following Chapter 3, we show how this emergent structure of the system can be exploited to compute the dynamics efficiently and accurately with a semi-classical numerical technique. Finally in Chapter 4, we turn to a quantum simulator based on ultra-cold Rydberg atoms, that naturally implements the type of model studied, and present two different experimental studies that show clear signatures of localization based on pairs of spins. While this cannot answer the question about the stability of MBL in infinitely large systems at arbitrarily late times, it nonetheless establishes once more that MBL can be a quite useful concept to understand the dynamics of real-world systems effectively.

Shifting focus from closed quantum systems to periodically driven systems, MBL seems to have a stabilizing effect on the dynamics even in the presence of strong driving. Usually, driving causes the system to absorb energy from the drive and heat up resulting in a featureless infinite temperature state. However, if the system exhibits MBL, then the energy absorption can be suppressed and the system can remain perpetually in an out-of-equilibrium state [53–56]. This allows for novel out-of-equilibrium phases of matter to exist that can show radically different properties than regular phases. One such new feature is the spontaneous breaking of time translation symmetry which is normally impossible [57]. This broken symmetry manifests as *stable oscillations* of the system that show a different frequency compared to the drive. A state breaking time translation symmetry is called a *time crystal* in analogy to ordinary crystals that break spatial translation symmetry.

Since this phenomenon seems to be closely linked to disorder as well, in Part III of this thesis, we study two periodically driven systems with unusual spatial inhomogeneity: In Chapter 7, we consider a spatially varying driving field and find it to dramatically enhance

the lifetime of time crystalline signatures in an otherwise clean Ising chain. Following this in Chapter 8, we consider again the spatially disordered Heisenberg XXZ model from Part II subject to periodic driving. We show preliminary measurements and undertake a theoretical exploration regarding the longevity of this time crystalline behavior based on the pair model.

This thesis consists of two major parts: Part II discussing localization in closed quantum systems caused by disorder in the interactions due to spatially random positions. And Part III about the effect of spatial inhomogeneity in the context of Floquet time crystals. Each part starts with an overview of the relevant concepts (Chapter 1 and Chapter 6 respectively) and ends with a discussion of the results including directions for future research (Chapter 5 and Chapter 9). This thesis closes in Part IV with a short, high-level summary of its findings.

Part II

PAIR LOCALIZATION IN SPATIALLY DISORDERED HEISENBERG SPIN MODELS

CONCEPTS: THERMALIZATION AND ABSENCE THEREOF IN CLOSED QUANTUM SYSTEMS

In this chapter, we give a brief overview of the concepts relevant for Part II of this thesis and establish the necessary context to interpret the results. However, we'll try to be brief and only summarize the essence of the matter. The interested reader is referred to the relevant literature for the details. Since the distinction between thermalizing and localized systems is at the core of this part of the thesis, we start by reviewing the current understanding of the thermalization process in closed quantum systems in general and contrast this with the typical picture of how localized systems evade thermalization. In particular, we discuss localization in long-range and bond-disordered systems. We close this chapter with a high-level description of the Rydberg-based quantum simulation experiment which naturally implements the specific disordered Hamiltonian studied here.

1.1 THERMALIZATION IN CLOSED QUANTUM SYSTEMS

The simplest picture of thermalization in a classical system is perhaps the gas in a box which initially is confined to one of the sides (cf. Figure 1.1). Upon removing the constraint, the gas quickly spreads throughout the box and soon after a new equilibrium is reached. Interestingly, we can understand this process in a purely statistical way, without knowing about the precise equations of motion. As long as the dynamics sufficiently explore the configuration space, i.e. are *ergodic*, we can postulate each possible configuration to be equally likely. This already explains why we find the gas to distribute itself throughout the box: There are just overwhelmingly more configurations where the particles occupy most of the box than configurations where the particles are concentrated, i.e. most configurations are *typical*. With this ansatz, we could also compute how much force we would need on average to slowly compress the gas back to one side and how much kinetic energy this process adds. Thus, the presence of a thermal equilibrium grants us enormous predictive power. The key features of a thermal equilibrium are:

- *Loss of memory*: One cannot tell on which side of the box the gas started.
- *Subsystem independence*: Every patch of space appears to be thermal with the same parameters (at least sufficiently away from the boundary).
- *Independence of microscopic details*: The full state of the system can be described using just a few macroscopic quantities, namely in this case the total (kinetic) energy, the number of particles and the volume of the box.

Since quantum systems become computationally intractable much faster than classical systems, it would be very helpful if such an approach could be applied as well. Fortunately, for many quantum systems an analogue to classical thermalization can indeed be found, which we can only sketch here. We refer the interested reader to one of the many great reviews on this topic for further details [3, 58–60].

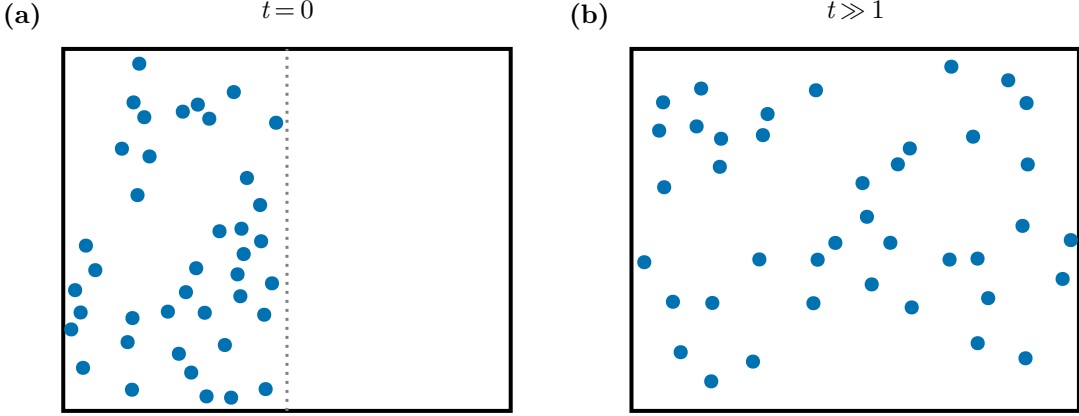


Figure 1.1: Gas in box. (a) Initially all particles are confined to the left. (b) At a later time the gas has spread evenly throughout the box.

Consider some quantum system governed by a Hamiltonian H which is prepared in some pure state $|\psi(t)\rangle = |\psi_0\rangle$ at $t = 0$. Written in the energy eigenbasis $H|k\rangle = E_k|k\rangle$, the state at some later time t can be written as

$$|\psi(t)\rangle = e^{-iHt}|\psi_0\rangle = \sum_k e^{-iE_k t}|k\rangle\langle k|\psi_0\rangle = \sum_k c_k e^{-iE_k t}|k\rangle. \quad (1.1)$$

Notably, due to the unitarity of the time evolution, the system's state at every time t can be reversed to $t = 0$ and thus the memory of the initial state is always preserved perfectly. This basic fact already means that we cannot expect *every* observable to be captured by a thermal description of a few parameters.

However, in practice it is impossible to measure e.g. the expectation value of some projector onto a highly-entangled, many-body state. Thus, for practical applications it would be sufficient, if the expectation values of some *simple observables* could be described by thermal ensembles. So suppose we restrict ourselves to measuring the expectation value of some *local observable* O which only acts on a small subsystem S , i.e. can be written as $O = O_S \otimes \mathbb{1}_{\bar{S}}$. Writing out the evolution of the expectation value, we see

$$\langle O(t) \rangle = \langle \psi(t) | O | \psi(t) \rangle \quad (1.2)$$

$$= \text{Tr} [(O_S \otimes \mathbb{1}_{\bar{S}}) |\psi(t)\rangle\langle\psi(t)|] \quad (1.3)$$

$$= \text{Tr } O_S \text{ Tr}_{\bar{S}} |\psi(t)\rangle\langle\psi(t)| \quad (1.4)$$

$$= \text{Tr } O_S \rho_S(t). \quad (1.5)$$

So the fact alone that we measure a property O on a subsystem makes this measurement effectively equivalent to measuring O on a mixed state! This simple observation is what enables equilibration and thermalization of local observables. Indeed, it has been shown that such a reduced state $\rho_S(t)$ is close to its equilibrium state

$$\omega_S = \lim_{\tau \rightarrow \infty} \frac{1}{\tau} \int_0^\tau dt \text{Tr}_{\bar{S}} \rho(t) \quad (1.6)$$

$$= \text{Tr}_{\bar{S}} \sum_k |c_k|^2 |k\rangle\langle k| \quad (1.7)$$

$$= \text{Tr}_{\bar{S}} \omega \quad (1.8)$$

for most times t under very mild conditions [61, 62]. The equilibration to this so-called diagonal ensemble ω is not yet equivalent to thermalization [63, 64]. For one ω still requires knowledge of an extensive amount of eigenstates occupation numbers $|c_k|^2$ and additionally the system might take very long to equilibrate as the derivation relies on the dephasing of off-diagonal elements. So in the worst case, equilibration takes up until $t_{\text{deph}} \propto 1/\delta$ where $\delta = \min_{k,k'} |E_k - E_{k'}|$ is the smallest energy gap of the Hamiltonian which generally shrinks exponentially with increasing system size.

To ensure thermalization additional assumptions are required. Considering the expectation value of O with respect to the diagonal ensemble ω

$$\langle O \rangle_\omega = \text{Tr } O \omega = \sum_k |c_k|^2 \langle k | O | k \rangle, \quad (1.9)$$

we can see that if all eigenstate expectation values $\langle k | O | k \rangle$ are equal to some $\langle k | O | k \rangle \approx O_{mc}$, then the precise distribution of $|c_k|^2$ is irrelevant and we have $\langle O \rangle_\omega = O_{mc}$. This can be thought of the direct pendant to the typicality of microstates in classical thermalization. It seems reasonable to assume that this $O_{mc} = O_{mc}(E)$ is a smooth function of the energy because states of similar energy should be able to show wildly different properties. This assumption that $\langle k | O | k \rangle = O_{mc}(E_k)$ is a smooth function for all eigenstates and all local observables called eigenstate thermalization hypothesis (ETH) [1, 2, 65]. Of course, it appears to be a strong assumption but it is physically well motivated¹ and indeed many systems have been shown to exhibit ETH.

However, ETH alone is not enough to ensure thermalization, we also need to demand that the c_k are concentrated in the spectrum around some mean \bar{E} . Then we have indeed

$$\langle O \rangle_\omega = O_{mc}(\bar{E}) = \langle O \rangle_{mc}(\bar{E}), \quad (1.10)$$

where $\langle O \rangle_{mc}(\bar{E})$ denotes the microcanonical ensemble expectation value at mean energy \bar{E} , i.e. the average over all eigenstates within a small energy window $[E - \Delta E, E + \Delta E]$. Physically, this restriction just means that one cannot expect extreme cases, e.g. a superposition of some state at low energy and another at high energy, to thermalize. Fortunately, these scenarios are rare. Usually, experiments initialize their systems in some reasonable state, e.g. product states with well-defined physical properties, which will also be concentrated in the spectrum due to ETH.

We remark that thermalization according to ETH reflects the key features of thermal equilibrium defined in the beginning of this section: The precise initial state is irrelevant and the only information needed to describe its equilibrium properties is its average energy (assuming the absence of other conservation laws). In a sense ETH translates the concept of typicality from the classical world into the quantum realm by demanding that every eigenstate itself looks already thermal when probed locally. Since thermal states are usually highly mixed, this implies that eigenstates are highly entangled, i.e. feature *volume-law entanglement* generically. This leads to the common sentiment that "the system acts as its own bath".

To conclude this introduction, Figure 1.2 shows a comparison of two concrete systems where one thermalizes (blue) and one is subjected to strong disorder which can prohibit thermalization as described in the following sections. The model itself is a long-range Heisenberg model that will be studied throughout whole Part II but the details are not relevant to recognize the striking difference between the weakly and strongly disordered cases. Panel (b) clearly shows that ETH is not fulfilled, eigenstate expectation values are

¹ There are also more mathematical motivations based on random matrix theory, see e.g. [59].

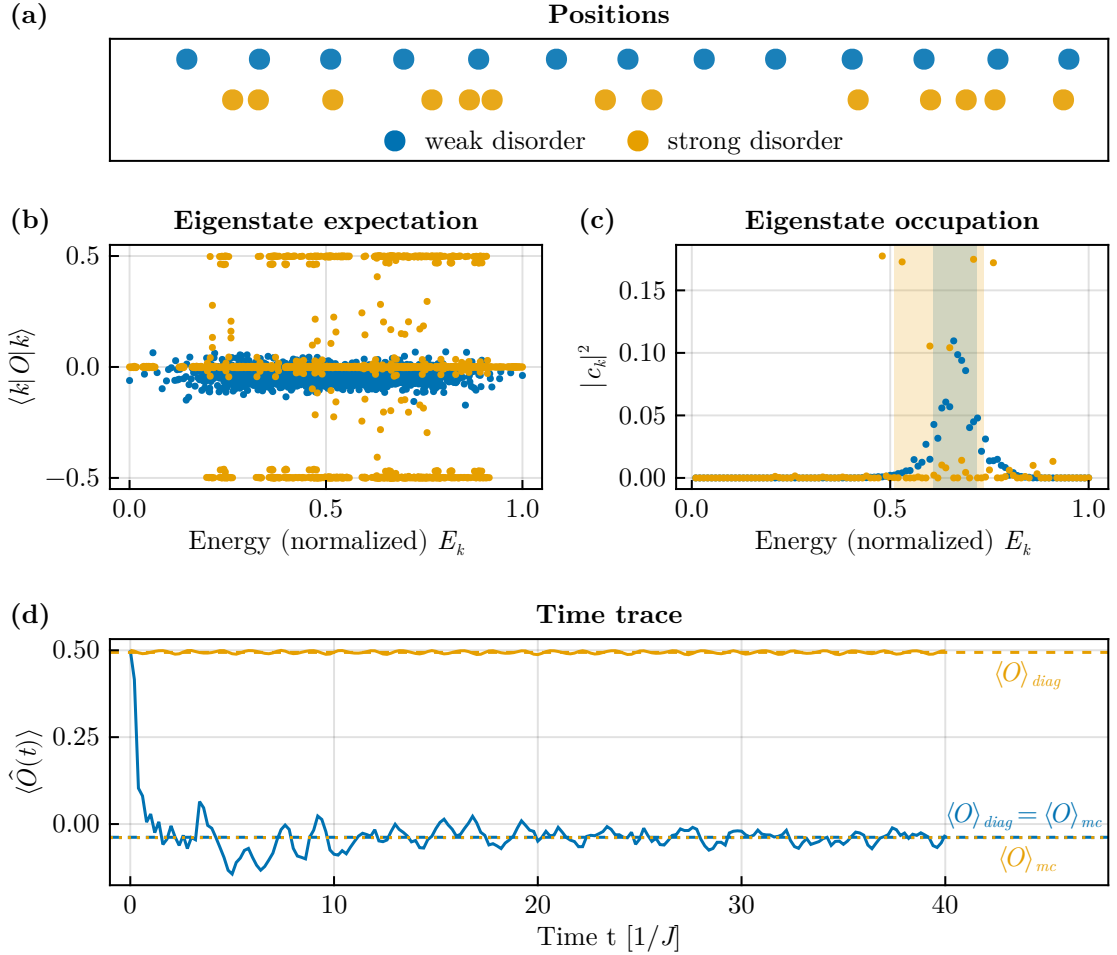


Figure 1.2: Comparison thermalizing and non-thermalizing system using a long-range Heisenberg model (cf. Equation 1.13) where $\Delta = 0.4, \alpha = 3$ and $h = 0$. The spins are randomly positioned as seen in (a). (b) shows the eigenstate expectation values for the observable $2S_z^{(10)}$. (c) shows the eigenstate occupation numbers (binned into 100 bins) w.r.t. the domain-wall state, where the left 7 spins are $|\downarrow\rangle$ and the other 6 are $|\uparrow\rangle$. The shaded region indicates the mean energy and its variance. The time traces of this operator and initial state are shown in (d). Also shown are the respective prediction by the diagonal and microcanonical ensembles.

highly discontinuous for the strongly disordered system. In contrast, for weak disorder they show no real energy dependence for the chosen observable (which is just the z -magnetization of a single spin). Similarly, but not as stark is the contrast for the eigenstate occupation numbers, i.e. the $|c_k|^2$, shown in panel (c) for the domain-wall state $|\downarrow\rangle^{\otimes 7} |\uparrow\rangle^{\otimes 6}$. This is a reasonable state and thus we can see that for weakly disordered system the eigenstate occupations cluster in the spectrum. Conversely for the strongly disordered system, they are spread roughly twice as far. Finally, these spectral properties are reflected in the time evolution of the expectation value of the chosen operator: While for thermalizing system the equilibrium value is reached quickly and agrees with the value obtained by the diagonal and microcanonical ensembles, for the non-thermal system the microcanonical prediction is very far from the actual values.

1.2 MANY-BODY LOCALIZATION

In 1958 Anderson discovered that a particle, that can hop between sites in a lattice with random on-site potentials, can become stuck completely [4]. Thus, this simple system does not thermalize at all since the memory of the initial state, i.e. where the particle started, is retained at all times. This scenario, now known as *Anderson localization*, was the starting point of a whole new branch of research on localization in disordered systems [17, 41, 66–69]. It was later generalized from single particles to interacting many-body spin systems where the phenomenon is called *many-body localization (MBL)* in honor to its conceptual predecessor [11–13].

The most studied model is the paradigmatic Heisenberg XXZ chain with random on-site potentials:

$$H_{XXZ} = J \sum_i \left(S_x^{(i)} S_x^{(i+1)} + S_y^{(i)} S_y^{(i+1)} + \Delta S_z^{(i)} S_z^{(i+1)} \right) + \sum_i h_i S_z^{(i)} \quad (1.11)$$

Here $S_\alpha^{(i)}$ denotes the spin- $\frac{1}{2}$ operator in direction $\alpha \in \{x, y, z\}$ on site i and $h_i \sim \mathcal{U}[-W, W]$ are independently drawn from a uniform distribution. The width of this distribution W thus regulates the strength of the disorder. As found in many studies, this model exhibits a crossover from a thermalizing regime into a localized regime² at around $W_c \approx 3-4$ for $\Delta = 1$ [14, 18, 20, 22, 70–81]. This means that at sufficiently strong disorder $W > W_c$, the properties of this model differ dramatically from those of a thermalizing system. Most importantly: the eponymous absence of particle transport, which means that local excitations remain put and do not disperse. Note, entanglement can spread albeit very slowly [73, 82–87]. From the spectral perspective, numerical studies confirmed the breakdown of ETH [88–91] and the related absence of volume-law entanglement of the eigenstates, which is replaced by *area-law entanglement* across the whole spectrum [14, 92].

1.2.1 LIOM picture

The properties of a many-body localized system detailed above suggest the interpretation that strong disorder leads to the emergence of new, quasi-local, conservation laws. This idea is further supported by the observation that the energy gap statistic changes from the Wigner-Dyson (typical for thermalizing systems) to a Poissonian distribution [70], which is typical for integrable systems. For the model with on-site disorder as defined in Equation 1.11, it is natural to assume that each $S_z^{(i)}$ will be quasi-conserved in the limit of strong disorder $W \rightarrow \infty$.

Indeed, this perspective of a many-body localized system as an effectively integrable model unifies all the observations made above. It means we can find a basis transformation to write the Hamiltonian in terms of mutually commuting, quasi-local, conserved operators $\tau^{(i)}$, called "local integrals of motion" (LIOM) or "l-bits" such that [15, 16, 93]

$$H = \sum_i h_i \tau^{(i)} + \sum_{i,j} h_{i,j} \tau^{(i)} \tau^{(j)} \dots \quad (1.12)$$

Here quasi-local means that the operator should essentially act on a single site and decay quickly, i.e. exponentially, when moving away from that site. Figure 1.3 shows numerical

² In this work, we follow the terminology of *regime* and *phase* as coined by Morningstar et al. [27].

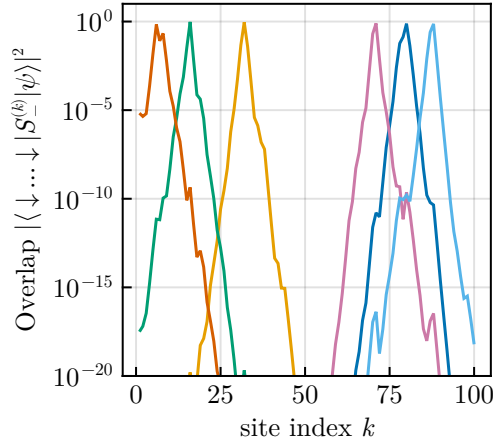


Figure 1.3: Real-space structure of a couple of eigenstates of the XXZ chain with random on-site potentials (cf. Equation 1.11) in the single excitation sector with $W = 15$. The exponential tails are clearly visible.

result for a few eigenstates in the single-excitation sector of the model from Equation 1.11, where we can see that the spin occupies essentially a single site with the occupation decaying exponentially with distance to that site.

Considering a system that can be approximated by a Hamiltonian of the form Equation 1.12, we can see directly that none of the key features of thermalization defined above hold for MBL systems. Since each of the $\tau^{(i)}$ is quasi-local and conserved, some memory of the initial state can always be retrieved by local measurements. From this directly follows, that the measurement depends strongly on the choice of subsystem. However, the *independence of microscopic details* is still partially given: The number of parameters grows with system size but only linearly in the number sites as expected for an integrable system. Thus, knowledge about the LIOMs is very useful and allows to make computations for large systems!

In general finding these LIOMs is not a trivial task. For models with random on-site potentials like Equation 1.11, one can guess that $\tau^{(i)} \approx S_z^{(i)}$ (see e.g. [94]) but for more complicated models like the long-range, bond-disordered system considered in the following chapters, it is not as obvious. While there exist different numerical schemes to compute LIOMs [94–98], we want to focus on gaining insight using an analytical approach falling under name of strong disorder renormalization group or real-space renormalization group (RSRG) [40–46, 99, 100].

1.2.2 MBL in long-range, bond-disordered systems

Considering the mental model for MBL, described above, which is caused by random on-site potentials, it is natural to assume that both stronger and more long-range interactions should be detrimental to localization. Consider a long-range version of Equation 1.11 such as

$$H = \sum_{i,j} \frac{J_{ij}}{|r_i - r_j|^\alpha} \left(S_x^{(i)} S_x^{(j)} + S_y^{(i)} S_y^{(j)} + \Delta_{ij} S_z^{(i)} S_z^{(j)} \right) + \sum_i h_i S_z^{(i)}, \quad (1.13)$$

where $|J_{ij}| = O(1)$, r_i are the locations of the spins and α regulates the spatial decay of the interaction. For this type of model, there are arguments restricting the presence of MBL based on the amount of possible *resonances* for a spin. In this context, two spins i

and j are in resonance if their coupling J_{ij} is larger than the energy difference $|h_i - h_j|$ due to the random potentials. Given a system with spatial dimension d , resonance counting rules out localization if $\alpha \leq 2d$ for systems with $|\Delta_{ij}| > 0$ [33–35, 101] or $\alpha \leq 1.5d$ in the case of an XX model, i.e. $\Delta = 0$ [36]. Later numerical works supported these predictions by numerically studying systems of < 40 spins [21, 102, 103].

Conceptually, these works continue the train of thought from models where random on-site potentials are the source of MBL and generalize to power-law interactions with random coefficients. However, there is also a complementary approach, when starting at models, where MBL is caused solely by disordered interactions, e.g. models like

$$H = \sum_i J_i \left(S_x^{(i)} S_x^{(i+1)} + S_y^{(i)} S_y^{(i+1)} + \Delta_i S_z^{(i)} S_z^{(i+1)} \right), \quad (1.14)$$

where the J_i are independently drawn from some distribution. These *bond-disordered* models also feature MBL (see e.g. [104]) but the LIOMs are much less obvious. They are usually tackled by the real-space renormalization group (RSRG) technique (see [40–43] for reviews). The general principle of the RSRG approach is to iteratively eliminate the strongest bond of the system by freezing the spins sharing this bond into one of the eigenstates of their interaction Hamiltonian and deriving new couplings for surrounding spins perturbatively. This is a good approximation, if the system is sufficiently disordered such that the strongest bond dominates all other couplings in its vicinity. Interestingly, the elimination step *increases* the disorder in the system, such that each successive elimination makes less and less error [99]. Thus, the system's coupling distribution flows towards the *infinite randomness fixed point* where the elimination step becomes exact and the coupling distribution converges to a power-law distribution. Originally, RSRG was used to find the ground state properties of bond-disordered systems [44, 45, 99, 105, 106] and was generalized later to also compute dynamical properties [46, 107–109] or study excited states [47, 104, 110]. This line of work culminated in a general theory of the MBL transition for these one-dimensional, bond-disordered, model with nearest neighbor interactions [100].

Generalizing nearest-neighbor, bond-disordered models to power-law interactions does not significantly change the story from the perspective of the RSRG approach and localization is predicted to persist even without on-site potentials [48, 49, 111]. Subsequently, numerical studies in small systems confirmed the presence of a localization crossover [50–52]. This causes tension with the resonance counting arguments which predict the total absence of localization, because without on-site potentials every spin is considered in resonance with every other spin. This dramatic difference ultimately boils down to the treatment of resonances: Where resonance counting treats every possible resonance on the same footing, RSRG essentially considers only the strongest resonance and eliminates it perturbatively. This elimination assumes a strong hierarchy of interaction timescales associated with the resonances. After the elimination, the other previously possible resonances are no longer resonant with the newly created states. In the end, it boils down to whether the RSRG perspective is justified, i.e. whether a given system has a strong enough separation of scales locally. In this thesis, we aim to contribute to an answer by studying a system that can also be realized by a Rydberg-based quantum simulator to examine the validity of the RSRG prescription in large system. The specific experiment is introduced in the next section.

1.3 USING COLD RYDBERG GASES TO PROBE THERMALIZATION

Rydberg atoms, i.e., atoms in highly excited states, are a versatile platform for quantum simulation experiments due to their long coherence times and high degree of tunability [112–115]. The particular setup considered in this thesis does not employ tweezers, i.e. small traps for single atoms that can be manipulated individually, but instead traps a large amount of ^{87}Rb atoms as a thermal cloud³. The subsequent Rydberg excitation thus produces a different spatial configuration in each run of the experiment. This has the down-side that local control is very limited. However, the great advantage of this setup is the larger number of Rydberg atoms, which can well be in the thousands, in comparison to experiments using tweezers, which top out at a few hundreds of Rydberg atoms [114].

Using two different Rydberg states to encode the spin- $\frac{1}{2}$ degrees of freedom, this experiment naturally realizes a Heisenberg XXZ model [116, 117]

$$H = \sum_{i < j} J_{ij} \left(S_x^{(i)} S_x^{(j)} + S_y^{(i)} S_y^{(j)} + \Delta S_z^{(i)} S_z^{(j)} \right). \quad (1.15)$$

Here the interactions $J_{ij} \propto |r_i - r_j|^{-\alpha}$ decay as power-law of the spatial separation with $\alpha = 3$ (dipole-dipole) or $\alpha = 6$ (van der Waals) depending on the chosen states (cf. Figure 1.4).

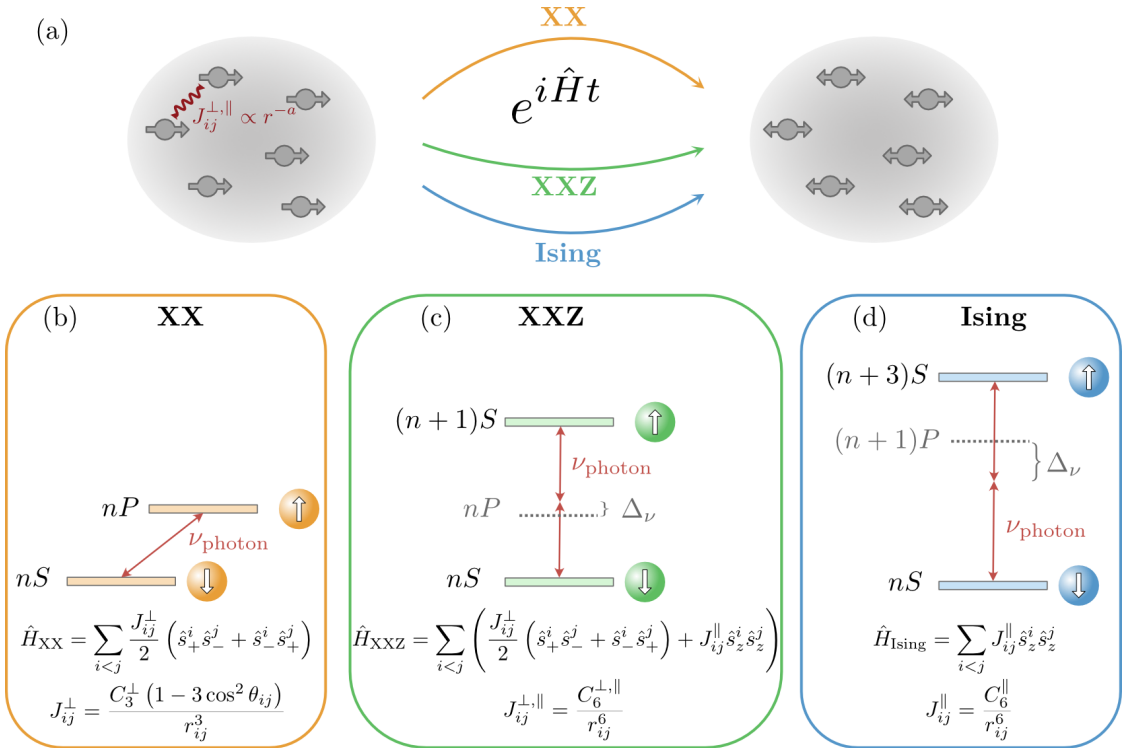


Figure 1.4: Schematic overview of the experimental features. (a) Spins are randomly distributed in space and feature power-law interactions and can evolve under different Heisenberg Hamiltonians. Depending on the choice of states, the experiment can realize XX (b), XXZ (c) and Ising (d) models. Taken from [C].

³ Note, the temperature of the cloud is very low. Thus, the atoms' position don't change much over the course of a run.

While the Rydberg atoms are positioned randomly in each shot, there is a way to control the strength of the randomness. This is enabled by the Rydberg blockade, which shifts the Rydberg excitation of a groundstate atom off resonances if another Rydberg atom is close by [118]. Thus, Rydberg atoms effectively enforce a certain minimal distance r_b among them, where r_b is the blockade radius. Tuning the sample's density changes the distances between the atoms, e.g. given the Wigner-Seitz radius a_0 , but keeps the blockade radius r_b constant. Using these two length scales, we can manipulate the width of the coupling distribution (cf. Figure 1.5): At high density, the spins need to pack tight and there is simply no room for large variations of the nearest neighbor distance r_{NN} [cf. Figure 1.5(a) and (d)]. Conversely, at very low densities there is almost no correlation in the spin's locations [cf. Figure 1.5(c) and (f)].

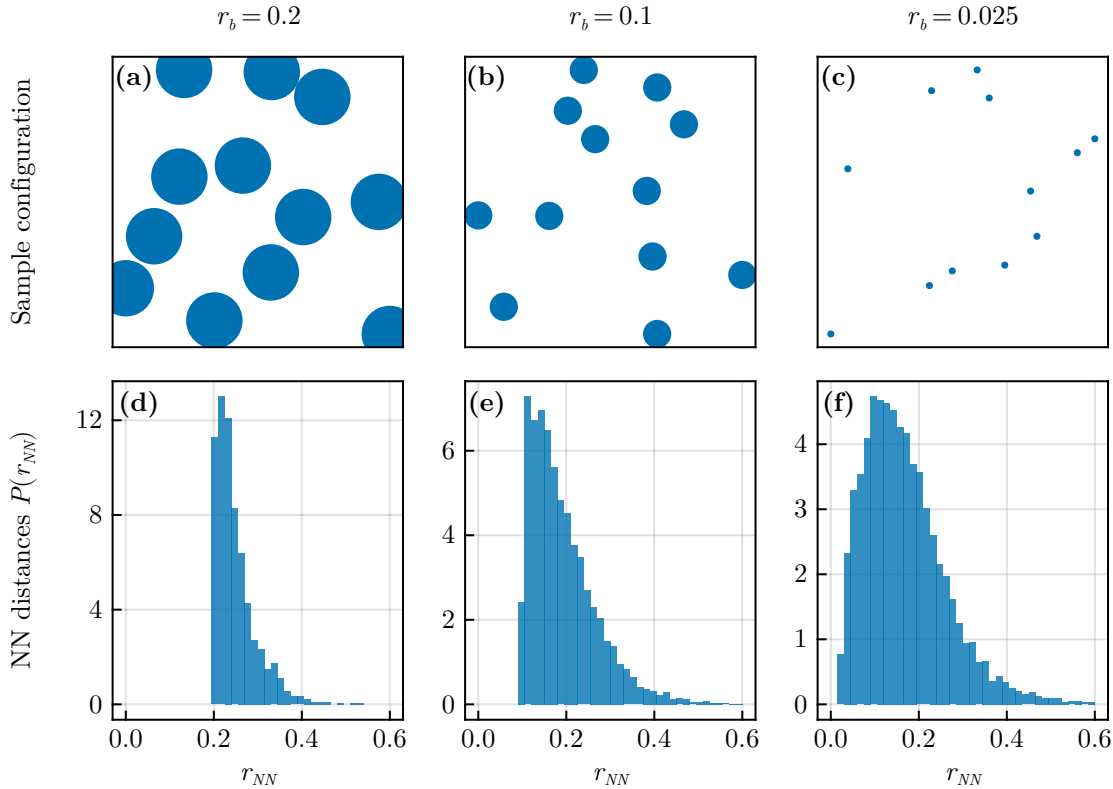


Figure 1.5: Example configurations (top row) and corresponding nearest-neighbor distance distributions (bottom row) for high density/weak disorder (left column), intermediate density/disorder (middle column) and low density/strong disorder (right column).

In summary, this Rydberg quantum simulator allows for the exploration of different Heisenberg-type models with different interaction power-law exponents and tunable disorder strength all within the same experiment. This makes it an ideal testbed for exploring the physics of disordered long-range models.

In this chapter, we address the question: Does the model defined in Equation 1.15 exhibit a localization crossover for sufficiently strong disorder? To this end, we compute the level-spacing ratio [18], Thouless parameter [74] and half-chain entropy to detect the crossover into a localized regime and use the shot-to-shot variance of the half-chain entropy to perform finite size scaling of the crossover's location. Indeed, all indicators confirm the presence of a localized regime. Remarkably, the location of the crossover in this system appears to be significantly more stable than in systems with random on-site potentials. Additionally, we employ the strong disorder/real-space renormalization group (RSRG) approach to show that the quasi-conserved quantities are given by strongly interacting pairs of spins, which demonstrate numerically by computing participation ratios between the approximated and exact eigenbases.

In summary, we find that for sufficiently strong disorder the complicated many-body system given by Eq. 1.15 can be well approximated by an integrable model of pairs:

$$\begin{aligned} H_{pairs} = & \sum_{\langle i,j \rangle} \left(S_x^{(i)} S_x^{(j)} + S_y^{(i)} S_y^{(j)} + \Delta S_z^{(i)} S_z^{(j)} \right) \\ & + \sum_{\langle i,j \rangle} \frac{\Delta}{4} (J_{i,i'} + J_{i,j'} + J_{j,i'} + J_{j,j'}) \left(S_z^{(i)} + S_z^{(j)} \right) \left(S_z^{(i')} + S_z^{(j')} \right) \end{aligned} \quad (2.1)$$

Here $\sum_{\langle i,j \rangle}$ denotes a sum over specific pairs of spins identified by RSRG. These pairs are found iteratively: One defines the two spins linked by the strongest coupling in the system to be a pair, removes them and then continues with the remaining spins until every spin is paired up. This model of pairs is validated experimentally in Chapter 4 and proves to give very accurate results.

Pair localization in dipolar systems with tunable positional disorder

Adrian Braemer^{1,*}, Titus Franz¹, Matthias Weidemüller¹, and Martin Gärttner^{1,2,3,†}

¹Physikalisches Institut, Universität Heidelberg, Im Neuenheimer Feld 226, 69120 Heidelberg, Germany

²Kirchhoff-Institut für Physik, Universität Heidelberg, Im Neuenheimer Feld 227, 69120 Heidelberg, Germany

³Institut für Theoretische Physik, Universität Heidelberg, Philosophenweg 16, 69120 Heidelberg, Germany



(Received 30 July 2022; accepted 16 October 2022; published 31 October 2022)

Strongly interacting quantum systems subject to quenched disorder exhibit intriguing phenomena such as glassiness and many-body localization. Theoretical studies have mainly focused on disorder in the form of random potentials, while many experimental realizations naturally feature disorder in the interparticle interactions. Inspired by cold Rydberg gases, where such disorder can be engineered using the dipole blockade effect, we study a Heisenberg XXZ spin model where the disorder is exclusively due to random spin-spin couplings, arising from power-law interactions between randomly positioned spins. Using established spectral and eigenstate properties and entanglement entropy, we show that this system exhibits a localization crossover and identify strongly interacting pairs as emergent local conserved quantities in the system, leading to an intuitive physical picture consistent with our numerical results.

DOI: [10.1103/PhysRevB.106.134212](https://doi.org/10.1103/PhysRevB.106.134212)

I. INTRODUCTION

Understanding how an isolated quantum system prepared out of equilibrium can exhibit thermal properties at late times, i.e., how it thermalizes, has challenged quantum physicists for almost a century. The eigenstate thermalization hypothesis (ETH) [1,2] offers a generic mechanism to explain this phenomenon but makes strong assumptions on the structure of energy eigenstates in terms of the matrix elements of local operators. Nonetheless, it has been shown numerically that a large class of quantum systems complies with ETH and thermalizes [3,4]. A notable exception are strongly disordered systems in which transport is absent and the system retains memory of the initial state at arbitrary times [5–8].

This phenomenon, called many-body localization (MBL), has been verified for small systems including, but not limited to, spin systems with random potentials [9–11], random nearest [12–14], and next-nearest-neighbor interactions [15,16], and power-law interactions [17–21] using a combination of exact numerical approaches and heuristic arguments like the strong disorder renormalization group (SDRG) [22–25] to generalize to large systems.

Recently, claims have been made that this localization phenomenology may not be stable in the thermodynamic limit due to thermal inclusions [26–34]. These are small, more ordered subregions thought to thermalize with their surroundings and thus slowly pushing the system toward thermalization. Unfortunately, these regions are very rare and thus only start appearing in large systems far beyond the reach of numerical methods. This raises the question whether this instability is relevant for quantum simulation experiments, being finite in

size and limited by coherence time. In this paper, we only focus on the phenomenology of localization in finite systems and subsequently use the term localized regime instead of a phase, following the terminology of Ref. [28].

Complementary to numerical works, there are a number of experimental results falling into roughly two classes: Experiments with single-particle resolution, including optical lattices [35–38] and trapped ions [39], and experiments based on macroscopic samples, like NV centers in diamond [40] or NMR systems [41]. The former offer precise control, but are rather limited in size, while the latter can realize much larger systems at the expense of flexibility, in particular, lack of programmable disorder. Cold gases of Rydberg atoms implement dipolar dynamics with random couplings (similar to NMR systems or NV centers) and allow for control of the disorder strength and even the power law of the interaction at rather large particle numbers [42], which makes them a powerful platform for studying localization phenomena.

Motivated by recent progress on quantum simulations with Rydberg atoms [42–45], we consider a power-law interacting spin system where the disorder is due to randomly positioned spins respecting a blockade condition, which induces disordered couplings. In this setup, the strength of the disorder can be tuned by changing the density of particles or, equivalently, the minimal distance between them. Starting in an ordered system, where the blockade radius is of order of the mean interparticle distance, we show numerically that this system exhibits a crossover to a localized regime at small blockade and apply a SDRG approach to derive a simple model based on strongly interacting pairs, which captures the properties of the eigenstates in the localized regime well. Our study thus adds to the body of numerical works on MBL, focusing on dipolar systems with tunable positional disorder, and is highly relevant to experimental efforts, as a wide range of quantum simulation platforms feature dipolar interactions.

*adrian.braemer@kip.uni-heidelberg.de

†martin.gaerttner@kip.uni-heidelberg.de

II. LOCALIZATION IN A RYDBERG GAS

A. System

We consider the Heisenberg XXZ spin model described by the Hamiltonian ($\hbar = 1$)

$$\hat{H} = \frac{1}{2} \sum_{i \neq j} J_{ij} \underbrace{\left(\hat{S}_x^{(i)} \hat{S}_x^{(j)} + \hat{S}_y^{(i)} \hat{S}_y^{(j)} + \Delta \hat{S}_z^{(i)} \hat{S}_z^{(j)} \right)}_{\equiv H_{\text{pair}}^{(i,j)}}, \quad (1)$$

where $\hat{S}_{\alpha}^{(k)}$ (with $\alpha \in \{x, y, z\}$) denotes the spin- $\frac{1}{2}$ operators acting on the k th spin. The coupling J_{ij} between spins i and j at positions x_i and x_j is given by $J_{ij} = \frac{C_{\alpha}}{|x_i - x_j|^{\alpha}}$, where C_{α} is an interaction coefficient which we set to $C_{\alpha} = 1$. In experimental realizations of this model with Rydberg atoms, the values of the anisotropy parameter Δ and interaction exponent α are controllable via the choice of the Rydberg states encoding the two spin states. The cases $\alpha = 3$, $\Delta = 0$ (dipolar exchange) and $\alpha = 6$, $\Delta \approx -0.7$ (van der Waals) have been realized experimentally [42,44]. For typical cloud temperatures and timescales of the spin dynamics, the atom positions can be regarded as fixed (frozen gas approximation).

During the initial Rydberg excitation, the spins are subjected to the Rydberg blockade [46], which means no two spins can be closer than some distance r_b , called the blockade radius. This feature allows one to tune the strength of disorder via the sample's density: In a very dilute sample, the mean interspin distance is much larger than the blockade radius r_b and thus positions are essentially uncorrelated. In the other extreme, the spins are tightly packed and exhibit strong spatial correlations.

We quantify the strength of disorder by the ratio W of the system's total volume V over total blocked volume V_{block} or, equivalently, by the ratio of Wigner-Seitz radius a_0 , which is half of the mean interspin distance, to the blockade radius r_b to the power of the dimension d :

$$W = \frac{V}{V_{\text{block}}} = \left(\frac{a_0}{r_b} \right)^d. \quad (2)$$

For $d = 1$, the minimal value of $W_{\min} = \frac{1}{2}$ is attained for a translationally invariant chain with spacing $2a_0 = r_b$, as illustrated in Fig. 1(a).

B. Effective pair description

This model differs from the random field Heisenberg model, which has been studied extensively in the MBL literature, as no disordered potentials are considered. Thus it may not be immediately apparent why this system features localization and what constitutes the local conserved quantities akin to the l -bits [47] in the standard scenario. Here we provide a phenomenological picture in the spirit of the SDRG, suggesting that localization should appear due to strongly interacting pairs.

Consider a strongly disordered cloud of N spins described by Eq. (1) like the example depicted in Fig. 1(b). Due to the power-law interactions, coupling strengths vary strongly between different pairs of atoms, symbolized by the width and brightness of the green lines. This motivates us to employ a perturbative treatment, in which we single out the strongest

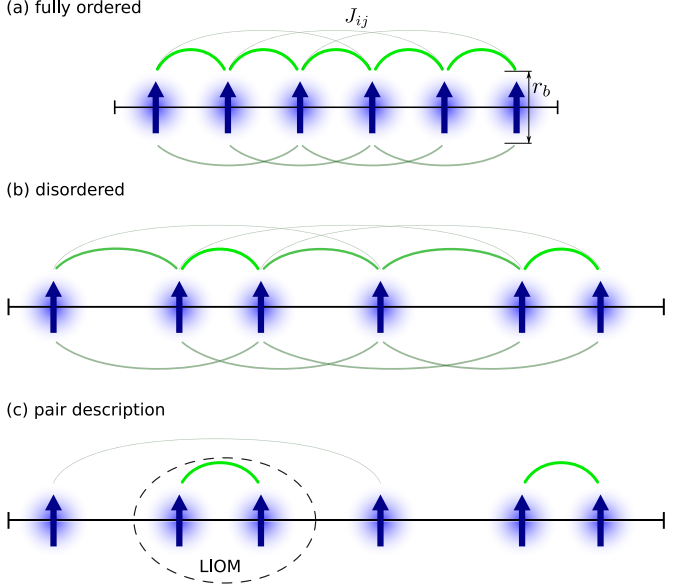


FIG. 1. Pair description. The blockade constraint (blue shadings) enables tuning of disorder in the couplings (green lines) from fully ordered (a) to disordered (b). In the latter case, a perturbative treatment to first order yields a description in terms of strongly correlated pairs (c) subject to an Ising-like interaction (not depicted). These pairs constitute local integrals of motion (LIOM).

pair coupling and consider all other couplings as a perturbation. In the example shown in Fig. 1(b), the two rightmost spins share the strongest coupling and we can see that it is much stronger than the other couplings of either one of the spins to the rest of the system. Using perturbation theory to first order, we find that the pair of spins almost decouples from the rest of the system, leaving only an effective Ising-like interaction, which is unimportant for the further procedure and thus not shown in the figure. For details on the calculations involved, see Appendix A.

We may now repeat this procedure of eliminating couplings between the pairs and the rest of system by identifying the next strongest interaction among the remaining spins which, in this example, is the coupling between the second and third spin. Eliminating the respective couplings as well leaves us with the effective pairs shown in Fig. 1(c). Note that in an ordered system, as shown in Fig. 1(a), this perturbative treatment is not applicable as not all neglected couplings can be considered small. We also note that the order of eliminations is not important as long as each time the inner-pair coupling is much larger than the couplings between the pair and the rest. Concretely, for the given example, choosing the coupling between spins 2 and 3 in Fig. 1(b) first in the pair elimination process does not change the result.

The great advantage of this ansatz is that we can now give a simple description of the whole many-body spectrum. Diagonalizing H_{pair} [see Eq. (1)], we find two maximally entangled eigenstates $|\pm\rangle = 1/\sqrt{2}(|\uparrow\downarrow\rangle \pm |\downarrow\uparrow\rangle)$ at energies $E_{\pm} = \pm 2 - \Delta$ and two degenerate states $|\uparrow\uparrow\rangle, |\downarrow\downarrow\rangle$ at energy $E_d = \Delta$, which we will refer to as $|\uparrow\uparrow\rangle, |\downarrow\downarrow\rangle$. The Ising-like interaction between pairs does not act on the entangled states $|\pm\rangle$ and is diagonal with respect to $|\uparrow\uparrow\rangle, |\downarrow\downarrow\rangle$. Thus, in the pair picture, the

eigenstates of the full system are now given by tensor products of these four pair eigenstates. We refer to this basis as the pair basis.

In the many-body spectrum, the degeneracy between the pair states $|\uparrow\uparrow\rangle$ and $|\downarrow\downarrow\rangle$ is lifted due to the emerging Ising-like interaction. However, we note that this splitting is small compared to the splitting between the other pair eigenstates as it emerges from first-order perturbation theory.

The pair picture is analogous to the l -bit picture often used in MBL, where strong local disorder potentials lead to the emergence of quasilocal conserved quantities $\hat{\tau}^{(i)} \sim \hat{\sigma}_z^{(i)}$ [47,48]. Here, we see that each projector on a pair's eigenstate constitutes an approximately conserved quantity and hence is a local integral of motion (LIOM). Thus, we established a description akin to the l -bit picture of MBL for this disordered Heisenberg model, where the role of LIOMs is taken by strongly interacting pairs.

While this ansatz is heuristic and neglects all higher resonances, that may play a crucial role in delocalizing the system, it will nonetheless turn out to be useful for interpreting and understanding the spectral and eigenstate properties reported in the following.

III. NUMERICAL RESULTS

To minimize boundary effects, we consider a one-dimensional system with periodic boundary conditions [49] of up to $N = 16$ spins governed by Eq. (1) and perform exact diagonalisation on the sector of smallest positive magnetization. We fix the interaction exponent to $\alpha = 6$, corresponding to a Van der Waals interactions, and set $\Delta = -0.73$ (cf. Ref. [42]). We do not expect a strong dependence of our results on the precise value of Δ as long as one steers clear from regions around points where additional symmetries emerge.

For each disorder strength W , we generate 2000 configurations of random spin positions, perform a full diagonalization and compute several well-established indicators for the localization transition from the spectrum. We always average over all eigenstates/-values as restricting to the bulk of the spectrum does not lead to qualitative changes in the observed behavior. The statistical error resulting from disorder averaging is smaller than the thickness of the lines in all figures unless indicated otherwise. For a description of the algorithm for choosing the configurations, we refer to Appendix C. All code used for this paper can be found in Ref. [50].

The following sections discuss different indicators of localization with the aim to establish the localization crossover in this model and employ the pair model for interpretation and predictions. The last section directly compares the pair basis to the eigenstates, thus demonstrating its validity.

A. Level spacing ratio

The spectral average of the level spacing ratio (LSR), defined as [51]

$$\langle r \rangle = \frac{1}{|\mathcal{H}|} \sum_n \min \left(\frac{E_{n+2} - E_{n+1}}{E_{n+1} - E_n}, \frac{E_{n+1} - E_n}{E_{n+2} - E_{n+1}} \right), \quad (3)$$

is a simple way of characterizing the distribution of differences between adjacent energy levels. For thermalizing

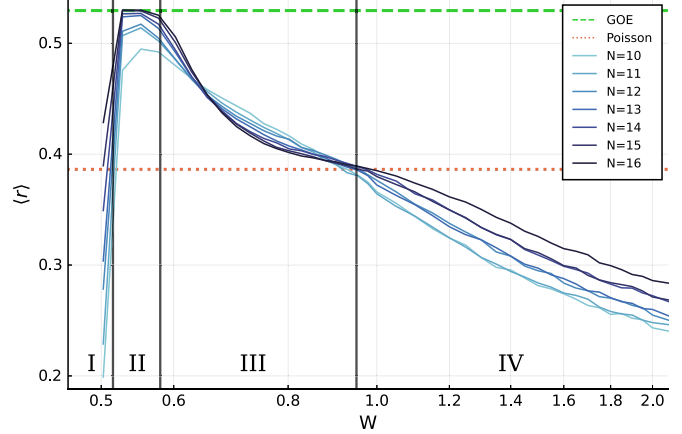


FIG. 2. Level-spacing ratio. With increasing disorder, the LSR shows a crossover from an ergodic value to its Poissonian value and below. We identify four major regions where the physics is governed by (I) translational symmetry breaking, (II) thermal behavior, (III) the localization crossover and (IV) localization. The horizontal lines show random-matrix theory predictions.

(ergodic) systems, the Hamiltonian is expected to show a mean LSR resembling a random matrix from the Gaussian orthogonal ensemble because its eigenvectors essentially look like random vectors. Thus one can use random matrix theory to obtain $\langle r \rangle_{\text{thermal}} = 4 - 2\sqrt{3} \approx 0.536$ [52].

On the other hand, in localized systems the eigenvalues follow a Poisson distribution, since they are essentially sums of randomly distributed energies from the l -bits the system consists of. Computing the mean LSR in this case yields $\langle r \rangle_{\text{MBL}} = 2 \ln 2 - 1 \approx 0.386$ [52].

Comparing with the numerical results in Fig. 2 and focusing on the central parts first, we find the mean LSR reaches its thermal value for large enough systems and weak disorder (II) dropping toward the Poissonian value for stronger disorder (III). With growing system size, the thermal plateau (II) broadens, marking a parameter region where the system appears ergodic. But while the plateau broadens, the drop-off (III) for increasing disorder strength becomes steeper, meaning the crossover becomes sharper as the system gets larger.

Considering very strong disorder (IV), the mean LSR drops even below the Poissonian value, which indicates level attraction. This effect can be explained by the pair model: As stated earlier, the $|\uparrow\uparrow\rangle$ and $|\downarrow\downarrow\rangle$ states' degeneracy is lifted by the effective Ising-like terms from first-order perturbation theory, which means the split is of smaller magnitude compared to the intra-pair interactions. For small systems with comparatively low spectral density, this means that the small lifting likely fails to mix the formerly degenerate states into their surrounding spectrum. Thus, the LSR still reflects the near degeneracy within the pairs, leading to level attraction. Based on this interpretation, we expect this effect to diminish for larger systems with the spectral density growing. In fact, this trend is already visible in Fig. 2.

A similar argument can be made at very weak disorder (I): Here the source of the degeneracy is the proximity to the perfectly ordered case at $W = 0.5$, which has an additional translation invariance. Weak disorder breaks that symmetry

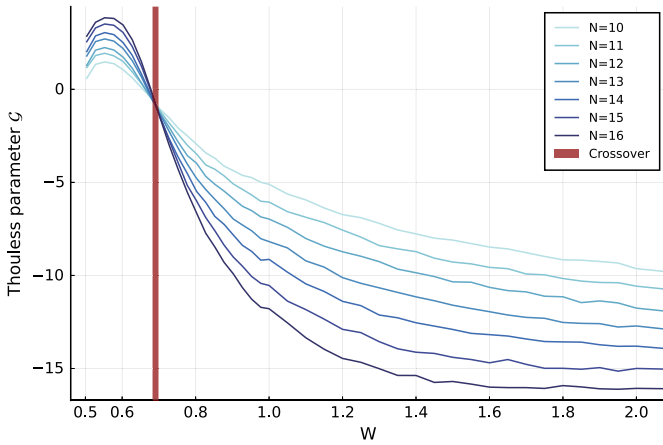


FIG. 3. Thouless parameter. Spectral and disorder averaged \mathcal{G} versus disorder strength W . Data shown uses local operator $\hat{V}_1 = 2\hat{S}_z^{(1)}$

but couples the symmetry sectors only weakly, leading again to a very small energetic splitting of degenerate states. We want to emphasize the reason for level attraction being very different in nature in (I) and (IV): Whereas in (I) the system is close to a system with obvious conserved quantities due to symmetries, in (IV) there is the emergent integrability of the MBL regime [8]. Nevertheless, we expect region (I) to become less pronounced for larger systems continuing the trend visible in Fig. 2.

We conclude that, in analogy to standard MBL, we find a crossover in the level spacing distribution from a regime with level repulsion to Poissonian gaps indicating a localization crossover. At very strong disorder, we even find a region with level attraction, the source of which can be explained by the effective pair model.

B. Thouless parameter

Complementary to eigenvalue statistics, we also probe eigenstate properties by computing the Thouless parameter

$$\mathcal{G}_n = \ln \frac{|\langle n | \hat{V} | n+1 \rangle|}{E'_{n+1} - E'_n}, \quad (4)$$

introduced by Serbyn *et al.* [53]. This quantity is akin to the Thouless conductance in single particle systems and quantifies how well two states $|n\rangle, |n+1\rangle$ with perturbed energies $E'_n = E_n + \langle n | V | n \rangle$ are coupled by a local perturbation \hat{V} . In the thermal phase, states of similar energy will have similar spatial structures, whereas in the localized phase, eigenstates are products of LIOM eigenstates and thus typically vary drastically from one to the next. One can derive the scaling of the average \mathcal{G} in the thermal regime to be $\mathcal{G} \propto \log |\mathcal{H}|$ and in the localized regime to be $\mathcal{G} \propto -\log |\mathcal{H}|$, leading to the natural definition of the location of the crossover to be the point where $\mathcal{G} = \text{const}$ [53].

Figure 3 shows results using local operator $\hat{V}_1 = 2\hat{S}_z^{(1)}$. Data for local operators $\hat{V}_2 = 4\hat{S}_z^{(1)}\hat{S}_z^{(2)}$ and $\hat{V}_3 = \hat{S}_+^{(1)}\hat{S}_-^{(2)} + \text{H.c.}$ is visually identical. There is a very clear point where all curves intersect each other, indicating the crossover's location.

To the right of the crossing point in the localized regime, the curves are roughly evenly spaced, reflecting the expectation of $\mathcal{G} \propto -\log |\mathcal{H}|$, clearly signaling the localized regime. The apparent absence of a drift of the transition point with system size is in contrast to observations in power-law interacting models with on-site disorder and will be further discussed in the next subsection.

C. Half-chain entropy

Having shown the presence of a localization crossover, we now demonstrate that our effective pair model is indeed a good approximation. We start by probing the half-chain entropy, $S = -\text{Tr} \rho_A \log_2 \rho_A$, with $\rho_A = \text{Tr}_B(\rho)$, i.e., the entanglement entropy between two halves of the chain. For that, we select $\lfloor \frac{N}{2} \rfloor$ consecutive spins and trace out the rest, resulting in two cuts due to the periodic boundary conditions, and average over all N possible choices of connected subsystems and all eigenstates.

In an ergodic system, all bulk states should exhibit volume-law entanglement, meaning $S \propto N$. In contrast, in a localized setting all states show area-law entanglement, which for $d = 1$ means $S = \text{const}$ [3,54].

To compute the half-chain entropy predicted by the pair model, we need to determine how many pairs are divided by each cut and how often these pairs are found in one of the entangled states $|\pm\rangle = 1/\sqrt{2}(|\uparrow\downarrow\rangle \pm |\downarrow\uparrow\rangle)$. Not all pairs consist of adjacent spins [see Fig. 1(c)], so a cut can separate more than one pair. The amount of cut bonds is easily determined from the position data alone by adding up the distances between paired spins. Respecting periodic boundary conditions of the system yields an additional factor of 2, since there are two cuts needed to divide the chain.

Considering the entropy contribution of a single bond, if we were to average over all possible configurations of pair states, each cut bond would contribute half a bit of entanglement on average, as half of the pair states are maximally entangled and the other half not entangled at all. However, here we consider the sector of smallest positive magnetization, which yields a slightly larger entropy, because it favors the entangled states $|\pm\rangle$ (which have zero net magnetization) over the fully polarized ones. This modification can be computed exactly (see Appendix B for details).

Taking into account both the effects of extended pairs and of the fixed total magnetization, we can compute a prediction for the entanglement entropy directly from the interaction matrix J_{ij} . Figure 4 shows both the numerically computed values for different system sizes (solid) and pair-model prediction (dashed).

We clearly see the change between the ergodic and localized regime for the numerically computed data. For strong disorder, all lines collapse, confirming on one hand the area law entanglement expected in the localized phase and, on the other hand, validating the pair model as it predicts the strong-disorder limit with high accuracy. Figure 4(b) magnifies the strong-disorder regime showing that the pair-model prediction in fact slightly overestimates the half-chain entropy for very strong disorder. This might indicate that there are spins that do not pair up perfectly, not forming a maximally entangled Bell pair. It is plausible that this happens at late stages of the

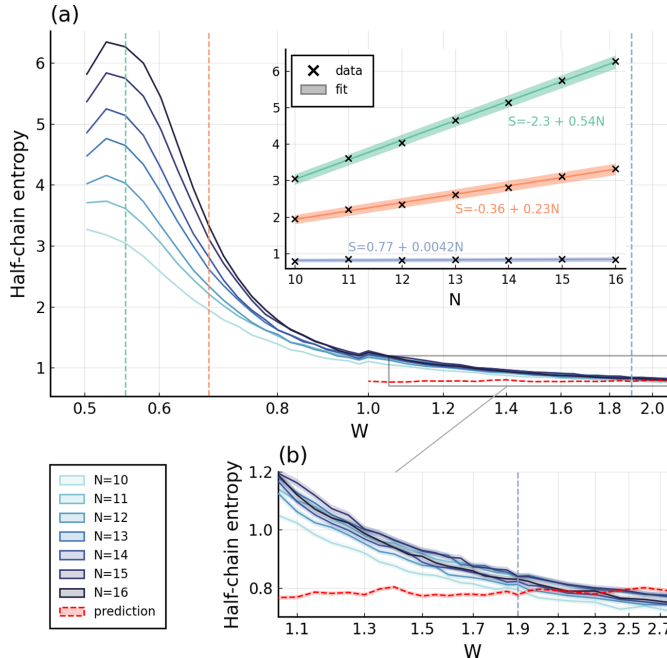


FIG. 4. Half-chain entropy. Average over possible cut locations and over disorder realizations for different system sizes as a function of disorder strength. Also shown is the prediction derived from a pair description, computed from position data for $N = 16$ (red dashed line), see B for details. Inset: Linear fits at fixed disorder strengths indicated by the vertical dashed lines in the main panel. Shaded areas indicate uncertainty from the fit; (b) magnifies the strongly disordered regime of (a). Shaded areas indicate statistical uncertainty from disorder averaging.

pair elimination procedure described in Sec. II B when the spins of a pair can have couplings that are stronger than the pair's internal coupling but the spins associated with these stronger couplings are already eliminated. We thus interpret this feature as an indication of the limitations of a simple pair description.

Another piece of information that we can readily access via the half-chain entropy is the location of the crossover. To determine it, we calculate the variance of the half-chain entropy over different disorder realizations and extract the maximum for each chain length N via a quadratic fit [15,55]. Figure 5 shows no strong dependence of the crossover point on N in the range of accessible system sizes. Indeed, the crossover does not seem to drift significantly, which is in contrast to models with onsite disorder, see, e.g., Refs. [18,55,56], where finite-size drifts of the transition point are commonly observed.

Interestingly, the crossover location is very close to the density given by Rényi's parking constant, or jamming limit, which is the maximal density attainable by randomly placing nonoverlapping unit intervals on the number line [57]. As in experiments with Rydberg spins, atom positions result from such a random process; this could imply that these experiments might not be able to reach the densities required for observing the fully ergodic regime. However, it is unclear how the crossover location generalizes to higher dimensions and larger systems.

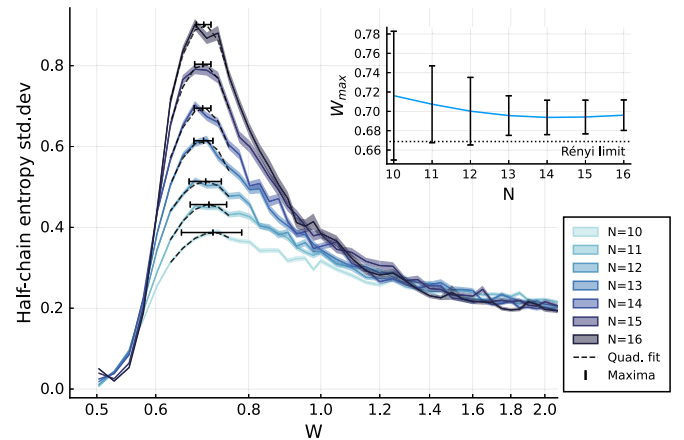


FIG. 5. Standard deviation of half-chain entropy. The main plot shows the standard deviation of the half-chain entropy across disorder realizations exhibiting a clear maximum around which a quadratic polynomial is fitted. Shaded areas indicate statistical uncertainty. Inset: Position of the maximum as extracted by the fits. Errors shown are statistical errors from the fits.

D. Participation ratio

Now that we have seen that the pair model captures the spatial entanglement structure of the exact eigenstates, we compare the predicted eigenstates directly to the exact ones by computing the participation ratio (PR). Intuitively, it measures how many states of a reference basis $\mathcal{B} = \{|b\rangle\}$ contribute to a given eigenstate $|\phi_n\rangle$:

$$\text{PR}_{\mathcal{B}}(|\phi_n\rangle) = \left(\sum_{b \in \mathcal{B}} |\langle b | \phi_n \rangle|^4 \right)^{-1}. \quad (5)$$

Usually, in the MBL context, one chooses a product basis as reference because a low PR relative to product basis means the eigenstates are close to product states. “Low” in this context means a sublinear scaling of PR with the dimension of the Hilbert space \mathcal{H} : $\text{PR} \propto |\mathcal{H}|^\tau$, where $\tau < 1$. In contrast, a thermalizing system always has $\text{PR} \propto |\mathcal{H}|$ with respect to any product basis [58–60].

Here we compare two different reference bases, the z -basis $\mathcal{Z} = \{|\uparrow\rangle, |\downarrow\rangle\}^{\otimes N}$ and the pair basis $\mathcal{P} = \{|\pm\rangle, |\uparrow\downarrow\rangle\}^{\otimes N/2}$, introduced above, to determine how well the pair model describes the eigenstates. If the pair basis \mathcal{P} was exactly equal to the eigenbasis, its PR would be exactly 1. In this case, the expected PR with respect to the z -basis, averaged over the Hilbert space, \mathcal{Z} will be $1.5^{N/2}$, because a single pair has an average PR of 1.5. However, we only consider the sector of smallest positive magnetization, which increases the expected PR by a similar line of reasoning as for the entropy in the previous section.

Figure 6(a) shows the PR relative to the two reference bases as a fraction of the Hilbert space dimension $|\mathcal{H}|$. We see that the weakly disordered regime indeed has ergodic eigenstates as the curves collapse onto each other. The small offset between the two reference bases is plausible, since a thermal systems eigenstates express volume law entanglement and thus the overlap with a product basis like \mathcal{Z} is minimal. The states of the pair basis contain pairwise entanglement and

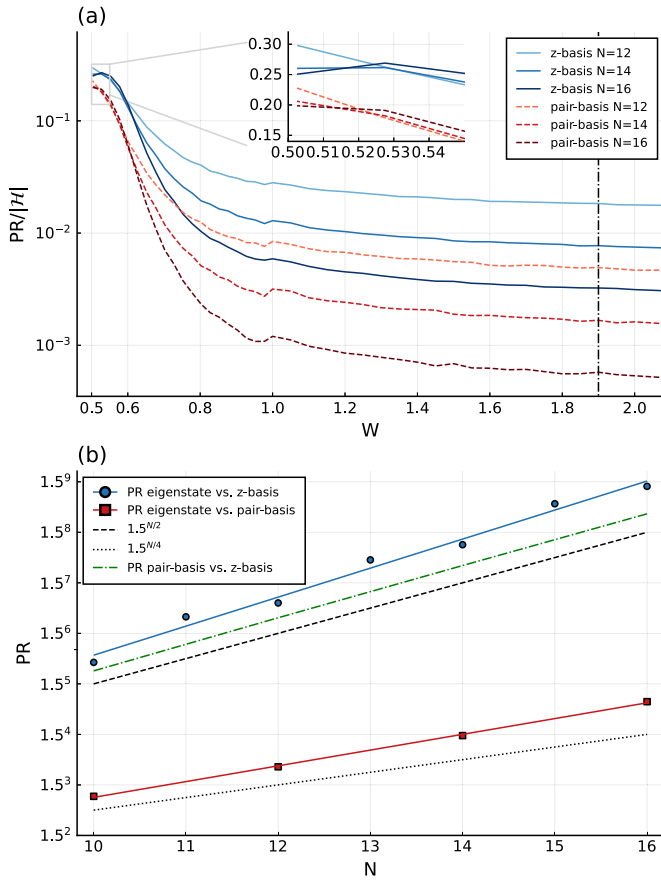


FIG. 6. Participation ratio. (a) PR relative to Hilbert space dimension $|\mathcal{H}|$ for different reference bases: z -basis in blue, pair basis in red. The inset shows a magnification of the region toward perfectly ordered systems. (b) shows the growth in absolute PR with increasing system size in the localized regime. The used value of W is indicated by the dash-dotted line in (a).

are thus a bit closer, which manifest as slightly lower PR. Around $W = 0.6$, the scaling with $|\mathcal{H}|$ starts to change to a sublinear relation as we crossover to the localized regime.

Checking the PR deep in the localized phase (at $W = 1.9$) in Fig. 6(b), we can see that the PR relative to the z -basis (blue line) is slightly, but systematically, larger than the pair model's prediction (dashed green line). Consistent with this observation, we see that the PR relative to the pair basis (red line), while being much smaller, is still not constant across system sizes.

We conclude that the pair states offer a good first-order approximation of the true eigenstates, but there are higher order resonances that lead to further hybridization for some states. The exponent of the remaining dependence on system size is close to $N/4$, which hints at effects stemming from interactions between pairs.

IV. CONCLUSIONS

We analyzed a disordered Heisenberg XXZ spin model with power-law interaction and positional disorder, which is naturally realized by many quantum simulation platforms. Among these, cold Rydberg gases allow for easy tuning of the

disorder via the sample's density due to the Rydberg blockade. By using standard MBL indicators, we showed numerically that this system undergoes a localization crossover, which we interpreted in terms of a simple physical model derived using an SDRG ansatz. This model, consisting of an effective Ising model of strongly interacting pairs of spins, was verified by considering the PR of eigenstates with the conjectured basis, which is drastically reduced compared to the PR relative to the z -basis. Still, there was a weak dependence on system size left, which means there are higher order corrections to our model. Nonetheless, we also showed that this simple model can already predict the entanglement entropy of the system nearly perfectly.

With this model at hand, we can now make predictions for large systems which may be tested in quantum simulation experiments. Of course, one of the most interesting questions will be whether the location of the crossover shifts toward stronger disorder for large systems, indicating a transition at infinite disorder strength in the thermodynamic limit. For this purpose, the easy tunability of the disorder is a great advantage as both sides of the crossover can be probed on the same platform by changing the system parameters. Remarkably, our small-scale numerical study showed almost no finite-size drift. This could indicate that localization in this model is more stable than in similar models against resonances. We leave this investigation for future work.

Note that the pair model cannot be used to predict the crossover itself as it essentially requires the assumption that one can find strongly interacting pairs, which is only justified in the strongly disordered regime. Recent arguments for the absence of localization postulate the existence of rare thermal subregions within the system [26,26–34]. This would of course break the base assumption of the pair model. A possible direction for future research would be to extend the model to include not only pairs but also larger clusters, which would require one to track all kinds of interactions between clusters of different sizes.

Interestingly, the dimensionality of the system does not directly influence the pair model. As long as the couplings are sufficiently disordered, such that pairs can be defined, it will be a good approximation. Thus, it suffices to study how the distribution of couplings changes with respect to the dimensionality d of the space and coupling power α . Similar to resonance counting arguments [61], we conjecture the requirement $d < \alpha$ for the pair model to be applicable. Hence, we expect our results, while acquired in $d = 1$, to generalize well to $d > 1$.

ACKNOWLEDGMENTS

We thank Dima Abanin for his stimulating input. For numerical simulations, we used the Julia programming language [62]. The authors acknowledge support by the state of Baden-Württemberg through bwHPC and the German Research Foundation (DFG) through Grant No. INST 40/575-1 FUGG (JUSTUS 2 cluster). This paper is supported by the Deutsche Forschungsgemeinschaft (DFG, German Research Foundation) under Germany's Excellence Strategy EXC No. 2181/1-390900948 (the Heidelberg STRUCTURES

TABLE I. Eigensystem of H_{pair} .

State k	Energy E_k	Vector $ k\rangle$
1	$2 - \Delta$	$\sqrt{2}^{-1}(\uparrow\downarrow\rangle + \downarrow\uparrow\rangle)$
2	Δ	$ \uparrow\uparrow\rangle$
3	Δ	$ \downarrow\downarrow\rangle$
4	$-2 - \Delta$	$\sqrt{2}^{-1}(\uparrow\downarrow\rangle - \downarrow\uparrow\rangle)$

Excellence Cluster) and under SFB 1225 ISOQUANT No. 273811115.

APPENDIX A: DERIVATION OF PAIR PICTURE

Here we derive the pair model of the main text by means of Schrieffer-Wolff transformations [63]. Starting with the full Hamiltonian of the system,

$$\hat{H} = \frac{1}{2} \sum_{i \neq j} J_{ij} \underbrace{(\hat{S}_x^{(i)} \hat{S}_x^{(j)} + \hat{S}_y^{(i)} \hat{S}_y^{(j)} + \Delta \hat{S}_z^{(i)} \hat{S}_z^{(j)})}_{\equiv H_{\text{pair}}^{(i)(j)}}. \quad (\text{A1})$$

Suppose without loss of generality that $J_{12} \gg J_{1j}, J_{2j}$ and set $H_0 = J_{12} H_{\text{pair}}^{(1)(2)}$ and $V = H_{XXZ} - H_0$. We label the eigenvectors and eigenenergies of H_{pair} as shown in Table I.

The projectors on these states are consequently named $P_k = |k\rangle\langle k| \otimes \mathbb{1}$, but since the middle two states are degenerate, we need to use the projector on the full eigenspace and call it $P_{23} = P_2 + P_3$.

To first order, only diagonal terms $P_k V P_k$ contribute, which in this case means the pair decouples and only an effective Ising term remains:

$$\hat{H} = \sum_{i,j} J_{ij} \hat{H}_{\text{pair}}^{(i)(j)} \quad (\text{A2})$$

$$\approx J_{12} \hat{H}_{\text{pair}}^{(1)(2)} + \sum_{i,j>2} J_{ij} \hat{H}_{\text{pair}}^{(i)(j)} + \hat{S}_z^{(1)(2)} \sum_{i>2} \tilde{\Delta}_i \hat{S}_z^{(i)} + O(\hat{V}^2), \quad (\text{A3})$$

where $2\hat{S}_z^{(1)(2)} = |\uparrow\uparrow\rangle\langle\uparrow\uparrow| - |\downarrow\downarrow\rangle\langle\downarrow\downarrow|$ is akin to a spin-1 magnetization operator and $\tilde{\Delta}_i = \Delta(J_{1i} + J_{2i})$ is the renormalized Ising coupling. Note that this first order term lifts the apparent degeneracy of the $|\uparrow\uparrow\rangle$ and $|\downarrow\downarrow\rangle$ states. This elimination is a good approximation if the interaction within the pair is much stronger than any other interaction between a spin of the pair and some other spin.

We can now repeat this elimination step with remaining spins by incorporating the effective Ising terms into V . This is justified because its coupling is small and is already first-order perturbation theory, and thus including it into the zeroth order of the next pair would mix expansion orders inconsistently.

Further eliminations now generate effective Ising terms between the states $|\uparrow\uparrow\rangle$ and $|\downarrow\downarrow\rangle$ of the eliminated pairs. After pairing up all spins, we find

$$\hat{H} = \sum_{i,j} J_{ij} \hat{H}_{\text{pair}}^{(i)(j)} \quad (\text{A4})$$

$$\approx \sum_{(i,j)} J_{ij} \hat{H}_{\text{pair}}^{(i)(j)} + \sum_{(i,j), (i',j')} \tilde{\Delta}_{(i,j), (i',j')} \hat{S}_z^{(i)(j)} \hat{S}_z^{(i')(j')} \quad (\text{A5})$$

where the sum over $\langle i, j \rangle$ denotes pairs of spins and $\tilde{\Delta}_{(i,j), (i',j')} = \Delta(J_{i,i'} + J_{j,i'} + J_{i,j'} + J_{j,j'})$.

Also note that with each elimination step, the mean interparticle distance grows and thus the disorder in the system increases [64,65] making it more likely for later elimination steps to be good approximations.

APPENDIX B: PAIR ENTROPY IN A SPECIFIC MAGNETIZATION SECTOR

Averaged over all states, each cut separating a pair gives an average entropy of $\frac{1}{2}$, since two of the pair's eigenstates are fully entangled and the other two possess no entanglement. However, when we consider a sector of fixed magnetization, this simple argument no longer holds as there are now dependencies among the eigenstates given by the external constraint. Sectors around zero magnetization will have more entropy on average and strongly magnetized sectors less, simply because the strongest magnetized eigenstates possess no entropy.

Given N the number pairs of spins where N_+ , N_- , and N_0 pairs occupy the states $|\uparrow\uparrow\rangle$, $|\downarrow\downarrow\rangle$, and $|\uparrow\downarrow\rangle \pm |\downarrow\uparrow\rangle$, we find the number of possible configuration with these amounts to be

$$C(N_+, N_-, N_0) = \binom{N}{N_0} \binom{N - N_0}{N_+} 2^{N_0}. \quad (\text{B1})$$

In the end, we need the number of configurations $\mathcal{C}(N, r) = \sum_{N_0} C(N, r, N_0)$ given a total amount of pairs N and a magnetization imbalance $r = N_+ - N_-$, where

$$\mathcal{C}(N, r, N_0) = \sum_{0 \leq N_+ \leq N} C(N_+, N_-, N_0) \delta_{N, N_+ + N_- + N_0} \delta_{r, N_+ - N_-}. \quad (\text{B2})$$

To evaluate this expression, we compute the generating function

$$\mathcal{Z}(x, y, z) = \sum_{N>0} x^N \sum_{-N \leq r \leq N} y^r \sum_{N_0 > 0} z^{N_0} C(N, r, N_0) \quad (\text{B3})$$

$$= \sum_{0 \leq N_+, N_-, N_0} x^{N_+ + N_0 + N_-} y^{N_+ - N_-} z^{N_0} C(N_+, N_-, N_0) \quad (\text{B4})$$

$$= \sum_{0 \leq N_-} \left(\frac{x}{y}\right)^{N_-} \sum_{0 \leq N_+} (xy)^{N_+} \binom{N_+ + N_-}{N_+} \times \sum_{N_0} \binom{N}{N_0} (2z)^{N_0} \quad (\text{B5})$$

$$= \frac{y}{y - 2xyz - xy^2 - x}, \quad (\text{B6})$$

where we used the fact that $(1-x)^{-k-1} = \sum_n \binom{n+k}{k} x^n$ twice and then a geometric series.

From that, it follows directly that

$$\mathcal{Z}(x, y, 1) = \sum_{N>0} x^N \sum_{-N \leq r \leq N} y^r \mathcal{C}(N, r) \quad (\text{B7})$$

$$= \frac{y}{y - 2xy - xy^2 - x} \quad (\text{B8})$$

$$= \frac{1}{1 - x \frac{(y+1)^2}{y}} \quad (B9)$$

$$= \sum_{0 \leq k} x^k \left(\frac{(y+1)^2}{y} \right)^k \quad (B10)$$

$$= \sum_{0 \leq k} x^k \sum_{0 \leq l \leq 2k} y^{l-k} \binom{2k}{l}, \quad (B11)$$

and thus by identification of terms

$$\mathcal{C}(N, r) = \binom{2N}{r+N}. \quad (B12)$$

Singling out a specific pair and asking how often it is in one of the entangled states given a set of configurations described by values for (N_+, N_0, N_-) , we find that its the case in

$$S(N_+, N_-, N_0) = 2C(N_+, N_-, N_0 - 1) = \frac{N_0}{N} C(N_+, N_-, N_0) \quad (B13)$$

configurations. Again we want to find this number for a total amount of pairs N and an magnetization imbalance $r = N_+ - N_-$. Fortunately, we can find the generating function $\mathcal{Z}_S(x, y, z)$ of $S(N, r, N_0) = \frac{N_0}{N} C(N, r, N_0)$ by means of \mathcal{Z} :

$$\mathcal{Z}_S(x, y, z) = \int \frac{dx}{x} z \frac{\partial}{\partial z} \mathcal{Z}(x, y, z). \quad (B14)$$

So, we compute

$$\mathcal{Z}_S(x, y, z=1) = \sum_N x^N \sum_r y^r \mathcal{S}(N, r) \quad (B15)$$

$$= \int \frac{dx}{x} \frac{2xy^2}{(y - x(y+1))^2} \quad (B16)$$

$$= \frac{2y^2}{(y+1)^2} \frac{1}{y - x(y+1)^2} \quad (B17)$$

$$= 2 \sum_k x^k \sum_l y^{l-k+1} \binom{2k-2}{l} \quad (B18)$$

$$\Rightarrow \mathcal{S}(N, r) = 2 \binom{2N-2}{r+N-1}. \quad (B19)$$

Thus, cutting a single pair contributes

$$\bar{\mathcal{S}}(N, r) = \frac{\mathcal{S}(N, r)}{\mathcal{C}(N, r)} \quad (B20)$$

$$= 2 \frac{N^2 - r^2}{4N^2 - 2N} \quad (B21)$$

bits of entropy, on average, over all states in a given magnetization sector (cf. Fig. 7).

For the prediction of the average entropy in Fig. 4, we extracted the size of the pairs from the position data, which directly determines how many times a pair is cut, when moving along the chain. The number of cut pairs is then divided by the

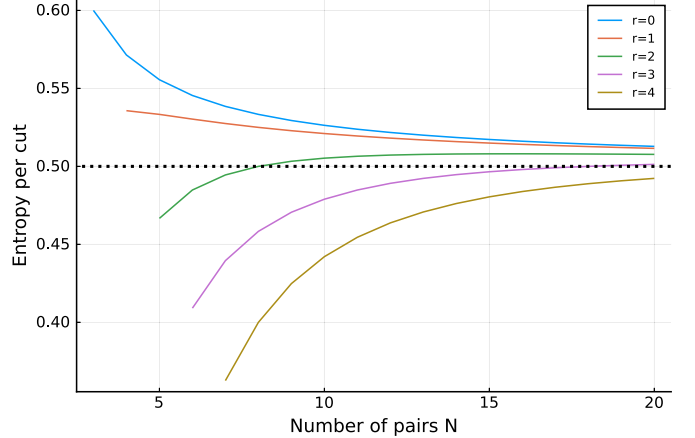


FIG. 7. Entropy value of a single cut for different magnetization sectors.

number of cuts made—which equal the number of spins—and multiplied by the average entropy contributed by cutting a pair, computed here.

APPENDIX C: DRAWING BLOCKADED POSITIONS

In the following, we restrict ourselves to N spins in $d = 1$ dimension and measure every distance in units of the blockade radius r_b . We define the density of spins $0 \leq \rho = \frac{1}{2W} \leq 1$, the corresponding volume of the space $L = \frac{N}{\rho}$, and set out to construct a scheme to efficiently generate a set of independently drawn positions $\{x_i\}$, that respect the blockade condition

$$|x_i - x_j| \geq r_b \quad \forall i \neq j. \quad (C1)$$

A priori, all positions are drawn i.i.d. from a uniform distribution over the full space $\mathcal{U}[0, L]$ and the naive way would be to just draw N positions and reject the sample if the blockade condition [Eq. (C1)] is violated. This is essentially equivalent to a random sequential adsorption process where the expected density in $d = 1$ is given by Renyi's parking constant $m \approx 0.748$ [57]. It directly follows that the rejection rate will become essentially 1 for any $\rho > m$ and we certainly will not get close to the fully ordered regime.

To circumvent this problem, we parameterize the positions like

$$x_i = is + \sigma_i, \quad (C2)$$

where $s = \frac{1}{\rho} = 2W$ is the mean interspin distance and $\sigma_i \sim \mathcal{U}[-\sigma, \sigma]$ are i.i.d. random variables. For $\sigma = \frac{L}{2}$, this ansatz is certainly equivalent to the naive scheme.

Note that, in the highly ordered case $\rho = 1 - \epsilon$, where ϵ is small, each realization of the experiment looks essentially like a regularly spaced chain with $s = \frac{1}{1-\epsilon} \approx r_b(1 + \epsilon)$ where each site has small fluctuations around the mean. This means, in this limit, we get away with choosing $\sigma \approx \epsilon$.

For our simulations, we used the just-described method in the region $W < 1.0$ and chose $\sigma = 1.5(\frac{1}{\rho} - 1)$. For $W \geq 1.0$,

we used the naive sampling strategy. One can see a slight jump in all plots at $W = 1.0$ where the sampling method changes.

-
- [1] M. Srednicki, *Phys. Rev. E* **50**, 888 (1994).
- [2] J. M. Deutsch, *Rep. Prog. Phys.* **81**, 082001 (2018).
- [3] C. Gogolin and J. Eisert, *Rep. Prog. Phys.* **79**, 056001 (2016).
- [4] L. D'Alessio, Y. Kafri, A. Polkovnikov, and M. Rigol, *Adv. Phys.* **65**, 239 (2016).
- [5] R. Nandkishore and D. A. Huse, *Annu. Rev. Condens. Matter Phys.* **6**, 15 (2015).
- [6] D. A. Abanin and Z. Papić, *Ann. Phys.* **529**, 1700169 (2017).
- [7] R. M. Nandkishore and S. L. Sondhi, *Phys. Rev. X* **7**, 041021 (2017).
- [8] D. A. Abanin, E. Altman, I. Bloch, and M. Serbyn, *Rev. Mod. Phys.* **91**, 021001 (2019).
- [9] M. Žnidarič, T. Prosen, and P. Prelovsek, *Phys. Rev. B* **77**, 064426 (2008).
- [10] D. J. Luitz, N. Laflorencie, and F. Alet, *Phys. Rev. B* **91**, 081103(R) (2015).
- [11] P. Sierant, M. Lewenstein, and J. Zakrzewski, *Phys. Rev. Lett.* **125**, 156601 (2020).
- [12] R. Vasseur, A. J. Friedman, S. A. Parameswaran, and A. C. Potter, *Phys. Rev. B* **93**, 134207 (2016).
- [13] I. V. Protopopov, R. K. Panda, T. Parolini, A. Scardicchio, E. Demler, and D. A. Abanin, *Phys. Rev. X* **10**, 011025 (2020).
- [14] T. Chanda, P. Sierant, and J. Zakrzewski, *Phys. Rev. Res.* **2**, 032045(R) (2020).
- [15] J. A. Kjäll, J. H. Bardarson, and F. Pollmann, *Phys. Rev. Lett.* **113**, 107204 (2014).
- [16] M. S. Bahovadinov, D. V. Kurlov, S. I. Matveenko, B. L. Altshuler, and G. V. Shlyapnikov, *Phys. Rev. B* **106**, 075107 (2022).
- [17] A. L. Burin, *Phys. Rev. B* **91**, 094202 (2015).
- [18] S. Schiffer, J. Wang, X.-J. Liu, and H. Hu, *Phys. Rev. A* **100**, 063619 (2019).
- [19] S. Roy and D. E. Logan, *SciPost Phys.* **7**, 042 (2019).
- [20] A. Safavi-Naini, M. L. Wall, O. L. Acevedo, A. M. Rey, and R. M. Nandkishore, *Phys. Rev. A* **99**, 033610 (2019).
- [21] Y. Mohdeb, J. Vahedi, and S. Kettemann, *Phys. Rev. B* **106**, 104201 (2022).
- [22] D. Pekker, G. Refael, E. Altman, E. Demler, and V. Oganesyan, *Phys. Rev. X* **4**, 011052 (2014).
- [23] A. C. Potter, R. Vasseur, and S. A. Parameswaran, *Phys. Rev. X* **5**, 031033 (2015).
- [24] R. Vosk, D. A. Huse, and E. Altman, *Phys. Rev. X* **5**, 031032 (2015).
- [25] C. Monthus, *J. Phys. A: Math. Theor.* **51**, 275302 (2018).
- [26] W. De Roeck and F. Huveneers, *Phys. Rev. B* **95**, 155129 (2017).
- [27] D. J. Luitz, F. Huveneers, and W. De Roeck, *Phys. Rev. Lett.* **119**, 150602 (2017).
- [28] A. Morningstar, L. Colmenarez, V. Khemani, D. J. Luitz, and D. A. Huse, *Phys. Rev. B* **105**, 174205 (2022).
- [29] D. Sels and A. Polkovnikov, *Phys. Rev. E* **104**, 054105 (2021).
- [30] D. Sels and A. Polkovnikov, *arXiv:2105.09348*.
- [31] D. Sels, *Phys. Rev. B* **106**, L020202 (2022).
- [32] T. Thiery, F. Huveneers, M. Müller, and W. De Roeck, *Phys. Rev. Lett.* **121**, 140601 (2018).
- [33] P. Ponte, C. R. Laumann, D. A. Huse, and A. Chandran, *Philos. Trans. R. Soc. London A* **375**, 20160428 (2017).
- [34] M. Pandey, P. W. Claeys, D. K. Campbell, A. Polkovnikov, and D. Sels, *Phys. Rev. X* **10**, 041017 (2020).
- [35] S. S. Kondov, W. R. McGehee, W. Xu, and B. DeMarco, *Phys. Rev. Lett.* **114**, 083002 (2015).
- [36] M. Schreiber, S. S. Hodgman, P. Bordia, H. P. Lüschen, M. H. Fischer, R. Vosk, E. Altman, U. Schneider, and I. Bloch, *Science* **349**, 842 (2015).
- [37] P. Bordia, H. P. Lüschen, S. S. Hodgman, M. Schreiber, I. Bloch, and U. Schneider, *Phys. Rev. Lett.* **116**, 140401 (2016).
- [38] A. Lukin, M. Rispoli, R. Schittko, M. E. Tai, A. M. Kaufman, S. Choi, V. Khemani, J. Léonard, and M. Greiner, *Science* **364**, 256 (2019).
- [39] J. Smith, A. Lee, P. Richerme, B. Neyenhuis, P. W. Hess, P. Hauke, M. Heyl, D. A. Huse, and C. Monroe, *Nat. Phys.* **12**, 907 (2016).
- [40] G. Kucsko, S. Choi, J. Choi, P. C. Maurer, H. Zhou, R. Landig, H. Sumiya, S. Onoda, J. Isoya, F. Jelezko, E. Demler, N. Y. Yao, and M. D. Lukin, *Phys. Rev. Lett.* **121**, 023601 (2018).
- [41] K. X. Wei, C. Ramanathan, and P. Cappellaro, *Phys. Rev. Lett.* **120**, 070501 (2018).
- [42] A. Signoles, T. Franz, R. F. Alves, M. Gärtner, S. Whitlock, G. Zürn, and M. Weidemüller, *Phys. Rev. X* **11**, 011011 (2021).
- [43] A. P. Orioli, A. Signoles, H. Wildhagen, G. Günter, J. Berges, S. Whitlock, and M. Weidemüller, *Phys. Rev. Lett.* **120**, 063601 (2018).
- [44] S. Geier, N. Thaicharoen, C. Hainaut, T. Franz, A. Salzinger, A. Tebben, D. Grimshndl, G. Zürn, and M. Weidemüller, *Science* **374**, 1149 (2021).
- [45] T. Franz, S. Geier, C. Hainaut, A. Signoles, N. Thaicharoen, A. Tebben, A. Salzinger, A. Braemer, M. Gärtner, G. Zürn, and M. Weidemüller, *arXiv:2207.14216*.
- [46] M. D. Lukin, M. Fleischhauer, R. Cote, L. M. Duan, D. Jaksch, J. I. Cirac, and P. Zoller, *Phys. Rev. Lett.* **87**, 037901 (2001).
- [47] D. A. Huse, R. Nandkishore, and V. Oganesyan, *Phys. Rev. B* **90**, 174202 (2014).
- [48] M. Serbyn, Z. Papić, and D. A. Abanin, *Phys. Rev. Lett.* **111**, 127201 (2013).
- [49] Only the closest copy of each spin is considered for the interaction.
- [50] <https://github.com/abraemmer/Pair-localization-paper>.
- [51] V. Oganesyan and D. A. Huse, *Phys. Rev. B* **75**, 155111 (2007).
- [52] Y. Y. Atas, E. Bogomolny, O. Giraud, and G. Roux, *Phys. Rev. Lett.* **110**, 084101 (2013).
- [53] M. Serbyn, Z. Papić, and D. A. Abanin, *Phys. Rev. X* **5**, 041047 (2015).
- [54] J. Eisert, M. Cramer, and M. B. Plenio, *Rev. Mod. Phys.* **82**, 277 (2010).
- [55] V. Khemani, S. P. Lim, D. N. Sheng, and D. A. Huse, *Phys. Rev. X* **7**, 021013 (2017).

- [56] D. Abanin, J. Bardarson, G. De Tomasi, S. Gopalakrishnan, V. Khemani, S. Parameswaran, F. Pollmann, A. Potter, M. Serbyn, and R. Vasseur, [Ann. Phys.](#) **427**, 168415 (2021).
- [57] A. Rényi, [Publ. Math. Inst. Hung. Acad. Sci.](#) **3**, 109 (1958).
- [58] M. Serbyn, Z. Papić, and D. A. Abanin, [Phys. Rev. B](#) **96**, 104201 (2017).
- [59] N. Macé, F. Alet, and N. Laflorencie, [Phys. Rev. Lett.](#) **123**, 180601 (2019).
- [60] D. J. Luitz, I. Khaymovich, and Y. Bar Lev, [SciPost Phys. Core](#) **2**, 006 (2020).
- [61] N. Y. Yao, C. R. Laumann, S. Gopalakrishnan, M. Knap, M. Müller, E. A. Demler, and M. D. Lukin, [Phys. Rev. Lett.](#) **113**, 243002 (2014).
- [62] J. Bezanson, A. Edelman, S. Karpinski, and V. B. Shah, [SIAM Rev.](#) **59**, 65 (2017).
- [63] S. Bravyi, D. P. DiVincenzo, and D. Loss, [Ann. Phys.](#) **326**, 2793 (2011).
- [64] D. S. Fisher, [Phys. Rev. B](#) **50**, 3799 (1994).
- [65] R. Vasseur, A. C. Potter, and S. A. Parameswaran, [Phys. Rev. Lett.](#) **114**, 217201 (2015).

3

EFFICIENT TIME EVOLUTION OF PAIR LOCALIZED SYSTEMS

After having found an analytical approximation applicable at strong disorder in the preceding chapter, here we show how to utilize this knowledge to achieve an efficient numerical computation of the dynamics. The key idea is to employ the cluster truncated Wigner approximation [119], which is a semiclassical simulation method that solves the dynamics of only small clusters of spins exactly and treats interactions among clusters on a mean-field level. By using the pairing procedure of Chapter 2 to define the clusters, we find that this method is highly accurate not only at strong disorder and short-range interactions but also in regimes of comparatively weak disorder and long-range interactions. Thus, our method represents a numerically efficient scheme to compute arbitrary dynamical quantities in these kinds of spatially disordered spin systems.

Cluster truncated Wigner approximation for bond-disordered Heisenberg spin models

Adrian Braemer^{1,*}, Javad Vahedi^{2,†}, and Martin Gärttner^{2,‡}

¹Physikalisches Institut, Universität Heidelberg, Im Neuenheimer Feld 226, 69120 Heidelberg, Germany

²Institut für Festkörpertheorie und -optik, Friedrich-Schiller-Universität Jena, Max-Wien-Platz 1, 07743 Jena, Germany



(Received 1 July 2024; revised 1 August 2024; accepted 2 August 2024; published 19 August 2024)

We present a comprehensive numerical investigation of the cluster truncated Wigner approximation (cTWA) applied to quench dynamics in bond-disordered Heisenberg spin chains with power-law interactions. We find that cTWA yields highly accurate results over a wide parameter range. However, its accuracy hinges on a suitable choice of clusters. By using a clustering strategy inspired by the strong disorder renormalization group and real-space renormalization group (RSRG), clusters of two spins are sufficient to obtain essentially exact results in the regime of strong disorder. Surprisingly, even for rather weak disorder, e.g., in the presence of very long-range interactions, this choice of clustering outperforms a naive choice of clusters of consecutive spins. Additionally, we develop a discrete sampling scheme for the initial Wigner function, as an alternative to the originally introduced scheme based on Gaussian approximations. This sampling scheme puts cTWA on the same conceptional footing as regular discrete TWA for single spins and yields some reduction in the Monte Carlo shot noise compared to the Gaussian scheme.

DOI: [10.1103/PhysRevB.110.054204](https://doi.org/10.1103/PhysRevB.110.054204)

I. INTRODUCTION

Long-range interactions arise in several physical scenarios within disordered quantum many-body systems. For example, in doped semiconductors containing randomly positioned magnetic impurities, interactions occur via exchange couplings that depend on their spatial separation [1–3]. These interactions exhibit different behaviors depending on the state of the system. In insulating phases, the interaction strength decreases exponentially, as denoted by $J(r) \propto \exp(-r/\xi)$, while in metallic phases the interactions operate through the Ruderman-Kittel-Kasuya-Yosida (RKKY) mechanism, following a power-law decay described by $J(r) \propto r^{-d}$, where d represents the dimension of the host system. Interestingly, sufficiently random, power-law interacting systems can even feature ultraslow relaxation known from classical spin glasses as observed in local two-level systems formed by tunneling ions interacting through dipole-dipole and elastic forces [4,5].

Moreover, recent experimental progress has enabled the manipulation and investigation of cold atoms or molecules featuring strong dipole-dipole interactions in diverse setups, including optical lattices [6–8], Rydberg gases [9–11], and trapped ions [12–16]. This has, in turn, spurred theoretical interest in studying quantum many-body dynamics in systems characterized by varying interaction ranges.

However, the potential of these studies is often limited by the lack of suitable computational tools. Considering that the Hilbert space of the system grows exponentially with the system size, the exact solution of quantum dynamics is limited

to rather small systems. Even employing sophisticated tools, e.g., based on Krylov subspaces [17–21], typically allows simulating systems of only few tens of spins. Leaving the realm of exact methods, one usually tries to approximate the wave functions with a variational ansatz such as matrix product states (MPS) [22] and solves the dynamics within this variational manifold. While these MPS based methods, such as time-dependent density matrix renormalization group, have been used very successfully to simulate large, one-dimensional many-body systems with nearest-neighbor interactions [23,24], they struggle for higher-dimensional or long-range interacting systems due to the rapid generation of entanglement [25,26].

In the search for effective approaches to deal with many-body systems and the entanglement problem, phase-space methods have emerged as promising candidates. Among them, the truncated Wigner approximation (TWA) [27,28], based on the Wigner-Weyl correspondence, stands out as a practical and widely adaptable strategy for exploring the dynamics of quantum many-body systems, even in higher-dimensional settings with long-range interactions [29–32]. At its heart, TWA approximates the dynamics of the Wigner function, i.e., the phase-space analog of the wave function, by particles following the classical mean-field equations of motion. The initial conditions of these particles are sampled from a Gaussian approximation of the initial Wigner function. While *a priori* TWA is exact only for short times, numerical experiments have shown it to yield accurate results at intermediate or even late times in some cases [33].

Although TWA was originally developed in the context of bosonic systems where a clear classical limit exists, it can also be applied to spin systems. Remarkably, for finite-dimensional quantum systems there exists a discrete formulation of the quantum phase space [34]. For spin systems prepared in a

*Contact author: adrian.braemer@physi.uni-heidelberg.de

†Contact author: javad.vahedi@uni-jena.de

‡Contact author: martin.gaerttner@uni-jena.de

product state, discrete TWA (dTWA) exploits this to dramatically improve accuracy [35] and to capture quantum revivals [16,36–45].

Another extension aims at incorporating more quantum interactions into the equations of motion, which in traditional TWA are essentially mean-field equations for single particles [46]. This so-called cluster TWA (cTWA) does so by grouping spins together into clusters and then assigning classical variables to all degrees of freedom within these clusters [47]. Thus, all quantum interaction within a cluster is treated exactly and only interactions between clusters are approximated semiclassically. In the limit of clusters consisting of single spins, cTWA is identical to (d)TWA while in the opposing limit, where the whole system constitutes a single cluster the exact quantum evolution is recovered. Thus, one has a tuning parameter to assess the convergence of the simulation which the usual (d)TWA lacks. While in principle cTWA is compatible with the discrete phase-space formulation, literature on their combination is quite sparse. A conceptual precursor, dubbed GDTWA, exists in [48] where the discrete sampling was extended to larger $SU(N)$ spins. In a recent paper a variant of discrete sampling is applied to a Bose-Hubbard model [49].

In this paper, we present a generalization of both cTWA and dTWA combining the discrete sampling scheme of the latter with the capability of treating clusters of spins of the former, which we term dcTWA. We then systematically evaluate the performance of these methods in the context of quench dynamics for bond disordered XX and XXZ long-range interacting spin- $\frac{1}{2}$ models. More precisely, we study the dynamics of an initial Néel state by means of the decay of the staggered magnetization and the buildup of Rényi entropy in a two-spin subsystem for different interaction ranges and disorder strengths and compare the results from the semi-classical methods to exact diagonalization. While in the weakly disordered regime a bigger cluster size is beneficial generally, we find that in the strongly disordered regime the physics is well captured by clusters of size 2 if they are chosen following a pairing rule known from the real-space renormalization group (RSRG) approach to bond-disordered systems. Our analysis of the statistical uncertainties reveals that although the averaged results from cTWA and dcTWA are similar, dcTWA shows less sampling noise and thus converges faster.

II. MODEL AND METHODS

A. Model

We study the behavior of a disordered spin chain with long-range interactions, described by the Hamiltonian

$$H = \sum_{i < j} J_{ij} (\hat{s}_i^x \hat{s}_j^x + \hat{s}_i^y \hat{s}_j^y + \Delta \hat{s}_i^z \hat{s}_j^z), \quad (1)$$

where N spins ($\hat{s}_i = \frac{1}{2}\hat{\sigma}_i$) are randomly positioned at locations r_i along a lattice of length L with lattice spacing a , resulting in a density $f = N/L$. The interactions J_{ij} between pairs of sites i and j are long range, characterized by a power-law decay with parameter α : $J_{ij} = J_0 |(r_i - r_j)/a|^{-\alpha}$. Throughout our study we set $J_0 = 1$ and $a = 1$, and employ open boundary conditions.

The disorder in this model arises from the random arrangement of spins along the chain, leading to different spin-spin couplings. Previous studies of this model with $\Delta = 0$ focused on the entanglement entropy in the ground state [50] and excited states [51] as well as the dynamical growth of the entanglement entropy after a quench [52]. These studies found good agreement between numerically exact results and analytical calculations based on the real-space renormalization group for low density ($f = 10\%$) and interaction exponents $\alpha \gtrsim 1.8$.

We explore the system dynamics by initializing it in a Néel state and subsequently computing dynamic observables. These observables encompass the staggered magnetization $M^{\text{st}}(t) = \sum_i (-1)^i \langle \hat{s}_i^z(t) \rangle / N$ and the Rényi-2 entropy $S_2(t)$ evaluated over a two-spin subsystem. The Rényi-2 entropy belongs to a continuum of entropy measures defined as $S_\gamma[\hat{\rho}_A(t)] = \frac{1}{1-\gamma} \log_2 (\text{tr}[\hat{\rho}_A(t)^\gamma])$, where $\gamma \geq 1$. In this context, $\hat{\rho}_A(t) \equiv \text{Tr}_B \hat{\rho}(t)$ signifies the reduced density matrix associated with a subsystem A , and $\hat{\rho}(t)$ represents the density matrix of the entire system. Expanding the two-site reduced density matrix $\hat{\rho}_{ij} = \frac{1}{4} \sum_{\alpha\beta} \langle \hat{\sigma}_i^\alpha \hat{\sigma}_j^\beta \rangle \hat{\sigma}_i^\alpha \hat{\sigma}_j^\beta$ in a basis of Pauli strings gives a clear recipe for extracting the Rényi-2 entropy from the expectation values of observables:

$$S_2[\hat{\rho}_{ij}(t)] = -\log_2(\text{tr}[\hat{\rho}_{ij}(t)]^2) \quad (2)$$

$$= 2 - \log_2 \left(\sum_{\alpha\beta} \langle \hat{\sigma}_i^\alpha \hat{\sigma}_j^\beta \rangle^2 \right), \quad (3)$$

where we used the trace orthogonality of the Pauli strings. This expression has a clear physical meaning: The more correlations the subsystem retains after tracing out the environment, the weaker the entanglement is.

B. Cluster truncated Wigner approximation (cTWA)

Phase-space methods are powerful tools for simulating quantum system dynamics close to the classical limit. These methods have applications across various scientific domains, including quantum chemistry, optics, and condensed matter physics [28,34]. Among them, the TWA maps quantum degrees of freedom onto classical phase-space variables following classical equations of motion as in a mean-field treatment. Quantum fluctuations are taken into account by Monte Carlo sampling of initial conditions from the Wigner function, which guarantees accuracy on short timescales. However, for quantum systems close to the classical limit, e.g., highly occupied bosonic modes or collective spin models, TWA has been found to yield accurate results even at late times [28].

When applying TWA to spin systems, usually one considers 3 degrees of freedom per spin: its X , Y , and Z magnetization [35]. Mapping these to classical variables treats all quantum interactions between spins on a mean-field level, which is justified if the interactions are either weak or very long range and thus average out [33]. One avenue of incorporating more quantum effects into the dynamics, known as cluster TWA (cTWA), uses the degrees of freedom of clusters of spins instead of just the single-spin ones [47]. In effect, this means all quantum dynamics within a cluster is computed

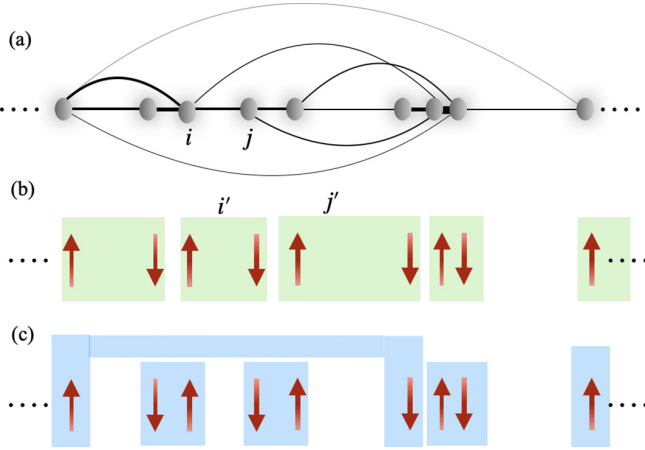


FIG. 1. (a) This diagram shows a long-range bond disorder spin chain where spins are randomly positioned along a lattice. The couplings are represented by solid lines J_{ij} , while stronger bonds are indicated by thicker lines. (b) The initial state is the Néel state, represented as $|\Psi_0\rangle = |\uparrow\downarrow\cdots\uparrow\downarrow\rangle$, where each arrow represents the spin direction. The green shaded box illustrates a naive clustering of spins into clusters of size 2. (c) Clustering inspired by the real-space renormalization group, as explained in the text.

exactly and only the interaction between clusters is approximated on a mean-field level. In the limit of a single cluster encompassing the whole system, cTWA is equivalent to an exact solution. Conversely, in the limit of clusters of single spins, cTWA reduces to regular TWA. Thus, cTWA offers a tuning parameter to steadily tune between TWA and an exact solution by means of increasing the cluster size. In order to be self-contained, we provide an overview of this method. For a more detailed introduction, we refer the reader to the paper by Wurtz *et al.* [47].

To illustrate the cTWA method, consider a system of interacting spins- $\frac{1}{2}$ described by the Hamiltonian

$$H = \sum_{ij} J_{ab}^{ij} \hat{\sigma}_a^i \hat{\sigma}_b^j + \sum_j B_a^j \hat{\sigma}_a^j. \quad (4)$$

Here, $a, b \in x, y, z$ are the indices of Pauli matrices, and i, j denote distinct spins on the lattice. The couplings J_{ab}^{ij} and fields B_a^j can be either short or long range.

The following steps outline the implementation of the operator cTWA:

(i) Divide the system into clusters indexed by $[i']$, as shown in Fig. 1(b). Define a complete operator basis $\{\hat{X}_p^{[i']}\}$, $p = 0, \dots, D^2 - 1$ for the Hilbert space of each cluster, where $D = 2^n$ is the dimension of the Hilbert space and n the number of spins making up the cluster. Ensure that the basis operators are trace orthogonal and satisfy $\text{Tr}[\hat{X}_p^{[i']} \hat{X}_q^{[j']}] = D \delta_{pq} \delta^{[i'][j']}$. Then any operator $O^{[i']}$ inside a cluster $[i']$ can be written as linear combination of the basis operators $\hat{O}^{[i']} = \sum_p o_p \hat{X}_p^{[i']}$.

(ii) Define structure constants f_{pqr} as

$$[\hat{X}_p^{[i']}, \hat{X}_q^{[j']}] = i f_{pqr} \delta_{[i'][j']} \hat{X}_r^{[i']}, \quad (5)$$

which project commutators onto the basis spanned by $\{\hat{X}_p^{[i']}\}$.

(iii) Express the Hamiltonian in terms of cluster operators $\hat{X}_\alpha^{[i']}$.

$$\hat{H} = \sum_{[i'][j']} \mathbf{J}_{pq}^{[i'][j']} \hat{X}_p^{[i']} \hat{X}_q^{[j']} + \sum_{[j']} \mathbf{B}_p^{[j']} \hat{X}_p^{[j']}. \quad (6)$$

The interactions \mathbf{J} and fields \mathbf{B} generally differ from the original parameters J_{ab}^{ij} , B_a^j . For instance, local fields now encompass connections among spins residing within a particular cluster, given that an operator $\sigma_a^i \sigma_p^j$ becomes linear in $\hat{X}_p^{[j']}$ when both spins i and j are part of the same cluster $[j']$.

(iv) Associate basis operators $\hat{X}_p^{[i']}$ with classical phase-space variables $x_\alpha^{[i']}$ satisfying canonical Poisson bracket relation $\{x_p^{[i']}, x_q^{[j']}\} = i f_{pqr} \delta_{[i'][j']} x_r^{[i']}$ defined by the structure constants

$$\hat{X}_p^{[i']} \rightarrow x_p^{[i']} - \frac{i}{2} x_q^{[i']} f_{pqr} \frac{\partial}{\partial x_r^{[i']}}, \quad (7)$$

(v) Represent the Hamiltonian and observables as functions of classical phase-space variables.

$$\hat{O}^{[i']} = \sum_p o_p \hat{X}_p^{[i']} \rightarrow O_{\mathbf{W}}(\{x\}) = \sum_p o_p x_p^{[i']} \quad (8)$$

with $o_p = \frac{1}{D} \text{Tr}[\hat{O} \hat{X}_p^{[i']}]$, and

$$\hat{H} \rightarrow H_{\mathbf{W}} = \sum_{[i'][j']} \mathbf{J}_{pq}^{[i'][j']} x_p^{[i']} x_q^{[j']} + \sum_{[j']} \mathbf{B}_p^{[j']} x_p^{[j']}, \quad (9)$$

where index \mathbf{W} indicates that this is the Weyl symbol corresponding to symmetric operator ordering.

(vi) Find or approximate the Weyl symbol of the initial state, i.e., its Wigner function. While it can assume negative values, we require that it is completely positive and thus can be thought of as a probability distribution. We present two possible definitions for the Wigner function below this implementation guide.

(vii) Solve the classical equations of motion for the phase-space variables:

$$\frac{dx_p^{[i']}(t)}{dt} = -\{x_p^{[i']}, H_{\mathbf{W}}\} = f_{pqr} \frac{\partial H_{\mathbf{W}}}{\partial x_q^{[i']}} x_r^{[i']}. \quad (10)$$

(viii) Find expectation values of observables by averaging the corresponding classical functions over phase-space points sampled from the Wigner function $\langle \hat{O}(t) \rangle = \lim_{M \rightarrow \infty} \frac{1}{M} \sum_m^M O_{\mathbf{W}}(\{x(t)\}_m)$, where M denotes the number of samples.

1. Gaussian Wigner function

Wurtz *et al.* [47] defined an approximate Gaussian Wigner function $\mathcal{W}(\{x\})$ describing the initial conditions for the system with the only requirement that the initial state factorizes between clusters such that $\mathcal{W}(\{x\}) = \prod_{[i']} \mathcal{W}^{[i']}(\{x_\alpha^{[i']}\})$, where

$$\mathcal{W}^{[i']}(x^{[i']}) = \frac{1}{Z} \exp \left[(x_p - \rho_p^{[i']}) \Sigma_{pq}^{[i']} (x_p - \rho_q^{[i']}) \right] \quad (11)$$

is simply a Gaussian. To determine coefficients $\rho_p^{[i']}$ and $\Sigma_{pq}^{[i]}$ from the initial density matrix on cluster $[i']$, we demand (cluster index $[i']$ suppressed)

$$\text{Tr}[\hat{\rho}\hat{X}_q] = \int \prod_p dx_p x_q \mathcal{W}(\{x\}), \quad (12)$$

$$\text{Tr}[\hat{\rho}(\hat{X}_q\hat{X}_r + \hat{X}_r\hat{X}_q)] = 2 \int \prod_p dx_p x_q x_r \mathcal{W}(\{x\}) \quad (13)$$

such that the moments match to second order.

2. Discrete Wigner function

While the Gaussian approximation of the Wigner function described above is quite general, it neglects the moments beyond the second order. dTWA, on the other side, can capture all moments of the single-spin observables for initial states that factorize between individual spins [35]. In the following, we briefly recapitulate the derivation dTWA's sampling to introduce the notation and then generalize the method to clusters of spins.

The key idea behind the dTWA is to replace the Gaussian approximation of the Wigner function with a discrete Wigner function defined via a discrete set of phase-point operators $\hat{\mathbf{A}}^{\otimes n} = \bigotimes_i^N \hat{A}^{[i]}$ where $\hat{A}^{[i]}$ are discrete phase-point operators that span the $SU(2)$ phase space of the i th spin. These are usually defined as $\hat{A}_{p,q}^{[i]} = [\mathbb{1} + \mathbf{r}(p,q) \cdot \hat{\sigma}] / 2$, $\hat{\sigma} = (\hat{\sigma}_x, \hat{\sigma}_y, \hat{\sigma}_z)$ are the Pauli matrices, and $\mathbf{r}(p, q)$ denotes suitable combinations thereof (cf. [34,35,37]): $\mathbf{r}(0, 0) = (1, 1, 1)$, $\mathbf{r}(0, 1) = (-1, -1, 1)$, $\mathbf{r}(1, 0) = (1, -1, -1)$, and $\mathbf{r}(1, 1) = (-1, 1, -1)$. In case the wave function factorizes, the Wigner function of the system is then given simply by the product of single-spin Wigner function given by $w^{[i]}(p, q) = \langle \hat{A}_{(p,q)} \rangle / 2$. Crucially, for all spin states pointing along one axis each value of $w^{[i]}(p, q)$ is positive and, since they sum to 1, one can interpret them as probability distribution to sample from. A schematic illustration is provided in Fig. 2.

Considering a system of n_c clusters of n spins each, we again seek to describe the state by a discrete Wigner function. The main difference to before is that each local Hilbert space is represented by a copy of $SU(D)$, where $D = 2^n$. In analogy to before, we introduce the phase-point operators $\hat{\mathbf{A}}^{\otimes n_c} = \bigotimes_{i'}^{n_c} \hat{A}_n^{[i']}$ with $\hat{A}_n^{[i']} = (\mathbb{1}_D + \mathbf{r}_n^{[i']} \cdot \mathbf{X}_n) / D$, where $\mathbf{r}_n^{[i']} = (r_1^{[i']}, \dots, r_{D^2-1}^{[i']})$ represents a vector of $D^2 - 1 = 4^n - 1$ real-valued parameters and \mathbf{X}_n corresponds to a vector of the operators of the operator basis for a cluster of n spins as used in cTWA. Note, we can construct the operator basis \mathbf{X}_n for n spins iteratively from an operator basis \mathbf{X}_1 for a single spin by taking tensor products $\mathbf{X}_n = (\mathbf{X}_1 \otimes \mathbb{1}, \mathbb{1} \otimes \mathbf{X}_{n-1}, \mathbf{X}_1 \otimes \mathbf{X}_{n-1})$. One can construct \mathbf{r}_n analogously:

$$\mathbf{r}_n(\mathbf{p}, \mathbf{q}) = [\mathbf{r}_1(p_1, q_1), \mathbf{r}_{n-1}(\tilde{\mathbf{p}}, \tilde{\mathbf{q}}), \mathbf{r}_1(p_1, q_1) \otimes \mathbf{r}_{n-1}(\tilde{\mathbf{p}}, \tilde{\mathbf{q}})] \quad (14)$$

with $\mathbf{p}, \mathbf{q} \in \{0, 1\}^n$ and $\tilde{\mathbf{p}}(\tilde{\mathbf{q}})$ denoting the vector derived from $\mathbf{p}(\mathbf{q})$ by dropping the first element. Suppressing the index n from now on, the Wigner function of a cluster is defined as before to be $w^{[i']}(p, q) = \langle \hat{A}_{(p,q)} \rangle / D$. If the quantum wave function factorizes between spins within a cluster, the Wigner function also factorizes and the result is essentially equivalent

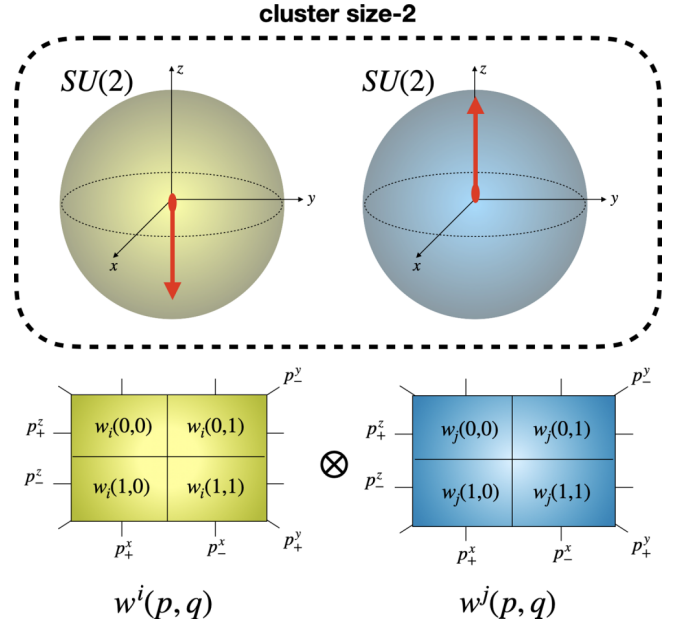


FIG. 2. A schematic of the discrete cluster truncated Wigner approximation. Considering a cluster of two spins, the individual Hilbert spaces (depicted as Bloch spheres) combine to the Hilbert space of the cluster. Shown below is a representation of the single-spin discrete Wigner functions in the spirit of [35]. The probabilities of a spin pointing along the $\pm x$, $\pm y$, and $\pm z$ directions are computed by summing over the vertical, diagonal, and horizontal lines, respectively. For product states within a cluster, one can simply take the tensor product of single-spin discrete Wigner functions to obtain Wigner functions for the cluster. In the case of clusters of size 2, the resulting Wigner function is four dimensional and contains 16 phase points.

to the single-spin case:

$$w^{[i']}(p, q) = \prod_i \langle \hat{A}_{(p_i, q_i)} \rangle / 2 = \prod_i w^{[i]}(p_i, q_i). \quad (15)$$

The key difference is in the phase-point vectors $\mathbf{r}_n(\mathbf{p}, \mathbf{q})$ connected to this Wigner function which now also encompass a much larger operator basis. In summary, if the initial wave function factorizes between spins, one can simply sample the initial values for the single-spin operators and compute the initial values for operators acting on multiple spins by appropriate products. For a more detailed description of the sampling process, see Appendix A.

As a concrete example, consider a cluster of two spins in a Néel state $|\uparrow\downarrow\rangle$. To generate a sample, one draws the four values for $\langle \hat{X}_1 \rangle$, $\langle \hat{Y}_1 \rangle$, $\langle \hat{X}_2 \rangle$, and $\langle \hat{Y}_2 \rangle$ randomly from $\{-1, 1\}$ and sets $\langle \hat{Z}_1 \rangle = -\langle \hat{Z}_2 \rangle = 1$. Then the rest of the correlators are computed from the products of these, e.g., $\langle \hat{X}_1 \hat{Y}_2 \rangle = \langle \hat{X}_1 \rangle \langle \hat{Y}_2 \rangle$ and so on. This means that the initial spin vectors are randomly drawn from one of the 16 spin configurations. All other states on the Bloch sphere can be sampled using the same configurations, followed by an appropriate rotation.

C. Clustering strategies

The cTWA necessitates a choice of clustering of the spins. While in ordered systems, it makes sense to simply choose

contiguous regions of desired size, in disordered systems it is not clear *a priori* that this is a reasonable choice. In this work, we evaluate two possible strategies for choosing the clustering:

(i) *Naive clustering method* [see Fig. 1(b)]. In this approach, clusters of spins are formed by starting from one end of the chain and grouping together every n consecutive spins. Thus, the resulting clusters are determined solely on the basis of this selection process, without taking into account any specific properties or interactions between the spins.

(ii) *Renormalization group clustering* [see Fig. 1(c)]. The RG clustering strategy takes inspiration from the real-space renormalization group (RSRG), also known as strong disorder renormalization group (SDRG), approaches to bond-disordered models which are used to construct approximate eigenstates [53–55]. These methods identify the two spins sharing the strongest coupling in the system and treat their couplings to the environment in a perturbative manner. Since this procedure effectively decouples the pair and leaves the form of the remaining Hamiltonian invariant, one can readily repeat this procedure with the remaining spins until all spins are paired up. Instead of computing eigenstates, we simply use the resulting partition of spins into clusters of size two as input for the cTWA. In this way, the strong intrapair interactions are treated fully quantum mechanically, while the effective interaction among pairs is treated semiclassically.

Based on the excellent results found by RSRG and SDRG, we expect the RG clustering to outperform the naive clustering method for strong disorder. However, the naive clustering scheme generalizes naturally to generate larger clusters, while it is unclear how to merge the clusters given by the RG scheme in a consistent manner.

III. RESULTS

In this section, we present the numerical results of our exploration of the quench dynamics of a disordered spin chain with long-range interactions. We compute the behavior of two dynamical observables initiated from a Néel state, namely, the staggered magnetization and the Rényi entropy $S_2(t)$ evaluated over a two-spin subsystem, using the different methods detailed above and compare to results obtained with exact diagonalization (ED). Our primary focus lies on evaluating the performance of the cluster truncated Wigner approximation (cTWA) relative to standard dTWA. To this end, we consider combinations of the aforementioned clustering schemes, the naive clustering and the one based on the strong disorder renormalization group, and the two approximations of the initial state, the Gaussian cTWA (gcTWA) and discrete cTWA (dcTWA). Our analysis aims to shed light on how cTWA captures the intricate behavior of the system under bond disorder and long-range interactions, and to elucidate the extent to which this approach provides insights into the quantum dynamics of the system under consideration. All curves shown are obtained using 1000 disorder samples and 1000 Monte Carlo trajectories unless specified otherwise. Disorder shots are identical across the methods. The code is freely available at [GitHub](#) [56].

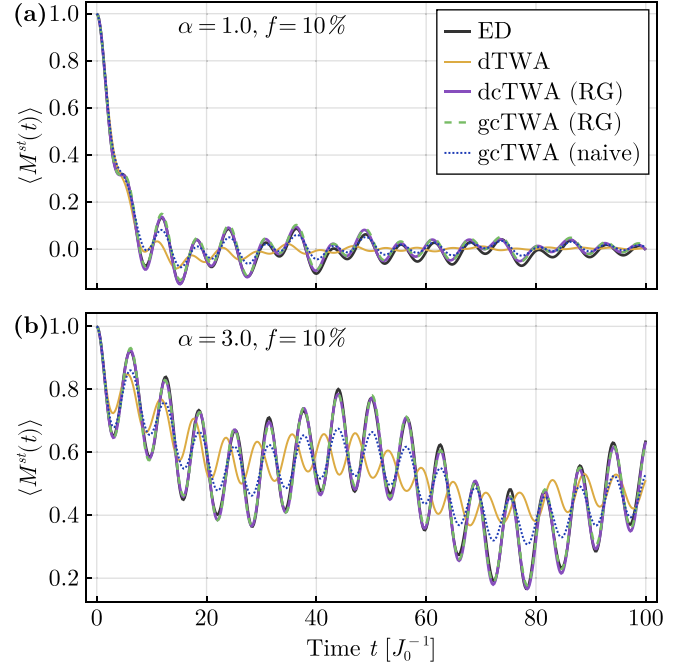


FIG. 3. The disorder-averaged staggered magnetization $\langle M^{\text{st}}(t) \rangle$ is shown for XX chain of $N = 16$ spins with a fixed filling of $f = 10\%$. The panels show results for long-range interactions with $\alpha = 1.0$ in (a) and short-range interactions with $\alpha = 3.0$ in (b). The semi-classical cluster methods using the RG-inspired clustering (green, dashed and purple, solid) overlap the exact results (black, solid) almost completely. dTWA (yellow, solid) and gcTWA with naive clustering (blue, dotted) deviate already early on ($t \approx 10 J_0$).

A. Bond-disordered XX chain

We begin our investigation by considering a bond-disordered XX chain ($\Delta = 0$). We explore various regimes by adjusting two key parameters: the power-decay exponent of the interaction, denoted as α , and the filling fraction of the lattice, denoted as f , which controls the strength of the disorder. Here a low filling fraction corresponds to strong disorder, while $f = 100\%$ represents a fully ordered system.

Figure 3 shows the disorder-averaged time evolution of the staggered magnetization $\langle M^{\text{st}}(t) \rangle$ with a fixed filling of $f = 10\%$, starting from the Néel state. The top panel corresponds to long-range interactions ($\alpha = 1$), while the bottom panel corresponds to short-range interactions ($\alpha = 3$). The staggered magnetization starts at a value of one, which reflects the perfect order inherent in the initial Néel state. It then undergoes a decay, caused by the spins exchanging magnetization as system evolves. At late times, we observe equilibration to a value close to zero. The general behavior is captured by all semiclassical methods.

Upon closer inspection, it becomes evident that the dTWA approach fails to accurately track the true dynamics and loses accuracy even at intermediate timescales starting around $t J_0 \approx 10$. In both cases, it predicts the location of the first oscillation approximately correctly but underestimates the amplitude. Subsequently, it systematically underestimates the amplitude of the oscillations of the staggered magnetization. Interestingly, gcTWA with the naive clustering does not fare much better. While it is generally more accurate with respect

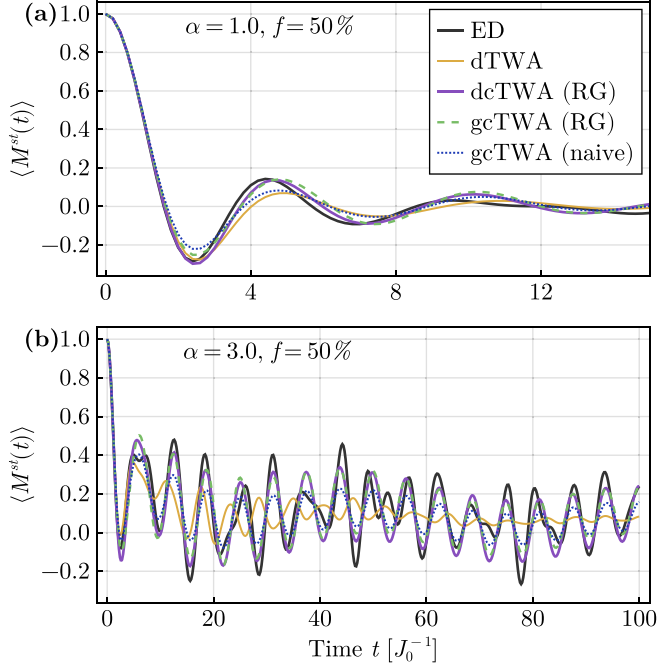


FIG. 4. Same as Fig. 3, but for filling fixed at $f = 50\%$ (weak disorder regime). Here, the methods using the RG-inspired clustering show some deviation from the exact results and for $\alpha = 1$ in panel (a) there are some differences between the Gaussian and discrete sampling schemes visible as well.

to the oscillation frequency, it also underestimates the amplitude. In contrast, both cTWA variants using the RG clustering yield essentially exact results even at late times. This is a very strong indicator that the dynamics is strongly shaped by the presence of strongly interacting pairs of spins where interactions among pairs are weak [57]. With this pair model we can explain the observed curves qualitatively: It is known that dTWA is unable to correctly capture the dynamics of even a single pair and can just approximate the decay timescale (cf. Appendix B). If the two spins forming a strongly interacting pair are not part of the same cluster, then cTWA treats the interactions within the pair semiclassically similar to dTWA and thus faces the same problems. Consequently, using the naive clustering will result in a mixture of “correctly” and “incorrectly” chosen pairs and thus cTWA with this type of clustering provides only a slight improvement over dTWA. The RG clustering, in turn, ensures that all strongly interacting pairs are treated as clusters and thus the predictions match the exact dynamics much more closely. In turn, the high degree of agreement between cTWA with the RG clustering is also testament to the quality of pair approximation.

To further explore the efficacy of cTWA in regimes of weak disorder, we increase the filling fraction to $f = 50\%$ and repeat the analysis (cf. Fig. 4). In this regime, we do not expect the pair approximation to be accurate anymore. Indeed, for the long-range case $\alpha = 1$ we find all semiclassical methods to overestimate the oscillation frequency similarly. Both RG clustering-based methods predict the amplitudes almost exactly correct, while dTWA and cTWA with naive clustering again clearly underestimate it. In the more short-range case $\alpha = 3$, the picture is more complex. dTWA performs worst

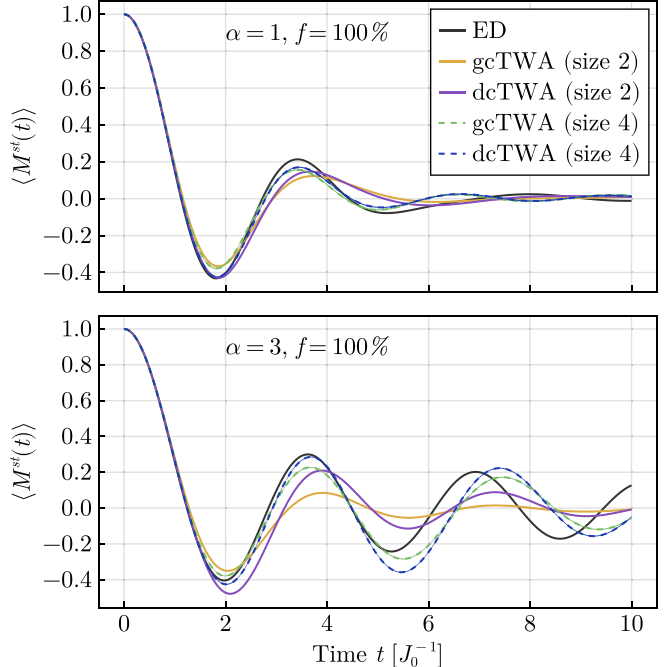


FIG. 5. Comparison of sampling schemes with different cluster sizes in a clean system (filling fraction $f = 100\%$). We compare TWA results for cluster sizes 2 (solid) and 4 (dashed) using the naive clustering and the different sampling schemes, Gaussian (lighter colors) and discrete (darker colors) to exact results [black (solid)]. Generally, cluster size 4 is more accurate than cluster size 2 and the discrete sampling scheme agrees with the exact results longer than the Gaussian sampling scheme. Other parameters are similar to Fig. 3.

out of all the methods and does not resolve the oscillation well and cTWA with naive clustering again essentially underestimates the amplitude. Interestingly, in this case there is a clear difference on intermediate timescales $t \approx 8J_0$ between both cTWA methods with RG clustering but different choice of sampling. The discrete sampling captures the first oscillation slightly better both in position and in amplitude before at later times the prediction collapses onto the cTWA curve employing a Gaussian Wigner function. Generally, all cluster-based methods still capture the dynamics qualitatively but not quite quantitatively over the whole time shown here.

For a better comparison of the sampling schemes, it is instructive to examine a perfectly ordered regime by setting the filling factor to $f = 100\%$. In this setting, the RG and naive clustering schemes result in the same choice of clusters and we use this opportunity to check the convergence with increasing cluster size. Figure 5 shows the staggered magnetization results for systems with both long-range ($\alpha = 1.0$) and short-range ($\alpha = 3.0$) spin interactions and for cluster sizes 2 and 4. Similar to the weakly disordered case before, cluster size 2 is insufficient to capture the relaxation dynamics quantitatively. In the short-range case ($\alpha = 3$) gcTWA (cluster size 2) struggles to reproduce the oscillatory behavior, which is reflected better by dcTWA. This likely stems from the fact that this coherent dynamics comes about due to the discrete nature of the spin $\frac{1}{2}$ which is mimicked by the discrete sampling procedure [35]. Conversely, for the long-range system

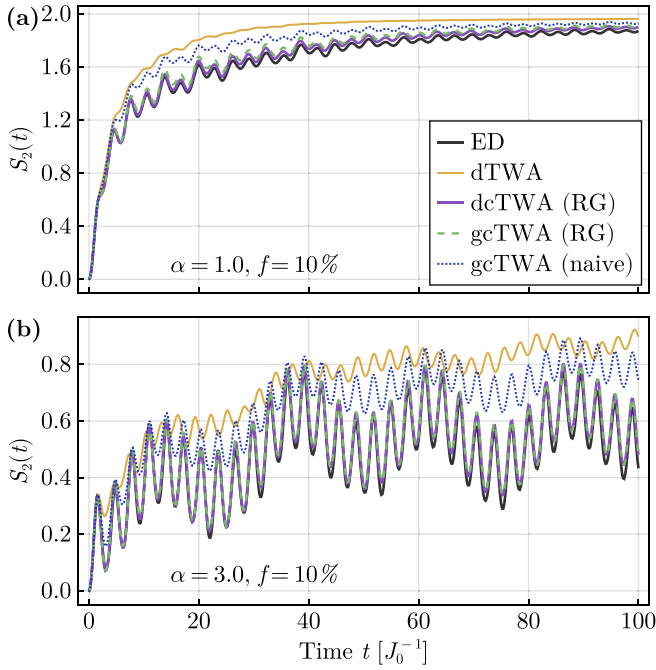


FIG. 6. The average Rényi entropy $\langle S_2(t) \rangle$ is calculated over all possible choices of two sites. This analysis is performed with the same parameter settings as in Fig. 3. The cTWA methods using the RG-inspired clustering [purple (solid) and green (dashed)] reproduce the exact entanglement dynamics [black (solid)] almost exactly with only very slight deviations at late time. Whereas the gcTWA with naive clustering [blue (dotted)] overestimates the entanglement and dTWA [yellow (solid)] even more so.

($\alpha = 1$), this effect is weaker as spins hybridize more due to the stronger interactions. Interestingly, for this setting dcTWA predicts the value of the first minimum more accurately than gcTWA. Increasing the cluster size to 4 spins improves the accuracy of both methods in both cases drastically and we do not find significant differences between the sampling schemes in the long-range case. However, for the short-range case, we find the discrete sampling scheme to approximate the true amplitude of the oscillation generally better than the Gaussian scheme.

To extend our investigation to more complicated, non-local observables, we study the Rényi entropy of two-spin subsystems and assess the efficacy of the semiclassical methods under scrutiny. More specifically, we consider the average Rényi entropy across all possible choices of two sites.

Starting with the strongly disordered setting at $f = 10\%$ in an analogy to above, Fig. 6 illustrates the dynamics of the average Rényi entropy with time in a strongly disordered setting. Since the initial state is a product state, entanglement starts at 0 for $t = 0$ and then starts to increase. We find that generally the semiclassical methods are able to capture the dynamics across the different settings probed qualitatively, as shown in Figs. 6 and 7. Perhaps surprisingly at first, these methods systematically overestimate the amount of entanglement present. This conundrum can be resolved, if one considers that the Rényi entropy is computed by estimating the expectation values of all intrapair correlators and less correlations means more entanglement of the pair with its

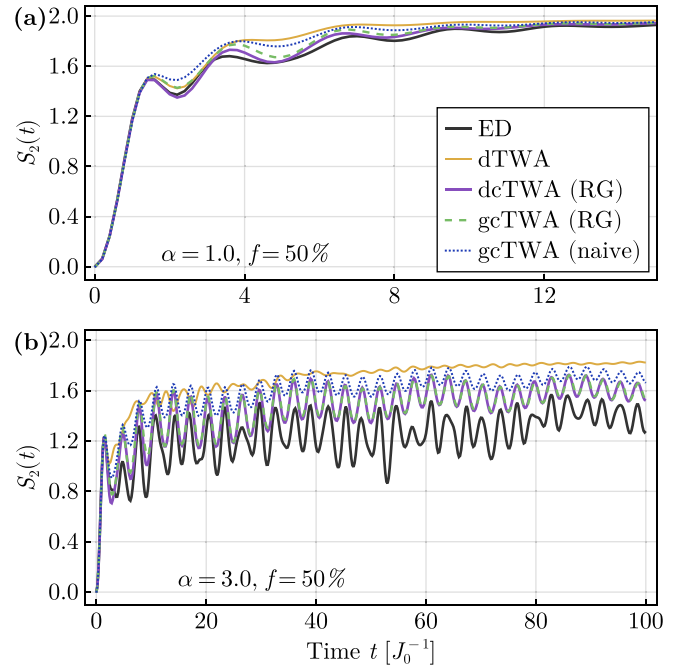


FIG. 7. Same as Fig. 6, but for density fixed at $f = 50\%$. In comparison to Fig. 6, the RG-based cTWA methods deviate from each other and also overestimate the true amount of entanglement present. In the long-range case (a) they do not capture the oscillation frequency correctly, however, in the short-range case (b) they do but underestimate the amplitude.

environment [cf. Eq. (3)]. The semiclassical methods miss out on some of the quantum correlations, thus tend to underestimate the total amount of correlations and consequently predict too much entanglement. Again, the quality of the result depends significantly on the scheme. The deviations are most pronounced for dTWA and the cTWA with naively chosen clusters. Conversely, both dcTWA and gcTWA with the RG clustering scheme approximate the exact dynamics very closely and only overestimate the entanglement by a few percent at late times.

In summary, we find that cTWA may offer tremendous improvements over the simpler dTWA. However, the improvement depends strongly on the choice of clusters. If the clustering does not respect the underlying physics, as is the case for the naive clustering strategy, cTWA showed only a very minor increase in accuracy. On the other hand, if the dominant physical processes are mostly contained within the chosen clusters, as is the case with the RG inspired clustering, cTWA can describe the dynamics of the system over all time intervals almost exactly. The results obtained with the Gaussian Wigner function were very similar compared to the discrete sampling with a slight advantage in favor of the discrete scheme for ordered, short-range systems.

B. Bond-disordered XXZ chain

In this section, we investigate the role of the anisotropy parameter Δ in the dynamics of the system. In the pair picture, a strong anisotropy increases the energy gap between the sectors of different absolute z magnetization. This does not

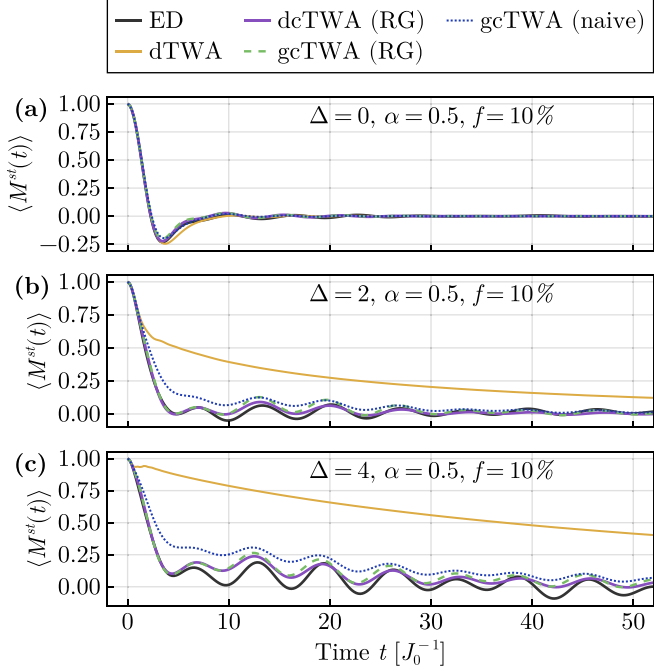


FIG. 8. The disorder-averaged staggered magnetization $\langle M^{st}(t) \rangle$ is shown for XXZ chain of size $N = 16$ with $\alpha = 0.5$ at $f = 10\%$. Different panels are shown different Δ . Results of cTWA, dTWA, and ED are shown with solid blue, dotted green, and solid blue, respectively.

alter the dynamics of a single pair initialized in a Néel state because dynamics is fully contained within the sector of zero magnetization. As such, we expect the choice of clusters to have a large impact on the quality of the approximation whenever the dynamics is heavily dominated by pair dynamics. To expand the domain of our study, we employ $\alpha = 0.5$ to evaluate settings with even more long-range interactions, which in principle should play to TWA's strengths. In the short-range case, we chose $\alpha = 6$, as motivated by the typical interaction exponent of van der Waals interactions in Rydberg atoms which are a possible platform to implement XXZ Heisenberg models (see, e.g., [58]). We note, however, that the qualitative differences to $\alpha = 3$ are minor.

Figures 8 and 9 show the dynamics of the staggered magnetization under long-range ($\alpha = 0.5$) and short-range ($\alpha = 6$) interactions, respectively. Starting again from the Néel state, we examine the evolution of the staggered magnetization by varying Δ , assessing how these adjustments affect the dynamics and how well semiclassical methods approximate the true dynamics. At $\Delta = 0$, all semiclassical methods give results matching the exact solution over almost the entire timescale for the long-range system ($\alpha = 0.5$), while in the short-range system ($\alpha = 6$) only the cTWA simulations using the RG-inspired clustering provide accurate results. dTWA performs worst by predicting oscillation with both wrong amplitude and frequency. gcTWA with naive clustering improves upon this due to the inclusion of more quantum correlations which results in a correct prediction of the frequency.

Increasing the Ising interaction [cf. Figs. 8, 9(b), and 9(c)] does not alter the exact dynamics qualitatively, but dTWA increasingly deviates from the exact results vastly

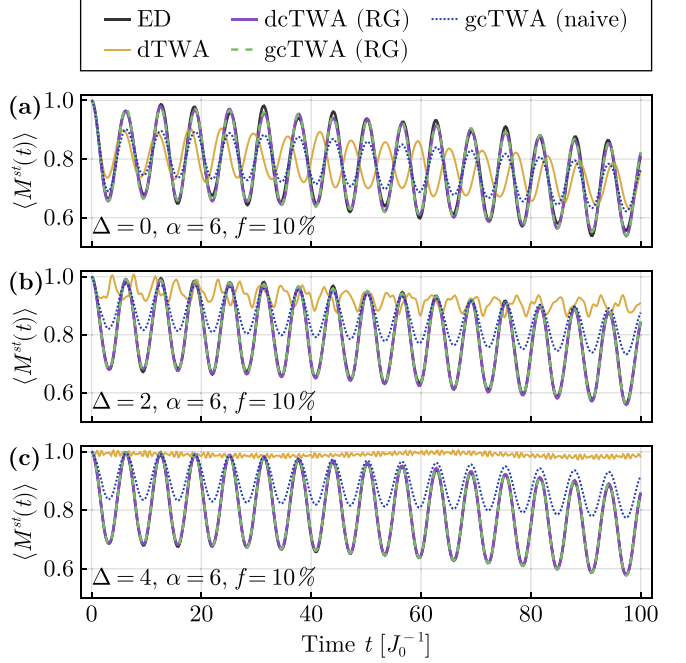


FIG. 9. Same as Fig. 8 but for $\alpha = 6.0$.

underestimating the rate of the initial decay. For the short-range system and $\Delta = 4$ the decay is almost completely suppressed. By contrast, gcTWA with naive clustering yields significantly better results than dTWA. For both systems, the gcTWA prediction qualitatively matches the exact data but is offset by an increasing amount with increasing Δ . Interestingly, both cTWA variants using the RG-inspired clustering match the reference rather closely over the entire time domain except for intermediate times for $\Delta = 4$ in the long-range system $\alpha = 0.5$, where the fluctuations are not reproduced exactly. Surprisingly, this hints at pairs still playing an important role for the dynamics in spite of the quite long-range interactions. For the short-range interactions with strong disorder, the precise match is no surprise as the dynamics is governed by pairs of spins of adjacent lattice sites in this regime.

Again, we employ the semiclassical methods to also extract the average pair Rényi entropy and compare to exact results. Starting with the long-range scenario, $\alpha = 0.5$, we find for $\Delta = 0$ all semiclassical approaches to converge to the true dynamics approximately (Fig. 10). Increasing Δ , we can see again how dTWA fails to capture the essential processes and predict much too slow dynamics (roughly one order of magnitude too slow). gcTWA with naive clustering fares rather well and only slightly underestimates the initial rise for $\Delta = 2$ very similar to gcTWA with RG-inspired clustering. Most interesting are the differences between gcTWA and dcTWA (both with RG clustering) since in this setting both methods seem to converge to slightly different results with dcTWA following the exact curve more closely at intermediate times (up to $t \approx 10J_0$). At late times all cTWA methods overestimate the amount of entanglement present. This trend continues for $\Delta = 4$ where the discrepancy is enhanced for all methods.

For the short-range interacting systems (cf. Fig. 11), we find that cTWA schemes based on the RG clustering to be in

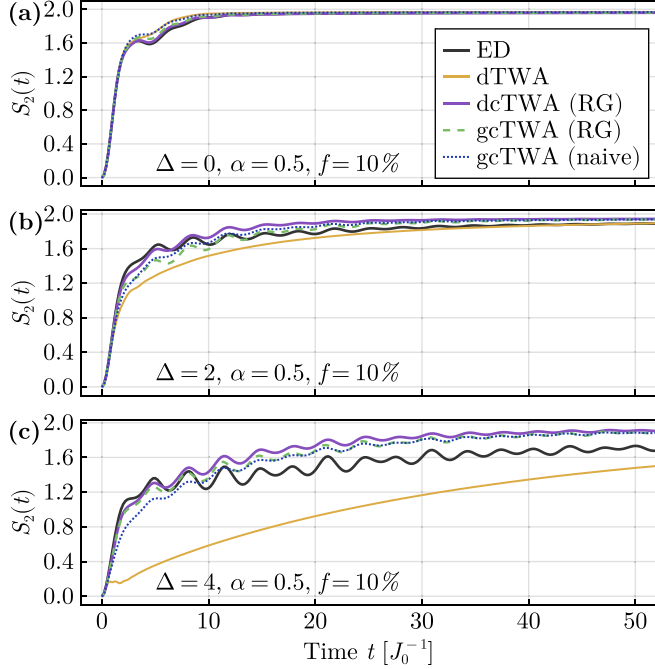


FIG. 10. The average Rényi entropy $\langle S_2(t) \rangle$ is calculated over all possible pairs of two sites. This analysis is performed with the same parameter settings as in Fig. 8.

excellent agreement with the exact results, while the naive clustering gcTWA and dTWA fail to capture the dynamics. This stark contrast to the long-range interacting systems likely originates in the much broader distribution of couplings caused by the much shorter interaction range. Since the RG clustering scheme incorporates the strongest of the relevant couplings, the system can show deviations only at very late timescales.

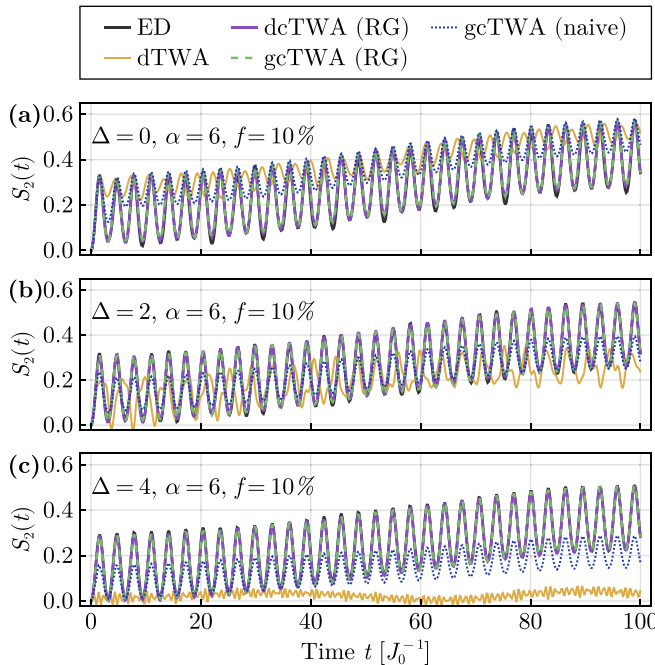


FIG. 11. Same as Fig. 10 but for $\alpha = 6.0$.

In order to understand why dTWA struggles to accurately capture the dynamics of even a single pair of spin interacting via an XXZ Hamiltonian $H = J(\sigma_x^1\sigma_x^2 + \sigma_y^1\sigma_y^2) + \Delta\sigma_z^1\sigma_z^2$ we need to consider its spectrum. Eigenstates of H are the maximally entangled Bell states $|\pm\rangle = (|\uparrow\downarrow\rangle \pm |\downarrow\uparrow\rangle)/\sqrt{2}$ at energies $E_{\pm} = \pm 2J - \Delta$ and the polarized states $|\uparrow\uparrow\rangle$ and $|\downarrow\downarrow\rangle$ with energy $E_p = \Delta$. Taking the Néel state $|\uparrow\downarrow\rangle = (|+\rangle + |-\rangle)/\sqrt{2}$ as initial state, the exact quantum dynamics only populates the two maximally entangled eigenstates. Since their energetic splitting depends on J only, the exact dynamics is independent of Δ and just encompasses the coherent flipping of both spins $|\uparrow\downarrow\rangle \leftrightarrow |\downarrow\uparrow\rangle$. dTWA essentially has access only to single-body terms and thus needs to approximate this process by two steps which will couple to the polarized states. This gives an intuitive understanding of the dependence on Δ for dTWA. The precise nature of this relation is quite intricate and not akin to, e.g., a two-photon transition. For further analysis of the two-spin case with dTWA, we refer to Appendix B. At this point, we want to remark that even cTWA of course captures the dynamics exactly if the two spins are part of the same cluster, but still the state is not represented exactly at all times. As we have shown in Appendix A, dcTWA can only represent states where the Wigner function is non-negative but one can ensure that all observables within a cluster have correct means and only higher moments deviate.

In summary, we find that even in very long-range systems and for strong Ising interactions the RG-inspired clustering yields quite accurate results at early and intermediate times. At late times, we see some deviations that increase with the strength of the Ising couplings which likely signals the breakdown of the pair approximation in this regime. For short-range interactions, the cTWA methods with RG clustering yield basically exact results in all cases studied here. Conversely, dTWA and gcTWA with the naive clustering strategy struggle due to the competition of the Ising and hopping interactions. We did not see a significant difference between discrete and Gaussian sampling in these settings.

C. Statistical error analysis

To highlight the merits of the discrete sampling scheme, we study the convergence of the staggered magnetization Monte Carlo samples by extracting standard deviation of the staggered magnetization across 10 000 trajectories of a single disorder shot. While previous analyses did not show large differences in result between the sampling schemes, Fig. 12(a) reveals the higher accuracy of the discrete sampling schemes which leads to a reduced number of samples required to achieve a given level of precision. Averaged over the timescale shown, we report approximately 8% smaller standard deviation for dcTWA with cluster size 2 and 15% reduction for cluster size 4. This translates to approximately 16%, and 28% fewer trajectories needed to achieve similar levels of accuracy.

We repeat this analysis for the Renyi entropy, where we estimate the standard deviation from 100 sets of 100 trajectories each [cf. Fig. 12(b)]. Again by averaging, we find a similar reduction of 14% and 29% reduction in standard deviation for cluster sizes 2 and 4, respectively.

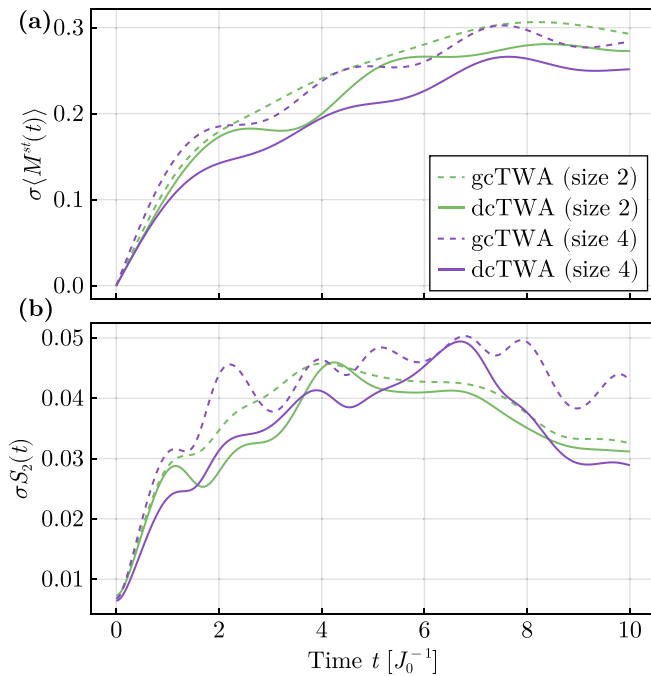


FIG. 12. Error analysis for a single shot with the parameters $\alpha = 1$, $f = 10\%$, $\Delta = 0$ and 10 000 trajectories. We compute the standard deviation of (a) the staggered magnetization and (b) average pair Renyi entropy estimated from batches of 100 trajectories. We use naive clustering to compare both cluster sizes 2 (green lines) and 4 (purple lines) as well as Gaussian sampling (dashed) and discrete sampling (solid).

IV. CONCLUSION

In this study, we conducted a comprehensive numerical investigation focusing on the cluster truncated Wigner approximation (cTWA) for modeling quench dynamics in disordered spin chains with power-law interactions. Through comparisons with the discrete truncated Wigner approximation (dTWA) and with exact diagonalization, we explored the performance of the cTWA on different timescales relevant to quench experiments and studied the influence of the choice of clusters on the prediction. Additionally, we introduced a sampling scheme for generating Monte Carlo trajectories which extends the discrete Wigner function known from dTWA to the realm of cTWA. Our analysis included both the XX and XXZ models with bond disorder initiated from a Néel state, and calculated dynamical observables such as staggered magnetization and two-site Rényi entropy.

We found that while cTWA generally yields improved accuracy compared to dTWA, the choice of clusters strongly impacts the results. Our results in the context of bond disorder show that a clustering strategy inspired by the strong disorder renormalization group could yield astonishingly precise results in the presence of strong disorder, while still being very accurate even for quite long-range interactions, weak disorder, and long times. XXZ models featuring strong Ising interactions were found to be challenging for all semiclassical methods presented here and we conclude that likely larger clusters are needed to capture the relevant physical processes accurately. In all of these systems, we only found minor

differences between the Gaussian and discrete sampling schemes in situations where the results were not converged in cluster size. However, a closer study of the statistical properties revealed the discrete sampling to exhibit smaller intrinsic Monte Carlo shot noise.

In conclusion, our study provides valuable insights into the effectiveness of cTWA in studying quench dynamics in bond-disordered spin systems. If using the correct clustering strategy, even clusters of size 2 yield close to exact results, where single-spin dTWA fails. Additionally, we conclude that the discrete sampling strategy introduced here is generally preferable to the Gaussian approximation due to less Monte Carlo shot noise and somewhat simpler implementation. We also want to emphasize that the method presented here is not intrinsically limited to one-dimensional systems and can be applied readily to higher-dimensional systems with arbitrary geometries. We expect cTWA to be able to perform well as long as the coupling matrix is sufficiently disordered. For spatially disordered systems, this should be the case as long as the power-law exponent is larger than the spatial dimension [59] and the density is sufficiently low. In more long-range or denser scenarios, it would likely be beneficial to generalize the clustering algorithm described here to larger clusters, e.g., based on heuristic renormalization group schemes such as [60,61]. Overall, our results highlight the potential of cTWA and its variants, such as dcTWA, as powerful tools for studying the complex dynamics of bond-disordered quantum systems.

ACKNOWLEDGMENTS

We thank O. Egorov for providing computational resources. We acknowledge State of Thuringia for funding of projects “2019 FGI 0017” (PhyClus) and “2022 FGI 0004” (Q-PHOC3). A.B. acknowledges support by the Deutsche Forschungsgemeinschaft (DFG, German Research Foundation) within the Collaborative Research Center SFB1225 (ISOQUANT). For the numerical work, we used the Julia programming language [62] and the following packages and tools: DrWatson.jl [63], Pluto.jl [64], DifferentialEquations.jl [65] with Verner’s integration schemes [66], Makie.jl [67], DataFrames.jl [68].

APPENDIX A: SAMPLING FROM DISCRETE WIGNER FUNCTIONS OF SPIN CLUSTERS

In this Appendix, we first recapitulate how to derive the concrete sampling rules of dTWA and then extend the scheme to clusters of multiple spins. Finally, we provide a concrete example of sampling rules for clusters of 2 spins. The concepts described here are similar to Appendix A in [37].

1. Recap: Sampling a single spin

Earlier in Sec. II B 2, we defined the phase-point operators for a single spin

$$\hat{A}_{p,q} = [\mathbb{1} + \mathbf{r}(p, q) \cdot \hat{\sigma}] / 2 \quad (\text{A1})$$

via a choice of phase-point vectors $\mathbf{r}(p, q)$. In principle there are many possible choices for $\mathbf{r}(p, q)$ but since there are a total of 8 discrete spin states, two sets of phase point operators are

enough to cover all possible states. We define the two sets of phase-point operators (see Fig. 2 in [40] for a visualization) via

$$r^1(0, 0) = (1, 1, 1), \quad (\text{A2a})$$

$$r^1(0, 1) = (-1, -1, 1), \quad (\text{A2b})$$

$$r^1(1, 0) = (1, -1, -1), \quad (\text{A2c})$$

$$r^1(1, 1) = (-1, 1, -1), \quad (\text{A2d})$$

and

$$r^2(0, 0) = (1, -1, 1), \quad (\text{A3a})$$

$$r^2(0, 1) = (-1, 1, 1), \quad (\text{A3b})$$

$$r^2(1, 0) = (1, 1, -1), \quad (\text{A3c})$$

$$r^2(1, 1) = (-1, -1, -1). \quad (\text{A3d})$$

With this choice, we can define the Wigner function of some quantum state $\hat{\rho}$ as

$$w^s(p, q; \hat{\rho}) = \frac{1}{2} \text{Tr } \hat{\rho} \hat{A}_{(p,q)}^s, \quad (\text{A4})$$

where $s = 1, 2$ denotes the set of phase-point operators. These are normalized for each set, i.e., $\sum_{p,q} w^s(p, q; \hat{\rho}) = \text{Tr } \hat{\rho} = 1$ independent of s , and thus quasiprobability distributions. In case all values of a $w^s(p, q; \hat{\rho})$ are positive, we can treat it as a probability distribution and sample initial conditions for the truncated Wigner approximation from it. For a single spin, it is always possible to rotate the phase-point operators to render the Wigner functions positive, so we can always sample from either one of the two possible choices of Wigner functions. In fact, it is crucial to employ both choices for sampling to prevent the introduction of spurious correlations (see example below) [33,40]. To be explicit, the complete sampling procedure for a single trajectory first randomly selects one of the phase-space representation and then draws a phase-space vector according to its Wigner function.

We illustrate this prescription using the state $\rho = |\uparrow\rangle\langle\uparrow|$ as an example. The Wigner functions read as

$$\mathbf{w}^1(\rho) = \begin{pmatrix} w^1(0, 0) & w^1(0, 1) \\ w^1(1, 0) & w^1(1, 1) \end{pmatrix} = \begin{pmatrix} \frac{1}{2} & \frac{1}{2} \\ 0 & 0 \end{pmatrix}, \quad (\text{A5a})$$

$$\mathbf{w}^2(\rho) = \begin{pmatrix} w^2(0, 0) & w^2(0, 1) \\ w^2(1, 0) & w^2(1, 1) \end{pmatrix} = \begin{pmatrix} \frac{1}{2} & \frac{1}{2} \\ 0 & 0 \end{pmatrix}. \quad (\text{A5b})$$

Choosing one these Wigner functions at random and then sampling from it is equivalent to drawing a sample from the set $\{r^1(0, 0), r^1(0, 1), r^2(0, 0), r^2(0, 1)\}$. In turn, this just means we need to set the z component to 1 and choose x and y independently from ± 1 . We remark that this prescription reproduces all moments of the spin operators $\langle (\hat{\sigma}_{x,y,z})^k \rangle$ in contrast to the Gaussian approximation which reproduces means and covariances only. Additionally, we remark that every possible phase point of \mathbf{w}^1 (\mathbf{w}^2) has the x and y components aligned (antialigned), which is the spurious correlation mentioned earlier. By using both Wigner functions, we avoid artifacts caused by this, making the simulation more accurate.

2. Generalization to clusters of spins

The prescription, we just outlined, readily generalizes to clusters of spins by taking tensor products of the phase-point operators. Consider a cluster of n spins: The joint Hilbert space is now $SU(D)$, where $D = 2^n$, given from the tensor product of Hilbert spaces of the single spins. In the following, we essentially repeat the construction from before applied to the cluster's Hilbert space and exploit its product structure. We denote the operator basis of a cluster of n spins by \mathbf{X}_n , which can be constructed recursively by

$$\hat{\mathbf{X}}_1 \equiv \hat{\sigma}, \quad (\text{A6a})$$

$$[\hat{\mathbf{X}}_n]_i = \begin{cases} \hat{\sigma}_i \otimes \mathbb{1}, & i \in \{1, 2, 3\} \\ \mathbb{1} \otimes \hat{\sigma}_{i-3}, & i \in \{4, 5, 6\} \\ [\hat{\mathbf{X}}_1 \otimes \hat{\mathbf{X}}_{n-1}]_{i-6}, & \text{else} \end{cases} \quad (\text{A6b})$$

where $[\cdot]_i$ denotes the i th component of the vector.

In much the same way, we can construct the phase-point vectors. However, we need to consider that we have two possible choices for each spin to make, so there are a total of 2^n sets of phase-point operators. Using $\mathbf{s} \in \{1, 2\}^n$, we can construct the phase-point vectors corresponding to the operator basis defined above as

$$\begin{aligned} \mathbf{r}_n^s(\mathbf{p}, \mathbf{q}) &= \mathbf{r}^{s_1}(p_1, q_1) \\ &\oplus \mathbf{r}_{n-1}^{\tilde{s}}(\tilde{\mathbf{p}}, \tilde{\mathbf{q}}) \\ &\oplus [\mathbf{r}^{s_1}(p_1, q_1) \otimes \mathbf{r}_{n-1}^{\tilde{s}}(\tilde{\mathbf{p}}, \tilde{\mathbf{q}})], \end{aligned} \quad (\text{A7})$$

where the vectors with tilde ($\tilde{\mathbf{s}}$, $\tilde{\mathbf{p}}$, and $\tilde{\mathbf{q}}$) are the same as the bare vectors without the first element, e.g., $\tilde{\mathbf{s}} = (s_2, \dots, s_n)$. From these building blocks, we can define the Wigner functions of the cluster as

$$w^s(\mathbf{p}, \mathbf{q}; \hat{\rho}) = \frac{1}{2^n} \text{Tr } \hat{\rho} \hat{A}_{(\mathbf{p}, \mathbf{q})}^s \quad (\text{A8})$$

$$= \frac{1}{4^n} \text{Tr } \hat{\rho} (\mathbb{1} + \mathbf{r}_n^s(\mathbf{p}, \mathbf{q}) \cdot \hat{\mathbf{X}}_n). \quad (\text{A9})$$

As can be checked easily via induction, this definition gives us a normalized Wigner function for every choice of \mathbf{s} .

Another short calculation shows that if the quantum state $\hat{\rho}$ factorizes between the spins, i.e., $\rho = \bigotimes_{i \leq n} \hat{\rho}_i$, then the Wigner function factorizes as well:

$$w^s\left(\mathbf{p}, \mathbf{q}; \bigotimes_{i \leq n} \hat{\rho}_i\right) = \prod_{i \leq n} w^{s_i}(p_i, q_i; \hat{\rho}_i). \quad (\text{A10})$$

This allows for efficient sampling.

To derive rules for sampling initial states, conceptually one needs to choose a random set of phase-point representations, i.e., draw \mathbf{s} randomly, and then choose a phase-space vector $\mathbf{r}_n^s(\mathbf{p}, \mathbf{q})$ with a probability determined by the corresponding Wigner function $w^s(\mathbf{p}, \mathbf{q})$. In case of a product initial state, this prescription simplifies dramatically because we choose the phase-space vector of each spin independently and compute the initial value of correlators by products [see Eq. (A8)].

We illustrate the prescription given above using the Néel state $\hat{\rho} = |\uparrow\downarrow\rangle\langle\uparrow\downarrow|$. Applying the rule for product states, we can immediately state the sampling scheme: Set $\langle\hat{\sigma}_z^1\rangle = -\langle\hat{\sigma}_z^2\rangle = 1$, choose $\langle\hat{\sigma}_x^1\rangle, \langle\hat{\sigma}_y^1\rangle, \langle\hat{\sigma}_x^2\rangle, \langle\hat{\sigma}_y^2\rangle$ randomly from $\{-1, 1\}$, and then compute the initial values of the correlators by products, e.g., $\langle\hat{\sigma}_x^1\hat{\sigma}_x^2\rangle = \langle\hat{\sigma}_x^1\rangle\langle\hat{\sigma}_x^2\rangle$.

Alternatively, we can employ the tedious route and compute all the Wigner functions. We start by computing the single-spin Wigner functions, which for $|\uparrow\rangle\langle\downarrow|$ are given in Eqs. (A5a) and (A5b). Similarly for $|\downarrow\rangle\langle\uparrow|$, we find

$$\mathbf{w}^1(|\downarrow\rangle) = \mathbf{w}^2(|\downarrow\rangle) = \begin{pmatrix} 0 & 0 \\ \frac{1}{2} & \frac{1}{2} \end{pmatrix}. \quad (\text{A11})$$

From this we can compute the full two-spin Wigner functions:

$$\begin{aligned} \mathbf{w}^{(1,1)} = \mathbf{w}^{(2,2)} &= \mathbf{w}^1(|\uparrow\rangle)\otimes\mathbf{w}^1(|\downarrow\rangle) \\ &= \begin{pmatrix} w^1(|\uparrow\rangle)(0,0)\cdot\mathbf{w}^1(|\downarrow\rangle) & w^1(|\uparrow\rangle)(0,1)\cdot\mathbf{w}^1(|\downarrow\rangle) \\ w^1(|\uparrow\rangle)(1,0)\cdot\mathbf{w}^1(|\downarrow\rangle) & w^1(|\uparrow\rangle)(1,1)\cdot\mathbf{w}^1(|\downarrow\rangle) \end{pmatrix} \\ &= \begin{pmatrix} 0 & 0 & 0 & 0 \\ \frac{1}{4} & \frac{1}{4} & \frac{1}{4} & \frac{1}{4} \\ 0 & 0 & 0 & 0 \\ 0 & 0 & 0 & 0 \end{pmatrix}, \end{aligned} \quad (\text{A12})$$

$$\mathbf{w}^{(1,2)} = \mathbf{w}^{(2,1)} = \begin{pmatrix} 0 & 0 & 0 & 0 \\ 0 & 0 & 0 & 0 \\ \frac{1}{4} & \frac{1}{4} & \frac{1}{4} & \frac{1}{4} \\ 0 & 0 & 0 & 0 \end{pmatrix}. \quad (\text{A13})$$

To generate a single sample, we first need to select one of the four Wigner functions, e.g., $w^{(1,1)}$. This Wigner function gives us the probability distribution to choose the state from, which in this case means we need to select one of the phase points (\mathbf{p}, \mathbf{q}) from the set

$$\left\{ \left[\begin{pmatrix} 0 \\ 1 \end{pmatrix}, \begin{pmatrix} 0 \\ 0 \end{pmatrix} \right], \left[\begin{pmatrix} 0 \\ 1 \end{pmatrix}, \begin{pmatrix} 0 \\ 1 \end{pmatrix} \right], \right. \\ \left. \left[\begin{pmatrix} 0 \\ 1 \end{pmatrix}, \begin{pmatrix} 1 \\ 0 \end{pmatrix} \right], \left[\begin{pmatrix} 0 \\ 1 \end{pmatrix}, \begin{pmatrix} 1 \\ 1 \end{pmatrix} \right] \right\} \quad (\text{A14})$$

with equal probability. Assuming we selected the first phase point, then the corresponding phase-space vector is given by

$$\begin{aligned} \mathbf{r}_2^{(1,1)} \left(\begin{pmatrix} 0 \\ 1 \end{pmatrix}, \begin{pmatrix} 0 \\ 0 \end{pmatrix} \right) &= \mathbf{r}^1(0,0) \oplus \mathbf{r}^1(1,0) \\ &\oplus [\mathbf{r}^1(0,0) \otimes \mathbf{r}^1(1,0)]. \end{aligned} \quad (\text{A15})$$

The corresponding initial values of the trajectory are given explicitly in Table I.

APPENDIX B: SINGLE PAIR DYNAMICS

To illustrate the inaccuracy of dTWA in the presence of XX interactions, we study the same system as in the main text for two spins. Repeating the definition here for convenience, we consider the Hamiltonian

$$\hat{H} = 2J(\hat{\sigma}_x^1\hat{\sigma}_x^2 + \hat{\sigma}_y^1\hat{\sigma}_y^2) + 2\Delta\hat{\sigma}_z^1\hat{\sigma}_z^2, \quad (\text{B1})$$

the initial state $|\psi_0\rangle = |\uparrow\downarrow\rangle$ and the observable $\hat{M}^{\text{st}} = \frac{1}{2}(\hat{\sigma}_z^1 + \hat{\sigma}_z^2)$. Since this Hamiltonian conserves total z

TABLE I. Coefficients for the phase-point vector given in Eq. (A15).

Index i	Operator X_i	Initial value	Term in Eq. (A15)
1	$\langle\hat{\sigma}_x^1\rangle$	1	$\mathbf{r}^1(0,0)$
2	$\langle\hat{\sigma}_y^1\rangle$	1	
3	$\langle\hat{\sigma}_z^1\rangle$	1	
4	$\langle\hat{\sigma}_x^2\rangle$	1	$\mathbf{r}^1(1,0)$
5	$\langle\hat{\sigma}_y^2\rangle$	1	
6	$\langle\hat{\sigma}_z^2\rangle$	-1	
7	$\langle\hat{\sigma}_x^1\hat{\sigma}_x^2\rangle$	1	$\mathbf{r}^1(0,0) \otimes \mathbf{r}^1(1,0)$
8	$\langle\hat{\sigma}_x^1\hat{\sigma}_y^2\rangle$	1	
9	$\langle\hat{\sigma}_x^1\hat{\sigma}_z^2\rangle$	-1	
10	$\langle\hat{\sigma}_y^1\hat{\sigma}_x^2\rangle$	1	
11	$\langle\hat{\sigma}_y^1\hat{\sigma}_y^2\rangle$	1	
12	$\langle\hat{\sigma}_y^1\hat{\sigma}_z^2\rangle$	-1	
13	$\langle\hat{\sigma}_z^1\hat{\sigma}_x^2\rangle$	1	
14	$\langle\hat{\sigma}_z^1\hat{\sigma}_y^2\rangle$	1	
15	$\langle\hat{\sigma}_z^1\hat{\sigma}_z^2\rangle$	-1	

magnetization $\hat{M}_z = \hat{\sigma}_z^1 + \hat{\sigma}_z^2$, the dynamics stays confined to the zero magnetization sector, where the state oscillates back and forth between $|\uparrow\downarrow\rangle \leftrightarrow |\downarrow\uparrow\rangle$. So the exact solution reads as $\langle\hat{M}^{\text{st}}(t)\rangle = \cos(8Jt)$. This is independent of Δ because the ZZ term $\hat{\sigma}_z^1\hat{\sigma}_z^2$ of course commutes with \hat{M}_z and thus cannot introduce additional couplings.

Setting $J = 1$ and using dTWA to solve the dynamics for several values of Δ , we see that the semiclassical solution is both influenced strongly by the value of Δ and yields inaccurate results even for $\Delta = 0$ (cf. Fig. 13).

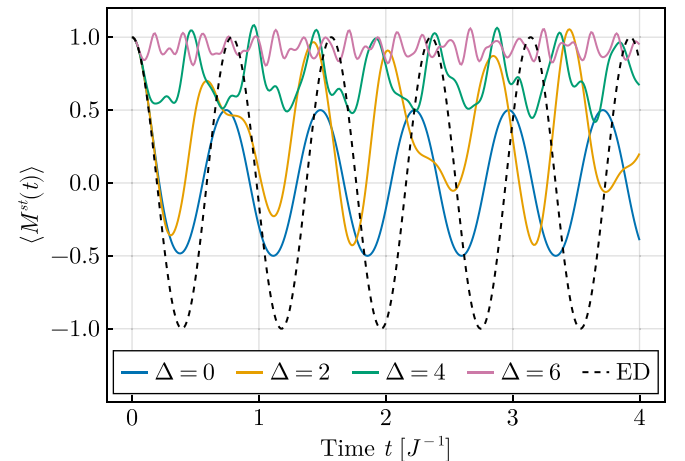


FIG. 13. Dynamics of the staggered magnetization for two spins with XXZ interaction for various anisotropies Δ . Shown is the exact solution [black (dashed)] and solutions obtained with dTWA [colors (solid)]. The exact dynamics are independent of Δ , so only a single curve is shown.

- [1] P. W. Anderson, Absence of diffusion in certain random lattices, *Phys. Rev.* **109**, 1492 (1958).
- [2] N. F. Mott, Impurity band conduction. Experiment and theory the metal-insulator transition in an impurity band, *J. Phys. Colloques* **37**, C4-301 (1976).
- [3] S. Kettemann, Towards a comprehensive theory of metal-insulator transitions in doped semiconductors, *Ann. Phys.* **456**, 169306 (2023).
- [4] L. D. Cesare, K. Lukierska-Walasek, I. Rabuffo, and K. Walasek, Two-spin cluster approach to the infinite-range quantum transverse XY spin-glass model, *Phys. Lett. A* **145**, 291 (1990).
- [5] L. De Cesare, K. Lukierska-Walasek, I. Rabuffo, and K. Walasek, Cavity-fields approach to quantum XY spin-glass models in a transverse field, *Phys. Rev. B* **45**, 1041 (1992).
- [6] A. de Paz, A. Sharma, A. Chotia, E. Maréchal, J. H. Huckans, P. Pedri, L. Santos, O. Gorceix, L. Vernac, and B. Laburthe-Tolra, Nonequilibrium quantum magnetism in a dipolar lattice gas, *Phys. Rev. Lett.* **111**, 185305 (2013).
- [7] B. Yan, S. A. Moses, B. Gadway, J. P. Covey, K. R. A. Hazzard, A. M. Rey, D. S. Jin, and J. Ye, Observation of dipolar spin-exchange interactions with lattice-confined polar molecules, *Nature (London)* **501**, 521 (2013).
- [8] P. Fersterer, A. Safavi-Naini, B. Zhu, L. Gabardos, S. Lepoutre, L. Vernac, B. Laburthe-Tolra, P. B. Blakie, and A. M. Rey, Dynamics of an itinerant spin-3 atomic dipolar gas in an optical lattice, *Phys. Rev. A* **100**, 033609 (2019).
- [9] J. Zeiher, J.-y. Choi, A. Rubio-Abadal, T. Pohl, R. van Bijnen, I. Bloch, and C. Gross, Coherent many-body spin dynamics in a long-range interacting Ising chain, *Phys. Rev. X* **7**, 041063 (2017).
- [10] H. Bernien, S. Schwartz, A. Keesling, H. Levine, A. Omran, H. Pichler, S. Choi, A. S. Zibrov, M. Endres, M. Greiner, V. Vuletić, and M. D. Lukin, Probing many-body dynamics on a 51-atom quantum simulator, *Nature (London)* **551**, 579 (2017).
- [11] A. Keesling, A. Omran, H. Levine, H. Bernien, H. Pichler, S. Choi, R. Samajdar, S. Schwartz, P. Silvi, S. Sachdev, P. Zoller, M. Endres, M. Greiner, V. Vuletić, and M. D. Lukin, Quantum Kibble–Zurek mechanism and critical dynamics on a programmable Rydberg simulator, *Nature (London)* **568**, 207 (2019).
- [12] R. Islam, C. Senko, W. C. Campbell, S. Korenblit, J. Smith, A. Lee, E. E. Edwards, C.-C. J. Wang, J. K. Freericks, and C. Monroe, Emergence and frustration of magnetism with variable-range interactions in a quantum simulator, *Science* **340**, 583 (2013).
- [13] P. Jurcevic, B. P. Lanyon, P. Hauke, C. Hempel, P. Zoller, R. Blatt, and C. F. Roos, Quasiparticle engineering and entanglement propagation in a quantum many-body system, *Nature (London)* **511**, 202 (2014).
- [14] P. Richerme, Z.-X. Gong, A. Lee, C. Senko, J. Smith, M. Foss-Feig, S. Michalakis, A. V. Gorshkov, and C. Monroe, Non-local propagation of correlations in quantum systems with long-range interactions, *Nature (London)* **511**, 198 (2014).
- [15] M. Gärttner, J. G. Bohnet, A. Safavi-Naini, M. L. Wall, J. J. Bollinger, and A. M. Rey, Measuring out-of-time-order correlations and multiple quantum spectra in a trapped-ion quantum magnet, *Nat. Phys.* **13**, 781 (2017).
- [16] A. Signoles, T. Franz, R. F. Alves, M. Gärttner, S. Whitlock, G. Zürn, and M. Weidemüller, Glassy dynamics in a disordered Heisenberg quantum spin system, *Phys. Rev. X* **11**, 011011 (2021).
- [17] A. Nauts and R. E. Wyatt, New approach to many-state quantum dynamics: The recursive-residue-generation method, *Phys. Rev. Lett.* **51**, 2238 (1983).
- [18] T. J. Park and J. C. Light, Unitary quantum time evolution by iterative Lanczos reduction, *J. Chem. Phys.* **85**, 5870 (1986).
- [19] L. Colmenarez and D. J. Luitz, Lieb-Robinson bounds and out-of-time order correlators in a long-range spin chain, *Phys. Rev. Res.* **2**, 043047 (2020).
- [20] J. Vahedi, Asymmetric transport in long-range interacting chiral spin chains, *SciPost Phys. Core* **5**, 021 (2022).
- [21] M. Faridfar and J. Vahedi, Thermodynamic behavior of spin-1 Heisenberg chain: A comparative study, *J. Supercond. Novel Magn.* **35**, 519 (2022).
- [22] U. Schollwoeck, The density-matrix renormalization group in the age of matrix product states, *Ann. Phys.* **326**, 96 (2011).
- [23] G. Vidal, Efficient classical simulation of slightly entangled quantum computations, *Phys. Rev. Lett.* **91**, 147902 (2003).
- [24] S. R. White and A. E. Feiguin, Real-time evolution using the density matrix renormalization group, *Phys. Rev. Lett.* **93**, 076401 (2004).
- [25] M. P. Zaletel, R. S. K. Mong, C. Karrasch, J. E. Moore, and F. Pollmann, Time-evolving a matrix product state with long-ranged interactions, *Phys. Rev. B* **91**, 165112 (2015).
- [26] S. Paeckel, T. Köhler, A. Swoboda, S. R. Manmana, U. Schollwöck, and C. Hubig, Time-evolution methods for matrix-product states, *Ann. Phys.* **411**, 167998 (2019).
- [27] P. B. Blakie, A. Bradley, M. Davis, R. Ballagh, and C. Gardiner, Dynamics and statistical mechanics of ultra-cold Bose gases using c-field techniques, *Adv. Phys.* **57**, 363 (2008).
- [28] A. Polkovnikov, Phase space representation of quantum dynamics, *Ann. Phys.* **325**, 1790 (2010).
- [29] A. K. Tuchman, C. Orzel, A. Polkovnikov, and M. A. Kasevich, Nonequilibrium coherence dynamics of a soft boson lattice, *Phys. Rev. A* **74**, 051601(R) (2006).
- [30] S. M. Davidson, D. Sels, and A. Polkovnikov, Semiclassical approach to dynamics of interacting fermions, *Ann. Phys.* **384**, 128 (2017).
- [31] K. Nagao, M. Kunimi, Y. Takasu, Y. Takahashi, and I. Danshita, Semiclassical quench dynamics of Bose gases in optical lattices, *Phys. Rev. A* **99**, 023622 (2019).
- [32] S. R. Muleady, M. Yang, S. R. White, and A. M. Rey, Validating phase-space methods with tensor networks in two-dimensional spin models with power-law interactions, *Phys. Rev. Lett.* **131**, 150401 (2023).
- [33] C. D. Mink, D. Petrosyan, and M. Fleischhauer, Hybrid discrete-continuous truncated Wigner approximation for driven, dissipative spin systems, *Phys. Rev. Res.* **4**, 043136 (2022).
- [34] W. K. Wootters, A Wigner-function formulation of finite-state quantum mechanics, *Ann. Phys.* **176**, 1 (1987).
- [35] J. Schachenmayer, A. Pikovski, and A. M. Rey, Many-body quantum spin dynamics with Monte Carlo trajectories on a discrete phase space, *Phys. Rev. X* **5**, 011022 (2015).
- [36] J. Schachenmayer, A. Pikovski, and A. M. Rey, Dynamics of correlations in two-dimensional quantum spin models with long-range interactions: A phase-space Monte-Carlo study, *New J. Phys.* **17**, 065009 (2015).

- [37] L. Pucci, A. Roy, and M. Kastner, Simulation of quantum spin dynamics by phase space sampling of Bogoliubov-Born-Green-Kirkwood-Yvon trajectories, *Phys. Rev. B* **93**, 174302 (2016).
- [38] O. L. Acevedo, A. Safavi-Naini, J. Schachenmayer, M. L. Wall, R. Nandkishore, and A. M. Rey, Exploring many-body localization and thermalization using semiclassical methods, *Phys. Rev. A* **96**, 033604 (2017).
- [39] A. P. Orioli, A. Safavi-Naini, M. L. Wall, and A. M. Rey, Nonequilibrium dynamics of spin-boson models from phase-space methods, *Phys. Rev. A* **96**, 033607 (2017).
- [40] S. Czischek, M. Gärttner, M. Oberthaler, M. Kastner, and T. Gasenzer, Quenches near criticality of the quantum Ising chain—power and limitations of the discrete truncated Wigner approximation, *Quantum Sci. Technol.* **4**, 014006 (2018).
- [41] A. P. Orioli, A. Signoles, H. Wildhagen, G. Günter, J. Berges, S. Whitlock, and M. Weidemüller, Relaxation of an isolated dipolar-interacting Rydberg quantum spin system, *Phys. Rev. Lett.* **120**, 063601 (2018).
- [42] B. Sundar, K. C. Wang, and K. R. A. Hazzard, Analysis of continuous and discrete Wigner approximations for spin dynamics, *Phys. Rev. A* **99**, 043627 (2019).
- [43] R. Khassseh, A. Russomanno, M. Schmitt, M. Heyl, and R. Fazio, Discrete truncated Wigner approach to dynamical phase transitions in Ising models after a quantum quench, *Phys. Rev. B* **102**, 014303 (2020).
- [44] M. Kunimi, K. Nagao, S. Goto, and I. Danshita, Performance evaluation of the discrete truncated Wigner approximation for quench dynamics of quantum spin systems with long-range interactions, *Phys. Rev. Res.* **3**, 013060 (2021).
- [45] W. Morong, S. R. Muleady, I. Kimchi, W. Xu, R. M. Nandkishore, A. M. Rey, and B. DeMarco, Disorder-controlled relaxation in a three-dimensional Hubbard model quantum simulator, *Phys. Rev. Res.* **3**, L012009 (2021).
- [46] S. M. Davidson and A. Polkovnikov, $SU(3)$ semiclassical representation of quantum dynamics of interacting spins, *Phys. Rev. Lett.* **114**, 045701 (2015).
- [47] J. Wurtz, A. Polkovnikov, and D. Sels, Cluster truncated Wigner approximation in strongly interacting systems, *Ann. Phys.* **395**, 341 (2018).
- [48] B. Zhu, A. M. Rey, and J. Schachenmayer, A generalized phase space approach for solving quantum spin dynamics, *New J. Phys.* **21**, 082001 (2019).
- [49] K. Nagao and S. Yunoki, Two-dimensional correlation propagation dynamics with a cluster discrete phase-space method, *arXiv:2404.18594*.
- [50] Y. Mohdeb, J. Vahedi, N. Moure, A. Roshani, H.-Y. Lee, R. N. Bhatt, S. Kettemann, and S. Haas, Entanglement properties of disordered quantum spin chains with long-range antiferromagnetic interactions, *Phys. Rev. B* **102**, 214201 (2020).
- [51] Y. Mohdeb, J. Vahedi, and S. Kettemann, Excited-eigenstate entanglement properties of XX spin chains with random long-range interactions, *Phys. Rev. B* **106**, 104201 (2022).
- [52] Y. Mohdeb, J. Vahedi, R. N. Bhatt, S. Haas, and S. Kettemann, Global quench dynamics and the growth of entanglement entropy in disordered spin chains with tunable range interactions, *Phys. Rev. B* **108**, L140203 (2023).
- [53] E. Altman and R. Vosk, Universal dynamics and renormalization in many-body-localized systems, *Annu. Rev. Condens. Matter Phys.* **6**, 383 (2015).
- [54] R. Vasseur, A. C. Potter, and S. A. Parameswaran, Quantum criticality of hot random spin chains, *Phys. Rev. Lett.* **114**, 217201 (2015).
- [55] F. Iglói and C. Monthus, Strong disorder RG approach—a short review of recent developments, *Eur. Phys. J. B* **91**, 290 (2018).
- [56] <https://github.com/abraemer/DiscreteCTWAPaper>
- [57] A. Braemer, T. Franz, M. Weidemüller, and M. Gärttner, Pair localization in dipolar systems with tunable positional disorder, *Phys. Rev. B* **106**, 134212 (2022).
- [58] S. Geier, N. Thaicharoen, C. Hainaut, T. Franz, A. Salzinger, A. Tebben, D. Grimshndl, G. Zürn, and M. Weidemüller, Floquet Hamiltonian engineering of an isolated many-body spin system, *Science* **374**, 1149 (2021).
- [59] N. Y. Yao, C. R. Laumann, S. Gopalakrishnan, M. Knap, M. Müller, E. A. Demler, and M. D. Lukin, Many-body localization in dipolar systems, *Phys. Rev. Lett.* **113**, 243002 (2014).
- [60] R. Vosk, D. A. Huse, and E. Altman, Theory of the many-body localization transition in one-dimensional systems, *Phys. Rev. X* **5**, 031032 (2015).
- [61] I. V. Protopopov, R. K. Panda, T. Parolini, A. Scardicchio, E. Demler, and D. A. Abanin, Non-Abelian symmetries and disorder: A broad nonergodic regime and anomalous thermalization, *Phys. Rev. X* **10**, 011025 (2020).
- [62] J. Bezanson, A. Edelman, S. Karpinski, and V. B. Shah, Julia: A fresh approach to numerical computing, *SIAM Rev.* **59**, 65 (2017).
- [63] G. Datseris, J. Isensee, S. Pech, and T. Gál, DrWatson: The perfect sidekick for your scientific inquiries, *J. Open Source Software* **5**, 2673 (2020).
- [64] F. van der Plas, M. Dral, P. Berg, P. Γεωργακόπουλος, R. Huijzer, M. Bocheński, A. Mengali, C. Burns, B. Lungwitz, H. Priyashan, J. Ling, G. Wu, S. Kadowaki, E. Zhang, F. S. S. Schneider, I. Weaver, Xiu-zhe (Roger) Luo, J. Gerritsen, R. Novosel, Supanat *et al.*, *Fonsp/Pluto.jl*: V0.19.42, Zenodo.
- [65] C. Rackauckas and Q. Nie, DifferentialEquations.jl—a performant and feature-rich ecosystem for solving differential equations in Julia, *J. Open Res. Software* **5**, 15 (2017).
- [66] J. H. Verner, Numerically optimal Runge–Kutta pairs with interpolants, *Numer. Algo.* **53**, 383 (2010).
- [67] S. Danisch and J. Krumbiegel, Makie.jl: Flexible high-performance data visualization for Julia, *J. Open Source Software* **6**, 3349 (2021).
- [68] M. Bouchet-Valat and B. Kamiński, DataFrames.jl: Flexible and fast tabular data in Julia, *J. Stat. Soft.* **107**, 1 (2023).

4

EVIDENCE OF PAIR LOCALIZATION IN THE DYNAMICS OF RYDBERG SPINS

In this chapter, we apply the previously derived effective model of pairs interpret experimental results from a Rydberg-based quantum simulator. While the experiment is limited to global control and readout, we make great use of its ability to implement Heisenberg models with different anisotropy and various density (which translates to disorder strength).

We find the pair model to yield an excellent agreement with the observed behavior explaining both the relaxation dynamics and rescaling thereof [C] as well as the dependence of the steady state magnetization on the strength of the transverse field [D].

4.1 ANISOTROPY-INDEPENDENT RELAXATION DYNAMICS

In this paper, we utilize the ability of the Rydberg quantum simulator to implement XX, XXZ and Ising models to measure the relaxation of the x -magnetization when starting from a fully magnetized state. For disordered Ising models prior work has shown the relaxation to follow a stretched exponential form well-known from spin glasses [117, 120–122]. It has been conjectured that this type of slow, hierarchical relaxation is a common feature of strongly disordered quantum systems [123].

Indeed we find that for all three models the relaxation curves are fitted well by stretched exponentials. Moreover, we also find a scaling law for the characteristic decay time scale which hints at a common origin of the relaxation. This mechanism is explained by the pair model, which yields that for all three models the relaxation is caused essentially by oscillations of the magnetization of pairs. Since each pair has a different oscillation frequency these individual oscillations dephase and thus cause the total magnetization to decay. From the parameter dependence of these pair oscillations, we recover the characteristic timescale for the global magnetization’s decay. This is a clear indicator of an effective pair localization at least for experimentally relevant timescales.

Observation of anisotropy-independent magnetization dynamics in spatially disordered Heisenberg spin systems

T. Franz^{1,2,*}, S. Geier^{1,*}, C. Hainaut^{1,3}, A. Braemer¹, N. Thaicharoen^{1,4}, M. Hornung¹, E. Braun¹, M. Gärttner⁵, G. Zürn¹, and M. Weidemüller^{1,†}

¹Physikalisches Institut, Universität Heidelberg, Im Neuenheimer Feld 226, 69120 Heidelberg, Germany

²Max-Planck-Institut für Quantenoptik, Hans-Kopfermann-Str. 1, 85748 Garching, Germany

³Université de Lille, CNRS, UMR 8523-PhLAM-Laboratoire de Physique des Lasers Atomes et Molécules, F-59000 Lille, France

⁴Department of Physics and Materials Science, Faculty of Science, Chiang Mai University, Chiang Mai 50200, Thailand

⁵Institut für Festkörpertheorie und Optik, Friedrich-Schiller-Universität Jena, Max-Wien-Platz 1, 07743 Jena, Germany



(Received 28 September 2022; accepted 20 June 2024; published 5 August 2024)

An important step towards a comprehensive understanding of far-from-equilibrium dynamics of quantum many-body systems is the identification of unifying features that are independent of microscopic details of the system. We experimentally observe such robust features in the magnetization relaxation dynamics of disordered Heisenberg XX, XXZ, and Ising Hamiltonians. We realize these Heisenberg spin models with tunable anisotropy parameter and power-law interactions in an ensemble of Rydberg atoms by encoding the spin in suitable Rydberg state combinations. We consistently observe stretched-exponential relaxation of magnetization for all considered spin models, collapsing onto a single curve after appropriate rescaling of time. This robust short-time relaxation behavior is explained by a perturbative treatment that exploits the strong disorder in pairwise couplings, which leads to a description in terms of approximately independent pairs of spins. In numerical simulations of small systems, we show that these pairs of spins constitute approximate local integrals of motion, which remain at least partially conserved on a timescale exceeding the duration of the relaxation dynamics of the magnetization.

DOI: [10.1103/PhysRevResearch.6.033131](https://doi.org/10.1103/PhysRevResearch.6.033131)

I. INTRODUCTION

Far-from-equilibrium dynamics of isolated quantum systems after a quench displays a wide range of emergent phenomena, such as dynamical phase transitions [1,2], quantum many-body scars [3–5], and many-body localization (MBL) [6–10]. The time evolution of these systems generally depends strongly on the type of interactions and the distribution of interaction strengths between the particles [11]. A notable exception are systems showing (metastable) prethermal phases, where relaxation dynamics can show universal behavior, i.e., the dynamics become independent of details of the microscopic model [12–17].

When considering the role of disorder for the dynamics of quantum many-body systems, a striking characteristic of the dynamics is that they can be nonergodic [18], which is found for example in spin glasses where relaxation becomes extremely slow [19] or in MBL systems where the dynamics might be completely frozen [20]. Anomalously slow relaxation was also observed in disordered quantum spin systems

that feature subexponential dynamics [21–25]. Remarkably, in all these different classical and quantum systems, in the strong disorder regime, the subexponential dynamics are well described by the same functional form, the stretched exponential law. This raises the question of the origin of this robust behavior and whether it is affected by the modification of symmetry properties of the Hamiltonian.

In classical systems, the answer to these questions is provided by the seminal work of Klafter and Shlesinger, who found that a scale-invariant distribution of timescales is the common underlying mathematical structure that induces stretched-exponential relaxation [26]. Indeed, the authors proposed an intuitive understanding by considering the *parallel channels* model where an ensemble of initially fully polarized spins are coupled to an external bath at a different strength sampled from a scale-invariant distribution. Due to the coupling to the bath, each spin decays exponentially on a different timescale. Thus, the global polarization of the system yields a stretched exponential form resulting from the averaging over all the spins.

For isolated quantum systems, where the dynamics are unitary, there is no notion of decay due to a bath. However, in a disordered system where the spins are randomly positioned in space, the interaction strengths between the spins can be distributed scale invariantly. For example, it was shown analytically for the dynamics of the quantum Ising model that this scale-invariant distribution of coupling strengths induces a stretched exponential relaxation [27]. The derivation of the analytic solution is only possible because the Ising model

*These authors contributed equally to this work.

†Contact author: weidemueller@uni-heidelberg.de

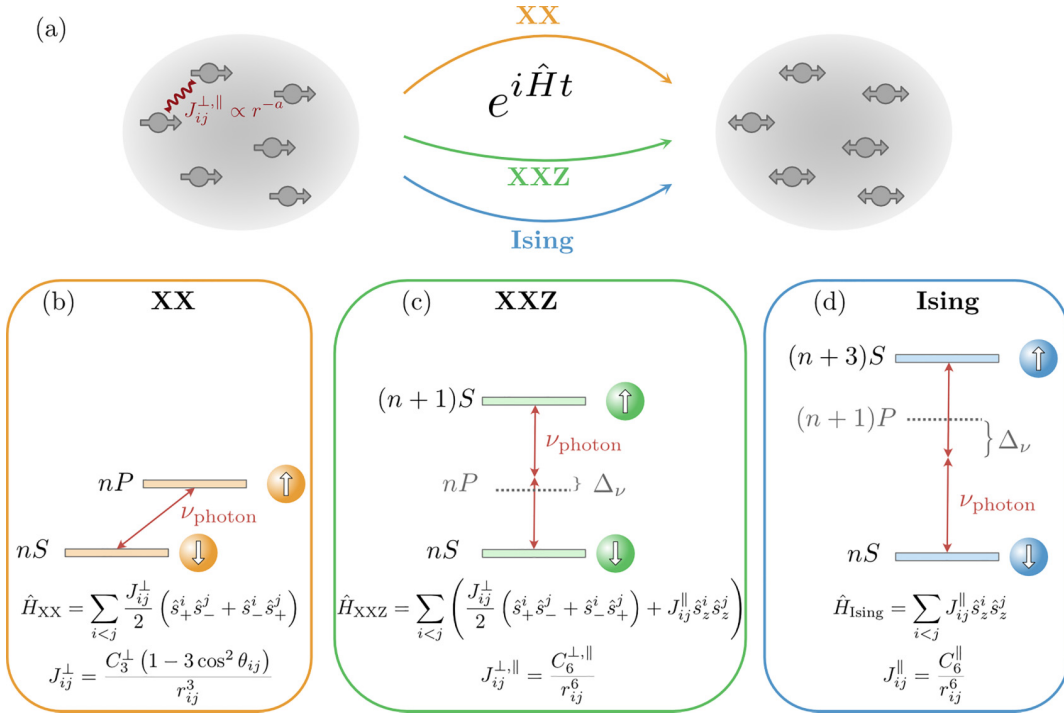


FIG. 1. Rydberg quantum simulator platform. (a) Illustration of out-of-equilibrium disordered spin systems relaxing with respect to different Hamiltonians. (b) Illustration of the experimental realization of a Heisenberg XX Hamiltonian by coupling a Rydberg $|nS\rangle$ state to a $|nP\rangle$ state, possessing opposite parity. The interaction is of dipolar nature and falls off as r_{ij}^{-3} . Coupling two Rydberg states with the same parity results in a Heisenberg XXZ Hamiltonian for state combinations $|nS\rangle$ and $|(n+1)S\rangle$ (c), while state combinations $|nS\rangle$ and $|(n+3)S\rangle$ results in a Ising Hamiltonian (d). In the two latter cases, the interactions are of van der Waals nature with a r_{ij}^{-6} dependence.

features an extensive number of conserved quantities, i.e., it is integrable. For nonintegrable models, where no analytic solution exists, generic mechanisms for describing the relaxation dynamics after a quantum quench remain largely unknown. Investigating the exact time evolution numerically is challenging due to the exponential growth of the Hilbert space with system size in quantum many-body systems. Semiclassical simulations, neglecting quantum effects beyond initial quantum fluctuations, suggest that nonintegrable Heisenberg XYZ Hamiltonians present out-of-equilibrium dynamics that follows a stretched exponential law like the Ising model independent of their symmetry [28]. An alternative route is implementing the desired unitary time evolution experimentally using quantum simulation experiments with tunable parameters, which is the approach we pursue here [29–32].

In this paper, we use different combinations of states of highly excited Rydberg atoms to realize different types of spin Hamiltonians thus making use of the full versatility of this platform [9,21,33–37]. Rydberg atoms are ideally suited to study unitary quantum dynamics because the timescales of the interacting dynamics vastly exceed those of the typical decoherence mechanisms. We observe the relaxation dynamics of three different Heisenberg Hamiltonians: the integrable Ising model and the nonintegrable XX and XXZ models with power-law interactions and positional disorder [see Fig. 1(a)]. For all models, we observe the same characteristic decay of magnetization, well described by a stretched exponential function, which causes the data to collapse onto a single curve after the appropriate rescaling of time. We show that this

robust behavior is directly linked to the presence of strong disorder, which allows deriving an effective, integrable model consisting of pairs of spins.

II. HEISENBERG SPIN SYSTEMS ON A RYDBERG-ATOM QUANTUM SIMULATOR

We consider an interacting spin-1/2 system described by the following Heisenberg Hamiltonian ($\hbar = 1$)

$$\hat{H} = \sum_{i < j} (J_{ij}^{\perp}/2(\hat{s}_+^i \hat{s}_-^j + \hat{s}_-^i \hat{s}_+^j) + J_{ij}^{\parallel} \hat{s}_z^i \hat{s}_z^j). \quad (1)$$

Here, $\hat{s}_{\pm}^i = \hat{s}_x^i \pm i \hat{s}_y^i$, where \hat{s}_{α}^i ($\alpha \in x, y, z$) are the spin-1/2 operator of spin i and $J_{ij}^{\perp,\parallel} = C_a^{\perp,\parallel}/r^a$. These types of Heisenberg XXZ Hamiltonians with disordered couplings feature a rich phenomenology of different phases and relaxation behaviors [38]. The Ising case, where $J_{ij}^{\perp} = 0$, features additional symmetries under local spin rotations \hat{s}_z^i that commute with the Hamiltonian, which make the Ising model integrable. For $J_{ij}^{\perp} \neq 0$, \hat{s}_z^i are no longer conserved and the Hamiltonian is nonintegrable. We provide a comprehensive description of how to engineer this Hamiltonian with different combinations of Rydberg states in the Appendix [39,40]. Figure 1 illustrates the state combinations that can be used to realize the Heisenberg XX, XXZ, and Ising models. For the rest of this paper, the three spin models are realized by state combinations $|61S\rangle - |61P\rangle$ (XX, $J^{\parallel}/J^{\perp} = 0$,

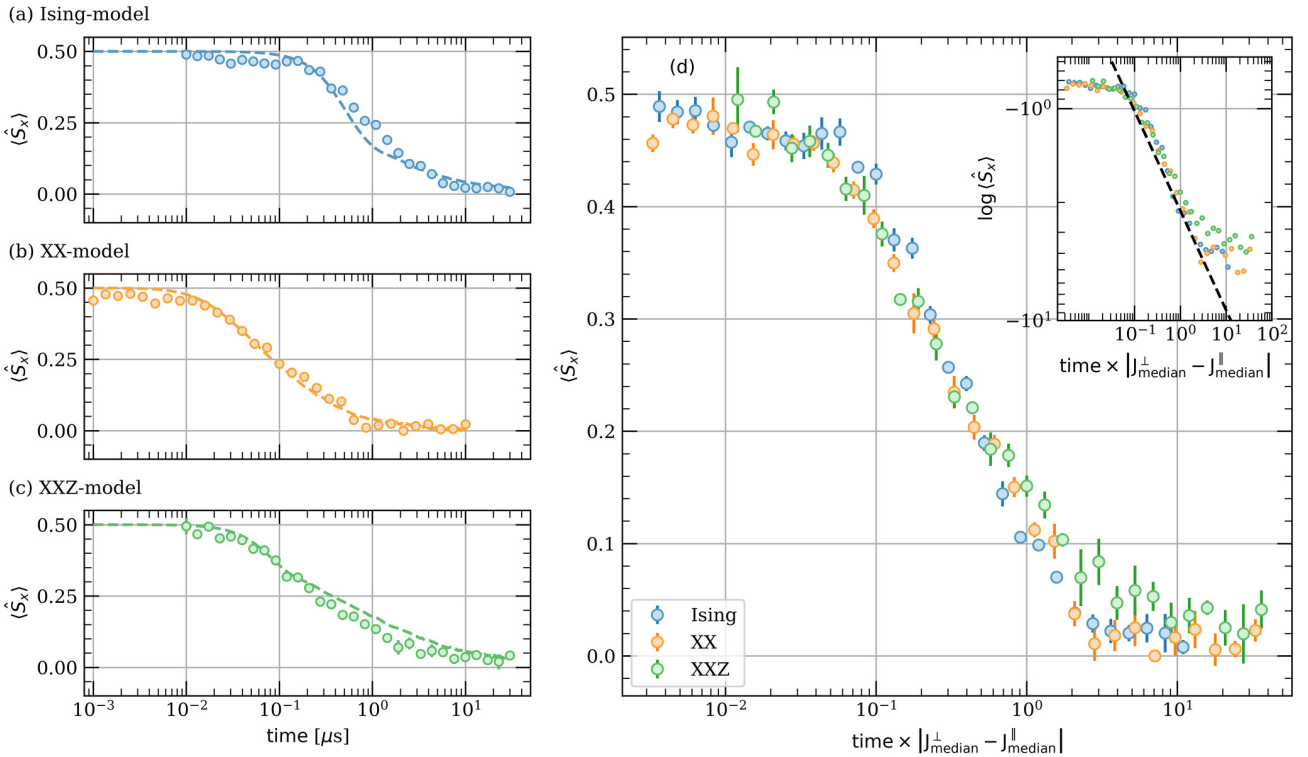


FIG. 2. Relaxation dynamics of disordered quantum spin systems. Magnetization dynamics as a function of time for the Ising model (a), the XX model (b), and the XXZ model (c). The dashed lines stem from DTWA simulations. (d) Magnetization dynamics of the three models as a function of the time rescaled by the typical interaction strength $2\pi|J_{\text{median}}^{\perp} - J_{\text{median}}^{\parallel}| = 2.3 \text{ MHz}$ (Ising model), 21 MHz (XX model), 7.6 MHz (XXZ model). (Inset) Data points of (c) plotted on as loglog vs log. The dashed line is a guide to the eye, indicating a stretched exponential relaxation with $\beta = 0.5$. The error bars denote the standard error of the mean.

$a = 3$), $|61S\rangle - |62S\rangle$ (XXZ, $J^{\parallel}/J^{\perp} = -0.7$, $a = 6$), and $|61S\rangle - |64S\rangle$ (Ising, $J^{\parallel}/J^{\perp} = -400$, $a = 6$).

III. EXPERIMENTAL OBSERVATION OF MODEL INDEPENDENT RELAXATION DYNAMICS

The experiment starts with trapping rubidium-87 atoms loaded in a crossed dipole trap at a temperature of $20 \mu\text{K}$ (see Appendix for experimental details). The atoms are excited from the ground $|g\rangle = |5S_{1/2}, F = 2, m_F = 2\rangle$ to the Rydberg state $|61S_{1/2}, m_j = 0.5\rrangle$ by a two-photon transition with red (780 nm) and blue (480 nm) lasers that are detuned by $2\pi \times 98 \text{ MHz}$ from the intermediate state $|e\rangle = |5P_{3/2}, F = 3, m_F = 3\rangle$. For this state, the Rydberg lifetime of $100 \mu\text{s}$ exceeds the duration of the spin experiment of $30 \mu\text{s}$. The excitation process leads to a three-dimensional cloud of $N \approx 80 - 250$ Rydberg atoms that are distributed randomly. The van der Waals interaction during the excitation process imposes a minimal distance of $r_{\text{bl}} \approx 10 \mu\text{m}$ between the spins (Rydberg blockade effect). The state $|61S_{1/2}, m_j = 0.5\rangle$ is the $|\downarrow\rangle$ state of all three different spin systems, the main difference is the second Rydberg states that is addressed by choosing proper microwave coupling using an AWG setup (see Appendix for details).

After having excited the ground state atoms to the down spin state, we implement a Ramsey protocol in our Rydberg experiment. To initialize the dynamics a first $\pi/2$ -microwave

pulse is performed, which sets the whole system in the state $|\rightarrow\rangle^{\otimes N} = 1/\sqrt{2}(|\uparrow\rangle + |\downarrow\rangle)^{\otimes N}$ and we let the system evolve over $30 \mu\text{s}$. A second $\pi/2$ pulse at a different readout phase followed by optical de-excitation and field ionization allows a tomographic measurement of the x magnetization $\langle S_x \rangle = \sum_i \langle \hat{S}_x^i \rangle$ [21].

The resulting relaxation dynamics of the Ising, Heisenberg XX, and XXZ models are shown in Figs. 2(a)-2(c). At early times, the magnetization seems to be almost perfectly conserved at $\langle \hat{S}_x \rangle = 0.5$ before the relaxation begins. This effect is attributed to the Rydberg blockade that induces a maximal interaction strength that determines the system's fastest timescale. For each model, the system relaxes to zero magnetization, which can be understood by considering symmetry arguments: Indeed, the magnetization can be rewritten using the commutator relation for Pauli matrices $\langle \hat{S}_x \rangle = -i\langle [\hat{S}_y, \hat{S}_z] \rangle$. The latter term vanishes for each eigenstate $|\phi\rangle$ of the XXZ Hamiltonian because each eigenstate is also an eigenstate of $\hat{S}_z|\phi\rangle = \sum_i \hat{S}_z^{(i)}|\phi\rangle = S_z|\phi\rangle$ due to the global U(1) symmetry leading to $\langle [\hat{S}_y, \hat{S}_z] \rangle = S_z\langle [\hat{S}_y, 1] \rangle = 0$. The timescale of the dynamics occurring within less than $10 \mu\text{s}$ is comparable with the typical interaction strengths in the megahertz regime depending on the realized Heisenberg model (details on the distribution of interaction timescales can be found in the Appendix).

To compare the relaxation curves to numerical predictions, the spatial distribution of Rydberg spin positions needs to

be modeled realistically. We use a hard-sphere model where each Rydberg excitation is described by a superatom [41] with a given blockade radius and effective Rabi frequency [21]. For more details on the parameters of the models, see the Appendix. We simulate the exact time-evolution of the experiment using the discrete truncated Wigner approximation (dTWA) [42]. DTWA simulations agree well with the experimental data as shown in Figs. 2(a)–2(c). The small deviation between simulations and experiments can be mostly attributed to an inaccuracy of the atom distribution obtained from the simplified excitation model (see Appendix).

The dynamics under the three different spin model in Figs. 2(a)–2(c) look strikingly similar in a log-linear plot. Indeed, by rescaling time with the characteristic timescale of each system given by $|J_{\text{median}}^{\perp} - J_{\text{median}}^{\parallel}|$, all relaxation curves coincide within the experimental errors. Here,

$$J_{\text{median}}^{\perp,\parallel} = \text{median}_j \max_i |J_{ij}^{\perp,\parallel}| \quad (2)$$

is the median of the nearest neighbor interaction strengths. This choice of typical interaction timescale is motivated by the oscillation frequency of a single pair of interacting spins governed by (1), which will be further discussed in the following section. The striking collapse allows us to infer the functional form of the relaxation dynamics of the nonintegrable models: For the Ising model, it is known that the relaxation follows exactly the stretched exponential law $e^{-(t/\tau)^{\beta}}$ [27] with stretching exponent β and timescale τ . The logarithm of the stretched exponential law is a power law. Plotted on a double logarithmic scale, this power law becomes a linear function [dashed line in the inset of Fig. 2(d)]. In this representation, the rescaled experimental data also show a linear behavior. This confirms the hypothesis that the stretched exponential law is the unifying description of the magnetization relaxation for the integrable quantum Ising model as well as the nonintegrable XX and XXZ Hamiltonians in the strongly disordered regime. We note that the dynamics are only robust with respect to a parameter of the microscopic model, the anisotropy J^{\parallel}/J^{\perp} , whereas the macroscopic geometry and also the dimension of the cloud may lead to different dynamics (see Appendix). In addition, we also measured the relaxation dynamics for various initial states (for one Hamiltonian) possessing different magnetization and again find similar relaxation dynamics at late times (see Appendix E).

IV. APPROXIMATE DESCRIPTION THROUGH STRONGLY INTERACTING PAIRS

In order to understand the regime where we have observed robust relaxation dynamics, we aim for a simplified model that includes only the relevant timescales of the system. To identify these, we exploit the strongly disordered nature of the system by adopting a perturbative approach in the spirit of the strong disorder renormalization group (SDRG) where the strongest coupling is integrated out iteratively [43–46].

In our model, the strongest coupled spins define a pair of spins. Crucially, the coupling within the pair will be much larger than all other couplings affecting the pair. This allows one to treat the coupling between this pair and the rest of the system perturbatively. To zeroth order, this pair of spins just

decouples from the system and evolves independently. This elimination step, where we remove the strongest coupling, can be repeated within the rest of the system. For our initial state, each individual pair undergoes coherent dynamics between the fully polarized state in plus and minus x direction [see Fig. 3(a)] [47]. The resulting oscillation of the magnetization [shown in Fig. 3(b)] is independent of the specific XXZ Hamiltonian. Only the frequency, given by $J_{ij}^{\perp} - J_{ij}^{\parallel}$, differs depending on the Ising and exchange interaction strengths. This independence is at the origin of the observed model independence of relaxation dynamics.

With this model in hand, we can compute the time evolution of the magnetization by a simple average of cosine oscillations as shown by the grey dash-dotted lines (pair, noninteracting) in Figs. 3(c)–3(e). The resulting relaxation dynamics show good agreement with the experimental data. However, especially for the Ising and XXZ model, this model underestimates the timescales of the dynamics. This is somewhat expected, considering that the pair couplings found by iterative elimination are, on average, smaller than the nearest neighbor couplings.

Taking the perturbative treatment to next order, one finds an effective Ising-like coupling between pairs, as derived recently in the Appendix of [48]. The effective Hamiltonian governing the dynamics was found to be

$$\hat{H}_{\text{eff}} \approx \sum_{\langle i,j \rangle} (J_{ij}^{\perp}/2(\hat{s}_+^i \hat{s}_-^j + \hat{s}_-^i \hat{s}_+^j) + J_{ij}^{\parallel} \hat{s}_z^i \hat{s}_z^j) + \sum_{\langle i,j \rangle, \langle k,l \rangle} J_{ijkl}^{\text{eff}} \hat{s}_z^{(i)(j)} \hat{s}_z^{(k)(l)} \quad (3)$$

$$J_{ijkl}^{\text{eff}} = J_{ik}^{\parallel} + J_{il}^{\parallel} + J_{jk}^{\parallel} + J_{jl}^{\parallel} \quad (4)$$

where $\langle i, j \rangle$ denotes the summation over paired spins i and j and $2\hat{s}_z^{(i)(j)} = \hat{s}_z^i + \hat{s}_z^j$.

Fortunately, this model is integrable and allows for derivation of an analytical solution for the evolution of $\langle \hat{S}_x(t) \rangle$ (see Appendix F), which reads

$$\langle \hat{S}_x^{\text{pair}} \rangle(t) = \frac{1}{N} \sum_{\langle i,j \rangle} \cos \left(\frac{1}{2} (J_{ij}^{\perp} - J_{ij}^{\parallel}) t \right) \prod_{\langle k,l \rangle} \cos^2 \left(\frac{1}{8} J_{ijkl}^{\text{eff}} t \right). \quad (5)$$

The first factor in each term originates from the pair dynamic to zeroth order, as described previously. The other factors are reminiscent of the Emch-Radin solution for the Ising model and stem from the effective Ising interaction among the pairs. This effective Ising model of pairs captures the overall demagnetization dynamics remarkably well for all observed times [see Figs. 3(c)–3(e)], yielding very similar (and in the case of XXZ, even better) results compared to dTWA.

From the analytical form of the time evolution, Eq. (5), we find that many different oscillation frequencies contribute to each spin's magnetization dynamics. Most of these frequencies are very small, however, and do not contribute to the early-time dynamics. Thus, a reasonable ansatz for rescaling to make the dynamics collapse is to consider only the fastest frequency for each spin. Due to the highly disordered nature of our system, this strongest coupling will essentially always correspond to the closest neighboring spin.

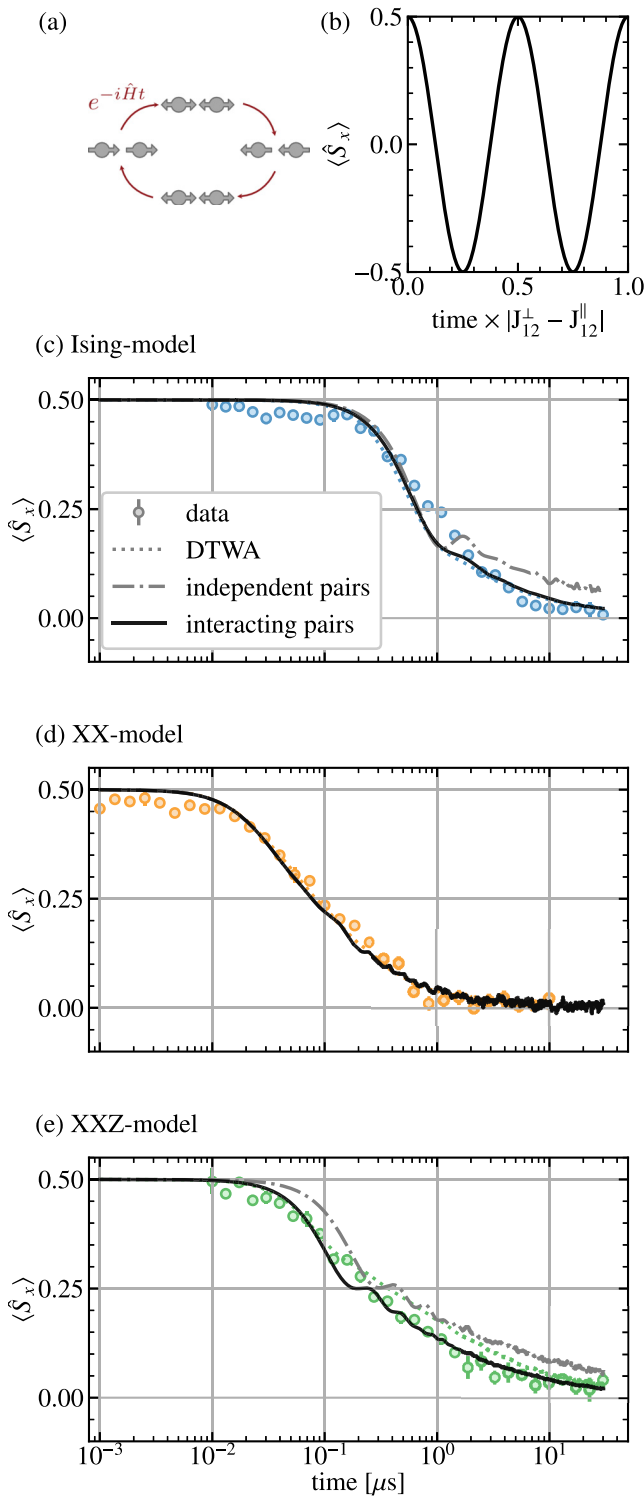


FIG. 3. Effective description by localized pairs. (a) Illustration of the oscillation of a single pair under an arbitrary XXZ Hamiltonian. A fully polarized state $|--\rangle$ (left) evolves via the maximally entangled Bell state $1/\sqrt{2}(|--\rangle + |--\rangle)$ (top) to the state $|--\rangle$ (right). Then, it returns to the origin via the other Bell state $1/\sqrt{2}(|--\rangle - |--\rangle)$ (bottom). (b) Oscillation of the magnetization for a single pair initialized in $|--\rangle$. [(c)–(e)] Comparison of the relaxation dynamics obtained by the pair approximation with/without effective Ising terms (solid black line/grey dash-dotted

This explains the rescaling found from the experimental data with median_{*i*} max_{*j*} $|J_{ij}^\perp - J_{ij}^\parallel|$.

V. SEPARATION OF TIMESCALES IN SPIN DYNAMICS

In the previous section, we revealed that the relaxation dynamics of a single-body observable is well captured by an ensemble of pairs with Ising-like interactions. This simple description in terms of pairs provides an integrable effective Hamiltonian, which is valid not only at early times but agrees surprisingly well with the data over the entire relaxation process, which lasts for over three decades in time. In the following section, we will more quantitatively address the question of whether the magnetization of each pair is conserved by evaluating the pair autocorrelator given by $\langle \hat{S}_z^{\text{pair}}(t) \hat{S}_z^{\text{pair}} \rangle$, where $\hat{S}_z^{\text{pair}} = \hat{s}_z^i + \hat{s}_z^j$. If the pair picture is perfect or if the system is an Ising model, this quantity stays $\langle \hat{S}_z^{\text{pair}}(t) \hat{S}_z^{\text{pair}} \rangle = 1$. On the other hand, if the correlations in the system are fully decohered, the autocorrelator assumes its minimal value of $\langle \hat{S}_z^{\text{pair}}(t) \hat{S}_z^{\text{pair}} \rangle = \frac{2}{N}$ for a system of size N due to symmetry constraints.

Our numerics presented in Fig. 4 for $N = 16$ spins in $d = 1$ with interaction exponent $\alpha = 2$ reveals three important points. Firstly, at $t|J_{\text{median}}^\parallel - J_{\text{median}}^\perp| \approx 0.2$ the global magnetization $\langle \hat{S}_x \rangle$ has decayed almost by half, while the pairs' magnetization autocorrelators are still close to 1. This justifies our simplistic pair picture and highlights the regime of universal dynamics. Secondly, at intermediate times up to 10^2 , the global magnetization relaxes fully to zero while the autocorrelator still features slow dynamics. This illustrates the existence of two timescales. Observing two distinct timescales shows that the system has not yet reached thermal equilibrium once the magnetization has relaxed to zero [17,22] but rather hints at prethermal behavior [12,14,16,49]. This generally means that a system does not directly relax to its “true” thermal state, but instead reaches a prethermal state. This is still a thermal state but with respect to a different, prethermal Hamiltonian, which in our case only contains mostly Ising-like interactions among pairs. At very late times, this prethermal description ceases to be a reliable description, but even in the infinite time limit (derived by the diagonal ensemble and indicated by arrows in Fig. 4), the pair autocorrelator remains at $\approx 1/2$, which is significantly above the lower limit of $\frac{2}{N} = 1/8$. This indicates that our integrable pair model is still a reasonable description of the system even at late times.

VI. CONCLUSION

Our paper demonstrates the ability of Rydberg atom quantum simulators to synthesize a variety of many-body Hamiltonians on a single experimental platform. By choosing the appropriate state combination, we realized XX, XXZ, and for the first time, a quantum Ising model within the Rydberg manifold. This versatility of the platform has enabled us to

line) and with DTWA (dotted line) and the experimental data of Fig. 2 for Ising (c), XX (d), and XXZ model (e).

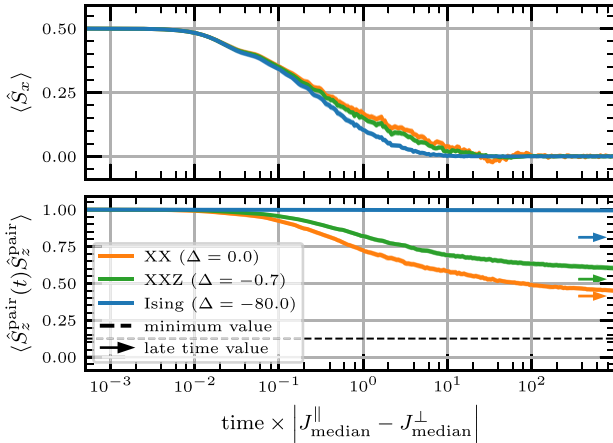


FIG. 4. Dynamics of the pair magnetization autocorrelator. Numerical simulation of $N = 16$ spins in $d = 1$ with interaction exponent $a = 2$ and a mean interspin distance $a_0 = 20r_b$. Line width shows statistical uncertainty from disorder averaging.

directly study and compare the relaxation dynamics of three different quantum spin systems far from equilibrium.

The central finding of this study is the robustness of the functional form of the relaxation curves with respect to parameter changes in the microscopic spin model, even across models featuring different symmetries, and the choice of initial state (cf. Appendix E). This discovery raises a fundamental question about the universality of relaxation dynamics in spatially disordered spin systems. To address this question comprehensively, we presented an approximate description of the system based on pairs of spins, exhibiting excellent agreement with both numerical simulations and experimental data. Moreover, this effective model is integrable and thus features an extensive number of conserved quantities allowing for an exact solution.

To assess the quality of the effective model, we studied the decay of these effectively conserved quantities in small systems via exact methods. We found them to decay on a much slower timescale, which might indicate that the system behaves prethermally: On the early timescale, the effective pair model to lowest order holds, and thus the relaxation appears universal.

The observed robustness hinges on a number of system properties: Firstly, universal relaxation is known to hold only in the strong disorder regime [21]. Secondly, we expect the dynamics to depend on global parameters of the system like the spatial dimension d and the range of interaction α , which both determine the distribution of couplings $J_{i,j}^{\perp,\parallel}$ (e.g., the stretch power has been analytically derived to be $\beta = d/\alpha$ in the case of the Ising model [27]). Therefore, it is crucial to compare experimental data only where the distributions of interaction strengths are comparable such that the underlying universal behavior becomes evident (see also Appendix C where the distribution of coupling for the experiments shown in this article are shown).

The accurate approximation of the relaxation dynamics by an integrable model of pairs indicates that the time evolution of disordered quantum spin systems cannot be viewed as direct thermalization. Instead, even at

later times when the global magnetization has completely relaxed to zero, the system can still exhibit local characteristics originating from quasiconserved pairs of spins. In order to investigate the deviations from the pair model and, hence, from the prethermal state, future experiments will require single-site resolution [50]. Further investigations could also study the influence of the energy density of the initial state on the dynamics, indicative of a possible phase transition [51].

ACKNOWLEDGMENTS

We thank A. Salzinger and A. Tebben for important contributions to maintaining the experimental apparatus. Furthermore, we thank H. Zhou, N. Leitao, and L. Martin for helpful discussions. This work is part of and supported by the Deutsche Forschungsgemeinschaft (DFG, German Research Foundation) under Germany's Excellence Strategy EXC2181/1-390900948 (the Heidelberg STRUCTURES Excellence Cluster), within the Collaborative Research Centre "SFB 1225 (ISOQUANT)," the DFG Priority Program "GiRyd 1929," the European Union H2020 projects FET Proactive project RySQ (Grant No. 640378), and FET flagship project PASQuans (Grant No. 817482), and the Heidelberg Center for Quantum Dynamics. The authors acknowledge support by the state of Baden-Württemberg through bwHPC and the German Research Foundation (DFG) through Grant No. INST 40/575-1 FUGG (JUSTUS 2 cluster) and used the Julia programming language for most of the numerics [52]. T.F. acknowledges funding by a graduate scholarship of the Heidelberg University (LGFG).

APPENDIX A: ENGINEERING HEISENBERG XXZ HAMILTONIANS BY DIFFERENT COMBINATIONS OF RYDBERG STATES

In the following, we provide a comprehensive description of how to engineer this Hamiltonian with different combinations of Rydberg states [40,41]. Especially, this gives us the opportunity to explain how to engineer an Ising Hamiltonian in a spin system realized by two different Rydberg states.

For general spin systems with global $U(1)$ symmetry, the coupling terms can be obtained by calculating the matrix elements of the interaction Hamiltonian \hat{H} . The Ising term

$$J_{ij}^{\parallel} = (E_{\uparrow_i\uparrow_j} + E_{\downarrow_i\downarrow_j}) - (E_{\downarrow_i\uparrow_j} + E_{\uparrow_i\downarrow_j}) \quad (\text{A1})$$

is defined as the energy difference between spins being aligned and being antialigned. Here, $E_{\alpha_i\beta_j} = \langle \alpha_i|\beta_j|\hat{H}|\alpha_i\beta_j \rangle$ are the interaction energy of spin i and j with $\alpha, \beta \in [\uparrow, \downarrow]$. The exchange term is determined by

$$J_{ij}^{\perp} = \langle \downarrow_i\uparrow_j|\hat{H}|\uparrow_i\downarrow_j \rangle. \quad (\text{A2})$$

For a system consisting of states with opposite parity, such as $|\downarrow\rangle = |nS\rangle$ and $|\uparrow\rangle = |nP\rangle$ [see Fig. 1(b)], where n is the principal quantum number, the dominant coupling is a direct dipolar interaction, which can be described by the Hamiltonian

$$\hat{H}_{\text{DDI}} = \frac{\hat{\mathbf{d}}_i \cdot \hat{\mathbf{d}}_j - 3(\hat{\mathbf{d}}_i \cdot \mathbf{e}_{rij})(\hat{\mathbf{d}}_j \cdot \mathbf{e}_{rij})}{r_{ij}^3}, \quad (\text{A3})$$

where $\hat{\mathbf{d}}_i$ is the dipole operator of atom i , $\mathbf{e}_{r_{ij}}$ is the unit vector connecting the two atoms, and r_{ij} their distance. Mapped Eq. (A3) on the spin Hamiltonian of Eq. (1), the resulting interaction coefficient is

$$J_{ij}^\perp = \frac{C_3^\perp(1 - 3\cos^2\theta_{ij})}{r_{ij}^3}. \quad (\text{A4})$$

Here, θ_{ij} is the angle between $\mathbf{e}_{r_{ij}}$ and the quantization axis and C_3^\perp the coupling parameter [36,37]. The Ising term J_{ij}^\parallel is zero since interaction energy shifts $E_{\alpha_i\beta_j}$ are dipole forbidden. Therefore, this is a way to realize an XX model as depicted in Fig. 1(b). In this paper, we have chosen $|61S\rangle$ and $|61P\rangle$ leading to $C_3^\perp/2\pi = 3.14 \text{ GHz}\mu\text{m}^3$.

In the case where the two chosen states possess the same parity, such as the two atoms being in the same state $|nS\rangle$, direct dipolar coupling is forbidden and the leading interaction is a second-order process through a virtually excited pair state $|m\rangle$ and can be described by

$$\hat{H}_{vdW} = -\frac{1}{\hbar} \sum_m \frac{\hat{H}_{DDI}|m\rangle\langle m|\hat{H}_{DDI}}{\Delta_v}. \quad (\text{A5})$$

Here, the Foerster defect Δ_v is the energy difference between the initial state and the virtually excited state $|m\rangle$. This Hamiltonian gives rise to power-law interactions $J_{ij} = C_6/r_{ij}^6$ that scales with n^{11} . Especially, this term is large if a pair state $|m\rangle$ with a small Foerster defect exists. Many experiments exploit these interactions to realize a spin system where the ground state is coupled to a single Rydberg state. These systems feature the Rydberg blockade effect and can be mapped on an Ising model [3,34,35].

Similar interactions also exist for a spin system realized with two different Rydberg states $|\downarrow\rangle = |nS\rangle$ and $|\uparrow\rangle = |(n+1)S\rangle$. In this case, the van der Waals Hamiltonian (A5)

TABLE I. Waists of the blue (480 nm) and red (780 nm) Rydberg excitation lasers used to realize the different models and the respective ground state cloud waists.

Model	blue exc. $\sigma_{x,y}$	red exc. $\sigma_{x,y}$	GS σ_x	GS $\sigma_{y,z}$
Ising	55 μm	1.5mm	64 μm	45 μm
XXZ	55 μm	1.5mm	64 μm	45 μm
XX	55 μm	1.5mm	62 μm	47 μm

also induces a spin exchange term because the two Rydberg states are coupled via the intermediate pair state $|m\rangle = |nP, nP\rangle$ [see Fig. 1(c)]. In the case of $n = 61$, both the Ising and exchange interactions terms are similar with $J^\parallel/J^\perp = -0.7$. Therefore, this spin system can be mapped onto an effective Heisenberg XXZ-Hamiltonian [21].

In order to realize an Ising Hamiltonian with two different Rydberg states, a state combination is needed where the exchange term (A2) is small requiring a large Foerster defect Δ_v [see Fig. 1(d)]. This can be achieved by coupling $|\downarrow\rangle = |nS\rangle$ to $|\uparrow\rangle = |(n+3)S\rangle$. In this case, the largest contribution to the exchange term comes from $|m\rangle = |(n+1)P, (n+1)P\rangle$. For example, for $n = 61$, this spin system is characterized by a ratio of $J^\parallel/J^\perp = 400$, which is a good approximation to an Ising Hamiltonian ($J^\perp = 0$).

APPENDIX B: EXPERIMENTAL IMPLEMENTATION OF VARIOUS SPIN MODELS

To realize the Heisenberg XX model, a single-photon microwave transition at $2\pi \times 16 \text{ GHz}$ with a Rabi frequency of $\Omega = 2\pi \times 18 \text{ MHz}$ couples the state $|\downarrow\rangle$ to $|\uparrow\rangle = |61P_{3/2}, m_j = 1/2\rangle$. To implement the XXZ Hamiltonian,

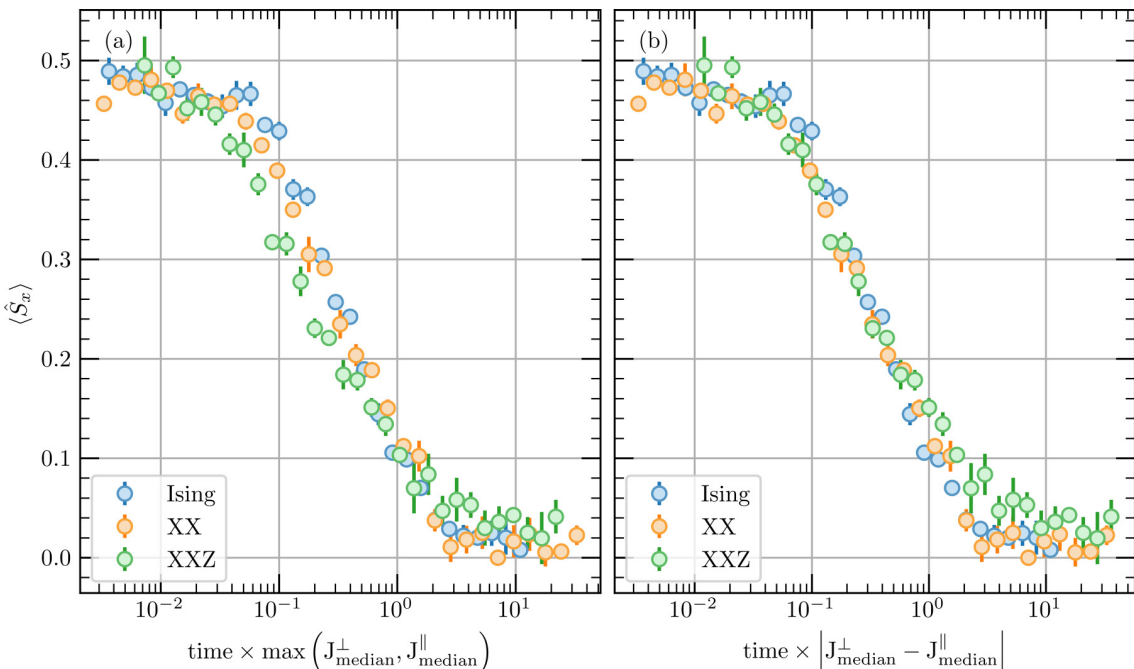


FIG. 5. Comparison of the scaling behavior for rescaling time either by the median interaction matrix (a) or by the median of the pair oscillation frequency (b). $\max(J_{\text{median}}^\perp, J_{\text{median}}^\parallel)$ is defined as J_{median}^\perp for the Heisenberg XX and XXZ model, and as J_{median}^\perp for the Ising model.

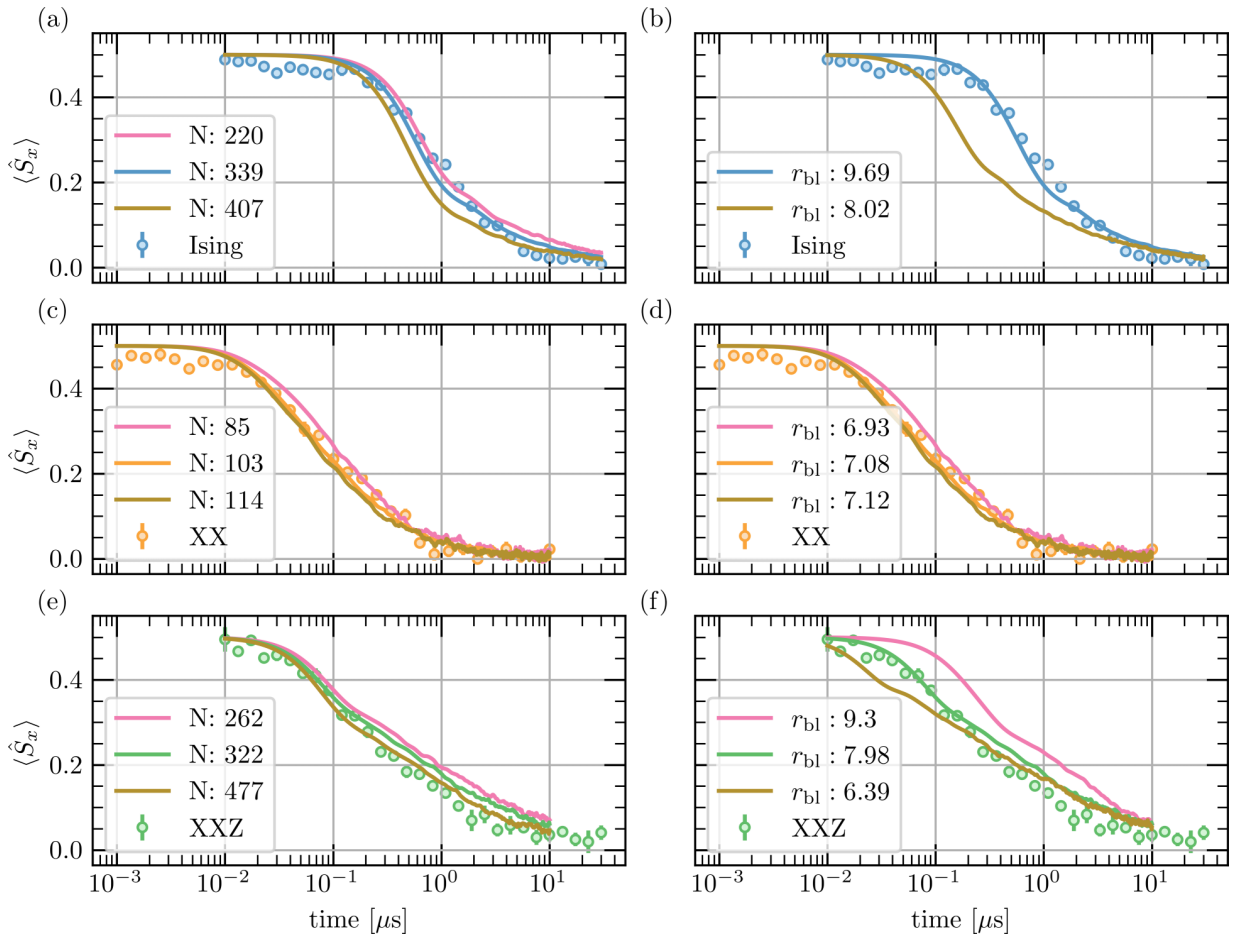


FIG. 6. Influence of the density and the blockade radius on the DTWA simulations. Left column: Simulations for the same blockade radius as in the main text for different particle numbers N . Right column: Simulations for the same particle number and various blockade radii. In all simulations the geometry of the cloud is the same.

two microwave photons at $2\pi \times 16$ GHz couple to $|\uparrow\rangle = |62S_{1/2}, m_j = 1/2\rangle$. Here, a single photon Rabi frequency of $\Omega = 2\pi \times 48$ MHz with a detuning $\Delta_v = 2\pi \times 170$ MHz leads to a two-photon Rabi frequency of $\Omega_{2v} = 2\pi \times 6.8$ MHz. To realize the Ising model, the state $|61S\rangle$ has to be coupled to $|64S_{1/2}, m_j = 0.5\rangle$ but the detuning of $\Delta_v = 2\pi \times 1.426$ GHz is too large and prevents an efficient coupling of the states with two microwave photons of the same frequency $2\pi \times 47$ GHz. Therefore, we combine two frequencies differing by $2\pi \times 1.563$ GHz such that the effective detuning to the intermediate state $|62P\rangle$ is $2\pi \times 136$ MHz. For a single photon Rabi frequency of $\Omega = 2\pi \times 30$ MHz this results in an effective two-photon Rabi frequency of $\Omega_{2v} = 2\pi \times 3.3$ MHz [see Figs. 1(b)–1(d) for the microwave photonic transitions]. The parameters of the laser waists and resulting geometries can be found in Table I.

APPENDIX C: DISTRIBUTION OF INTERACTION TIMESCALES IN THE SPIN SYSTEM

In the main text, we have highlighted that the typical timescale of the relaxation is given by the pair oscillation frequency $|J_{||} - J_{\perp}|$. For the Heisenberg XXZ Hamiltonian, both exchange and Ising interactions exist. Therefore, another

possibility of rescaling would only involve J_{\perp} , which would disregard the anisotropy $\delta = J_{||}/J_{\perp}$. In Fig. 5, we have compared both possibilities of rescaling time. The rescaling by the oscillation frequency shows a more precise collapse of the experimental data. This demonstrates that this frequency indeed determines the relevant timescale of the system. In addition, this indicates that the Rydberg interactions can be mapped onto the Heisenberg XXZ Hamiltonian with $\delta = -0.7$.

In Fig. 6, we show the sensitivity of the DTWA simulations to different densities and blockade radii. For most simulations, these parameters have only a small, quantitative effect on the simulated dynamics. A notable exception is the Ising system. Here, the Rydberg cloud is largely saturated and the blockade radius is the relevant length scale of the system. Therefore, a variation of the blockade radius changes drastically the early time dynamics. In contrast, the density of the sample featuring XX-interaction is low, therefore the blockade effect can be neglected. For the Heisenberg XXZ Hamiltonian, the simulations show that the blockade radius of $8.3 \mu\text{m}$ fits the observed dynamics slightly better than the value of $10 \mu\text{m}$ expected from the simplified excitation model assuming no phase noise of the laser.

Histograms showing the resulting distribution functions of couplings are shown in Fig. 7.

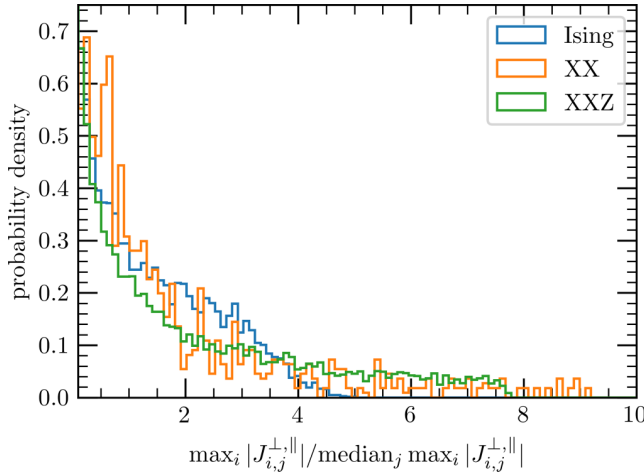


FIG. 7. Histograms of the distribution of interaction strengths for the experimental data shown in the main text. The histograms are obtained by averaging over 50 distributions of interaction strengths, with a bin size of $0.1 \text{median}_j \max_i |J_{i,j}^{\perp,||}|$.

APPENDIX D: INFLUENCE OF THE GAUSSIAN TRAP GEOMETRY ON THE RELAXATION DYNAMICS

The functional form of the relaxation dynamics in a strongly disordered spin system has been demonstrated to be independent of both the Rydberg blockade radius and the anisotropy of the Heisenberg XXZ Hamiltonian. However, the timescale of these dynamics is contingent upon the density and coupling constant. Consequently, there arises the necessity to rescale time by the median interaction strength $\text{median}_j \max_i |J_{i,j}|$.

In the context of a Gaussian trap geometry, we conduct an averaging procedure over varying local densities ρ . Assuming local density approximation, we average over different local relaxation dynamics, each characterized by a stretched exponential function, sharing a common stretching exponent β , while exhibiting distinct timescales $\tau(\rho)$. The collective summation of these relaxation curves again manifests as a stretched exponential decay. However, the details of the stretching exponent β depend on the shape of the Gaussian cloud (cf. Fig. 8).

Furthermore, finite-size effects come into play, with one-dimensional physics becoming relevant in an elongated cigar-shaped geometry and two-dimensional physics in a flat pancake geometry. Consequently, the measured stretched exponential does not align with the expected value of $\beta = d/\alpha$ (where d represents the dimension and α signifies the range of interactions) as anticipated from semiclassical simulations [28]. Instead, the observed value interpolates between various dimensions and exhibits slight variations in different experimental realizations when the trap geometry is altered.

Nevertheless, through a comparative analysis of experiments conducted in similar geometries, it remains feasible to investigate whether the dynamics are contingent upon the size of the blockade radius [21] or the anisotropy parameter Δ of the Heisenberg XXZ Hamiltonian (as explored in this study).

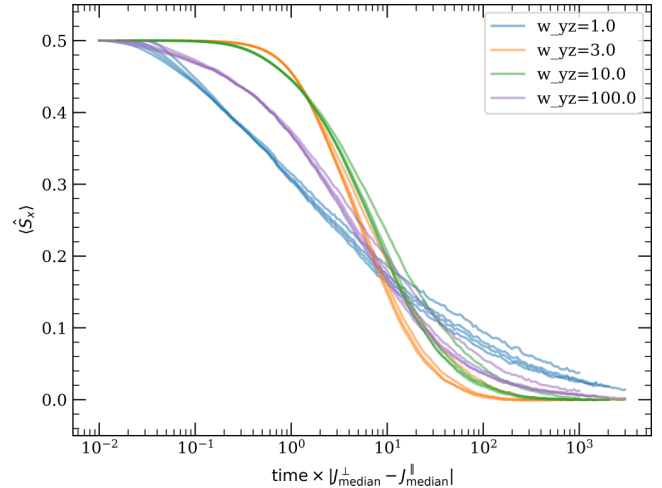


FIG. 8. MACE simulations of the relaxation of the magnetization for four different geometries of the Gaussian cloud where the aspect ratio of the waist w_x in x direction with respect to the waist w_{yz} in y and z direction is tuned. The product $w_x \times w_{yz}^2$ is fixed for all four geometries. For each geometry, we simulate the time evolution for different anisotropies $\frac{J_{\perp}^{\parallel}}{J_{\parallel}^{\parallel}} \in \{-2, -0.5, 0, 0.5, 2\}$.

APPENDIX E: RELAXATION UNDER INITIAL STATES WITH DIFFERENT MAGNETIZATION

In order to test if the universal relaxation behavior, originating from a pair picture approximation is even consistent for the relaxation of more general states than the fully

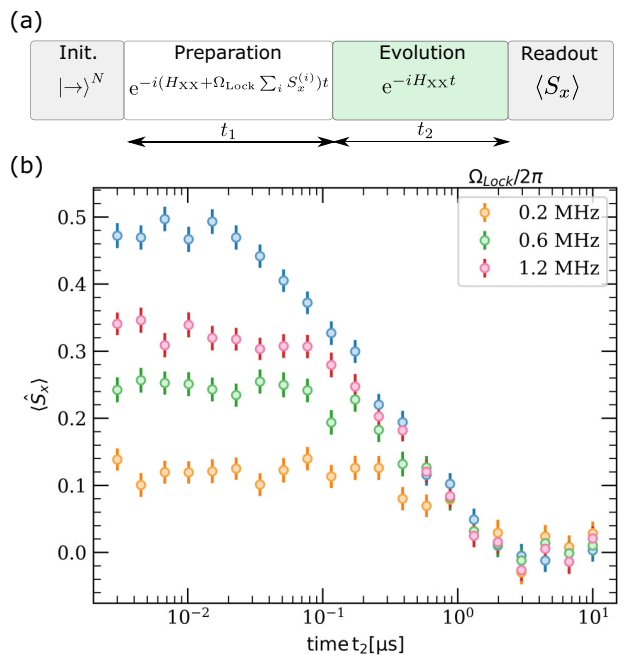


FIG. 9. Relaxation dynamics of initial states with different magnetization. (a) Experimental sequence consisting of an evolution under a spin locking field (preparation), followed by a measurement of the magnetization for the resulting relaxation dynamics for t_2 (evolution). (b) Magnetization dynamics after different $\Omega_{\text{Lock}}/2\pi$ applied in phase one.

x-polarized state, we probe the relaxation for initial states with different magnetization. The experimental protocol is shown in Fig. 9(a) and is similar to the one used in [53]. It consists of the following steps. In the preparation, spins are initially polarized along the *x* axis. A locking field Ω_{Lock} , which is also aligned along the *x* axis is applied for a time t_1 . During this time, as reported in [53], the magnetization will relax and approximately settle to a constant nonzero value that depends on the strength of the locking field. In the evolution, we then turn off the locking field and measure the resulting relaxation of the *x*-magnetization. The resulting relaxation over period t_2 is shown in Fig. 9(b). The magnetization starts with different values depending on the field strength applied during the preparation. We note that the locking time $t_2 = 2 \mu\text{s}$ is larger than the time it takes to directly relax to zero magnetization without phase one (blue points). We observed that for decreasing initial magnetization, the onset of the relaxation dynamics gets shifted to a later time (red, green, and yellow points). However, independent of this behavior, for later times, all curves overlap with the direct relaxation curve without field (blue points).

The observed dynamics can be understood within the pair approximation in the following way. During preparation, the locking field is only able to lock pairs with interactions smaller than the field strength Ω_{Lock} . These pairs stay polarized while pairs with stronger interactions oscillate and dephase. As reported in [53], magnetization takes an almost constant value. During the evolution, when the field is turned

off, the relaxation timescale is given by the remaining pairs that were locked and now start to oscillate. This timescale is longer for small fields where only weakly interacting pairs remained locked during the preparation. The overlapping at a later time is due to the fact that these pairs are also locked under larger fields. The data was taken for $|48S_{1/2}, m_j = 0.5\rangle$ and $|48P_{3/2}, m_j = 0.5\rangle$.

APPENDIX F: DERIVATION OF DEPOLARIZATION DYNAMICS

The goal is to compute the expectation value of $\langle \hat{S}_x(t) \rangle = \frac{1}{N} \sum_i \langle \hat{s}_x^i \rangle$ starting from the *x*-polarized state $|\psi_0\rangle = |\rightarrow\rangle^{\otimes N}$ governed by the effective Hamiltonian derived in [48]

$$\begin{aligned} \hat{H}_{\text{eff}} = & \sum_{\langle i, j \rangle} (J_{ij}^\perp (\hat{s}_x^i \hat{s}_x^j + \hat{s}_y^i \hat{s}_y^j) + J_{ij}^\parallel \hat{s}_z^i \hat{s}_z^j) \\ & + \sum_{\langle i, j \rangle, \langle k, l \rangle} J_{\text{eff}}^{ijkl} \hat{s}_z^{(i)(j)} \hat{s}_z^{(k)(l)} \end{aligned} \quad (\text{F1})$$

where $\langle i, j \rangle$ denotes the summation over paired spins *i* and *j* and $2\hat{s}_z^{(i)(j)} = \hat{s}_z^{(i)} + \hat{s}_z^{(j)}$.

Without loss of generality, we assume that spins 1 and 2 form a pair and compute $\langle \hat{s}_x^1(t) \rangle$. The evolution of $\langle \hat{S}_x(t) \rangle$ then follows simply by linearity. First we notice that all the terms in \hat{H}_{eff} commute with each other, allowing for direct computation of $\langle \hat{s}_x^1(t) \rangle$ by commuting \hat{s}_x^1 through the time evolution operators,

$$\hat{s}_x^1(t) = e^{it\hat{H}_{\text{eff}}} \hat{s}_x^1 e^{-it\hat{H}_{\text{eff}}} \quad (\text{F2})$$

$$= e^{itJ_{12}^\perp (\hat{s}_x^1 \hat{s}_x^2 + \hat{s}_y^1 \hat{s}_y^2)} e^{itJ_{12}^\parallel \hat{s}_z^1 \hat{s}_z^2} e^{it\hat{s}_z^{(1)(2)} \sum_{\langle k, l \rangle} J_{\text{eff}}^{12kl} \hat{s}_z^{(k)(l)}} \hat{s}_x^1 e^{-it\hat{s}_z^{(1)(2)} \sum_{\langle k, l \rangle} J_{\text{eff}}^{12kl} \hat{s}_z^{(k)(l)}} e^{itJ_{12}^\parallel \hat{s}_z^1 \hat{s}_z^2} e^{-itJ_{12}^\perp (\hat{s}_x^1 \hat{s}_x^2 + \hat{s}_y^1 \hat{s}_y^2)} \quad (\text{F3})$$

$$= e^{itJ_{12}^\perp (\hat{s}_x^1 \hat{s}_x^2 + \hat{s}_y^1 \hat{s}_y^2)} e^{it\hat{s}_z^1 \sum_{\langle k, l \rangle} J_{\text{eff}}^{12kl} \hat{s}_z^{(k)(l)}} e^{2itJ_{12}^\parallel \hat{s}_z^1 \hat{s}_z^2} e^{-itJ_{12}^\perp (\hat{s}_x^1 \hat{s}_x^2 - \hat{s}_y^1 \hat{s}_y^2)} \hat{s}_x^1. \quad (\text{F4})$$

Now we can just expand the exponentials using the usual formula for the exponential of Pauli matrices (note that $\hat{s}_x^1 \hat{s}_x^2 + \hat{s}_y^1 \hat{s}_y^2$ is akin to \hat{s}_x in a specific subspace) and take the expectation value with respect to the initial state to get the desired result,

$$\langle \hat{s}_x^1(t) \rangle = \frac{1}{2} \cos \left(\frac{J_{12}^\perp - J_{12}^\parallel}{2} t \right) \prod_{\langle k, l \rangle} \cos^2 \left(\frac{J_{\text{eff}}^{12kl}}{8} t \right). \quad (\text{F5})$$

-
- [1] M. Heyl, A. Polkovnikov, and S. Kehrein, Dynamical quantum phase transitions in the transverse-field Ising model, *Phys. Rev. Lett.* **110**, 135704 (2013).
 - [2] J. Zhang, G. Pagano, P. W. Hess, A. Kyprianidis, P. Becker, H. Kaplan, A. V. Gorshkov, Z.-X. Gong, and C. Monroe, Observation of a many-body dynamical phase transition with a 53-qubit quantum simulator, *Nature (London)* **551**, 601 (2017).
 - [3] H. Bernien, S. Schwartz, A. Keesling, H. Levine, A. Omran, H. Pichler, S. Choi, A. S. Zibrov, M. Endres, M. Greiner *et al.*, Probing many-body dynamics on a 51-atom quantum simulator, *Nature (London)* **551**, 579 (2017).
 - [4] M. Serbyn, D. A. Abanin, and Z. Papić, Quantum many-body scars and weak breaking of ergodicity, *Nat. Phys.* **17**, 675 (2021).
 - [5] D. Bluvstein, H. Levine, G. Semeghini, T. T. Wang, S. Ebadi, M. Kalinowski, A. Keesling, N. Maskara, H. Pichler, M. Greiner *et al.*, A quantum processor based on coherent transport of entangled atom arrays, *Nature (London)* **604**, 451 (2022).
 - [6] D. A. Abanin, E. Altman, I. Bloch, and M. Serbyn, *Colloquium: Many-body localization, thermalization, and entanglement*, *Rev. Mod. Phys.* **91**, 021001 (2019).
 - [7] J. Smith, A. Lee, P. Richerme, B. Neyenhuis, P. W. Hess, P. Hauke, M. Heyl, D. A. Huse, and C. Monroe, Many-body localization in a quantum simulator with programmable random disorder, *Nat. Phys.* **12**, 907 (2016).
 - [8] M. Schreiber, S. S. Hodgman, P. Bordia, H. P. Lüschen, M. H. Fischer, R. Vosk, E. Altman, U. Schneider, and I. Bloch,

- Observation of many-body localization of interacting fermions in a quasirandom optical lattice, *Science* **349**, 842 (2015).
- [9] A. Lukin, M. Rispoli, R. Schittko, M. E. Tai, A. M. Kaufman, S. Choi, V. Khemani, J. Léonard, and M. Greiner, Probing entanglement in a many-body-localized system, *Science* **364**, 256 (2019).
- [10] J.-Y. Choi, S. Hild, J. Zeiher, P. Schauß, A. Rubio-Abadal, T. Yefsah, V. Khemani, D. A. Huse, I. Bloch, and C. Gross, Exploring the many-body localization transition in two dimensions, *Science* **352**, 1547 (2016).
- [11] A. Polkovnikov, K. Sengupta, A. Silva, and M. Vengalattore, *Colloquium: Nonequilibrium dynamics of closed interacting quantum systems*, *Rev. Mod. Phys.* **83**, 863 (2011).
- [12] M. Ueda, Quantum equilibration, thermalization and prethermalization in ultracold atoms, *Nat. Rev. Phys.* **2**, 669 (2020).
- [13] P. Peng, C. Yin, X. Huang, C. Ramanathan, and P. Cappellaro, Floquet prethermalization in dipolar spin chains, *Nat. Phys.* **17**, 444 (2021).
- [14] M. Prüfer, P. Kunkel, H. Strobel, S. Lannig, D. Linnemann, C.-M. Schmied, J. Berges, T. Gasenzer, and M. K. Oberthaler, Observation of universal dynamics in a spinor Bose gas far from equilibrium, *Nature (London)* **563**, 217 (2018).
- [15] A. Rubio-Abadal, M. Ippoliti, S. Hollerith, D. Wei, J. Rui, S. L. Sondhi, V. Khemani, C. Gross, and I. Bloch, Floquet prethermalization in a Bose-Hubbard system, *Phys. Rev. X* **10**, 021044 (2020).
- [16] C. Eigen, J. A. P. Glidden, R. Lopes, E. A. Cornell, R. P. Smith, and Z. Hadzibabic, Universal prethermal dynamics of Bose gases quenched to unitarity, *Nature (London)* **563**, 221 (2018).
- [17] L. S. Martin, H. Zhou, N. T. Leitao, N. Maskara, O. Makarova, H. Gao, Q.-Z. Zhu, M. Park, M. Tyler, H. Park, S. Choi, and M. D. Lukin, Controlling local thermalization dynamics in a Floquet-engineered dipolar ensemble, *Phys. Rev. Lett.* **130**, 210403 (2023).
- [18] G. Benettin, R. Livi, and G. Parisi, Ergodicity: How can it be broken? in *Large Deviations in Physics*, Lecture Notes in Physics Vol. 885, edited by A. Vulpiani, F. Cecconi, M. Cencini, A. Puglisi, and D. Vergni (Springer, Berlin, Heidelberg, 2014), pp. 29–70.
- [19] M. Bernaschi, A. Billoire, A. Maiorano, G. Parisi, and F. Ricci-Tersenghi, Strong ergodicity breaking in aging of mean-field spin glasses, *Proc. Natl. Acad. Sci. USA* **117**, 17522 (2020).
- [20] S. A. Parameswaran, A. C. Potter, and R. Vasseur, Eigenstate phase transitions and the emergence of universal dynamics in highly excited states, *Ann. Phys. (Leipzig)* **529**, 1600302 (2017).
- [21] A. Signoles, T. Franz, R. F. Alves, M. Gärttner, S. Whitlock, G. Zürn, and M. Weidemüller, Glassy dynamics in a disordered Heisenberg quantum spin system, *Phys. Rev. X* **11**, 011011 (2021).
- [22] J. Choi, S. Choi, G. Kucsko, P. C. Maurer, B. J. Shields, H. Sumiya, S. Onoda, J. Isoya, E. Demler, F. Jelezko, N. Y. Yao, and M. D. Lukin, Depolarization dynamics in a strongly interacting solid-state spin ensemble, *Phys. Rev. Lett.* **118**, 093601 (2017).
- [23] G. Kucsko, S. Choi, J. Choi, P. C. Maurer, H. Zhou, R. Landig, H. Sumiya, S. Onoda, J. Isoya, F. Jelezko, E. Demler, N. Y. Yao, and M. D. Lukin, Critical thermalization of a disordered dipolar spin system in diamond, *Phys. Rev. Lett.* **121**, 023601 (2018).
- [24] C. Sommer, G. Pupillo, N. Takei, S. Takeda, A. Tanaka, K. Ohmori, and C. Genes, Time-domain Ramsey interferometry with interacting Rydberg atoms, *Phys. Rev. A* **94**, 053607 (2016).
- [25] N. Takei, C. Sommer, C. Genes, G. Pupillo, H. Goto, K. Koyasu, H. Chiba, M. Weidemüller, and K. Ohmori, Direct observation of ultrafast many-body electron dynamics in an ultracold Rydberg gas, *Nat. Commun.* **7**, 13449 (2016).
- [26] J. Klafter and M. F. Shlesinger, On the relationship among three theories of relaxation in disordered systems, *Proc. Natl. Acad. Sci. USA* **83**, 848 (1986).
- [27] P. Schultzen, T. Franz, S. Geier, A. Salzinger, A. Tebben, C. Hainaut, G. Zürn, M. Weidemüller, and M. Gärttner, Glassy quantum dynamics of disordered Ising spins, *Phys. Rev. B* **105**, L020201 (2022).
- [28] P. Schultzen, T. Franz, C. Hainaut, S. Geier, A. Salzinger, A. Tebben, G. Zürn, M. Gärttner, and M. Weidemüller, Semi-classical simulations predict glassy dynamics for disordered Heisenberg models, *Phys. Rev. B* **105**, L100201 (2022).
- [29] I. Bloch, J. Dalibard, and W. Zwerger, Many-body physics with ultracold gases, *Rev. Mod. Phys.* **80**, 885 (2008).
- [30] R. Blatt and C. F. Roos, Quantum simulations with trapped ions, *Nat. Phys.* **8**, 277 (2012).
- [31] I. M. Georgescu, S. Ashhab, and F. Nori, Quantum simulation, *Rev. Mod. Phys.* **86**, 153 (2014).
- [32] C. Gross and I. Bloch, Quantum simulations with ultracold atoms in optical lattices, *Science* **357**, 995 (2017).
- [33] A. Browaeys and T. Lahaye, Many-body physics with individually controlled Rydberg atoms, *Nat. Phys.* **16**, 132 (2020).
- [34] D. Jaksch, J. I. Cirac, P. Zoller, S. L. Rolston, R. Côté, and M. D. Lukin, Fast quantum gates for neutral atoms, *Phys. Rev. Lett.* **85**, 2208 (2000).
- [35] H. Weimer, M. Müller, I. Lesanovsky, P. Zoller, and H. P. Büchler, A Rydberg quantum simulator, *Nat. Phys.* **6**, 382 (2010).
- [36] D. Barredo, H. Labuhn, S. Ravets, T. Lahaye, A. Browaeys, and C. S. Adams, Coherent excitation transfer in a spin chain of three Rydberg atoms, *Phys. Rev. Lett.* **114**, 113002 (2015).
- [37] A. P. Orioli, A. Signoles, H. Wildhagen, G. Günter, J. Berges, S. Whitlock, and M. Weidemüller, Relaxation of an isolated dipolar-interacting Rydberg quantum spin system, *Phys. Rev. Lett.* **120**, 063601 (2018).
- [38] K. Slagle, Y. Z. You, and C. Xu, Disordered XYZ spin chain simulations using the spectrum bifurcation renormalization group, *Phys. Rev. B* **94**, 014205 (2016).
- [39] R. M. W. v. Bijnen, Quantum engineering with ultracold atoms, Ph.D. thesis, Technische Universiteit Eindhoven, Eindhoven, 2013.
- [40] S. Whitlock, A. W. Glaetzle, and P. Hannaford, Simulating quantum spin models using Rydberg-excited atomic ensembles in magnetic microtrap arrays, *J. Phys. B: At. Mol. Opt. Phys.* **50**, 074001 (2017).
- [41] M. D. Lukin, M. Fleischhauer, R. Cote, L. M. Duan, D. Jaksch, J. I. Cirac, and P. Zoller, Dipole blockade and quantum information processing in mesoscopic atomic ensembles, *Phys. Rev. Lett.* **87**, 037901 (2001).
- [42] J. Schachenmayer, A. Pikovski, and A. M. Rey, Many-body quantum spin dynamics with Monte Carlo trajectories on a discrete phase space, *Phys. Rev. X* **5**, 011022 (2015).

- [43] R. Vosk and E. Altman, Many-body localization in one dimension as a dynamical renormalization group fixed point, *Phys. Rev. Lett.* **110**, 067204 (2013).
- [44] D. Pekker, G. Refael, E. Altman, E. Demler, and V. Oganesyan, Hilbert-glass transition: New universality of temperature-tuned many-body dynamical quantum criticality, *Phys. Rev. X* **4**, 011052 (2014).
- [45] R. Vasseur, A. C. Potter, and S. A. Parameswaran, Quantum criticality of hot random spin chains, *Phys. Rev. Lett.* **114**, 217201 (2015).
- [46] R. Vasseur, A. J. Friedman, S. A. Parameswaran, and A. C. Potter, Particle-hole symmetry, many-body localization, and topological edge modes, *Phys. Rev. B* **93**, 134207 (2016).
- [47] P. Scholl, H. J. Williams, G. Bornet, F. Wallner, D. Barredo, L. Henriet, A. Signoles, C. Hainaut, T. Franz, S. Geier, A. Tebben, A. Salzinger, G. Zürn, T. Lahaye, M. Weidemüller, and A. Browaeys, Microwave engineering of programmable XXZ Hamiltonians in arrays of Rydberg atoms, *PRX Quantum* **3**, 020303 (2022).
- [48] A. Braemer, T. Franz, M. Weidemüller, and M. Gärttner, Pair localization in dipolar systems with tunable positional disorder, *Phys. Rev. B* **106**, 134212 (2022).
- [49] T. Langen, T. Gasenzer, and J. Schmiedmayer, Prethermalization and universal dynamics in near-integrable quantum systems, *J. Stat. Mech.: Theory Exp.* (2016) 064009.
- [50] L. Christakis, J. S. Rosenberg, R. Raj, S. Chi, A. Morningstar, D. A. Huse, Z. Z. Yan, and W. S. Bakr, Probing site-resolved correlations in a spin system of ultracold molecules, *Nature (London)* **614**, 64 (2023).
- [51] L. Rademaker and D. A. Abanin, Slow nonthermalizing dynamics in a quantum spin glass, *Phys. Rev. Lett.* **125**, 260405 (2020).
- [52] J. Bezanson, A. Edelman, S. Karpinski, and V. B. Shah, Julia: A fresh approach to numerical computing, *SIAM Rev.* **59**, 65 (2017).
- [53] T. Franz, S. Geier, A. Braemer, C. Hainaut, A. Signoles, N. Thaicharoen, A. Tebben, A. Salzinger, M. Gärttner, G. Zürn, and M. Weidemüller, Emergent pair localization in a many-body quantum spin system, [arXiv:2207.14216](https://arxiv.org/abs/2207.14216).

4.2 EMERGENT PAIR LOCALIZATION

Another way of validating the pair model is the comparison of the same model at different disorder strengths. This can be realized in a Rydberg based quantum simulator by tuning the systems' density as explained in Section 1.3.

In the following [D], we again use the x -magnetization as observable and track its steady-state value with respect to an external magnetic field aligned in x -direction as well. We find a clear qualitative difference between weak and strong disorder at small external fields: The strongly disordered system responds much stronger to the field, i.e. the steady-state magnetization grows very fast with increasing field strength, than the weakly disordered one. This leads to a sharp cusp-like curve, which we show to be incompatible with a thermal state. Instead, we find that a pair-based effective model reproduces this feature and can also match the full measurement data closely. Conversely, at weak disorder, i.e. high density, the steady-state magnetization behaves quite different. At weak field, the curve is very round which is reproduced nicely using a thermal description.

This experiment provides direct evidence for a pair localization transition. However, it is possible that this is a prethermal regime only and the signature vanishes at much later times. Testing for this experimentally will of course be very hard, if not impossible, depending on the timescale of this final relaxation.

Following the publication, we present an alternative to the mean-field model in Section 4.2.1. This conceptually simpler model allows for analytical computation of both the presumably thermal and pair localized magnetization curves. Thus, the qualitative difference between weak and strong disorder is tracked back to a qualitative difference of the distribution of relevant couplings. While this model is not as quantitative as the mean-field model contained in the publication, it nonetheless has the same qualitative features and thus highlights the physical origin of the behavior at weak field more directly.

Emergent pair localization in a many-body quantum spin system

Titus Franz,^{1,2,*} Sebastian Geier,¹ Adrian Braemer,^{1,3} Clément Hainaut,^{1,4}
 Adrien Signoles,^{1,5} Nithiwadee Thaicharoen,^{1,6} Annika Tebben,¹ Andre Salzinger,¹
 Martin Gärttner,^{1,3,7,8,†} Gerhard Zürn,¹ and Matthias Weidemüller^{1,‡}

¹*Physikalisches Institut, Universität Heidelberg, Im Neuenheimer Feld 226, 69120 Heidelberg, Germany*

²*Max-Planck-Institut für Quantenoptik, Hans-Kopfermann-Str. 1, Garching, Germany*

³*Kirchhoff-Institut für Physik, Universität Heidelberg,
Im Neuenheimer Feld 227, 69120 Heidelberg, Germany*

⁴*Univ. de Lille, CNRS, UMR 8523-PhLAM-Physique des Lasers, Atomes et Molécules, Lille, France*

⁵*PASQAL, 7 rue Léonard de Vinci, 91300 Massy, France*

⁶*Department of Physics and Materials Science, Faculty of Science,
Chiang Mai University, 239 Huay Kaeo Road, Muang, Chiang Mai, 50200, Thailand*

⁷*Institut für Theoretische Physik, Ruprecht-Karls-Universität Heidelberg,
Philosophenweg 16, 69120 Heidelberg, Germany*

⁸*Institute of Condensed Matter Theory and Optics,
Friedrich-Schiller-University Jena, Max-Wien-Platz 1, 07743 Jena, Germany*

(Dated: February 27, 2024)

Understanding how closed quantum systems dynamically approach thermal equilibrium presents a major unresolved problem in statistical physics. Generically, non-integrable quantum systems are expected to thermalize as they comply with the Eigenstate Thermalization Hypothesis. However, in the presence of strong disorder, the dynamics can possibly slow down to a degree that systems fail to thermalize on experimentally accessible timescales, as in spin glasses or many-body localized systems. In general, particularly in long-range interacting quantum systems, the specific nature of the disorder necessary for the emergence of a prethermal, metastable state—distinctly separating the timescales of initial relaxation and subsequent slow thermalization—remains an open question. We study an ensemble of Heisenberg spins with a tunable distribution of random coupling strengths realized by a Rydberg quantum simulator. We observe a drastic change in the late-time magnetization when increasing disorder strength. The data is well described by models based on pairs of strongly interacting spins, which are treated as thermal for weak disorder and isolated for strong disorder. Our results indicate a crossover into a pair-localized prethermal regime in a closed quantum system of thousands of spins in the critical case where the exponent of the power law interaction matches the spatial dimension.

I. INTRODUCTION

What is the fate of an isolated, strongly interacting, and possibly disordered quantum system initially prepared in a far-from-equilibrium state? In general, even if a strongly interacting quantum system is isolated from its environment, it is expected to thermalize [1–4]. As a notable exception to this rule, strongly disordered systems can retain retrievable memory of their initial state for arbitrarily long times, leading to a rich phenomenology ranging from glassy dynamics to many-body localization.

A comprehensive framework for understanding systems that do not undergo direct thermalization is provided by the concept of prethermalization [5–10]: Here, the Hamiltonian can be decomposed into a reference Hamiltonian H_0 , and a weak perturbation H_1 which

breaks at least one local conservation law of H_0 . In such instances, a metastable state exists whose properties can be calculated using the generalized Gibbs ensemble (GGE) of the reference Hamiltonian H_0 [11]. As an example, we can consider many-body localization (MBL) in the framework of prethermalization: Here, the reference Hamiltonian is given by a non-interacting ensemble of spins subject to a strongly disordered external field, and H_1 describes the interactions between nearest-neighbor spins. If these interactions are sufficiently weak, these systems remain localized [12, 13], and the conserved quantities become “dressed,” commonly referred to as l-bits [14, 15]. However, a different type of disorder naturally occurs in numerous systems, including cold atoms [16–23], ions [24] or nitrogen-vacancy centers [10, 25] where the couplings themselves are disordered, not the external field. In this case, discerning the reference Hamiltonian H_0 becomes nontrivial, and in previous studies, the depolarization dynamics in these systems is interpreted as direct thermalization [10, 25]. Yet, it is known from spin glasses that disorder in the couplings leads to a hierarchy of timescales,

* franzt@physi.uni-heidelberg.de

† martin.gaerttner@uni-jena.de

‡ weidemueller@uni-heidelberg.de

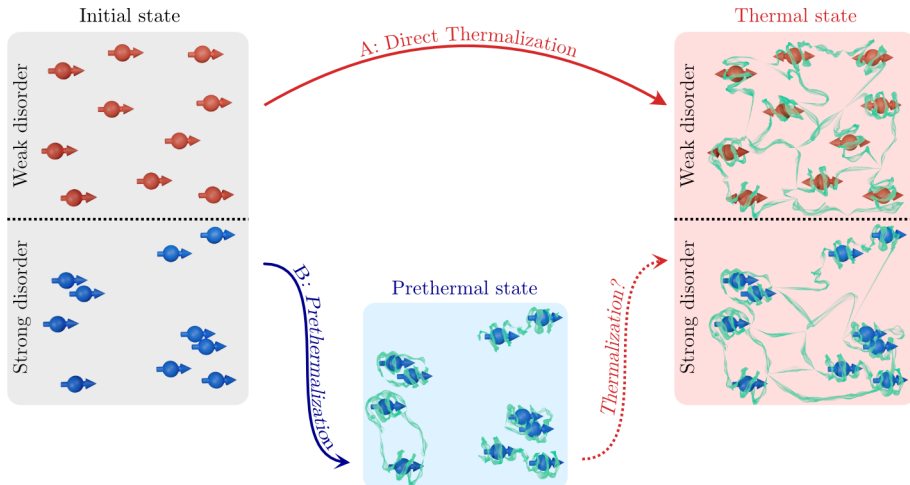


Figure 1. Thermal and non-thermal regimes. Schematic depiction of the dynamics of the system. Depending on the strength of disorder, initially, uncorrelated spins evolve either directly (via **A**) to a thermal state with correlations between all spins or (via **B**) to a prethermal state consisting of uncorrelated pairs of strongly correlated spins. Whether, in this case, thermalization occurs eventually remains an open question.

which slows down the dynamics such that on experimentally accessible timescales, these systems never reach thermal equilibrium.

Unfortunately, understanding if and how quantum systems thermalize is extremely challenging, as numerical simulations are limited to relatively small system sizes [26–28] and analytical solutions are scarce. Quantum simulation experiments with single-site resolution can investigate slightly larger systems with several tens of particles [29–33], but they can only probe finite time scales [17–19, 24].

In this study, we employ a Rydberg quantum simulator [34–36] to explore the thermalization dynamics in long-range interacting systems in 3D using a cloud of up to 6000 Rydberg spins with spatial disorder. In the weakly disordered regime, characterized by similar distances between particles (top row in Fig. 1), our experimental findings align with previous assertions of direct thermalization [25]. However, at strong disorder, we demonstrate the emergence of a localized prethermal state, verified through a non-analytical dependence of the late-time magnetization on an external field. Here, the hierarchy of interaction strengths allows us to effectively describe the Hamiltonian with a reference Hamiltonian H_0 , where strongly interacting pairs of spins remain localized for long times before interactions between pairs possibly lead to thermalization at even later times (bottom row in Fig. 1).

II. EXPERIMENTAL SETUP

We consider the quantum spin-1/2 Heisenberg XXZ-model (in units where $\hbar = 1$)

$$\hat{H}_{\text{int}} = \frac{1}{2} \sum_{i,j} J_{ij} \left(\hat{s}_x^{(i)} \hat{s}_x^{(j)} + \hat{s}_y^{(i)} \hat{s}_y^{(j)} + \delta \hat{s}_z^{(i)} \hat{s}_z^{(j)} \right), \quad (1)$$

with spin operators $\hat{s}_\alpha^{(i)} = \hat{\sigma}_\alpha^{(i)}/2$ ($\alpha \in \{x, y, z\}$) acting on spin i . The interactions between spins decay with a power law $J_{ij} = C_a r_{ij}^{-a} (1 - 3 \cos(\theta_{ij})^2)$, where r_{ij} are the distances between the spins i and j and θ_{ij} is the angle with respect to the quantization axis defined by the magnetic field. The parameters δ and a are determined by the choice of Rydberg states (cf. [35]). In our experiment, we encode the spin degree of freedom in the Rydberg states $|\downarrow\rangle = |48S\rangle$ and $|\uparrow\rangle = |48P\rangle$ leading to dipolar interactions as described by Eq. (1) with $\delta = 0$, $a = 3$ and $C_3/(2\pi) = 1.15 \text{ GHz } \mu\text{m}^3$. Additional data for a Van-der-Waals interacting system ($a = 6$, $C_6/(2\pi) = 507 \text{ GHz } \mu\text{m}^6$, $\delta \approx -0.7$ and no angular dependence on θ_{ij}) is shown in Appendix B.

The spins are distributed randomly with an imposed minimal distance r_{bl} resulting in a random but correlated distribution of couplings J_{ij} (Fig. 1). This geometry is naturally given in the experiment where the Rydberg blockade effect forbids two excitations being closer than r_{bl} . The blockade constraint allows tuning the strength of the disorder: For the weak disorder measurements, we chose the density such that the typical interparticle distance of $a_0 \sim 6.8 \mu\text{m}$ is comparable to the blockade radius of $4.6 \mu\text{m}$, whereas in the strongly disordered case, the blockade radius of $5.0 \mu\text{m}$

is much smaller compared to the typical interparticle distance $a_0 \approx 11.2 \mu\text{m}$ (see methods for more details on the Rydberg atoms' distribution). In both cases, the median interaction strengths of $J_{\text{median}}/(2\pi) = \text{median}_i(\max_j |J_{ij}|)/(2\pi) = 2.8 \text{ MHz}$ (weak disorder) or $J_{\text{median}}/(2\pi) = 1.1 \text{ MHz}$ (strong disorder) is large compared to typical decoherence rates like the decay rate of the Rydberg atoms of $\Gamma/(2\pi) = 0.018 \text{ MHz}$. The maximal duration of the experiment of $10 \mu\text{s}$ is chosen such that the Rydberg decay can still be considered small.

By coupling the spin states with a microwave field Ω , we perform a Ramsey protocol (schematically depicted in Fig. 2 **a**) where a first $\pi/2$ pulse initially prepares the system in the fully x -polarized state $|\psi_0\rangle = |\rightarrow\rangle_x^{\otimes N} = 2^{-N/2}(|\uparrow\rangle + |\downarrow\rangle)^{\otimes N}$ (see methods for details of the experimental protocol) which shows no classical dephasing or dynamics in a mean-field description where for each atom, the effective field is aligned with the polarization of the atoms (see Fig. 2 **a** center). With a second $\pi/2$ -pulse, we read out the average magnetization $\langle \hat{S}_x \rangle = \langle \sum_i \hat{s}_x^{(i)} \rangle / N$. Since this observable is an average over local (single-spin) observables, it should relax to its thermal value if the system is locally thermalizing.

III. HIERARCHY OF RELAXATION TIME SCALES

The blue dots in Fig. 2 **b** (strong disorder) and the red dots in Fig. 2 **c** (weak disorder) labeled with 0.0 MHz show the time evolution of the magnetization under \hat{H}_{int} . In both regimes, the magnetization relaxes to zero, following a stretched exponential law as discussed in previous work [37–39], and reaches a steady-state on a time scale of $\sim 2\pi/J_{\text{median}}$ in units of the inverse median nearest neighbor interaction strength. This depolarization dynamics is a direct consequence of the symmetry of the interaction Hamiltonian as all eigenstates already have vanishing x -magnetization due to the conservation of $\sum_i \hat{s}_z^{(i)}$ ¹.

This situation changes when adding a homogeneous transverse field term to the Hamiltonian

$$\hat{H}_{\text{ext}} = \Omega \sum_i \hat{s}_x^{(i)}, \quad (2)$$

which breaks the $U(1)$ symmetry and leads to a finite late-time magnetization as the data in Fig. 2 **b** and **c** shows. As a result, the dynamics still feature an initial fast relaxation on the time-scale of $2\pi/J_{\text{median}}$, fol-

lowed by a slowly relaxing regime. The stronger the applied magnetic field, the sooner the metastable regime is reached, and the higher the magnetization value becomes.

The finite late-time value of the magnetization of these curves may be understood on a qualitative level by a simple, intuitive, spin-locking model [40]. At strong field $\Omega \gg J_{\text{median}}$, the inter-spin interaction cannot overcome the magnetic forces and so the spins stay put. Lowering the external field strength weakens this lock and the spins can start dephasing due to their interactions.

As a consistency check, we compare the experimental data to semiclassical truncated Wigner approximation (dTWA) (solid lines in Fig. 2 **b** and **c**). All simulated curves agree well with the experimental data except for the strongest magnetic field strength, confirming the quality of our quantum simulation of the Heisenberg model. The deviations at strong magnetic field (see grey dots in Fig. 2 **b** are likely caused by an experimental imperfection as the strong field may lead to additional couplings to other Rydberg states. This induces population loss to states, which are not measured, thus reducing the total magnetization. Therefore, all experimental data at external field strength above 5 MHz are greyed out.

IV. PRETHERMALIZATION IN DISORDERED SPIN SYSTEMS

The striking difference between strongly and weakly disordered cases becomes apparent when examining the dependence of the plateau value on the external field measured after $10 \mu\text{s}$ (see Fig. 2 **d** and **e**). For strong disorder, there is a sharp cusp at $\Omega = 0 \text{ MHz}$, which is not present for weak disorder, where the curve is very smooth. Note that this is not an artifact of the difference in absolute scale of the x-axis caused solely by the on average weaker interactions in the strongly disordered case. Relative to their respective median interaction strength J_{median} , both plots cover a similar range. For a generic, thermalizing system, it is plausible to expect a smooth parametric dependence based on the Eigenstate Thermalization Hypothesis (ETH). We will argue that the cusp feature is a clear signature of a non-thermal state, consistent with a generalized Gibbs ensemble with extensively many conserved quantities.

To explain the curve in the strongly disordered regime, characterized by a small blockade radius r_{bl} and significant variations in the nearest neighbor inter-spin distances, we employ a model based on pairs of strongly interacting spins: For strong positional disorder, close-by spins form pairs that approximately decouple from the rest of the system as the energy splitting between their eigenstates will typically be much larger than any

¹ From the conservation of \hat{S}_z , i.e. $[\hat{S}_z, \hat{H}_{\text{int}}] = 0$, it follows that $\langle \hat{S}_x \rangle = -i\langle [\hat{S}_y, \hat{S}_z] \rangle = 0$ for every eigenstate.

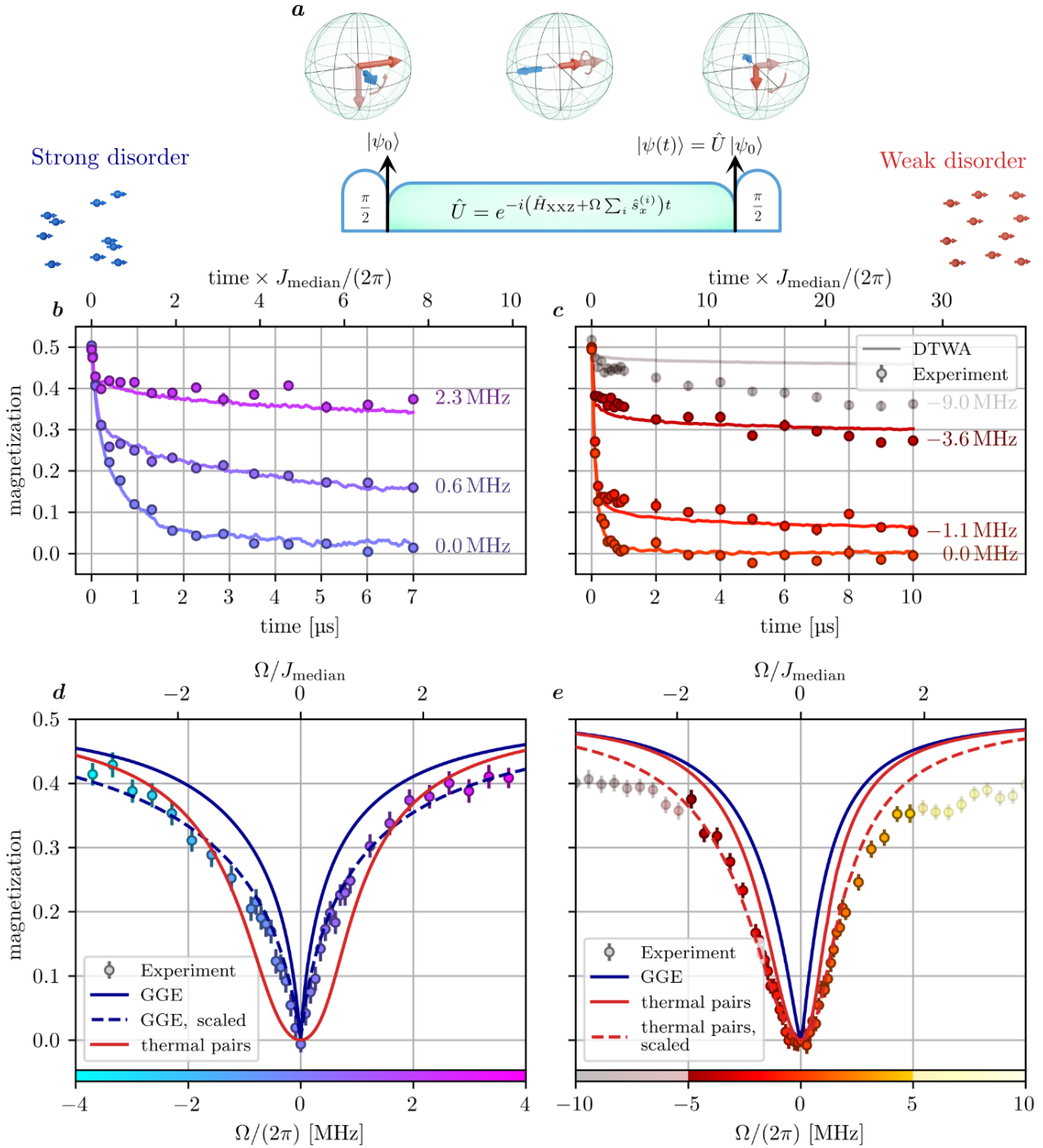


Figure 2. Late-time magnetization for different strength of disorder for a spin system interacting with dipole-dipole interactions. **a** Experimental protocol: A $\pi/2$ pulse (blue arrow in the Bloch sphere) rotates the spins from the z (light red arrow) to the x -direction (red arrow). During the subsequent time evolution, the system interacts via the Heisenberg Hamiltonian (1) while a spin locking field at Rabi frequency Ω is applied. The final magnetization is read out after a second $\pi/2$ -pulse. **b** (strong disorder) and **c** (weak disorder): Measured spin relaxation dynamics for varying transverse field strengths. The solid lines show semiclassical DTWA simulations. **d** (strong disorder) and **e** (weak disorder): Magnetization after 10 μs as a function of field strength Ω . The solid blue (red) lines show the magnetization expected from a GGE (4) (canonical ensemble (5)). The dashed lines show the same simulations rescaled by a global factor to best fit the experimental data.

other terms in the Hamiltonian affecting the pair [41–45]. In the presence of an external field, such a pair, initially in a fully polarized state, will undergo coherent oscillations and depolarize only very slowly as it does not become entangled with the rest of the system until very late times [38]. Thus, the depolarization dynamics arises due to dephasing among pairs oscillating at different frequencies due to different interaction strengths.

Thus, returning to the notion of prethermalization introduced above, H_0 is given by the part of the full Hamiltonian that acts on single pairs, while interactions between the pairs form the weak part H_1 . Since H_0 factorizes into contributions of the individual pairs, we can make a prediction for the prethermal steady state magnetization. On average, each pair contributes

$$\overline{\langle \hat{S}_x \rangle_{\text{pair}}} = \frac{\Omega^2}{2(\Omega^2 + j^2)} \quad (3)$$

to the total magnetization, where $j = J(\delta - 1)$ and J the pair's coupling (see Appendix C for a detailed derivation). The distribution of pair couplings can be found numerically by sampling blockaded positions. To calculate the steady-state value, we use a self-consistent mean-field approach to assign each pair an effective field strength Ω_i taking into account the interaction with its surroundings. This leads to the asymmetry around $\Omega = 0$, as for $\Omega > 0$, the mean-field contribution adds to the static part and thus results in a larger effective field, while for $\Omega < 0$ the converse is true. This effect is much more prominent in the case of $\alpha = 6$ as shown in the appendix in Fig. 4.

In essence, this mean-field pair model describes the system as a generalized Gibbs ensemble

$$\rho_{\text{GGE}} \propto \exp \left(- \sum_i \beta_i H_{\text{pair},i}^{(\text{mf})} \right) \quad (4)$$

of pairs governed by $H_{\text{pair},i}^{(\text{mf})}$, where the Lagrange multipliers β_i are fixed by energy conservation. Using this model, we find qualitative agreement with the experimental data in the case of strong disorder (blue, solid line in Fig. 2d). If the interaction strength of the pair simulation is artificially increased by a factor of 1.75 (dashed blue line), we find even perfect agreement with the experiment. We conjecture that this factor is needed to take into account interactions beyond the nearest neighbor.

Thus, we have shown that the system is consistent with a prethermal description in the sense, that we found a quasi-stationary state inconsistent with a thermal ensemble description yet matching a generalized Gibbs ensemble. Furthermore, this prethermal state is localized as the pairs' eigenspaces constitute local integrals of motion.

In the less disordered regime, this model of isolated pairs also predicts a sharp, narrow shape (see blue, solid line in Fig. 2 e) which does not match the experimental data even on a qualitative level. In this regime, the approximation of isolated pairs of spins is no longer valid, and we need to consider the build-up of entanglement between different pairs of spins, which leads to fast thermalization. While the full treatment of the highly correlated many-body system of 6000 spins is not feasible on a classical computer, we can make the first order approximation that the system itself acts as a thermal bath for each pair and imposes that all pairs thermalize to the same global temperature (see also Appendix C):

$$\rho_{\text{can}} \propto \exp \left(-\beta \sum_i H_{\text{pair},i}^{(\text{mf})} \right) \quad (5)$$

Here, β is defined implicitly by energy conservation $\text{Tr } \rho_{\text{can}} \hat{H} = \langle \psi_0 | \hat{H} | \psi_0 \rangle$. We find qualitative agreement between this model (red, solid line) and experimental data. The agreement can be improved by increasing the interactions by a factor of 1.4 (red, dashed line) that effectively takes into account the correlations between distant spins that are neglected in the pair description of eq. 5. The deviation at strong field is likely caused by coupling to different Rydberg states as remarked earlier.

As a consistency check, we also try to explain the data in the strong-disorder regime with the canonical ensemble description (see Fig. 2 d) which clearly fails to reproduce the observed sharp cusp around $\Omega = 0$ MHz.

V. CONCLUSION AND DISCUSSION

We studied the relaxation dynamics of power-law interacting spins by observing the change in the parametric dependence of the late-time magnetization on an external field. By finding simple models based on pairs of strongly interacting spins, we explained the measured data both in the weak and strong disorder regime revealing a fundamental change in the dynamical properties of the system on experimentally accessible timescales. Our results indicate the presence of a crossover from a thermalizing regime to a prethermal pair-localized regime caused by positional disorder.

The method for observing prethermal localization used in this work is inherently versatile and may also be applied to study thermalization in other systems. The signature that distinguishes thermalized from localized systems is the smooth dependence of the steady-state magnetization(, which is absent in the latter). This consideration becomes particularly crucial when the system's components, such as the pairs of spins in this study, experience rapid dephasing. This dephasing generally occurs on a much faster timescale compared

to the build-up of entanglement between these components, resulting in thermalization. This insight calls for the reevaluation of claims made in [10, 25], given that the relaxation of the magnetization in spatially disordered spin systems reflects only the dephasing but not the thermalization process.

Notably, our system implements a critical case where the power law dependence of the interaction strength with distance a equals the spatial dimension $d = 3$. In this regime, theoretical results for large systems are scarce due to competing scales. In Appendix B, we show a similar experiment for a Van-der-Waals interacting system where $a = 2d = 6$. In this case, the magnetization behaves qualitatively as in the strongly disordered case of $\alpha = 3$ and also shows a sharp cusp. This indicates that prethermalization caused by localized pairs of spins is a robust effect independent of the spatial dimension as long as disorder is sufficiently strong.

This study paves the way toward exploring the late-time dynamics of far-from-equilibrium systems with power-law interactions and disordered couplings, which are ubiquitous in nature. For these systems, it is yet an open question if they show (prethermal) many-body localization similar to the standard model of MBL where the on-site potential is disordered. Recent theoretical and numerical results indicate that localization and the consequent absence of thermalization are excluded in dimensions $d > 1$ and for power law interactions [23, 46]. However, the type of spatial disorder investigated in this study differs significantly from that in traditional MBL systems, rendering most conventional arguments about instability and eventual thermalization not directly applicable. Intriguingly, first numerical studies [45] suggest that for the type of disorder studied here, localization effects are surprisingly robust to finite size drifts, a significant issue for the numerical investigation of the standard model of MBL. To draw parallels between our findings of prethermalization and prethermal MBL, it will be decisive to investigate the scaling of the relaxation timescale with the strength of disorder which is expected to be exponential in the case of prethermal MBL [47]. However, a proper definition of the strength of disorder in case the disordered couplings, opposed to disordered on-site detuning, remains an open question. Finally, an exciting avenue for future research is to explore the relation between the slow relaxation dynamics observed in this work and quantum spin glasses. In quantum spin glasses, the combination of frustration, low energies and disorder leads to exceptionally slow relaxation dynamics, a phenomenon being highly relevant to the approach of quantum computation via quantum annealing [48, 49].

METHODS

Here we provide further details on the numeric simulations, the experimental protocol and the spatial configuration of the Rydberg cloud.

Details on experimental implementation. We start the experiment by trapping 10^6 Rubidium-87 in a cigar shaped dipole trap with a diameter of $300\text{ }\mu\text{m}$ (long axis) and $70\text{ }\mu\text{m}$ (short axis) at a temperature of $10\text{ }\mu\text{K}$. We consider this gas to be frozen since the atoms move only a distance of $d_{\text{kin}} = t_{\text{exp}} \sqrt{\frac{3kT}{m}} = 0.5\text{ }\mu\text{m}$ during an experimental cycle of $t_{\text{exp}} = 10\text{ }\mu\text{s}$ which is small compared to the Rydberg blockade radius of $r_{\text{bl}} \approx 5\text{ }\mu\text{m}$. After optically pumping the atoms into the state $|5S(F=2, m_F=2)\rangle$, we optically excite the atoms to the spin state $|\downarrow\rangle$ via a two-photon off-resonant excitation process (single-photon detuning of 98 MHz and two-photon Rabi frequency of 1 MHz). A global microwave $\pi/2$ -pulse prepares the fully polarized initial state $|\psi_0\rangle = |\rightarrow_x\rangle^{\otimes N}$. For the dipolar interacting spin system, we couple the states $|48S\rangle$ and $|48P\rangle$ resonantly with a single-photon transition at 35 GHz . This frequency is generated by mixing a 5 GHz signal of the Keysight M8190A AWG with an Anritsu MG3697C signal generator. In the case of Van-der-Waals interactions, the state $|61S\rangle$ is coupled resonantly to $|62S\rangle$ via a two-photon transition at a microwave frequency of 16.546 GHz which can be directly generated with a Keysight M8190A arbitrary waveform generator (AWG).

The same microwave setup is used to realize the spin locking field where a phase shift of 90 degrees needs to be added such that the field aligns with the spins. This allows us to implement the transverse field term, Eq. (2), with field strengths up to $\Omega/(2\pi) = 10\text{ MHz}$. After a time evolution t , the x -magnetization is rotated tomographically onto the z -axis by applying a second $\pi/2$ -pulse with various phases. Finally, the magnetization is obtained from a measurement of the population of one of the two spin states via field ionization, and the other spin state is optically deexcited to the ground state. A visual representation of the measurement protocol can be found in Fig. 2 **a**, and a more detailed explanation of the determination of the magnetization was reported in a previous publication [37].

Details on the Rydberg distribution. In this work, we can tune the disorder with the Rydberg blockade effect, which imposes a minimal distance r_{bl} between the spins. At small blockade radius, the spins are distributed randomly in the cloud, while a large radius introduces strong correlation between the atom positions and, hence, the coupling strength. To quantify the disorder strength, we compare the blockade radius to typical interparticle distance, which can be estimated from the Wigner-Seitz radius $a_0 = [3/(4\pi\rho)]^{1/3}$. We ad-

just this parameter in our experiment by controlling the Rydberg fraction, which is dependent on the excitation time t_{exc} . In addition, we tune the Rydberg density ρ by varying the volume of the ground state atoms with a short time-of-flight period after turning off the dipole trap and before exciting to the Rydberg states. We measure the resulting Rydberg density through depletion imaging [50] where we deduce the Rydberg distribution from the missing ground state atoms after Rydberg excitation. The measured parameters of the Rydberg distribution are presented in detail in Table I in the appendix.

To estimate the Rydberg blockade radius, we model the excitation dynamics by the simplified description introduced in [37] which assumes a hard-sphere model for the Rydberg blockade effect. This model sets an upper limit on the blockade radius $r_{\text{bl}} = \sqrt[6]{\frac{C_6}{\Gamma_{\text{eff}}}}$ by estimating the effective linewidth of the laser, based on the duration of the excitation pulse and power broadening. The latter is calculated self-consistently, taking into account the enhancement factor induced by collective Rabi oscillations within a superatom [51, 52].

This established model of the Rydberg cloud can be benchmarked using the experimentally measured time evolution, which is known to be well described by semiclassical Discrete Truncated Wigner Approximation (DTWA) in case no locking field is applied [37] (see Fig. 3 in appendix A). This simulation is highly sensitive with respect to the blockade radius and the density, and can therefore be used to determine these experimental parameters in case of weak and strong disorder. From the excitation model, we can also compute the median of the nearest neighbor interaction strength J_{median} which ranges from 1.1 MHz to 2.8 MHz depending on the experimental setting (see table I). The resulting time evolution can be considered unitary for up to $10\text{ }\mu\text{s}$, which is an order of magnitude larger than the timescale of the experiment $2\pi/J_{\text{median}}$.

Appendix A: Semiclassical DTWA simulations

In previous work [37, 53], we could show that the semiclassical Discrete Truncated Wigner Approximation (DTWA) is well suited to describe the relaxation of the magnetization under the interaction Hamiltonian (1) defined in the main text. The main principle of DTWA is to sample classical time evolutions over different initial states such that the quantum uncertainty of the initial state is respected [54]. In Fig. 3, we compare the time evolution obtained from DTWA simulations to the experimental data (red dots) in the case of weak (left panels) and strong disorder (right panels). It turns out that the resulting dynamics depend sensitively on the blockade radius and on density. However, the same fitted parameters describes the time evolution for different locking fields (top panels) and the dependence of the late-time magnetization on the field strength. As mentioned in the main text, the observed discrepancy of DTWA simulations and experimental data observed for large fields in the weakly disordered regime (Fig. 3 c) can be most likely attributed to experimental imperfections such as coupling to other Rydberg states due to power broadening of the microwave transition.

Appendix B: Data for Van der Waals interactions

By encoding the spin degree of freedom in different Rydberg states, it is possible to realize different Hamiltonians with different range of interactions. In addition to a dipolar interacting Hamiltonian with $a = d = 3$ as shown in the main text, we can also create a spin system with less long-range Van der Waals interactions. For this purpose, we couple the Rydberg state $|\downarrow\rangle = |61S\rangle$ to $|\uparrow\rangle = |62S\rangle$ which results in a Heisenberg XXZ Hamiltonian as described by Eq. (1) with $\delta = -0.7$, $a = 6$ and $C_6/(2\pi) = 507 \text{ GHz } \mu\text{m}^6$ (see also Table I for an overview over the experimental parameters).

Similar to the experimental results presented in the main article, also the Van der Waals interacting system shows a slow relaxation dynamics on a timescale of $\approx 2\pi/J_{\text{median}}$ (see Fig. 4 a). Applying an external field Ω also slows down the relaxation dynamics considerably. It should be noted, that the external field has to be realized by a two-photon microwave transition as the transition between the two spin states is dipole forbidden. Therefore, the single photon Rabi frequencies are required to be much larger compared to the dipolar interacting spin system, which might potentially lead to a stronger coupling to different Rydberg states inducing addition decay of the magnetization, especially at late times.

The dependence of the late-time magnetization (taken after 10 μs) on the spin locking field Ω of the

Van der Waals interacting system is shown in Fig. 4 b. Compared to the dipolar interacting case presented in the main text, the curve is even more asymmetric. This effect can be explained by the isotropic repulsive interactions in the Van der Waals case, whereas dipolar couplings vary as $1 - 3 \cos(\theta)^2$ depending on the angle θ between the inter-spin axis and the quantization axis. Most importantly, also the Van der Waals interacting system features a sharp cusp around $\Omega = 0 \text{ MHz}$. In this regard, the curve strongly resembles the case of strong disorder in dipolar interacting systems presented in the main text. At first sight, this result might be surprising as the spin system is even more blockaded with a ratio of blockade radius to typical interaction range of $r_{\text{bl}}/a_0 = 5.7/7.8 = 0.73$ than the weakly disordered dipolar system where $r_{\text{bl}}/a_0 = 4.6/6.8 = 0.68^2$. However, the shorter-range interaction increases the effective disorder in the system as the nearest-neighbor interaction becomes much stronger compared to the next-nearest neighbor coupling. This proves that, especially for short-range interactions decaying faster than $a = d$, the existence of a prethermal state is a ubiquitous phenomenon in spatially disordered quantum spin systems.

Appendix C: Derivation of the effective model

In this appendix, we derive how to describe the system in terms of localized pairs, which constitute the approximate local integrals of motion for the GGE description of the system. Starting from the physics of a single, isolated pair, we will derive the GGE, the description in terms of thermal pairs, and the self-consistent mean-field equations, which partly take into account interactions beyond the nearest neighbor. This approximation provides an intuitive picture that allows us to explain all the observed features of the long-time magnetization (positivity, cusp, asymmetry).

For a single interacting pair, in the basis

² Due to the Van der Waals interactions being a second order process, the typical interaction strength are much weaker compared to the dipolar interacting case. To compensate for this effect, we increase the density which increases the interaction strength.

	Dipolar interactions (weak disorder)	Dipolar interactions (strong disorder)	Van-der-Waals interactions
Rydberg states	$ 48S_{1/2}\rangle \leftrightarrow 48P_{3/2}\rangle$	$ 48S_{1/2}\rangle \leftrightarrow 48P_{3/2}\rangle$	$ 61S_{1/2}\rangle \leftrightarrow 62S_{1/2}\rangle$
decay rate $\Gamma/(2\pi)$	0.018 MHz	0.018 MHz	0.0096 MHz
t_{exc}	10 μs	1 μs	5 μs
Excitation volume	$59 \mu\text{m} \times 44 \mu\text{m} \times 36 \mu\text{m}$	$59 \mu\text{m} \times 34 \mu\text{m} \times 30 \mu\text{m}$	$69 \mu\text{m} \times 43 \mu\text{m} \times 37 \mu\text{m}$
N_{Ryd}	6895	775	2907
r_{bl}	4.6 μm	5.0 μm	5.7 μm
a^0	6.8 μm	11.2 μm	7.8 μm
$J_{\text{median}}/(2\pi)$	2.8 MHz	1.1 MHz	0.5 MHz

Table I. Experimental parameters. t_{exc} specifies the duration of the optical excitation to the Rydberg state, the Rydberg volume is specified by the radii ($1/e^2$) of the Rydberg cloud, N_{Ryd} denotes the derived Rydberg number, r_{bl} the blockade radius and J_{median} the obtained median nearest-neighbor interaction.

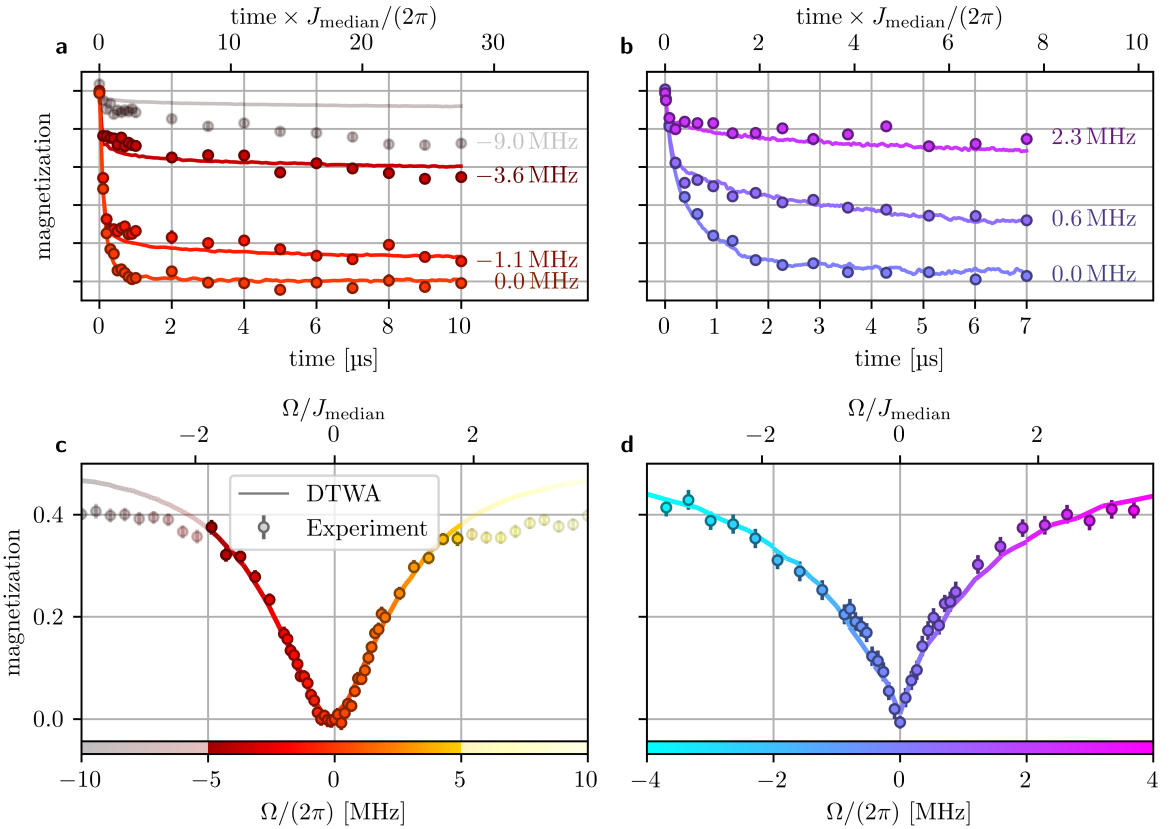


Figure 3. **Simulation of the experimental data shown in the main text with DTWA simulations** Time evolution of the magnetization in case of weak (a) and strong (b) disorder. The dependence of the late-time magnetization are shown in c (weak disorder) and a (strong disorder). The experimental parameters are shown in Table I.

$\{| \rightarrow \rightarrow \rangle, | \rightarrow \leftarrow \rangle, | \leftarrow \rightarrow \rangle, | \leftarrow \leftarrow \rangle\}$, Hamiltonian (1) reads

$$\hat{H}_{\text{pair}} = 4J \left(\Delta \hat{s}_x^{(1)} \hat{s}_x^{(2)} + \hat{s}_y^{(1)} \hat{s}_y^{(2)} + \hat{s}_z^{(1)} \hat{s}_z^{(2)} \right) + \Omega \sum_{i=1}^2 \hat{s}_z^{(i)} \quad (\text{C1})$$

$$= \begin{pmatrix} J + \Omega & 0 & 0 & J(\Delta - 1) \\ 0 & -J & J(\Delta + 1) & 0 \\ 0 & J(\Delta + 1) & -J & 0 \\ J(\Delta - 1) & 0 & 0 & J - \Omega \end{pmatrix} \quad (\text{C2})$$

where we defined $J = J_{12}/4$. Out of the four eigenstates of this Hamiltonian, only two have non-zero overlap with the initial state $|\rightarrow \rightarrow \rangle$ (see table II). Therefore, each interacting pair can be seen as an effective two-level system on its own, with a modified interaction between these "renormalized" spins. This ansatz of diagonalizing the strongest interacting pairs first can be seen as a first step in a real-space strong-disorder renormal-

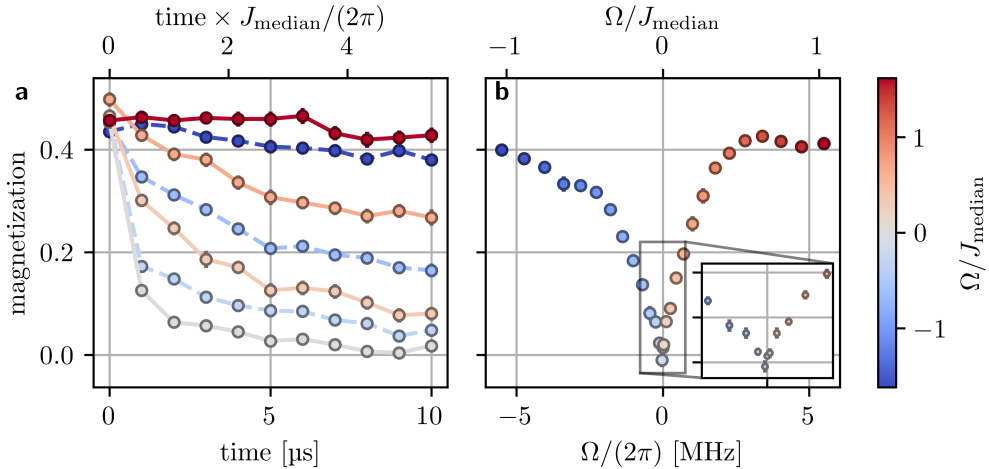


Figure 4. Experimental data for a quantum spin system with Van der Waals interactions. **a**, Measured spin relaxation dynamics for varying transverse field strengths ranging from $\Omega/(2\pi) = -5.5$ MHz (dark blue) to 5.5 MHz (dark red). **b**, Magnetization after 10 μ s as a function of field strength Ω (see Table I for a summary of the experimental parameters). The inset shows a zoom into the data for small values of Ω .

ization group treatment [55–58]. Here, we do not aim to proceed further in this renormalization scheme, but instead, we use the basis of eigenstates of strongly interacting pairs to derive an intuitive understanding of the physics within mean-field theory.

Diagonal ensemble: In contrast to a single spin which does not show any dynamics, a strongly interacting pair features oscillatory dynamics. Using the definition given in the main text, we can calculate the diagonal ensemble expectation value for single pair:

$$\overline{\langle \hat{S}_x \rangle_{\text{pair}}} = \frac{\Omega^2}{2(\Omega^2 + j^2)} \quad (\text{C3})$$

where we introduced $j = J(\Delta - 1)$. It should be noted that this diagonal ensemble does not describe the steady-state but rather the time average over the oscillations. The magnetization expectation value predicted by the diagonal ensemble of a single interacting pair represents an inverted Lorentz profile with width $j/2$, which features a quadratic dependence on Ω around zero (see Figure 5 **a**). However, if we average over multiple pairs with different interaction strengths j , the diagonal ensemble value becomes more meaningful since we can assume that the different oscillation frequencies dephase. Also, the behavior of the magnetization changes: For example, assuming a uniform distribution

of $j \in [0, \Delta_j]^3$, we obtain

$$\frac{1}{\Delta_j} \int_0^{\Delta_j} \overline{\langle \hat{S}_x \rangle_{\text{pair}}} dj = \frac{\Omega}{2\Delta_j} \arctan\left(\frac{\Delta_j}{\Omega}\right) \quad (\text{C4})$$

which shows the non-analytic cusp feature at $\Omega = 0$ (see Figure 5 **b**). Close to the non-analytic point, the magnetization increases linearly with a slope $\frac{\pi}{4\Delta_j}$ inversely proportional to the width of the distribution of interaction strengths. Therefore, we can conclude that the non-analyticity is a direct consequence of disorder and the resulting broad distribution of nearest neighbor interaction strengths.

Canonical and generalized Gibbs ensemble: To calculate the properties of a system in thermal equilibrium, we evaluate the density matrix $\hat{\rho}_{\text{canonical}}$ of the canonical ensemble

$$\hat{\rho}_{\text{canonical}} = \frac{\sum_i e^{-\beta E_i} |\psi_i\rangle \langle \psi_i|}{\sum_i e^{-\beta E_i}} \quad (\text{C5})$$

where β is the inverse temperature of the system. For a single pair of spins, this ensemble can be used to calculate the expectation value of the magnetization:

$$\langle \hat{s}_x^p \rangle_{\text{canonical}}(\beta) = -\frac{h}{2\sqrt{h^2 + j^2}} \tanh\left(\sqrt{h^2 + j^2}\beta\right) \quad (\text{C6})$$

³ For distributions like $j \in [j_{\min}, \Delta_j]$ that do not feature arbitrary small interaction strengths, a small region of approximate size $\Omega < |\frac{j_{\min}}{\Delta_j}|$ exists where magnetization is a smooth function of external field.

Eigenvalue E_i	Eigenvector $ \psi_i\rangle$	Occupation $ \langle\psi_0 \psi_i\rangle ^2$	Magnetization $\langle \hat{S}_x \rangle_{\psi_i}$
$J\Delta$	$\frac{1}{\sqrt{2}}(\rightarrow\leftarrow\rangle + \leftarrow\rightarrow\rangle)$	0	0
$-J(2 + \Delta)$	$\frac{1}{\sqrt{2}}(\rightarrow\leftarrow\rangle - \leftarrow\rightarrow\rangle)$	0	0
$J - \sqrt{\Omega^2 + J^2(\Delta - 1)^2}$	$\sqrt{\frac{1}{2} - \frac{\Omega}{2\sqrt{\Omega^2 + j^2}}} \rightarrow\rightarrow\rangle + \sqrt{\frac{1}{2} + \frac{\Omega}{2\sqrt{\Omega^2 + j^2}}} \leftarrow\leftarrow\rangle$	$\frac{1}{2} - \frac{\Omega}{2\sqrt{\Omega^2 + j^2}}$	$-\frac{\Omega}{2\sqrt{\Omega^2 + j^2}}$
$J + \sqrt{\Omega^2 + J^2(\Delta - 1)^2}$	$\sqrt{\frac{1}{2} + \frac{\Omega}{2\sqrt{\Omega^2 + j^2}}} \rightarrow\rightarrow\rangle + \sqrt{\frac{1}{2} - \frac{\Omega}{2\sqrt{\Omega^2 + j^2}}} \leftarrow\leftarrow\rangle$	$\frac{1}{2} + \frac{\Omega}{2\sqrt{\Omega^2 + j^2}}$	$\frac{\Omega}{2\sqrt{\Omega^2 + j^2}}$

Table II. Properties of the four eigenstates of a single interacting spin pair. To simplify notation, we introduced $j = J(\Delta - 1)$.

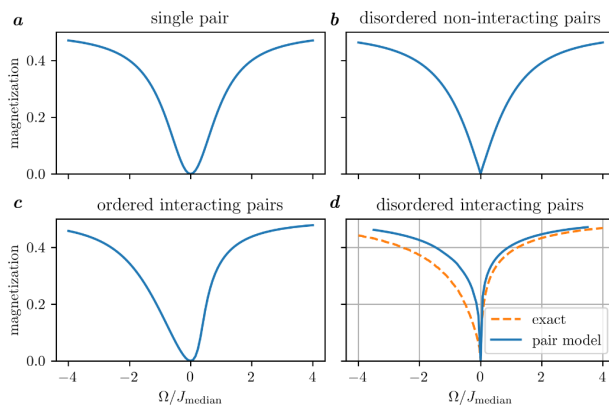


Figure 5. The diagonal ensemble expectation value of the magnetization as a function of applied external field Ω for a single pair (a), a disorder average of single pairs with interaction chosen randomly in the interval $J \in [0, 1]$ (b), a system of identical pairs that interact with mean field interaction $J_{\text{inter}} = 1.5 * J$ (c), and a realistic random distribution with power-law interactions, as described in the text (d). For the latter, the dashed orange line shows the full quantum mechanical solution obtained by exact diagonalization for the same system.

In a system coupled to a thermal bath, the inverse temperature β would be determined by the temperature of the bath. However, in a closed system, the energy is conserved, which fixes the inverse temperature such that the energy of the canonical ensemble equals the energy of the initial state. In a generalized Gibbs ensemble, where the energy of each pair of spins is conserved, this leads to the equation

$$\langle \hat{H}_{\text{pair}} \rangle_{\text{canonical}}(\beta) \stackrel{!}{=} \langle \hat{H}_{\text{pair}} \rangle_{|\psi_0\rangle} \quad (\text{C7})$$

$$\Leftrightarrow -\sqrt{h^2 + j^2} \tanh\left(\sqrt{h^2 + j^2}\beta\right) + J \stackrel{!}{=} h + J \quad (\text{C8})$$

This equation can be solved analytically and results in exactly the diagonal ensemble from Eq. C3. This result

is not surprising considering the following argument: Only two out of four eigenstates of the pair of spins can be occupied due to symmetry arguments. Thus, any mixture of these states is completely determined by only two variables. Out of those, one is fixed by normalization and the other by energy, and all ensembles are strictly equivalent.

In the generalized Gibbs ensemble, we have considered an ensemble of perfectly isolated pairs, where each pair i has equilibrated to a different inverse temperature β_i . A first approximation to estimate the magnetization of a thermalized ensemble of disordered spins can be obtained by assuming weak interactions between each pair of spins that do not affect the eigenstates but lead to thermalization such that every spin relaxes to a canonical ensemble with one global $\beta = \beta_i$ for all pairs i . In this case, eq. (C7) has to be solved for β for the sum of all pairs:

$$\sum_i \langle \hat{H}_{\text{pair},i} \rangle_{\text{canonical}}(\beta) \stackrel{!}{=} \sum_i \langle \hat{H}_{\text{pair},i} \rangle_{|\psi_0\rangle}. \quad (\text{C9})$$

For this value of β , the canonical ensemble expectation value for the average magnetization can be calculated using equation (C5).

Self-consistent mean-field equations: To obtain an even more realistic model and to understand additional features like the asymmetry of the cusp, we add a mean-field interaction between pairs. For this purpose, we replace the external field with an effective mean-field acting on spin i :

$$\Omega \rightarrow \Omega_i = \Omega + \sum_j J_{ij}^{\text{inter}} \langle \hat{s}_x^{(j)} \rangle \quad (\text{C10})$$

As a first example, we may consider a periodic chain of equally spaced pairs where all pairs are identical and the mean-field shift arising from interactions between the pairs is J^{inter} . In this case, the diagonal ensemble expectation value can be calculated by solving the self-

consistent equation

$$\overline{\langle \hat{S}_x \rangle} = \frac{1}{2} \frac{\left(\Omega + J^{\text{inter}} \overline{\langle \hat{S}_x \rangle} \right)^2}{\left(\Omega + J^{\text{inter}} \overline{\langle \hat{S}_x \rangle} \right)^2 + j^2}. \quad (\text{C11})$$

Since the right-hand side of the equation only contains squares, the magnetization is still positive or zero. Therefore, for positive external fields Ω , the effective field is larger than the external field ($\Omega_i \geq \Omega$), leading to an enhanced spin locking effect. Consequently, mean-field leads to an increased magnetization compared to the case of independent pairs. For negative Ω , the external field is anti-aligned with the mean-field, and the resulting magnetization is decreased. Thus, the dependence of the magnetization as a function of field strength is asymmetric (see Figure 5 c). In conclusion, we can attribute the asymmetry to mean-field interaction between different pairs.

In order to model the disordered spin system realized experimentally, we apply the pair model to an ensemble of spins with randomly chosen positions. We cluster the spins i into pairs p in such a way that the sum over all pair distances is minimized. Naturally, the interaction

j_p of a pair p consisting of spins i and j is given by the interaction strength between the spins. The interaction strength J_{pq}^{inter} between pair p and q can be obtained from the strongest interaction J_{ij} where spin i is in pair p and j in q respectively. Now, we solve the system of self-consistent equations

$$\overline{\langle \hat{s}_x^p \rangle} = \frac{1}{2} \frac{\left(\Omega + \sum_q (J_{pq}^{\text{inter}} \overline{\langle \hat{s}_x^q \rangle}) \right)^2}{\left(\Omega + \sum_q (J_{pq}^{\text{inter}} \overline{\langle \hat{s}_x^q \rangle}) \right)^2 + j_p^2}. \quad (\text{C12})$$

The resulting magnetization curve obtained after disorder averaging (see blue line in Figure 5 d) closely resembles the exact diagonal ensemble prediction (orange line). Importantly, all qualitative features are captured, including a positive magnetization which is asymmetric with respect to the external field and shows a sharp cusp at zero field. The remaining discrepancy between the pair model and the exact solution, in particular the stronger asymmetry of the exact solution, can be attributed to clusters of spins containing more than two atoms where quantum fluctuations decrease the magnetization even further than predicted by the pair mean-field model.

-
- [1] P. Reimann, Physical Review Letters **101**, 190403 (2008).
- [2] J. M. Deutsch, Physical Review A **43**, 2046 (1991).
- [3] M. Srednicki, Journal of Physics A , 14 (1999).
- [4] M. Srednicki, Physical Review E **50**, 888 (1994).
- [5] M. Ueda, Nature Reviews Physics **2**, 669 (2020).
- [6] P. Peng, C. Yin, X. Huang, C. Ramanathan, and P. Cappellaro, Nature Physics **17**, 444 (2021).
- [7] M. Prüfer, P. Kunkel, H. Strobel, S. Lannig, D. Linemann, C.-M. Schmied, J. Berges, T. Gasenzer, and M. K. Oberthaler, Nature **563**, 217 (2018).
- [8] A. Rubio-Abadal, M. Ippoliti, S. Hollerith, D. Wei, J. Rui, S. Sondhi, V. Khemani, C. Gross, and I. Bloch, Physical Review X **10**, 021044 (2020).
- [9] C. Eigen, J. A. P. Glidden, R. Lopes, E. A. Cornell, R. P. Smith, and Z. Hadzibabic, Nature **563**, 221 (2018).
- [10] L. S. Martin, H. Zhou, N. T. Leitao, N. Maskara, O. Makarova, H. Gao, Q.-Z. Zhu, M. Park, M. Tyler, H. Park, S. Choi, and M. D. Lukin, Physical Review Letters **130**, 210403 (2023).
- [11] T. Langen, T. Gasenzer, and J. Schmiedmayer, Journal of Statistical Mechanics: Theory and Experiment **2016**, 064009 (2016).
- [12] D. M. Basko, I. L. Aleiner, and B. L. Altshuler, Annals of Physics **321**, 1126 (2006).
- [13] J. Z. Imbrie, Journal of Statistical Physics **163**, 998 (2016).
- [14] M. Serbyn, Z. Papić, and D. A. Abanin, Physical Review Letters **111**, 127201 (2013).
- [15] D. A. Huse, R. Nandkishore, and V. Oganesyan, Physical Review B **90**, 174202 (2014).
- [16] S. S. Kondov, W. R. McGehee, W. Xu, and B. DeMarco, Physical Review Letters **114**, 083002 (2015).
- [17] M. Schreiber, S. S. Hodgman, P. Bordia, H. P. Lüschen, M. H. Fischer, R. Vosk, E. Altman, U. Schneider, and I. Bloch, Science **349**, 842 (2015).
- [18] P. Bordia, H. P. Lüschen, S. S. Hodgman, M. Schreiber, I. Bloch, and U. Schneider, Physical Review Letters **116**, 140401 (2016).
- [19] J.-y. Choi, S. Hild, J. Zeiher, P. Schauß, A. Rubio-Abadal, T. Yefsah, V. Khemani, D. A. Huse, I. Bloch, and C. Gross, Science **352**, 1547 (2016).
- [20] A. M. Kaufman, M. E. Tai, A. Lukin, M. Rispoli, R. Schittko, P. M. Preiss, and M. Greiner, Science **353**, 794 (2016).
- [21] A. Lukin, M. Rispoli, R. Schittko, M. E. Tai, A. M. Kaufman, S. Choi, V. Khemani, J. Léonard, and M. Greiner, Science **364**, 256 (2019).
- [22] L. Wadleigh, N. Kowalski, and B. DeMarco, “Interacting Stark localization dynamics in a three-dimensional lattice Bose gas,” (2022), arXiv:2211.12336 [cond-mat].
- [23] J. Léonard, S. Kim, M. Rispoli, A. Lukin, R. Schittko, J. Kwan, E. Demler, D. Sels, and M. Greiner, “Signatures of bath-induced quantum avalanches in a many-body-localized system,” (2022), arXiv:2012.15270 [cond-mat, physics:quant-ph].
- [24] J. Smith, A. Lee, P. Richerme, B. Neyenhuis, P. W. Hess, P. Hauke, M. Heyl, D. A. Huse, and C. Monroe, Nature Physics **12**, 907 (2016).

- [25] G. Kucsko, S. Choi, J. Choi, P. C. Maurer, H. Zhou, R. Landig, H. Sumiya, S. Onoda, J. Isoya, F. Jelezko, E. Demler, N. Y. Yao, and M. D. Lukin, Physical Review Letters **121**, 023601 (2018).
- [26] J. Šuntajs, J. Bonča, T. Prosen, and L. Vidmar, Physical Review B **102**, 064207 (2020).
- [27] J. Šuntajs, J. Bonča, T. Prosen, and L. Vidmar, Physical Review E **102**, 062144 (2020).
- [28] P. Sierant and J. Zakrzewski, Physical Review B **105**, 224203 (2022).
- [29] I. Bloch, J. Dalibard, and W. Zwerger, Reviews of Modern Physics **80**, 885 (2008).
- [30] T. Esslinger, Annual Review of Condensed Matter Physics **1**, 129 (2010).
- [31] I. Bloch, J. Dalibard, and S. Nascimbène, Nature Physics **8**, 267 (2012).
- [32] C. Gross and I. Bloch, Science **357**, 995 (2017).
- [33] A. Browaeys and T. Lahaye, Nature Physics **16**, 132 (2020).
- [34] A. Browaeys and T. Lahaye, Nature Physics **16**, 132 (2020).
- [35] A. Signoles, T. Franz, R. F. Alves, M. Gärttner, S. Whitlock, G. Zürn, and M. Weidemüller, Physical Review X **11**, 011011 (2021).
- [36] S. Geier, N. Thaicharoen, C. Hainaut, T. Franz, A. Salzinger, A. Tebben, D. Grimshndl, G. Zürn, and M. Weidemüller, Science **374**, 1149 (2021).
- [37] A. Signoles, T. Franz, R. Ferracini Alves, M. Gärttner, S. Whitlock, G. Zürn, and M. Weidemüller, Physical Review X **11**, 011011 (2021).
- [38] P. Schultzen, T. Franz, S. Geier, A. Salzinger, A. Tebben, C. Hainaut, G. Zürn, M. Weidemüller, and M. Gärttner, Physical Review B **105**, L020201 (2022).
- [39] P. Schultzen, T. Franz, C. Hainaut, S. Geier, A. Salzinger, A. Tebben, G. Zürn, M. Gärttner, and M. Weidemüller, Physical Review B **105**, L100201 (2022).
- [40] H. Günther, *NMR Spectroscopy: Basic Principles, Concepts and Applications in Chemistry*, third, completely revised and updated edition ed. (Wiley-VCH, Weinheim, 2013).
- [41] R. Vosk and E. Altman, Physical Review Letters **110**, 067204 (2013).
- [42] D. Pekker, G. Refael, E. Altman, E. Demler, and V. Oganesyan, Physical Review X **4**, 011052 (2014).
- [43] R. Vasseur, A. C. Potter, and S. A. Parameswaran, Physical Review Letters **114**, 217201 (2015).
- [44] R. Vasseur, A. J. Friedman, S. A. Parameswaran, and A. C. Potter, Physical Review B **93**, 134207 (2016).
- [45] A. Braemer, T. Franz, M. Weidemüller, and M. Gärttner, Physical Review B **106**, 134212 (2022).
- [46] A. Morningstar, L. Colmenarez, V. Khemani, D. J. Luitz, and D. A. Huse, Physical Review B **105**, 174205 (2022).
- [47] D. M. Long, P. J. D. Crowley, V. Khemani, and A. Chandran, Physical Review Letters **131**, 106301 (2023).
- [48] A. Rajak, S. Suzuki, A. Dutta, and B. K. Chakrabarti, Philosophical Transactions of the Royal Society A: Mathematical, Physical and Engineering Sciences **381**, 20210417 (2022).
- [49] M. Bernaschi, I. G.-A. Pemartín, V. Martín-Mayor, and G. Parisi, “The Quantum Transition of the Two-Dimensional Ising Spin Glass: A Tale of Two Gaps,” (2023).
- [50] M. Ferreira-Cao, V. Gavryusev, T. Franz, R. F. Alves, A. Signoles, G. Zürn, and M. Weidemüller, Journal of Physics B: Atomic, Molecular and Optical Physics **53**, 084004 (2020).
- [51] H. Weimer, R. Löw, T. Pfau, and H. P. Büchler, Physical Review Letters **101**, 250601 (2008).
- [52] M. Gärttner, K. P. Heeg, T. Gasenzer, and J. Evers, Physical Review A **86**, 033422 (2012).
- [53] A. P. Orioli, A. Signoles, H. Wildhagen, G. Günter, J. Berges, S. Whitlock, and M. Weidemüller, Physical Review Letters **120**, 063601 (2018).
- [54] J. Schachenmayer, A. Pikovski, and A. M. Rey, Physical Review X **5**, 011022 (2015).
- [55] D. Pekker, G. Refael, E. Altman, E. Demler, and V. Oganesyan, Physical Review X **4**, 011052 (2014).
- [56] R. Vasseur, A. J. Friedman, S. A. Parameswaran, and A. C. Potter, Physical Review B **93**, 134207 (2016).
- [57] R. Vasseur, A. C. Potter, and S. A. Parameswaran, Physical Review Letters **114**, 217201 (2015).
- [58] R. Vosk and E. Altman, Physical Review Letters **110**, 067204 (2013).

4.2.1 Origin of the cusp-like signature

To derive the qualitative behavior of the steady-state magnetization $\langle M(\Omega) \rangle$ with respect to external field Ω , we use a simple two-component model where each spin is either fully polarized or fully demagnetized. We assume that a spin's final state depends solely on the ratio of the strongest coupling J towards another spin and the strength of the external field Ω . If the field dominates, i.e. $|\Omega| > J$, the spin stays polarized as it is locked by the field. Conversely, if the coupling dominates, i.e. $|\Omega| < J$, then the interactions lead to depolarization and the spin loses its magnetization. Thus, in this simplified model, the only quantity determining the steady-state magnetization is the distribution of relevant couplings $P(J)$:

$$\langle M(\Omega) \rangle = \frac{1}{2} \int_0^{|\Omega|} dJ P(J) \quad (4.1)$$

In the regime of weak disorder, it only natural to assume that the most relevant coupling for a spin is given by its strongest coupling, i.e. the coupling to its nearest neighbor. Thus, at weak disorder, we want to use the nearest-neighbor coupling distribution $P_{NN}(J)$. In contrast, at strong disorder, the pair model (cf. Chapter 2) results in a different distribution of pair couplings $P_{pair}(J)$. To compute these coupling distributions analytically, we go to the limit of vanishing blockade radius, i.e. $r_b \rightarrow 0$, and assume that spins are distributed randomly with uniform density ρ in d dimensional space. Fixing some spin, this gives us the number of spins in spherical shell of size r and width dr as

$$w_u(r) dr = d\rho \Omega_d r^{d-1} dr = d\lambda (\lambda r)^{d-1} dr \quad (4.2)$$

where $\Omega_d = \frac{\pi^{d/2}}{\Gamma(n/2+1)}$ is the volume of a d -dimensional unit sphere and $\lambda^d = \rho \Omega_d$ is akin to the inverse mean distance between spins. We use this setup to compute both the distribution of nearest neighbor coupling $P_{NN}(J)$ and the distribution of pair couplings $P_{pair}(J)$ in the following sections.

4.2.1.1 Nearest-neighbor coupling distribution $P_{NN}(J)$

The distribution of the nearest neighbor couplings can be found using a simple ansatz [124]. Consider some fixed spin and the density of spin $w(r)$ at distance r . Then, the probability $P_{NN}(r)$ of finding the nearest neighbor of that fixed spin at distance r should be proportional to both the probability of having a spin in that distance and the probability of having no closer neighbor. This gives us the following integral-equation

$$P_{NN}(r) = w(r) * \left(1 - \int_0^r dr' P_{NN}(r') \right) \quad (4.3)$$

which can be solved straight-forwardly by noting that it has the form $f' = -wf$ and using separation of variables. The solution reads:

$$P_{NN}(r) = w(r) \exp \left(- \int_0^r dr' w(r') \right) \quad . \quad (4.4)$$

Plugging in the distance distribution for uniform spin density $w_u(r)$ (cf. Equation 4.2) gives us a so-called Weibull distribution:

$$P_{NN}(r) = d\lambda^d r^{d-1} \exp(-\lambda^d r^d) \quad (4.5)$$

Finally, changing variables¹ from distance r to coupling $J = r^{-\alpha}$ yields the sought-after distribution of nearest-neighbor couplings

$$P_{NN}(J) = \beta \lambda^d J^{-\beta-1} \exp\left(-\lambda^d J^{-\beta}\right) \quad (4.6)$$

where $\beta = \frac{d}{\alpha}$.

4.2.1.2 Distribution of pair couplings $P_{pair}(J)$

We can derive the distribution of pair lengths in a similar fashion to Equation 4.3. The key insight about the difference between a nearest neighbor and the partner of a pair in the RSRG sense is that the two partners of the pair are in some sense each other's partner. In contrast, the "nearest neighbor" property does not need to be reflexive. Denoting the pair coupling distribution as $P_{pair}(J)$, we write down the respective integral equation, which is very similar to Equation 4.3, except that the second factor gets squared because *both spins* may not be part of a smaller pair:

$$P_{pair}(r) = w(r) * \left(1 - \int_0^r dr' P_{pair}(r')\right)^2 \quad (4.7)$$

This equation can be solved in the same way as Equation 4.3 and yields²:

$$P_{pair}(r) = \frac{w(r)}{\left(1 + \int_0^r dr' w(r')\right)^2} \quad (4.8)$$

Employing the distance distribution for uniform spin density $w_u(r)$ (cf. Equation 4.2) again gives us that the pair distances follow a *log-logistic distribution* for spins of uniform density:

$$P_{pair}(r) = \frac{d\lambda^d r^{d-1}}{(1 + \lambda^d r^d)^2} \quad (4.9)$$

Changing to distance r to coupling $J = r^{-\alpha}$ yields:

$$P_{pair}(J) = \frac{\beta \lambda^d J^{-\beta-1}}{(1 + \lambda^d J^{-\beta})^2} \quad (4.10)$$

4.2.1.3 Analytical steady-state magnetization

Having derived both the distribution of nearest-neighbor coupling $P_{NN}(J)$ (cf. Equation 4.6) and pair coupling distribution $P_{pair}(J)$ (cf. Equation 4.10), we can compute the steady-state magnetization of our simple model by using Equation 4.1:

$$M_{NN}(\Omega) = \frac{1}{2} \int_0^{|\Omega|} dJ P_{NN}(J) = \frac{1}{2} \exp(-\lambda^d |\Omega|^{-\beta}) \quad (4.11)$$

$$M_{pair}(\Omega) = \frac{1}{2} \int_0^{|\Omega|} dJ P_{pair}(J) = \frac{1}{2 + 2\lambda^d |\Omega|^{-\beta}} \quad (4.12)$$

¹ Note, the change of variables also needs to transform the measure, i.e. we transform $P(r)dr \rightarrow P(J)dJ$

² Equation 4.8 was derived by a different method for $d = 3$ by former Master student Péter Kaposvári in his Master thesis [125].

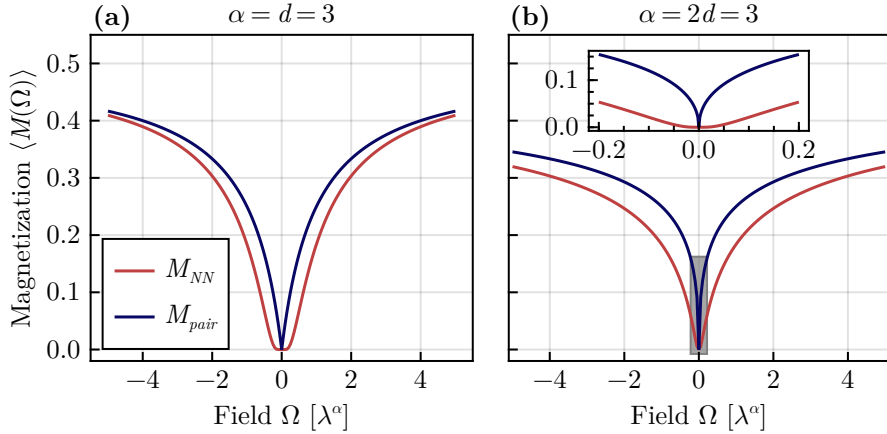


Figure 4.1: Steady-state magnetization curves of the two-component model using the same color scheme as Fig. 2 (d) and (e) of [D]. Parameters, α and d correspond to (a) Fig. 2 (b) Fig. 4. The inset shows a zoom around $\Omega = 0$ to highlight the qualitative difference between the curves.

The resulting curves, shown in Figure 4.1, show the same qualitative features as their counterparts in [D]. Thus, this simple model gives us insight in the key mechanism behind the qualitative change of the steady-state magnetization behavior: At weak field $|\Omega| \ll 1$, the magnetization is determined by the weakest interactions $J < |\Omega| \ll 1$ which stem from long distances $r \gg 1$. For nearest neighbors, the distribution of distances is suppressed exponentially $\propto \exp(-r^d)$ (cf. Equation 4.5), which creates the very smooth, round shape at weak field. Conversely, if the relevant lengths are given by the pairing procedure, the exponential suppression is weakened to an algebraic decay $\propto r^{-d-1}$. Intuitively, this is because while with increasing distance r the number of potential partners increases, it also becomes less likely that they are still available. This competition then leads to a much slower decay of the relevant lengths resulting in enhanced sensitivity to the external magnetic field.

4.2.1.4 Discussion

The two-component model developed here is of course much simpler than the mean-field used in [D] but we argue that it captures the essential physics nonetheless. The two main conceptual differences are: The mean field model considers the magnetization response of pairs, which is a Lorentzian [cf. Eq. (C3)], and additionally solves the equations self-consistently to capture the influence of a pairs magnetization on other pairs in the vicinity. The latter is responsible for the asymmetry of the ensemble's magnetization because the induced magnetization enhances (weakens) the effective magnetic field if external field and initial polarization are aligned (anti-aligned) to each other. This effect is showcased in Figure 4 in the appendix of [D]. However, apart from the asymmetry, the qualitative features remain unchanged.

To check the effect of the Lorentzian magnetization function, we can generalize the two-component model slightly at the cost of it being no longer analytically solvable. Conceptually, we replace the idea of "binary" spins, that are either locked by the field or dominated by interaction, by more general constituents that just follow some activation function, i.e. a function $m(\omega)$ that gives the resulting magnetization for a given ratio

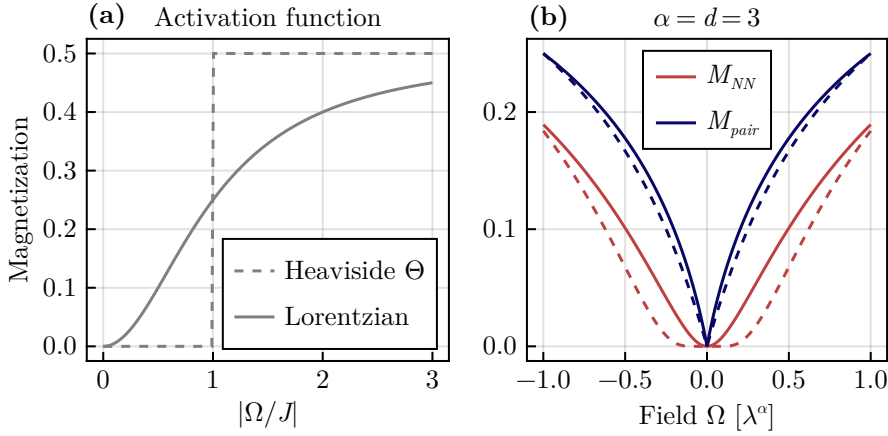


Figure 4.2: Comparison of the two-component model (dashed lines) with another model where the constituents' magnetization is given by a Lorentzian (solid lines). (a) steady-state magnetization of the constituent. (b) predictions of both model for $\alpha = d = 3$ [same parameters as Figure 4.1(a)].

$\omega = \Omega/J$ of field strength Ω and relevant coupling J . Then the total steady-state magnetization reads

$$\langle M(\Omega) \rangle = \frac{1}{2} \int_0^\infty dJ P(J) m\left(\frac{\Omega}{J}\right). \quad (4.13)$$

The two-component model is recovered with $m(\omega) = \Theta(\omega - 1)$ where Θ denotes the Heaviside function. For a pair, the magnetization follows a Lorentzian curve (cf. Equation C3 of [D]), which in this notation is given by $m_L(\omega) = \frac{\omega^2}{1+\omega^2}$. As Figure 4.2 shows, this also does not significantly alter the qualitative behavior at weak external field. Thus, we conclude that the observed qualitative change of the steady-state magnetization stems from a fundamental change in character of the distribution of relevant couplings.

CONCLUSION

In Part II of this thesis, we studied long-range Heisenberg models subject to spatial disorder through the lens of many-body localization. We found that this type of disorder indeed leads to a MBL-like regime in small systems, where the dynamics is governed by the presence of quasi-local, conserved quantities. These are made up of pairs of strongly interacting spins. This result, when combined with cTWA, leads to a very efficient and accurate method to calculate the time evolution of observables also in regimes of weak disorder. We showed two experimental signatures that we traced back to pairs being responsible for the dynamics and thus corroborated the model's applicability and predictive power in real-world scenarios.

Of course an experiment can only offer data on finite times and finite system sizes and thus the big question of the existence of MBL in power-law systems [34–36, 126] or even in general cannot be answered experimentally [27, 29, 39, 127]. However, we have shown that MBL can be a very useful perspective on the dynamics even in $d = \alpha = 3$, at least on experimentally accessible timescales. Since we have seen that the experiment can access both thermalizing regime and the localized regime (cf. [D]), we can use it to locate the critical disorder strength and perform finite size scaling. Thus, we can check experimentally both the presence of a *prethermal* MBL regime (cf. [39]) and the drift of the crossover. Usually in models with on-site disorder, the crossover shows significant drift (see e.g. [20]) which is absent in the model studied here (see Fig. 5 of [A]).

Due to experimental limitations, so far we only probed the global magnetization, which the pair model describes sufficiently accurate. In order to test its range of validity and shed more light on the properties of the system, it would be interesting to study more complex observables. A recent preprint [128] found that already simple 2-point correlation functions like $\langle S_x^{(i)} S_x^{(j)} \rangle$ show significantly different late time behavior than predicted by the pair model. Accessing these in the current experiment could perhaps be realized through measurement of the variance of $\langle \sum_i S_x^{(i)} \rangle$. Another direction for future measurements are *out-of-time-order correlators* (OTOC) written as

$$F(t) = \langle W^\dagger(t) V^\dagger W(t) V \rangle. \quad (5.1)$$

Here W and V are unitary operators that act locally. With this setup, the OTOC quantifies how much *information* has been exchanged between the locations W and V act on [129–132]. Thus, OTOCs carry allow for a detailed diagnostic of the thermalization process (or lack thereof). This appears to be true even for OTOCs of global observables [133]. However, measuring OTOCs is not an easy task since they generally require reversing the arrow of time for the system. While involved, this can be achieved robustly by changing the states that encode the spin as demonstrated recently [F]. Another proposal based on Floquet Hamiltonian engineering is also in preparation [G]. These methods also open the wide field of echo protocols, which find use e.g. in quantum enhanced sensing [134–136].

Addressing the question of the presence of MBL in systems with power-law interaction on the more theoretical side, one could extend RSRG-X to calculate higher order corrections of the pair model, which to our knowledge was not done so far. This extension owes to the fact that in power-law interacting systems the base Hamiltonian already contains

interactions among spins that belong to different pairs. As such, performing the iterative elimination that RSRG-X prescribes, implicitly assumes that the eliminated couplings also form a strong hierarchy which is generally not true. Thus, one should eliminate all pairs simultaneously to obtain effective interactions among the pairs. Preliminary results starting from an XX model ($\Delta = 0$) indicate that this effective model of pairs assumes XXZ form, similar to a calculation by Burin [36]. However, the simple interpretation of an ensemble of pairs is lost, as this effective model depends on the choice of the sectors of the pairs. This makes further study significantly harder since for N_p pairs there are 2^{N_p} slightly different copies of the system, similar to the problem with RSRG-t described in [43]. Interestingly, this picture likely can be reconciled with the iterative pairs criterion from [34] because the states described therein can be found in specific copies. This implies the presence of eigenstates which entangle arbitrarily distant sites. Conversely, choosing an entangled pair state for each pair results in very weak perturbative couplings signaling the existence of eigenstate close to product states between pairs. Consequently, the system contains both extended and localized states and it is hard to gauge what properties a typical state would show. To summarize, it seems that considering effective pair-pair interactions gives rise to a multi-faceted picture of a system with both long-range entangled and localized states. This contradicts the idea of the existence of a global set of conserved quantities and thus would rule out MBL for these systems in a technical sense. Instead, the conjectured form of the eigenstates features strong dynamical bottlenecks which are a hallmark of Hilbert space fragmentation [137–139], which was recently found in a closely related model [140].

A completely different route to understand the dynamics of disordered systems originates in the observation that a simple disorder-averaged expectation value can be seen as the expectation value of a single mixed state (overline denotes average w.r.t. disorder realization)

$$\overline{\langle \psi(t) | O | \psi(t) \rangle} = \text{Tr } O \overline{|\psi(t)\rangle\langle\psi(t)|} = \text{Tr } O \bar{\rho}(t). \quad (5.2)$$

The time evolution of this effective state $\bar{\rho}(t) = \Lambda_t[\rho_0]$ is governed by a dynamical map Λ_t , i.e. a super-operator mapping the initial density operator to the effective state at a later time. In general, this evolution is dissipative and non-markovian but it can be mapped to a Lindblad description under certain conditions [141–144]. Although spatial symmetries are usually broken in each shot, the averaging can lead to a restoration of these symmetries in the dynamical map Λ_t . This bears great potential as spatially disordered systems oftentimes do not have a canonical order of the constituents and thus enjoy permutation invariance on average! Thus, this approach has the power to dispel the curse of dimensionality and might allow for the (numerical) simulation of large systems far beyond the reach of current methods. In a forthcoming publication [H], we explore this idea and show that one can indeed exploit the average symmetry to find a Taylor expansion of a time-dependent effective Lindbladian¹ for simple disorder distributions. While the numerical results already look promising, more work is required to generalize this approach to more realistic distributions such as the couplings arising from power-law interactions between randomly located sites.

¹ A Lindbladian is defined by $\dot{\bar{\rho}} = \mathcal{L}_t[\bar{\rho}]$. If Λ_t^{-1} exists, then \mathcal{L}_t exists and reads: $\mathcal{L}_t = \dot{\Lambda}_t \circ \Lambda_t^{-1}$.

Part III

PERIODICALLY DRIVEN QUANTUM SYSTEMS WITH SPATIAL INHOMOGENEITY

6

CONCEPTS: PERIODICALLY DRIVEN SYSTEMS AND TIME CRYSTALS

The second major part of the thesis switches gear and focuses on the effects of spatial inhomogeneities in Floquet systems, i.e. systems that undergo periodic driving. While there has been a lot of attention in the literature for Floquet systems with disorder in the interactions already, most studies focus on the prototypical MBL model. Thus, the consequences of pair localization or influence of disorder in the drive remain largely unstudied. Before, we explore these in the following chapters, first we give a brief overview of the relevant concepts from the field of Floquet systems. For a more in-depth review, we refer the interested reader to e.g. [145]. Subsequently, we also cover the basics of thermalization in Floquet systems (see e.g. [60] for more context) and then briefly summarize the phenomenon of time crystals in particular [56, 146, 147].

6.1 INTRODUCTION TO FLOQUET SYSTEMS

Starting with the basics, a Floquet system is a system governed by a time-dependent Hamiltonian $H(t)$ with period T , i.e.

$$H(t) = H(T + t) \quad . \quad (6.1)$$

The time evolution operator evolving the initial state to some time t reads formally

$$U(t) = \mathcal{T} \exp(-i \int_0^t dt' H(t')) \quad (6.2)$$

where $\mathcal{T} \exp$ is the time-ordered exponential. Exploiting the periodicity, we can split the time evolution operator

$$U(t) = \mathcal{T} \exp(-i \int_0^t dt' H(t')) \quad (6.3)$$

$$= U(t - nT) \left[\mathcal{T} \exp(-i \int_0^T dt' H(t')) \right]^n \quad (6.4)$$

$$= U(t - nT)(U_F)^n \quad (6.5)$$

into n applications of an operator U_F , which advances the state a full cycle, and a *micromotion* part $U(t - nT)$ governing the dynamics within a cycle. Restricting observation to *stroboscopic* times where $t = nT$, we can understand the dynamics by considering only the time-independent operator

$$U_F = \mathcal{T} \exp(-i \int_0^T dt' H(t')) \equiv \exp(-iTH_F) \quad (6.6)$$

where H_F is an effective, time-independent Hamiltonian, called *Floquet Hamiltonian*. However, there are some difficulties with this approach: First of all, H_F is ill-defined because its eigenvalues are only defined mod $\frac{2\pi}{T}$. Hence, they are usually called *quasienergies*.

Secondly, H_F is generally infeasible to calculate exactly and might be grossly non-local. Nonetheless, in many cases one can find approximations to H_F that sufficiently describe the system's dynamics.

In the following, we restrict the discussion to a typical setup where $H(t)$ consists of two parts: A part where the system undergoes dynamics according to its interactions H_{int} and another part where the drive H_{drive} is active and no other internal dynamics takes place:

$$H(t) = \begin{cases} H_{int} & 0 \leq t < t_{int} \\ H_{drive} & t_{int} \leq t < T = t_{int} + t_d \end{cases} \quad (6.7)$$

$$\Rightarrow U_F = \exp(-it_d H_{drive}) \exp(-it_{int} H_{int}) \quad (6.8)$$

A simple way of approximating such a H_F is through the *Magnus expansion*, which is guaranteed to converge in the *high frequency limit*, i.e. if $t_{int}\|H_{int}\| + t_d\|H_{drive}\| \ll \pi$ [148]. In this simple case, it amounts to applying the well-known Baker-Campbell-Hausdorff formula to Equation 6.8. The first few terms are given by:

$$H_F = \sum_k H_F^{(k)} \quad (6.9)$$

$$H_F^{(1)} = \frac{1}{T} (t_{int} H_{int} + t_d H_{drive}) \quad (6.10)$$

$$H_F^{(2)} = \frac{t_d t_{int}}{2T} [H_{drive}, H_{int}] \quad (6.11)$$

Apart from being simple to calculate in most cases, the Magnus expansion is hermitian in every order and preserves the symmetries of the Floquet operator U_F . Additionally, for models featuring only two-body terms, the occurring operators only grow by a single site per order. This features make the Magnus expansion central to many approaches to Floquet systems.

In cases where one of the participating operators is not small, there exists another approach to approximate H_F with similar properties which is based on a replica resummation trick [149].

6.2 THERMALIZATION IN FLOQUET SYSTEMS

The Floquet Hamiltonian H_F allows to understand the dynamics of Floquet systems in the same terms as in closed quantum systems. So when viewed at stroboscopic times, the system thermalizes in accordance to H_F . However, when considering longer and longer times, higher and higher orders of the Magnus expansion become relevant leading to a slow drift of the equilibrium state. This phenomenon is called *Floquet prethermalization* [60]. The general physical intuition is that the drive pumps energy into the system heating it up until it reaches a featureless infinite temperature state [150, 151]. It has been shown that the timescale this heating occurs on grows exponentially with the driving frequency $\omega \propto T^{-1}$ [152, 153].

However, similar to closed systems, there are exceptions to this rule. For example, it has been shown that an interaction Hamiltonian featuring MBL can preserve the localization even under driving provided the driving frequency is sufficiently large [53, 154, 155]. This Floquet MBL is just one example of large variety of phenomena related to the late and intermediate time behavior of periodically driven systems.

6.3 TIME CRYSTALS

An interesting consequence of the absence of thermalization (e.g. due to Floquet MBL) is the existence of out-of-equilibrium phases of matter exhibiting new, exotic properties. One such feature is the existence of states that *spontaneously break time translation symmetry* which is ruled out in equilibrium phases [57] but can be observed in Floquet systems [54, 56, 147, 156]. Such a state is dubbed *time crystal* in analogy to regular crystals that spontaneously break spatial translation symmetry. A prototypical example of a system with time crystalline behavior [56, 146] is a driven MBL system, where the LIOMs $\tau_z^{(i)} \approx \sigma_z^{(i)}$ are close to σ_z and the drive approximately flips the system about its x -axis, i.e.

$$H_{int} = \sum_i h_i \tau_z^{(i)} + \sum_{ij} J_{ij} \tau_z^{(i)} \tau_z^{(j)} + \dots \quad (6.12)$$

$$H_d = \exp \left[i(1-\epsilon)\pi \sum_i \sigma_x^{(i)} \right]. \quad (6.13)$$

It is easy to see that at $\epsilon = 0$, all the $\sigma_z^{(i)}$ are quasi-conserved in magnitude but switch their sign every period because $\sigma_x \sigma_z \sigma_x = -\tau_z$. Thus, we can write

$$U_F = X \exp(-i \sum_{ij} J_{ij} \tau_z^{(i)} \tau_z^{(j)} + \dots) \quad (6.14)$$

where $X \propto \prod_i \sigma_x$ and the exponential contains only the terms commuting with X . This means any z -basis state is (close to) an eigenstate of U_F^2 but not of U_F , which is the realization of time translation symmetry-breaking [146]. The dynamics of such a state show a *subharmonic response* because they oscillate with an integer multiple of the system's driving frequency.

Crucially, this phenomenon is stable to perturbations! Leaving the exactly soluble point at $\epsilon = 0$, all of these features persist in a finite region of the parameter space. Thus, time crystals truly represent an out-of-equilibrium phase of matter. Apart from the prototypical model above, there are many different scenarios where they can arise [56, 147] and they have also been studied experimentally on a variety of platforms (e.g. [23, 157–159]).

7

STABILIZATION BY SPATIAL VARIATION OF THE DRIVE

In this chapter, we consider a clean, i.e. disorder-free, Ising spin chain with periodic driving and explore the influence of a spatially inhomogeneous drive on the dynamics. Remarkably, we find the time dynamics to be very sensitive to even small variations of said drive. In fact, limiting the spatial inhomogeneity of the drive to a single site, while all other sites experience the same driving, is already sufficient to manipulate the lifetime of the time crystalline signatures greatly. For initial states polarized in z -direction, this remarkable sensitivity to even minor deviations of the driving field is closely related to the spontaneous symmetry breaking of the groundstate of the Ising model. For generic states at high temperatures, the long-lived, period-doubled, oscillations are retained on the outer most spins only. We uncover the topological origin of this observation and exemplify it by slightly altering the systems geometry in way which removes the stabilization. These results persist in the presence of disorder or the addition of integrability breaking interactions. In summary, this work showcases a dramatic consequence of the long-range spatiotemporal order that is required to create a time crystal.

Metronome spin stabilizes time-crystalline dynamics

Niklas Euler^{1,2,*}, Adrian Braemer^{1,*}, Luca Benn,¹ and Martin Gärttner^{1,2,†}

¹Physikalisches Institut, Ruprecht-Karls-Universität Heidelberg, Im Neuenheimer Feld 226, 69120 Heidelberg, Germany

²Institut für Festkörpertheorie und Optik, Friedrich-Schiller-Universität Jena, Max-Wien-Platz 1, 07743 Jena, Germany



(Received 7 February 2024; revised 13 May 2024; accepted 14 May 2024; published 3 June 2024)

We investigate a disorder-free quantum Ising chain subject to a time-periodic drive that rotates each spin by an angle $\pi(1 - \epsilon_i)$. In case all spins experience the same deviation ϵ and the system is initialized in a fully polarized state, the dynamics is known to be time crystalline: the magnetization of the system exhibits period-doubled oscillations for timescales that grow exponentially with the length of the chain. In this work, we study the effect of a deviation ϵ that differs between spins. We find that reducing ϵ for a single spin drastically enhances the lifetime of spatiotemporal order, suggesting the name metronome spin. Employing perturbative arguments in an average Hamiltonian picture, we explain this observation for initial states with macroscopic bulk magnetization. Furthermore, in the case of random bit-string initial states, we report the enhancement of the lifetime of a topological edge mode, which can also be understood in the same picture. Finally, we discuss an altered geometry in which the metronome spin is not directly part of the chain, affecting the dynamics in different ways in the two scenarios considered. Our findings unveil the intricate dynamics that emerge in Floquet systems under the influence of a spatially varying drive, thereby uncovering new avenues for Floquet engineering.

DOI: [10.1103/PhysRevB.109.224301](https://doi.org/10.1103/PhysRevB.109.224301)

I. INTRODUCTION

For the longest time, stable physical phases of matter were thought to be a concept exclusive to equilibrium physics. However, with the pioneering work of Wilczek and Shapere [1,2], Watanabe and Oshikawa [3,4], and others, it became clear that out-of-equilibrium phases of matter are not only possible but also offer features beyond equilibrium phases [5,6]. One of the most prevalent categories of systems in which such phases have been demonstrated is Floquet setups, that is, periodically driven systems. Instead of heating up, they can display long-lived period-doubled spatiotemporal order with remarkable stability with respect to perturbations of the drive. Due to their discrete time-translation symmetry breaking, they have been dubbed Floquet time crystals or discrete time crystals (DTC) and have gained significant attention among the theoretical and experimental communities over the last decade [7,8].

Initially, many-body localization (MBL) was considered to be the main mechanism for stabilizing the long-lived dynamics [9–12]. However, over the years, a multitude of other processes have been shown to lead to time-crystalline behavior in different systems, including weakly broken symmetries [13], prethermalization [14–16], domain-wall confinement [17], among others [18–21]. Experimentally, time-crystalline dynamics has been observed on a variety of platforms, such as nitrogen vacancy centers [22–24], NMR systems [25–27], ultracold atoms [28,29], trapped ions [30], Rydberg atoms [31,32], and also superconducting qubits [33,34], to name a few. Most of the above time-crystal realizations demonstrate

long-lasting but finite spatiotemporal order, whereas some, e.g., the MBL DTC, lay claim to stability up to infinite times, even though this is controversially discussed by the community [16,35–38]. Numerical simulations have shown crystal lifetimes that exceed typical experimental timescales [5,33], thus it remains difficult to convincingly disprove infinitely long-lived order. Remarkably, two different realizations of absolutely stable [39] DTCs were recently reported [40,41]. These systems promise stability towards arbitrary perturbations, even if they break the discrete time-translation symmetry of the drive.

In most Floquet setups, drives are typically realized by periodically rotating all constituents by a fixed angle. One of the most striking features of time-crystalline order is the stability with respect to such a drive. The spatiotemporal structure is present not only at isolated points in parameter space (dictated by intrinsic symmetry of the interactions) but has also been observed for drives that systematically over- or undershoot the targeted rotation angles for the entire system by up to $\epsilon \lesssim 15\%$ in every drive period [30,33]. Contrary to the naive expectation, these errors do not accumulate and lead to rapid dephasing but are instead compensated for through the different stabilization mechanisms mentioned above. This defining characteristic of a DTC motivates the classification as an out-of-equilibrium phase of matter, as extended areas of stability can be identified with respect to the parameters of the system and drive, e.g., the interaction strength and the deviation of the driving angle [10,11]. Until recently [42], drives and perturbations have typically been considered to be spatially uniform, i.e., equal for all constituents of the system. The question of whether and how the stability of spatiotemporal order extends to regimes where parts of the system are driven at different values of ϵ remains largely unanswered. It is especially unclear whether this structure

*These authors contributed equally to this work.

†martin.gaerttner@uni-jena.de

is destabilized by a small subsystem driven at much higher values of ϵ , or whether a modest amount of particles driven at small ϵ can stabilize an otherwise unstable system.

To investigate the impact of the spatial dependence of the drive, we consider a disorder-free spin-1/2 chain with nearest-neighbor Ising interactions and periodic driving through numerical simulations. When initialized in a fully magnetized state, such a system's magnetization is known to exhibit period-doubled oscillations for a time growing exponentially with system size, which we will call lifetime [14,43–45]. Interestingly, by reducing the rotation angle deviation ϵ for a single spin of the chain, we find a drastic enhancement of the magnetization lifetime of the entire chain, as if the single spin was acting like a metronome that keeps the other spins on beat. We employ a time-averaged effective description, which allows us to explain the observed behavior with the help of symmetry arguments for the bulk of the chain.

Building on these results, we study how generic initial states behave in the presence of a metronome spin. Again, we find analogous lifetime enhancements in magnetization auto-correlators, however, only for the outermost spins stemming from the existence of a topological edge mode. Finally, we present a system geometry in which these two mechanisms can be clearly discerned. Our results offer new insights into how local perturbations in the chain can have a strong impact on the overall lifetime of large systems. This opens up new possibilities in the design and implementation of extended, (meta)stable phases of matter out of equilibrium, even in systems without disorder.

Following this introduction, we first give a more detailed description of the investigated system and the numerical methods used in Sec. II. The results for bulk and edge stabilization are presented in Sec. III and subsequently discussed in Sec. IV.

II. MODEL AND METHODS

We study the effects of spatially nonuniform Floquet driving through numerical simulation of a spin-1/2 chain. The Floquet sequence investigated in this work consists of two parts: in a first step, the spins interact through nearest-neighbor Ising couplings with open boundary conditions, as shown in Fig. 1(a). Second, the spins are subjected to unitary rotations by $\pi(1 - \epsilon_i)$, with i indicating the site index. We consider the case where the first spin is driven with $\epsilon_{i=1} = \epsilon'$ and all other spins with $\epsilon_{i>1} = \epsilon$ [Fig. 1(b)]. Thus, this configuration represents a uniformly driven chain with a local perturbation at one boundary site, obeying a spin-flip symmetry in the absence of z fields. One cycle of this time-periodic evolution is captured by the Hamiltonian

$$H = \begin{cases} H_{\text{int}} = \sum_{i=1}^{L-1} J_{i,i+1} s_z^i s_z^{i+1} + \sum_{i=1}^L h_i s_z^i, & 0 \leq t \leq t_1 \\ H_x = \sum_{i=1}^L (1 - \epsilon_i) s_x^i, & t_1 < t < t_1 + \pi =: T \end{cases}, \quad (1)$$

with $s_{\{x,y,z\}}^i = \sigma_{\{x,y,z\}}^i / 2$ being the single-spin operators. The evolution governed by this Hamiltonian induces (imperfect)

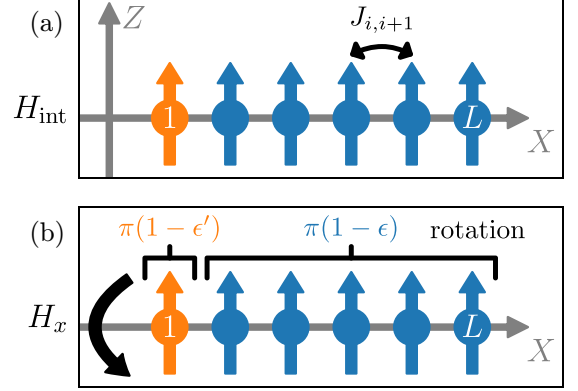


FIG. 1. An illustration of the two-step Floquet cycle of the one-dimensional (1D) system considered in this work. (a) The interaction phase of the cycle given by an Ising Hamiltonian with nearest-neighbor couplings. (b) The driving phase of the Floquet cycle, realized through single-spin s_x rotations. While the majority of the spins in the chain (here drawn in blue) is subjected to imperfect flips around the x axis given by $\pi(1 - \epsilon)$, one spin at site index $i = 1$ has a differing drive-angle deviation $\epsilon_{i=1} = \epsilon'$, resulting in $\pi(1 - \epsilon')$ rotations.

periodic flipping of the magnetization of the spin chain with period $2T$, which is twice the original period of the Hamiltonian. Here, we are especially interested in how decreasing the deviation of the rotation angle, ϵ' , for a single spin, which we call the metronome spin, affects the dynamics of spatially distant spins at late times. While we set $h_i = 0$ in the main text, we also study chains with random fields and disordered couplings in Appendix A and disorder-free chains with the metronome in the center, $\epsilon_{i=\frac{L+1}{2}} = \epsilon'$, in Appendix B.

The stroboscopic evolution of the system, that is, evaluated only once at the beginning of every cycle, is given by the Floquet evolution operator U_F , which propagates the system through one cycle of the Floquet sequence. To gain a better understanding of the stroboscopic dynamics, one would like to find a time-independent Floquet Hamiltonian H_F that generates the Floquet time evolution operator, such that

$$U_F = e^{-iH_x\pi} e^{-iH_{\text{int}}t_1} =: e^{-iH_F T}. \quad (2)$$

In most cases, there is no straightforward way to obtain H_F analytically, but one can expand H_F in the so-called Magnus series [46,47]. By construction, H_F is guaranteed to be Hermitian at all orders. We give the first two terms of the expansion,

$$H_F = H_F^{(0)} + H_F^{(1)} + \dots, \quad (3a)$$

$$H_F^{(0)} = \frac{1}{T} \int_0^T dt H(t), \quad (3b)$$

$$H_F^{(1)} = \frac{1}{2Ti} \int_0^T dt \int_0^t dt' [H(t), H(t')], \quad (3c)$$

with the first term $H_F^{(0)}$ often being referred to as the average Hamiltonian.

By computing the average over one period, one has to include the large $\pi(1 - \epsilon_i)s_x^i$ rotations in $H_F^{(0)}$,

$$H_{F,1P}^{(0)} = \frac{1}{t_1 + \pi} \left[t_1 \left(\sum_{i=1}^{L-1} J_{i,i+1} s_z^i s_z^{i+1} + \sum_{i=1}^L h_i s_z^i \right) + \pi \sum_{i=1}^L (1 - \epsilon_i) s_x^i \right], \quad (4)$$

which is detrimental to the convergence of the Magnus series [47]. As stated earlier, the magnetization-flipping dynamics is period doubled with respect to the time-dependent Hamiltonian. Therefore, if averaged over two periods, one not only mostly cancels the spin rotations but also averages out any random y/z fields. The newly obtained two-period averaged effective Hamiltonian has the form of a transverse-field Ising model (TFIM),

$$H_{F,2P}^{(0)} = \frac{1}{t_1 + \pi} \left(t_1 \sum_{i=1}^{L-1} J_{i,i+1} s_z^i s_z^{i+1} - \pi \sum_{i=1}^L \epsilon_i s_x^i \right), \quad (5)$$

hereafter only referred to as $H_F^{(0)}$. Alternatively, this Hamiltonian can also be derived by applying a toggling-frame transformation and subsequently taking the average over one cycle [8]. This effective description retains the spin-flip symmetry present in the original time-dependent model.

III. RESULTS

In this section, we investigate numerically the lifetimes of various multispin and single-spin observables at stroboscopic times. We employ exact evolution according to the full Floquet unitary given in Eq. (2) in addition to the effective evolution with an TFIM as derived in Eq. (5) for comparison. Here, we study systems with $L = 14$ spins and set $J_{ij} := J = 1$, $h_i = 0$, $\epsilon = 0.1$, $t_1 = 1$, and $\epsilon' = 10^{-5}$, if not otherwise specified.

A. Bulk lifetime enhancement for polarized initial states

We start by considering the dynamics of the global magnetization $\langle \sum_i \sigma_z^i \rangle / L$ for a polarized initial state $|\Psi_{\text{init}}\rangle = |\uparrow \dots \uparrow\rangle$, as shown on a logarithmic time axis in Fig. 2. Only even period numbers are probed, so that the underlying spin-flipping dynamics is hidden in the shown simulation. The magnetization shows an initial decline that lasts $\approx 10^2$ periods of the drive, largely independent of the presence of a metronome spin. Subsequently, for both with and without metronome spin we observe slow oscillations of the magnetization, which manifest themselves as extended plateaus of nonvanishing magnetization due to the log-linear axes choice in Fig. 2. The macroscopic magnetization indicates that large parts of the chain retain some of its initial polarization. The duration of this plateau is strongly dependent on the angle deviation of the metronome spin drive ϵ' and, in the case of an active metronome spin, lasts $\approx 10^7$ periods instead of $\approx 10^3$ periods without the metronome. The single-spin magnetization of the metronome spin, $\langle \sigma_z^1 \rangle$, as shown on the right axis of Fig. 2, qualitatively demonstrates the same behavior and has a lifetime similar to that of $\langle \sum_i \sigma_z^i \rangle / L$. For all data taken,

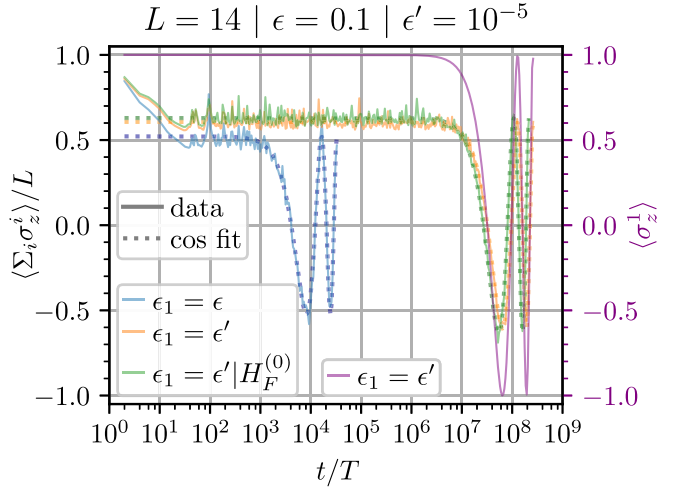


FIG. 2. The global z magnetization of the spin chain of length $L = 14$ starting in a fully polarized state subjected to different driving schemes. We show the exact stroboscopic dynamics of the chain at even period numbers with and without a metronome spin at one boundary site and the average Hamiltonian given in Eq. (5). Configurations that include a metronome spin display a lifetime enhancement of several orders of magnitude. All data are well described through numerical cosine fits. On the second axis (in purple font) the single-spin magnetization of the metronome spin itself is displayed. The lifetime of the magnetization of the metronome coincides with the lifetime of the total magnetization. For better visibility, only the first two oscillation cycles are plotted for each curve.

the evolution under the two-period average of the Floquet Hamiltonian $H_F^{(0)}$ is in satisfactory agreement with the full Floquet evolution (the green line shows this for the case with metronome spin), indicating that it is a sufficiently good description of the full stroboscopic evolution. Therefore, we can safely focus on the simpler time-independent $H_F^{(0)}$ to better understand the observed behavior.

Our chosen polarized initial state is the superposition of the two lowest-energy eigenstates of $H_F^{(0)}$ which, for $\epsilon \ll J$, are well approximated by the two parity states, $|\pm\rangle_L = (|\uparrow \dots \uparrow\rangle \pm |\downarrow \dots \downarrow\rangle)/\sqrt{2}$. At finite ϵ , states with domain-wall excitations are admixed (domain-wall dressing), leading to the observed initial fast decay. The energy gap between the two lowest-lying states is $\propto \epsilon^L$ in the uniform case by a perturbative argument, considering that all L spins are being flipped through off-resonant coupling to excited states. Thus, the gap vanishes in the limit $L \rightarrow \infty$, making the two states degenerate. In the case of $L = 14$ presented here, the gap is still finite and leads to slow Rabi oscillations of period T_R between the two polarized states, which explains the observed behavior. The data show good agreement with the numerical cosine fits $\propto \cos(2\pi t/T_R)$, as also plotted in Fig. 2, with $T_R(\epsilon_1 = \epsilon) = (1.641 \pm 0.006)10^4 T$ and $T_R(\epsilon_1 = \epsilon') = (1.281 \pm 0.004)10^8 T$. This difference in the length of the period of four orders of magnitude is expected in the average Hamiltonian picture, as the energy gap given above is inversely proportional to the Rabi-oscillation period $T_R \propto \epsilon^{-L}$. By endowment of one spin with reduced ϵ' , one obtains

$$T_R \propto \epsilon^{-L+1} (\epsilon')^{-1}, \quad (6)$$

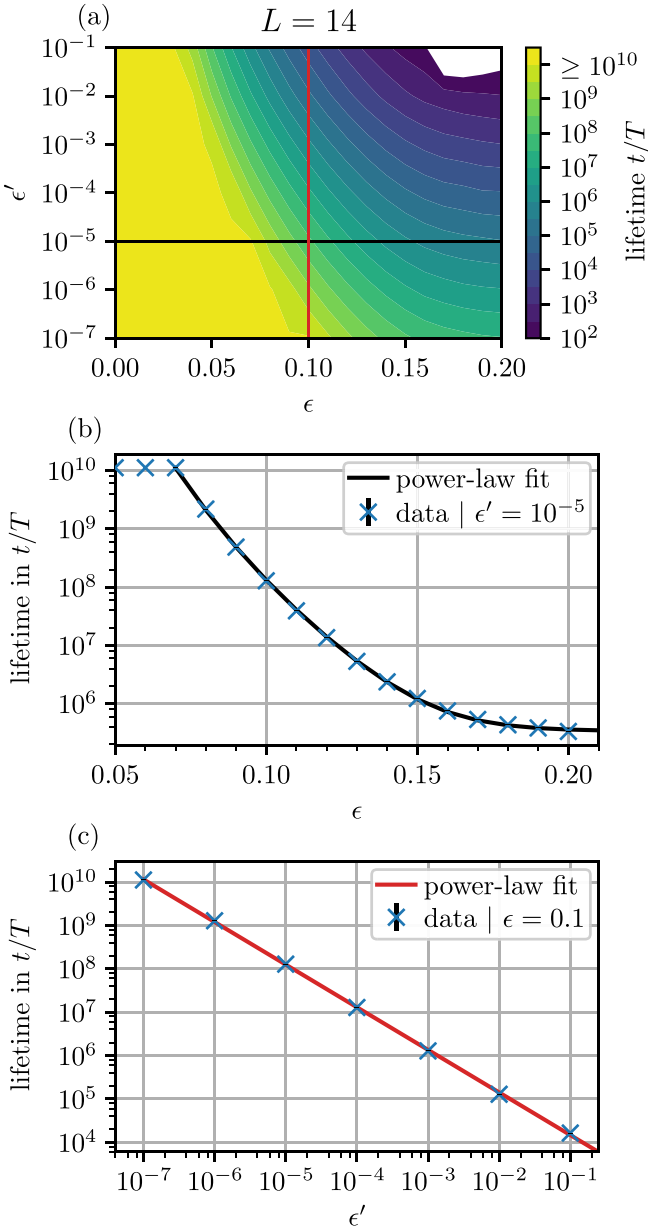


FIG. 3. The lifetime of the global z magnetization $\langle \sum_i \sigma_z^i \rangle / L$ for a range of drive deviation parameters ϵ and ϵ' including a metronome spin on one boundary site is shown in (a). (b) A horizontal cut through this plane at fixed $\epsilon' = 10^{-5}$. (c) A vertical cut at fixed $\epsilon = 0.1$, as indicated by the black and red lines in (a), respectively. All data points have been obtained through cosine fits, as shown in Fig. 2. Lifetimes above $t = 10^{10}T$ and below $t = 10^2T$ cannot be adequately resolved and are therefore exempt from the fit.

which yields the observed difference for the values used of $\epsilon = 0.1$ and $\epsilon' = 10^{-5}$.

Next, we systematically investigate the dependence of the global magnetization lifetime T_R on the deviations of the drive angle. For this, we repeat the procedure explained above for a number of combinations of the values of ϵ and ϵ' . The results are shown in Fig. 3(a), where we have probed a wide regime of drive parameters. At small ϵ , we observe lifetimes that exceed the resolved duration of 10^{10} Floquet cycles (yellow region). For fixed $\epsilon = 0.1$, we find that T_R is approximately inversely

proportional to ϵ' , $T_R \propto (\epsilon')^\alpha$ with $\alpha = -0.982 \pm 0.007$, as shown in Fig. 3(b), which is consistent with the reasoning presented in Eq. (6). For fixed $\epsilon' = 10^{-5}$, the recorded lifetimes follow a power law with offset, $T_R/T \approx a\epsilon^\beta + (3.35 \pm 0.09)10^5$, with $\beta = -12.29 \pm 0.03$. This value of β roughly agrees with the expectation $\beta = -13$ implied by Eq. (6). However, the observed convergence to a nonzero lifetime in the limit of large ϵ is not predicted by this perturbative picture [cf. Eq. (6)].

This behavior can be understood by taking $\epsilon' \rightarrow 0$. In this limit, the dynamics of the metronome spin effectively decouple from the bulk of the chain, since the metronome cannot leave the manifold of $\{|\uparrow\rangle, |\downarrow\rangle\}$, alternating between the two states in every Floquet cycle. One can now write down a Hamiltonian restricted to the bulk of the chain, where the coupling between the metronome and its neighboring spin, $s_z^1 s_z^2$, can be replaced by an effective field on the second spin of the chain,

$$H_{F,\text{bulk}}^{(0)} = \frac{1}{T} \left(\tilde{h} s_z^2 + t_1 \sum_{i=2}^{L-1} J_{i,i+1} s_z^i s_z^{i+1} - \pi \sum_{i=2}^L \epsilon_i s_x^i \right). \quad (7)$$

The new field term effectively breaks the spin-flip symmetry of the original Hamiltonian $H_F^{(0)}$ in the bulk and thus introduces an energy gap between the two polarized states. Therefore, the prepared polarized state is no longer the superposition of the two lowest-energy eigenstates but, rather, very close to the lowest eigenstate of $H_{F,\text{bulk}}^{(0)}$, resulting in a stable magnetization plateau. For cases where $\epsilon' \ll 1$ the metronome spin stays close to the $\{|\uparrow\rangle, |\downarrow\rangle\}$ manifold for extended periods of time before it and, subsequently, the rest of the chain dephases. However, in the large ϵ limit, large parts of the chain farther away from the metronome lose their magnetization much earlier due to domain-wall excitations. Still, since the metronome is largely decoupled in its dynamic from the rest of the chain, it retains nonvanishing magnetization even at late times, keeping the magnetization plateau alive, albeit at a lower value $\langle \sum_i \sigma_z^i \rangle / L \sim \mathcal{O}(1/L)$. This explains the observed saturation behavior in the lifetime dependence at large ϵ in Fig. 3(b).

B. Edge-mode enhancement for random bit-string initial states

Next, we investigate how the introduction of a metronome affects the dynamics of different initial states beyond the fully polarized case. To this end, we subject an ensemble of random bit-string states, i.e., states where every spin is either $|\uparrow\rangle$ or $|\downarrow\rangle$ chosen randomly, to the Floquet sequence given in Eq. (1). As the magnetization of these states vanishes on average, we instead consider local magnetization autocorrelators in the rotating frame, $\langle \sigma_z^i(0) \sigma_z^i(t/T) \rangle (-1)^{\lfloor t/T \rfloor} =: Z_i$. Three autocorrelators of selected spin sites, averaged over a set of 500 bit-string initial states, are shown in Fig. 4. The three panels show the autocorrelators of the metronome spin on the site $i = 1$ in Fig. 4(a), of a spin in the bulk of the chain on site $i = 8$ in Fig. 4(b), and at the other chain boundary on site $i = 14$ in Fig. 4(c).

First, the results for the autocorrelator of the metronome spin itself are in line with the results for the metronome single-spin magnetization in Fig. 2 (right axis). The

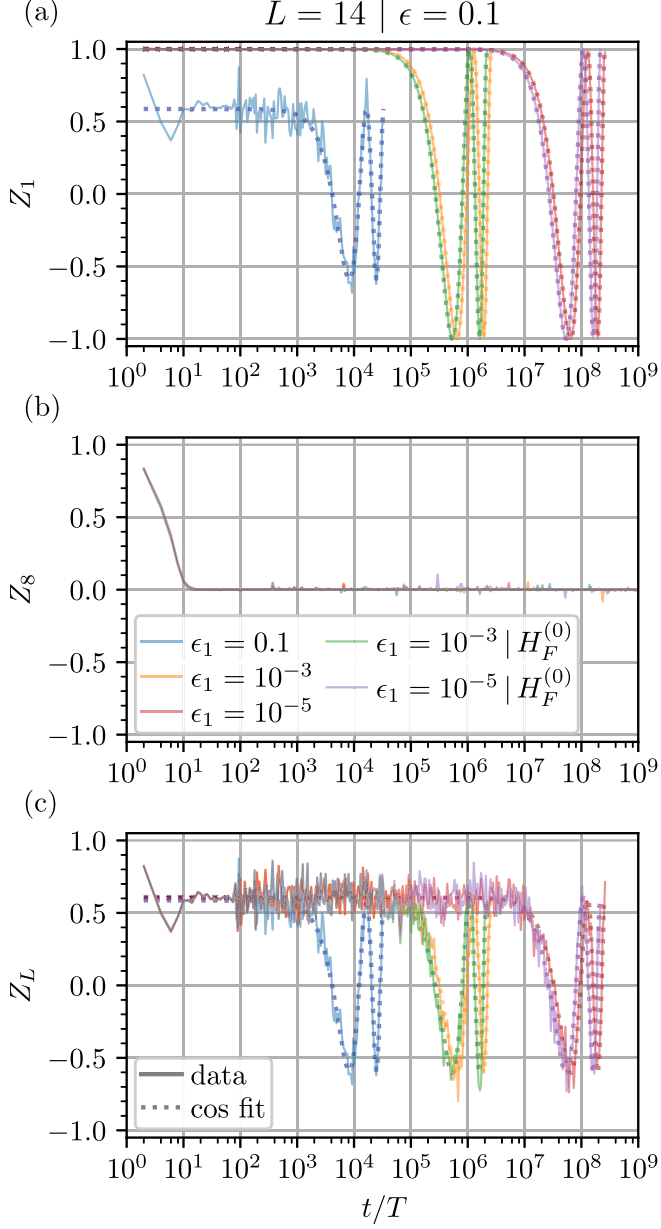


FIG. 4. The z -magnetization autocorrelators Z_i averaged over 500 random initial bit-string states for three different sites in a chain of $L = 14$ spins with open boundary conditions. (a) The autocorrelator for the metronome spin at the left boundary of the chain at site index $i = 1$. (b) The autocorrelator for a spin in the middle of the chain at site index $i = 8$. (c) The autocorrelator for the right boundary site with $i = 14$. We observe a long-lived edge mode with clear lifetime enhancement through the introduction of a metronome spin.

autocorrelator oscillates with full amplitude, $-1 \leq Z_1 \leq 1$, even at late times. Second, for sites in the bulk, we observe a rapid decline in the autocorrelator to zero, regardless of the value of ϵ' . Third, we see a plateau of the autocorrelator of the opposite boundary site analogous to the dynamics of the metronome site itself, as presented in Fig. 4(c). These characteristics are consistent with those of a strong π mode (SPM) [48]. This phase encompasses rapid bulk heating, but also robust period-doubled edge modes, and is closely related

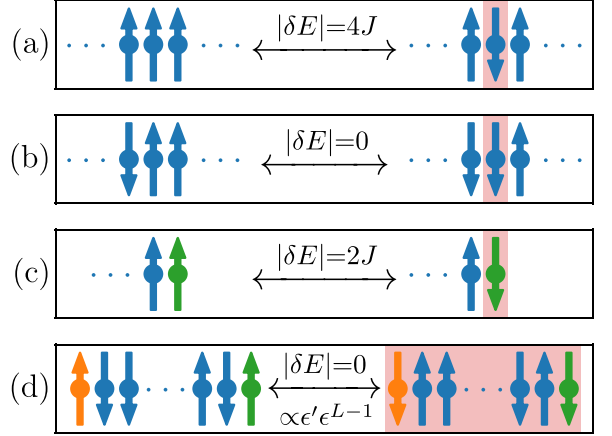


FIG. 5. A visual summary of the different spin-flipping processes and their associated energy differences. The spins in the bulk are colored blue, whereas the metronome is colored orange, and the right edge spin is colored green. Flipped spins are highlighted with a red background. (a) The creation or annihilation of two domain walls in the bulk of the chain. If the two adjacent spins are aligned, flipping the central spin results in an energy difference of $|\delta E| = 4J$. (b) The free propagation of a domain wall. If the two adjacent spins of a central spin are antialigned, flipping the central spin is energetically degenerate, i.e., $|\delta E| = 0$. Therefore, domain walls can propagate freely along the chain, utilizing this mechanism to iteratively flip the next spin at the domain wall. (c) The flipping of the edge spin. Flipping an edge spin always results in an energy difference of $|\delta E| = 2J$, half of the bulk value, since it is coupled to only one neighboring spin. Consequently, the edge spins cannot participate in the domain-wall dynamics shown in (b). The resulting coupling for the first three processes is $\propto \epsilon$. (d) The flipping of the entire chain. Flipping all spins together preserves the domain-wall structure of the chain and thus does not have an associated energy difference. This resonant process flips the edge spins at an effective rate $\propto \epsilon' \epsilon^{L-1}$.

to a symmetry-protected topological (SPT) phase [48–51]. This phase has recently been observed in the system under investigation [52]. Our data show a clear enhancement of the lifetime of the autocorrelator at the boundary sites, Z_L , through the introduction of the metronome spin, even though the two boundaries are separated by $L - 2 = 12$ spins coupled only through nearest-neighbor interactions. In particular, it is not necessary to apply the stabilized drive directly to one of the two edge modes. Additional simulations of a chain with a central metronome spin reveal a similar behavior with edge-mode lifetime enhancement. More details on this additional investigation can be found in the Appendix B.

This behavior can be understood by considering the spectral structure of the average Hamiltonian $H_F^{(0)}$, which we motivate in the following by a dynamical perspective. In the regime of small transverse field, the spectrum of the TFIM approximately decomposes into blocks of states with equal number of domain walls, i.e., adjacent spins pointing in opposite direction. The interaction term yields an energy difference of $2J$ per domain wall between these blocks. The action of the field term is twofold in this view: it causes spin flips, which, in the bulk of the chain, can either create or annihilate two adjacent domain walls [see Fig. 5(a)] or move an existing

domain wall by one site [see Fig. 5(b)]. The former changes the number of domain walls by ± 2 and is thus off resonant, i.e., comes at an energy cost. However, the latter leaves the total number of domain walls invariant and thus is resonant, i.e., domain walls can propagate freely within the bulk. At the edges of the chain, any spin flip always creates or annihilates a single domain wall. This observation is at the heart of the topological protection of the edge spins: Flipping an edge spin is the only process that changes the number of domain walls by an odd amount, and thus is always off resonant, unless both edge spins are flipped. This picture is analogous to previous work [53], in which the authors describe how Majorana fermions are protected on the boundary sites due to an approximate conservation law. One process that is always resonant and simultaneously flips both edge spins is flipping all spins [see Fig. 5(d)] as it corresponds to the global symmetry of the system. All other processes that alter the edge spins are strongly suppressed, because after diagonalizing the resonant domain-wall dynamics in the bulk, the resulting eigenstates do not feature any other resonant transitions. This leads to the observed oscillations with frequency $\propto \epsilon' \epsilon^{L-1}$ as in the case of the fully polarized initial state.

To better illustrate that last point, we translate the dynamical perspective above onto the static eigenstates of the average Hamiltonian $H_F^{(0)}$. Starting with the global parity symmetry, all eigenstates $|\phi_{\pm}\rangle \propto |\phi\rangle \pm |\bar{\phi}\rangle$ are also eigenstates of the parity operator and thus are an equal superposition of a state $|\phi\rangle$ and its spin-flipped counterpart $|\bar{\phi}\rangle$. For weak field $\epsilon \ll J$, the domain-wall number is approximately conserved, which means that each eigenstate predominantly consists of states from the same domain-wall-number sector with only minor admixtures from adjacent sectors. The observation from the dynamical viewpoint in the previous paragraph, namely that domain walls can propagate freely, here means that within the same domain-wall-number sector, the location of domain walls is ill-defined and the eigenstates are a superposition of all possible placements (see Fig. 6).

With this characterization of the eigenstates, the explanation of the observations made above is straightforward (see sketch Fig. 6). Taking a bit-string initial state and expanding it in the eigenstate basis, we find it to overlap with many different eigenstates from the same sector of the domain-wall-number operator. These eigenstates dephase rapidly $\propto \mathcal{O}(\epsilon)$ and lead to the decay of autocorrelators in the bulk, as seen in Fig. 4(b). By contrast, the edge spins can only change due to the dephasing between the parity sectors, which happens $\propto \mathcal{O}(\epsilon' \epsilon^{L-1})$. Since the splitting is identical for all components, this leads to the long coherent oscillations seen at late times in Fig. 4(a) and 4(c). The initial decay of the edge spin opposite to the metronome [see Fig. 4(c)] is caused by the admixture of wave-function components with a different number of domain walls. The observation that a nonzero number of domain walls will lead to rapid bulk dephasing and thus only a polarized initial state can show long-range order is in line with an earlier study [54]. There, the authors describe a prethermal phase, which they claim can generally only be realized in long-range interacting systems in one dimension. In short-range interacting systems, only the polarized (zero-temperature) initial state displays long-lived spatiotemporal order, as it is the only state with vanishing domain-wall number.

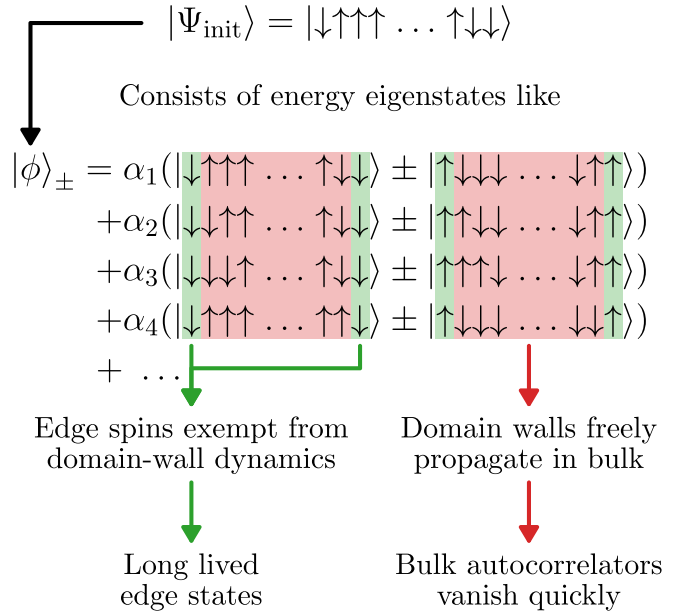


FIG. 6. An illustration of the topological edge-mode protection mechanism. The system is initially prepared in a random bit-string state $|\Psi_{\text{init}}\rangle$. Expanded in the energy eigenbasis of the average Hamiltonian $H_F^{(0)}$, the initial state has overlap with many eigenstate pairs $|\phi\rangle_{\pm}$ with the same number of domain walls. These eigenstate pairs each comprise a superposition of all possible domain wall placements since domain walls can move freely (highlighted in red). The dephasing between eigenstate pairs leads to the vanishing autocorrelators in the bulk. However, since domain walls cannot propagate through the edges, edge spins (marked in green) are protected from the domain-wall dynamics. Instead, they show long coherent oscillations due to the exponentially small energy gap between the parity sectors.

C. Adapted model with external metronome spin

To clearly separate the two described stabilization mechanisms introduced in Secs. III A and III B, we modify the geometry of the model as shown in Fig. 7(a). Instead of attaching the metronome spin to one end of the chain, as previously shown in Fig. 1, the metronome is coupled to the central spin, which itself is still coupled to its two neighbors in the chain. Thus, the two boundary spins are driven in the same way, and they are connected by a direct line of not actively stabilized spins in the bulk. By the reasoning outlined in Sec. III A, one expects similar results for polarized initial states compared to the standard layout of Fig. 1, as the argument relating to the effective symmetry breaking in the bulk still holds. However, the new configuration includes three edges and one central spin coupled to three neighbors, one of which being the metronome spin. One important conceptual difference to the linear configuration is that here the number of domain walls in the main part of the chain is less strictly conserved. This results in a much weaker edge protection, as the coupling between adjacent domain wall sectors is no longer strongly suppressed.

To test these hypotheses, we compute the z -magnetization autocorrelators of a boundary site, Z_L , and of the new metronome site, Z_m , with the results given in Figs. 7(b), 7(c). The observed lifetime behavior is in full agreement with

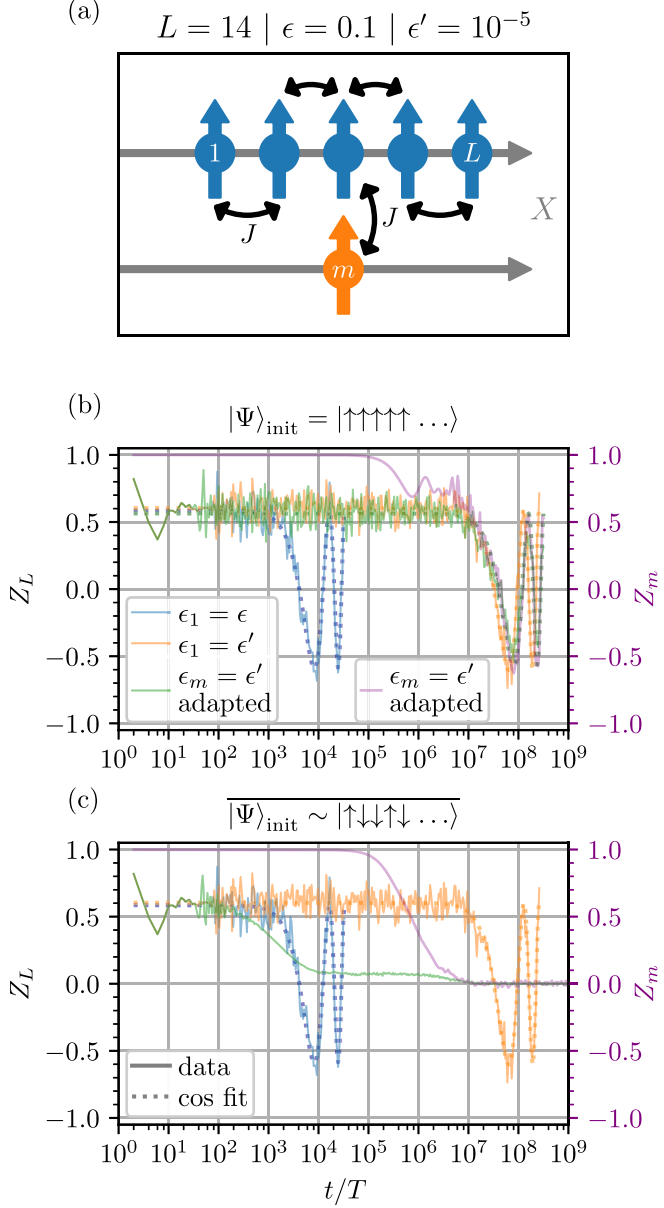


FIG. 7. The setup of the adapted system with $L - 1$ spins in a chain with an additional externally coupled metronome spin attached to the center. (a) A schematic visualization of the adapted geometry. The lifetimes of the boundary-site z -magnetization autocorrelators Z_L are shown in the next two panels for different initial states. (b) The autocorrelator of the polarized initial state. The blue and orange lines show the results for the case without metronome spin and with a metronome spin in the chain, respectively, for reference. Both configurations with a metronome display similar lifetime enhancements of the autocorrelator. (c) The autocorrelator averaged over 500 random initial bit-string states. The adapted system shows a much earlier decay of the autocorrelators compared to the configuration with the metronome spin in the chain and retains only a remnant of the original magnetization for the duration of the metronome lifetime. On the second axis in (b) and (c) (in purple font) the magnetization autocorrelator Z_m of the metronome spin itself in the adapted setup is displayed.

the previous predictions. In the fully polarized case, we see analogous results, whereas for random bit-string states, the

averaged autocorrelator of the edge spin (green curve) decreases rapidly to an intermediate plateau before vanishing completely. The timescale of the larger first decay is comparable to the lifetime of the nonstabilized chain ($t/T \approx 10^3$), and the second late-time decay coincides with the dephasing of the metronome spin. The initial decay stems from the multitude of different couplings between domain-wall sectors and the small remaining autocorrelations are protected by the spin-flip parity that is broken on timescales $\ll \epsilon'$ where the metronome is still fully polarized.

IV. CONCLUSION

In this work, we have shown that near-resonant driving of a single spin can significantly increase the lifetime of long-range order in periodically driven systems. In particular, the stabilization is not based on disorder-induced MBL; instead, we have identified two distinct mechanisms that lead to long-lived bulk and edge spins, respectively. For polarized states, an argument concerning the breaking of spin-flip symmetry was found to explain the increased bulk magnetization lifetimes. Subsequent studies revealed a lifetime enhancement of stable oscillations on the boundary spins in arbitrary bit-string initial states. We argued that the reason for the slowed edge-mode decay is that the metronome spin leads to a suppression of resonant higher-order processes. Finally, we discussed another setup with external stabilization to the chain and thus no edge-mode enhancement to clearly highlight the two different mechanisms identified before.

Thus, our work introduces novel stabilization mechanisms suitable for ordered and, in particular, finite-size systems. The bulk-stabilization argument relies on the effective symmetry breaking introduced through one metronome spin, which is not affected by the length of the chain. Similarly, the energy offset of flipping edge spins compared to the bulk is linked to open boundary conditions, leading to enhancement of stable oscillation even for short chains. Therefore, both processes enable arbitrarily long-lived oscillations without taking the thermodynamic limit.

We point out that the stabilization mechanism of the model is not based on the Hamiltonian being integrable. The core concept is linked to the underlying approximate conservation of the domain-wall number and the spin-flip symmetry, the latter of which is broken by the metronome in the bulk of the chain. We expect to find similar results in other spin systems as long as these conditions are met. To corroborate this statement, we have studied the same model as in Eq. (1), but added next-nearest-neighbor interactions, $\sim J_{i,i+2} s_z^i s_z^{i+2}$, which break the integrability of the Hamiltonian (cf. Appendix C). As expected, we find that decreasing ϵ for one of the spins yields lifetime enhancements analogous to the regular TFIM model, which encourages further study of applications in other models.

One potential future extension of this work is the study of two- and three-dimensional setups. The existence of MBL and thus disorder-stabilized DTC in these systems has been the subject of ongoing debate in recent years, which makes the study of alternative stabilization mechanisms an interesting direction. Moreover, the search for analogous stabilization mechanisms in other paradigmatic spin models, such as the

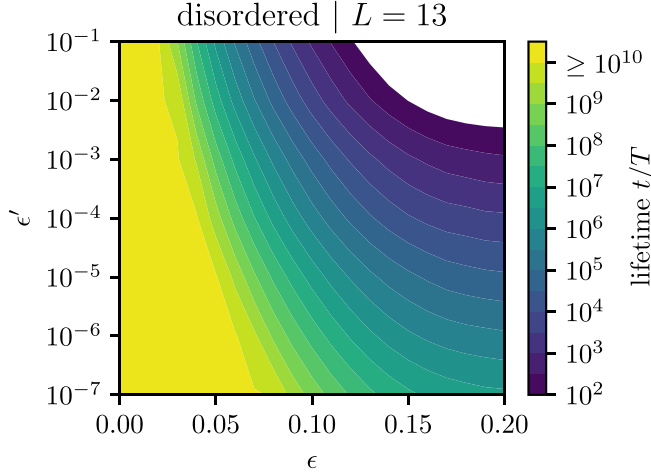


FIG. 8. The disorder-averaged lifetimes of the global chain z magnetization with $N = 13$ spins, starting in the fully polarized initial state. The data were obtained by numerical sigmoid fits. Lifetimes above $\geq 10^{10}T$ and below $\leq 10^2T$ cannot be adequately resolved.

Heisenberg XX and XXZ models, could lead to new insights into out-of-equilibrium dynamics in quantum many-body systems.

ACKNOWLEDGMENTS

We thank Matthias Weidmüller, Roderich Mössner, Sebastian Geier, and Razvan Gurau for fruitful discussions. This work is supported by the Deutsche Forschungsgemeinschaft (DFG, German Research Foundation) under Germany's Excellence Strategy EXC2181/1-390900948 (the Heidelberg STRUCTURES Excellence Cluster) and within the Collaborative Research Center SFB1225 (ISOQUANT). The authors acknowledge support by the state of Baden-Württemberg through bwHPC and the DFG through Grant No. INST 40/575-1 FUGG (Helix and JUSTUS2 clusters). For the numerical work, we used the JULIA programming language [55].

APPENDIX A: DISORDERED COUPLINGS AND FIELDS

The stabilization mechanism proposed in Sec. IIIA is not based on the presence of disorder in the system. To study the interplay of disorder with the metronome, we repeat the drive-parameter scan of Fig. 3 for a disordered system. Specifically, we subject a polarized initial state to realizations of the Hamiltonian of Eq. (1), where the parameters $J_{i,i+1}$ and h_i are uniform iid random variables according to $J_{i,i+1} \sim \mathcal{U}(0.5, 1.5)$ and $h_i \sim \mathcal{U}(-1, 1)$, in analogy to simulations shown in Ref. [5]. The resulting average over 250 disorder realizations of the Floquet unitary is shown in Fig. 8. Since the increase in complexity due to the disorder average required a reduction in the size of the system to $L = 13$, we also give the analogous data set for a disorder-free chain of the same length in Fig. 9. The averaged time traces approximately follow a sigmoid shape $\propto 1/(1 + \exp(\alpha t))$, as different disorder realizations have different Rabi oscillation frequencies and cancel

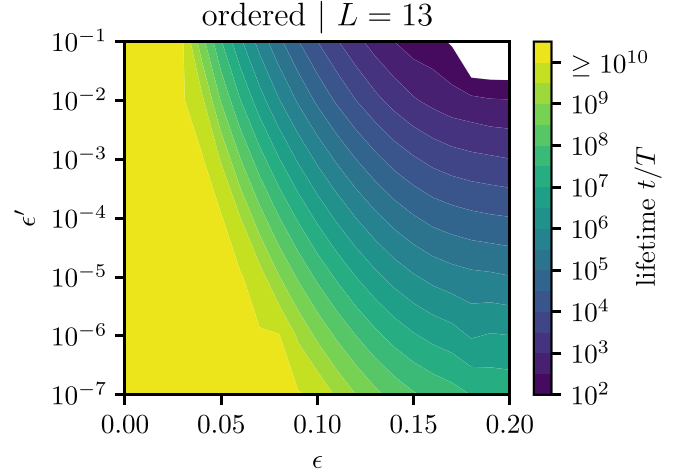


FIG. 9. The lifetimes of the global ordered-chain z magnetization with $N = 13$ spins, starting in the fully polarized initial state. The data were obtained through numerical cosine fits. Lifetimes above $\geq 10^{10}T$ and below $\leq 10^2T$ cannot be adequately resolved.

out at late times. The times plotted in Fig. 8 correspond to $t = 1/\alpha$, so the magnetization has decreased to $\sim 1/(1 + e) \approx 26.9\%$ of the plateau value. Comparing the two figures reveals that the behavior is qualitatively the same. However, making direct quantitative comparisons between the two data sets is not directly possible due to the differences discussed in the determination of the lifetime.

APPENDIX B: METRONOME SPIN AT THE CENTER OF THE CHAIN

Up until now, we have studied systems with the metronome attached to the end of a linear chain or to the side of it, coupled to the central spin of the chain. Now, we replace a central spin on the index $i = \lfloor (L+1)/2 \rfloor =: m$, i.e., $\epsilon_m = \epsilon'$. For odd chain lengths (here $L = 13$), the spin is exactly in the middle of the chain, and the system has a spatial inversion symmetry, reducing the numerical complexity. The global z magnetization of a polarized initial state is depicted in Fig. 10. The global magnetization of the centrally stabilized system has many similarities with that of the original setup with stabilization at the boundary, as shown in Fig. 2. The system demonstrates Rabi oscillations with a similar frequency and initial magnetization amplitude. However, after $\approx 10^5$ Floquet drive cycles, the metronome-spin magnetization temporarily decays to the chain average (right axis) in Fig. 10, before the subsequent Rabi oscillations set in.

The metronome is coupled to two neighboring spins subjected to the standard drive angle deviation, ϵ , instead of the previous single spin. Therefore, the observed reduced time of the initial decay compared to the boundary metronome is consistent with this difference in chain configuration. Before that decay, the dynamics of the metronome can, in good approximation, again be considered to be largely independent of the rest of the chain. Thus, the metronome effectively decouples the two half-chains, acting as a rotating field on its two neighbors. After the decay, the two chains are coupled

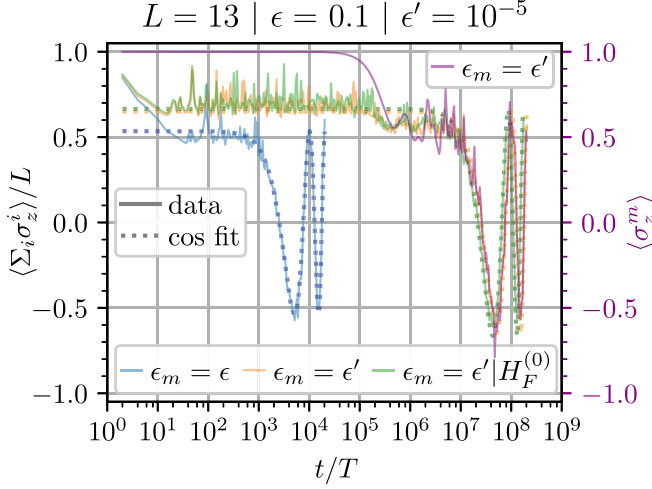


FIG. 10. The global z magnetization of the spin chain of length $L = 13$ starting in a fully polarized state subjected to different driving schemes. We show the exact stroboscopic dynamics of the chain at even period numbers with and without a metronome spin at the central site as well as the average Hamiltonian given in Eq. (5). The configurations that include a metronome spin display lifetime enhancements by several orders of magnitude. All data are well described through numerical cosine fits. On the second axis (in purple font) we display the single-spin magnetization of the metronome spin itself. The dephasing of the magnetization of the metronome coincides with the dephasing of the plateau.

again, leading to the intermediate plateau before the late-time Rabi oscillations.

APPENDIX C: NNN INTERACTIONS

Here we want to study a modified version of the original interaction Hamiltonian H_{int} given in Eq. (1). We include additional next-to-nearest-neighbor (NNN) interactions to the model,

$$H_{\text{int}}^{\text{NNN}} = H_{\text{int}} + \sum_{i=1}^{L-2} J_{i,i+2} s_z^i s_z^{i+2}, \quad (\text{C1})$$

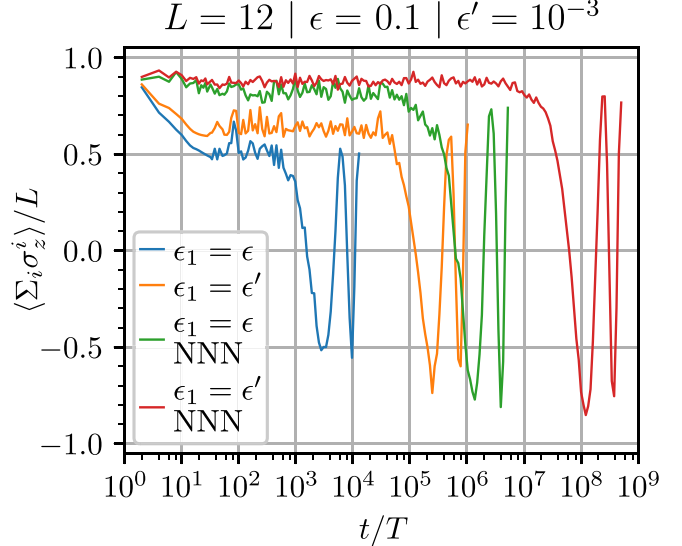


FIG. 11. The global z magnetization of the spin chain of length $L = 12$ starting in a fully polarized state subjected to different interaction Hamiltonians. We show the exact stroboscopic dynamics of the chain at even period numbers with and without a metronome spin at one boundary site, for both the standard and the integrability-breaking model (denoted NNN). Configurations that include a metronome spin display a lifetime enhancement of several orders of magnitude. For better visibility, only the first two oscillation cycles are plotted for each curve.

which break the integrability of the new effective Floquet Hamiltonian. We study the global magnetization of a polarized initial state of $L = 12$ spins subjected to the modified Floquet sequence with $H_{\text{int}}^{\text{NNN}}$ replacing the original interaction Hamiltonian H_{int} . We give the results for $J_{i,i+2} = 0.6$ and $\epsilon' = 10^{-3}$ in Fig. 11.

Both the standard model evolved through H_{int} (blue and orange curves) and the modified model evolved through $H_{\text{int}}^{\text{NNN}}$ (green and red curves) experience qualitatively comparable lifetime enhancements $\sim 1/\epsilon'$ through the addition of a metronome spin.

-
- [1] F. Wilczek, Quantum time crystals, *Phys. Rev. Lett.* **109**, 160401 (2012).
 - [2] A. Shapere and F. Wilczek, Classical time crystals, *Phys. Rev. Lett.* **109**, 160402 (2012).
 - [3] H. Watanabe and M. Oshikawa, Absence of quantum time crystals, *Phys. Rev. Lett.* **114**, 251603 (2015).
 - [4] While Ref. [3] proved the impossibility of time crystals in equilibrium states of short-range interacting systems, a recent work observed stable time-periodic oscillations in the ground state of a system at equilibrium with long-range multispin interactions [56].
 - [5] D. V. Else, B. Bauer, and C. Nayak, Floquet time crystals, *Phys. Rev. Lett.* **117**, 090402 (2016).
 - [6] D. V. Else, C. Monroe, C. Nayak, and N. Y. Yao, Discrete time crystals, *Annu. Rev. Condens. Matter Phys.* **11**, 467 (2020).
 - [7] K. Sacha, Modeling spontaneous breaking of time-translation symmetry, *Phys. Rev. A* **91**, 033617 (2015).
 - [8] V. Khemani, R. Moessner, and S. L. Sondhi, A brief history of time crystals, arXiv:1910.10745.
 - [9] D. A. Abanin, W. D. Roeck, and F. Huveneers, Theory of many-body localization in periodically driven systems, *Ann. Phys. (NY)* **372**, 1 (2016).
 - [10] V. Khemani, A. Lazarides, R. Moessner, and S. L. Sondhi, Phase structure of driven quantum systems, *Phys. Rev. Lett.* **116**, 250401 (2016).
 - [11] N. Y. Yao, A. C. Potter, I.-D. Potirniche, and A. Vishwanath, Discrete time crystals: Rigidity, criticality, and realizations, *Phys. Rev. Lett.* **118**, 030401 (2017).
 - [12] H. Burau, M. Heyl, and G. De Tomasi, Fate of algebraic many-body localization under driving, *Phys. Rev. B* **104**, 224201 (2021).

- [13] D. J. Luitz, R. Moessner, S. L. Sondhi, and V. Khemani, Prethermalization without temperature, *Phys. Rev. X* **10**, 021046 (2020).
- [14] D. V. Else, B. Bauer, and C. Nayak, Prethermal phases of matter protected by time-translation symmetry, *Phys. Rev. X* **7**, 011026 (2017).
- [15] S. A. Weidinger and M. Knap, Floquet prethermalization and regimes of heating in a periodically driven, interacting quantum system, *Sci. Rep.* **7**, 45382 (2017).
- [16] D. M. Long, P. J. D. Crowley, V. Khemani, and A. Chandran, Phenomenology of the prethermal many-body localized regime, *Phys. Rev. Lett.* **131**, 106301 (2023).
- [17] M. Collura, A. De Luca, D. Rossini, and A. Lerose, Discrete time-crystalline response stabilized by domain-wall confinement, *Phys. Rev. X* **12**, 031037 (2022).
- [18] W. W. Ho, S. Choi, M. D. Lukin, and D. A. Abanin, Critical time crystals in dipolar systems, *Phys. Rev. Lett.* **119**, 010602 (2017).
- [19] A. Russomanno, F. Iemini, M. Dalmonte, and R. Fazio, Floquet time crystal in the Lipkin-Meshkov-Glick model, *Phys. Rev. B* **95**, 214307 (2017).
- [20] Z. Gong, R. Hamazaki, and M. Ueda, Discrete time-crystalline order in cavity and circuit QED systems, *Phys. Rev. Lett.* **120**, 040404 (2018).
- [21] B. Huang, Y.-H. Wu, and W. V. Liu, Clean floquet time crystals: Models and realizations in cold atoms, *Phys. Rev. Lett.* **120**, 110603 (2018).
- [22] S. Choi, J. Choi, R. Landig, G. Kucska, H. Zhou, J. Isoya, F. Jelezko, S. Onoda, H. Sumiya, V. Khemani, C. von Keyserlingk, N. Y. Yao, E. Demler, and M. D. Lukin, Observation of discrete time-crystalline order in a disordered dipolar many-body system, *Nature (London)* **543**, 221 (2017).
- [23] J. Choi, H. Zhou, S. Choi, R. Landig, W. W. Ho, J. Isoya, F. Jelezko, S. Onoda, H. Sumiya, D. A. Abanin, and M. D. Lukin, Probing quantum thermalization of a disordered dipolar spin ensemble with discrete time-crystalline order, *Phys. Rev. Lett.* **122**, 043603 (2019).
- [24] G. He, B. Ye, R. Gong, Z. Liu, K. W. Murch, N. Y. Yao, and C. Zu, Quasi-floquet prethermalization in a disordered dipolar spin ensemble in diamond, *Phys. Rev. Lett.* **131**, 130401 (2023).
- [25] J. Rovny, R. L. Blum, and S. E. Barrett, ^{31}P NMR study of discrete time-crystalline signatures in an ordered crystal of ammonium dihydrogen phosphate, *Phys. Rev. B* **97**, 184301 (2018).
- [26] J. Rovny, R. L. Blum, and S. E. Barrett, Observation of discrete-time-crystal signatures in an ordered dipolar many-body system, *Phys. Rev. Lett.* **120**, 180603 (2018).
- [27] S. Autti, V. B. Eltsov, and G. E. Volovik, Observation of a time quasicrystal and its transition to a superfluid time crystal, *Phys. Rev. Lett.* **120**, 215301 (2018).
- [28] J. Smits, L. Liao, H. T. C. Stoof, and P. van der Straten, Observation of a space-time crystal in a superfluid quantum gas, *Phys. Rev. Lett.* **121**, 185301 (2018).
- [29] S. Pal, N. Nishad, T. S. Mahesh, and G. J. Sreejith, Temporal order in periodically driven spins in star-shaped clusters, *Phys. Rev. Lett.* **120**, 180602 (2018).
- [30] J. Zhang, P. W. Hess, A. Kyriyanidis, P. Becker, A. Lee, J. Smith, G. Pagano, I.-D. Potirniche, A. C. Potter, A. Vishwanath, N. Y. Yao, and C. Monroe, Observation of a discrete time crystal, *Nature (London)* **543**, 217 (2017).
- [31] K. Wadenpfuhl and C. S. Adams, Emergence of synchronization in a driven-dissipative hot rydberg vapor, *Phys. Rev. Lett.* **131**, 143002 (2023).
- [32] X. Wu, Z. Wang, F. Yang, R. Gao, C. Liang, M. K. Tey, X. Li, T. Pohl, and L. You, Observation of a dissipative time crystal in a strongly interacting Rydberg gas, [arXiv:2305.20070](https://arxiv.org/abs/2305.20070).
- [33] X. Mi, M. Ippoliti, C. Quintana, A. Greene, Z. Chen, J. Gross, F. Arute, K. Arya, J. Atalaya, R. Babbush *et al.*, Time-crystalline eigenstate order on a quantum processor, *Nature (London)* **601**, 531 (2022).
- [34] P. Frey and S. Rachel, Realization of a discrete time crystal on 57 qubits of a quantum computer, *Sci. Adv.* **8**, eabm7652 (2022).
- [35] J. Šuntajs, J. Bonca, T. Prosen, and L. Vidmar, Quantum chaos challenges many-body localization, *Phys. Rev. E* **102**, 062144 (2020).
- [36] D. Sels and A. Polkovnikov, Dynamical obstruction to localization in a disordered spin chain, *Phys. Rev. E* **104**, 054105 (2021).
- [37] P. Sierant and J. Zakrzewski, Challenges to observation of many-body localization, *Phys. Rev. B* **105**, 224203 (2022).
- [38] A. Morningstar, L. Colmenarez, V. Khemani, D. J. Luitz, and D. A. Huse, Avalanches and many-body resonances in many-body localized systems, *Phys. Rev. B* **105**, 174205 (2022).
- [39] C. W. von Keyserlingk, V. Khemani, and S. L. Sondhi, Absolute stability and spatiotemporal long-range order in Floquet systems, *Phys. Rev. B* **94**, 085112 (2016).
- [40] F. Machado, Q. Zhuang, N. Y. Yao, and M. P. Zaletel, Absolutely stable time crystals at finite temperature, *Phys. Rev. Lett.* **131**, 180402 (2023).
- [41] K. Giergiel, J. Wang, B. J. Dalton, P. Hannaford, and K. Sacha, Discrete time crystals with absolute stability, *Phys. Rev. B* **108**, L180201 (2023).
- [42] S. T. Schindler and H. H. Sheinfux, Floquet engineering with spatially non-uniform driving fields, [arXiv:2311.00845](https://arxiv.org/abs/2311.00845).
- [43] T. Mori, T. Kuwahara, and K. Saito, Rigorous bound on energy absorption and generic relaxation in periodically driven quantum systems, *Phys. Rev. Lett.* **116**, 120401 (2016).
- [44] D. A. Abanin, W. De Roeck, W. W. Ho, and F. Huveneers, Effective Hamiltonians, prethermalization, and slow energy absorption in periodically driven many-body systems, *Phys. Rev. B* **95**, 014112 (2017).
- [45] W. C. Yu, J. Tangpanitanon, A. W. Glaetzle, D. Jaksch, and D. G. Angelakis, Discrete time crystal in globally driven interacting quantum systems without disorder, *Phys. Rev. A* **99**, 033618 (2019).
- [46] W. Magnus, On the exponential solution of differential equations for a linear operator, *Commun. Pure Appl. Math.* **7**, 649 (1954).
- [47] S. Blanes, F. Casas, J. A. Oteo, and J. Ros, The Magnus expansion and some of its applications, *Phys. Rep.* **470**, 151 (2009).
- [48] D. J. Yates, F. H. L. Essler, and A. Mitra, Almost strong $(0, \pi)$ edge modes in clean interacting one-dimensional Floquet systems, *Phys. Rev. B* **99**, 205419 (2019).
- [49] A. Y. Kitaev, Unpaired Majorana fermions in quantum wires, *Phys.-Usp.* **44**, 131 (2001).

- [50] T. Senthil, Symmetry-protected topological phases of quantum matter, *Annu. Rev. Condens. Matter Phys.* **6**, 299 (2015).
- [51] J. Kemp, N. Y. Yao, C. R. Laumann, and P. Fendley, Long coherence times for edge spins, *J. Stat. Mech.* (2017) 063105.
- [52] D. J. Yates, A. G. Abanov, and A. Mitra, Long-lived period-doubled edge modes of interacting and disorder-free Floquet spin chains, *Commun. Phys.* **5**, 43 (2022).
- [53] D. V. Else, P. Fendley, J. Kemp, and C. Nayak, Prethermal strong zero modes and topological qubits, *Phys. Rev. X* **7**, 041062 (2017).
- [54] F. Machado, D. V. Else, G. D. Kahanamoku-Meyer, C. Nayak, and N. Y. Yao, Long-range prethermal phases of nonequilibrium matter, *Phys. Rev. X* **10**, 011043 (2020).
- [55] J. Bezanson, A. Edelman, S. Karpinski, and V. B. Shah, Julia: A fresh approach to numerical computing, *SIAM Rev.* **59**, 65 (2017).
- [56] V. K. Kozin and O. Kyriienko, Quantum time crystals from Hamiltonians with long-range interactions, *Phys. Rev. Lett.* **123**, 210602 (2019).

8

OUTLOOK: CAN PAIRS STABILIZE TIME CRYSTALLINE DYNAMICS?

In this chapter, we revisit the model discussed in Chapter 2 and explore the question whether this form of disorder can sustain a time crystalline phase. The concrete protocol we study is similar to the previous chapter: After some interaction period τ , all spins are flipped around the x -axis with angle $\phi = \pi(1 - \epsilon)$. Hence, the Floquet unitary is given by:

$$U_F = \exp \left[-i\pi(1 - \epsilon) \sum_i S_x^{(i)} \right] \exp(-i\tau H_{XX}) \quad (8.1)$$

The dynamics are initialized in a z -polarized state $|\psi_0\rangle = |\uparrow \dots \uparrow\rangle$ and the observable tracked is the total z -magnetization $M_z = N^{-1} \sum_i S_z^{(i)}$.

Preliminary experimental results of this protocol published in [160] indicate that interactions indeed stabilize the magnetization dynamics (cf. Figure 8.1)¹. Running the experiment with a rather short wait time of $\tau_1 = 5\text{ns}$ finds period doubling for $\epsilon = 0$ [cf. Figure 8.1(b) left] as expected due to symmetry. However, this signature is not stable to perturbations of the drive as increasing the drives deviation to $\epsilon = 2\%$ replaces the stable period-doubled oscillations by a beating signal [cf. Figure 8.1(c) left]. However, increasing the wait time to $\tau_2 = 45\text{ns}$ [cf. Figure 8.1(d) left] clearly reconstitutes the time crystalline signature. This is reflected by the so-called crystalline fraction [cf. Figure 8.1(b-d) right], which is defined as the normalized Fourier weight at $\nu = 1/2$ [23]. A systematic parameter sweep shows that increasing the interaction time τ not only leads to a larger crystalline fraction but also extends the range of ϵ where time crystalline behavior can be observed [cf. Figure 8.1(e)]. Thus, there is a clear stabilization effect due to the interactions which could imply the system to enter a time crystalline phase.

8.1 TIME CRYSTAL PROTOCOL WITH PAIRS

In the following, we use the pair model to derive the functional form of the envelope of $|M_z(n)|$. The first obvious step is to just apply the pair model to solve the dynamics. So replacing $H_{XX} \rightarrow \sum_{\langle i,j \rangle} H_{pair}^{(i,j)}$, we find that U_F factorizes completely between pairs:

$$U_F \approx \sum_{\langle i,j \rangle} \exp[-i(1 - \epsilon)\pi(S_x^i + S_x^j)] \exp[-i\tau H_{pair}^{(i,j)}] \equiv \sum_{\langle i,j \rangle} U_{F,pair}^{(i,j)}. \quad (8.2)$$

$$\langle M_z \rangle(n) = \frac{1}{N} \sum_{\langle i,j \rangle} \left\langle \uparrow\uparrow \left| (U_{F,pair}^{(i,j)\dagger})^n (S_z^{(i)} + S_z^{(j)}) (U_{F,pair}^{(i,j)})^n \right| \uparrow\uparrow \right\rangle \equiv \frac{1}{N} \sum_{\langle i,j \rangle} \left\langle M_{z,pair}^{(i,j)}(n) \right\rangle \quad (8.3)$$

¹ Note that the graphic uses a different definition for the rotation angle. It uses $\phi = \epsilon\pi$ and thus $\epsilon = 1$ means perfect flips. In contrast, this thesis uses $\phi = (1 - \epsilon)\pi$ with $\epsilon = 0$ corresponding to perfect flips.

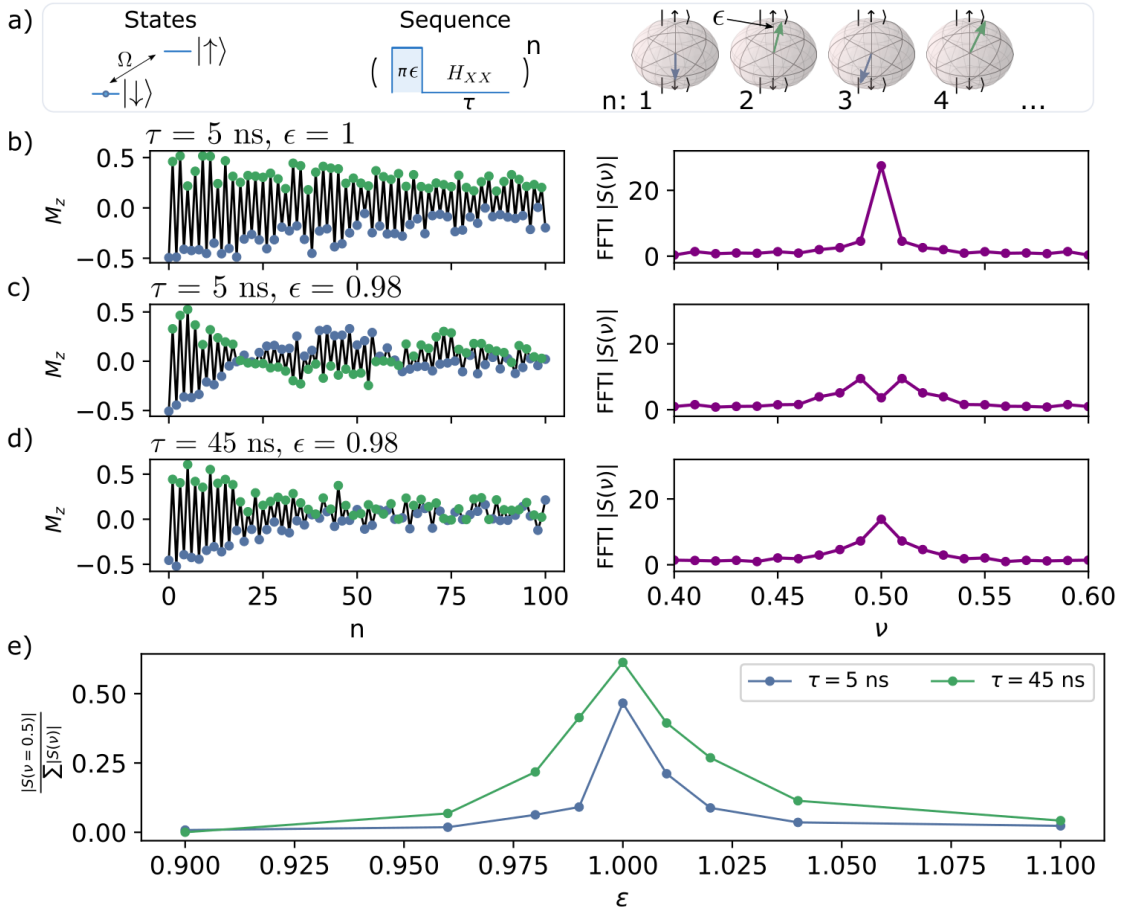


Figure 8.1: Preliminary experimental results on time-crystalline signatures in a spatially disordered XX model. a) sketches the experimental sequence. Then experimental results for perfect rotation (b), short interaction times and imperfect rotation (c) and longer interaction times with imperfect rotation (d) follow. Left column depict the magnetization's time trace, while right column shows the Fourier transform of the signal. e) Then plots the normalized Fourier weight at $\nu = 0.5$ versus rotational deviation ϵ . Taken with permission from Ref. [160]

Now we can exploit that $U_{F,pair}^{(i,j)}$ commutes with $S_x^{(i)} S_x^{(j)}$ to decompose the 4-dimensional Hilbertspace of each pair into two 2-dimensional subspaces. Thus, we can compute the exponential $U_{F,pair}^n$ analytically and find:

$$2 \left\langle M_{z,pair}^{(i,j)}(n) \right\rangle \approx 2 \cos(n\bar{J}) \cos n\theta + 2 \sin(n\bar{J}) \sin(n\theta) \underbrace{\frac{\sin \tau \cos \phi}{\sin \theta}}_{\equiv f} \quad (8.4)$$

$$= (1+f) \cos [n(\bar{J}-\theta)] + (1-f) \cos [n(\bar{J}+\theta)] \quad (8.5)$$

where $\bar{J} = \frac{J\tau}{4}$ and $\cos \theta = \cos \bar{J} \cos \phi$.

To find the shape of the envelope, we assume $\epsilon \ll 1$ which is equivalent to $\phi \ll 1$ in a toggling frame where we swap the orientation of the z -axis in every step. Furthermore, we will consider only pairs where the interaction is stronger than the driving, i.e. $\bar{J} > \phi$. The other pairs with $\bar{J} < \phi$ essentially oscillate around the x -axis with some deviation and thus dephase slowly among themselves on a timescale $\propto \epsilon$. For the interaction dominated

pairs, we can neglect the second term of Equation 8.5 since its coefficient $(1 - f)$ gets rather small because

$$f = \frac{\sin \bar{J} \cos \phi}{\sqrt{1 - \cos^2 \bar{J} \cos^2 \phi}} \approx \frac{\cos \phi}{\sqrt{1 - \frac{\phi^2}{\sin^2 \bar{J}}}} \approx 1 + \frac{1}{2} \phi^2 \left(\frac{1}{\sin^2 \bar{J}} - 1 \right) \approx 1. \quad (8.6)$$

Additionally, we can approximate θ for $\bar{J} < \pi$ as

$$\theta = \arccos(\cos \bar{J} \cos \phi) \approx \arccos(\cos \bar{J}(1 - \frac{\phi^2}{2})) \approx \bar{J} - \frac{\phi^2}{2 \tan \bar{J}}, \quad (8.7)$$

which further justifies neglecting the second term, since not only its amplitude is small but it also oscillates quickly and therefore it averages out when considering the dynamics on a longer timescale. Putting these results together we find for the approximate magnetization dynamics of an interaction dominated pair:

$$\langle S_z^1 + S_z^2 \rangle(n) \approx \cos n(\bar{J} - \theta) \approx \cos(n \frac{\phi^2}{2 \tan \bar{J}}) \quad (8.8)$$

From Figure 8.2(c), we can see that this approximation (blue line) matches the exact data (gray) essentially exactly.

In principle, we now need to average this expression (Equation 8.8) over the appropriate part of the pair coupling distribution $P_{pair}(J)dJ$ (cf. Equation 4.10). This is analytically infeasible. Instead, we can exploit that this distribution is very broad (cf. Figure 8.2(a)), which leads to *phase-wrapping*. This is the curious property of Floquet systems that their coupling are confined to a circle and strong coupling then just "wrap around". Another way this manifests is the periodicity of Equation 8.8 where any \bar{J} can be mapped back to the interval $[0, \pi/2]$. Since the coupling distribution is so broad that most couplings wrap around multiple times, the distribution thus becomes effectively uniform (cf. Figure 8.2(b)). Exploiting this fact, we can approximate the average:

$$\langle M_z(n) \rangle = \frac{1}{2} \int_{4\phi/\tau}^{\infty} dJ P_{pair}(J) \langle S_z^1 + S_z^2 \rangle(n) \quad (8.9)$$

$$\approx \frac{1}{2} \kappa \frac{2}{\pi} \int_0^{\pi/2} d\bar{J} \langle S_z^1 + S_z^2 \rangle(n) \quad (8.10)$$

$$= \frac{1}{2} \kappa \exp \left(-n \frac{\phi^2}{2} \right) \quad (8.11)$$

Here $\kappa = \int_{4\phi/\tau}^{\infty} dJ P_{pair}(J)$ denotes the fraction of pairs that are dominated by their interaction. Figure 8.2(c) confirms this to be a reasonable approximation. The slight deviation likely stem from the fact that the effective, phase-wrapped, coupling distribution shows a systematic deviation from a uniform distribution. This is likely due to the assumption that all couplings $\bar{J} > \phi$ are subject to the phase-wrapping. However the pair coupling distribution shows a slight curve in the regime $\phi \leq \bar{J} \leq \pi$, which explains the slight emphasis on smaller phase-wrapped couplings².

² A uniform distribution with a logarithmic x -axis would appear as a linear slope since the height of the bin is proportional to its width.

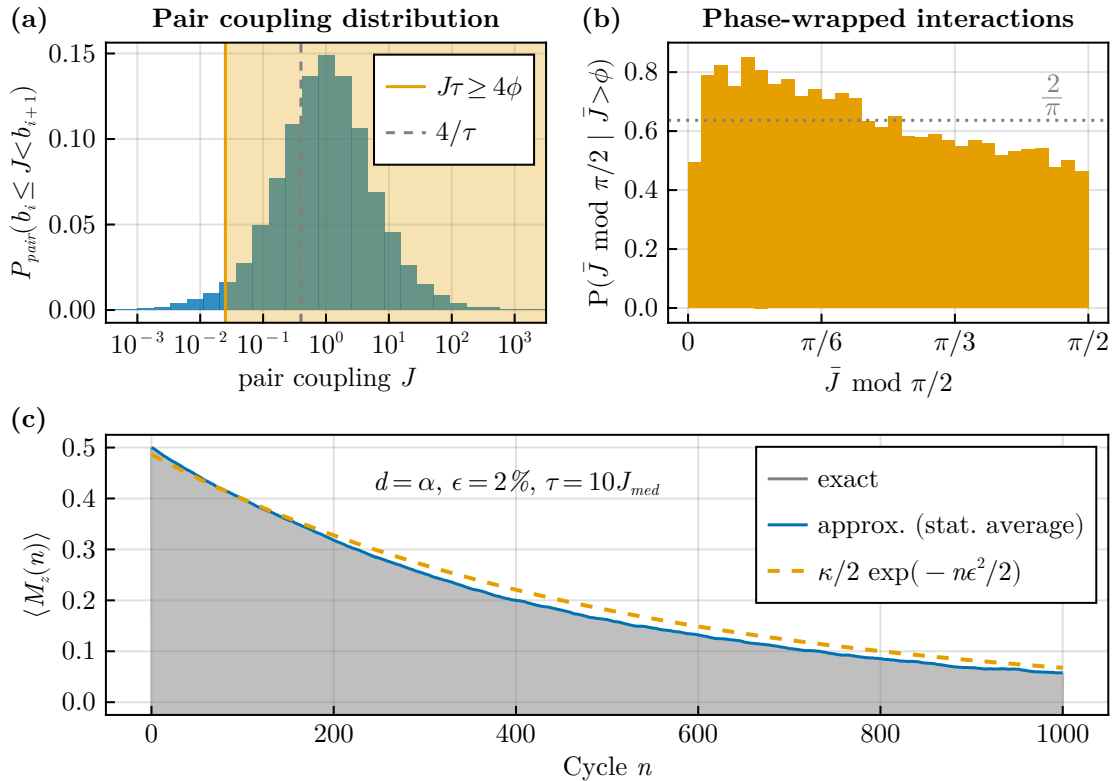


Figure 8.2: Preliminary result of the pair model applied to the time crystal protocol for $d = \alpha$, $\epsilon = 2\%$ and $\tau = 10J_{\text{med}}$. (a) shows the distribution of the pair couplings as given by Equation 4.10. The yellow shaded area indicates the region where the approximation is applied. The gray, dashed, line indicates where $\bar{J} = 1$ and thus phase wrapping sets in. (b) Resulting distribution if the couplings contained in the yellow area of panel (a) are phase wrapped. The gray, dotted, line is a guide to the eye and marks a uniform distribution. (c) Compares the time traces resulting from averaging exact pair dynamics (gray), averaging the approximated pair dynamics and (blue) and the approximate analytical average (yellow dashed).

8.2 DISCUSSION

The first-order pair model predicts a stabilization effect due to interactions, which shifts the decay timescale from $\mathcal{O}(\epsilon)$ to $\mathcal{O}(\epsilon^2)$. However, this stabilization does not increase with system size, because the pairs do not interact among each other. Therefore, the time crystalline signature is only a transient effect according to the pair model. However, it is unclear whether this model captures the relevant physics of the situation. One way to check this is by experiment of course, where one could try to confirm the scaling of the decay timescale $\tau_{decay} \propto \epsilon^2$ and perform more extensive numerical checks in small systems.

From the theoretical side, there are some more possible mechanisms that could stabilize the time crystalline signature. For one, the Rydberg spins also generate some on-site potential due to van der Waals interactions, which were neglected so far. This term can be combined with the driving field to effectively slight deviations in the rotation axis. As we have seen in the previous Chapter 7, such a spatially dependent drive can have a huge influence on the lifetime of the system. However, since this does not cause further interactions between pairs and thus the dynamics stay constricted to small Hilbert spaces, it is unlikely that this effect would have a large impact in this scenario.

A likely more fruitful approach is to incorporate pair-pair interactions. For an XXZ model, we derived (cf. Chapter 2) that these pair-pair interactions are effectively a kind of Ising model of pairs. Since disordered Ising models are known to feature time crystalline phases, we deem this avenue quite promising to study. Unfortunately, these terms thwart the integrability and so one will need to resort to numerics or find some other clever approach to tackle this problem analytically. The extension of this idea to XX models is also not straight-forward as it requires a better understanding of the next order of perturbation theory, which was already discussed previously in Chapter 5.

While we could not confirm the presence of time crystal in this preliminary analysis of the pair model, we also did not rule it out. However, just the base pair description does not lend itself to produce a stable time crystal. Hence, new insights beyond bare pairs are required to draw a definitive conclusion on this matter.

CONCLUSION

In Part III of this thesis, we have demonstrated time-crystalline behavior shares a close relationship not only to disordered interactions but also to disorder in the driving part. The unifying concept, that is key to understanding the described phenomena, is the role of long-range order within the eigenstates (described well in e.g [54, 156]). In Chapter 7, the high sensitivity of the lifetime of the whole system to the variation of the driving field on just a single site is testament to the underlying long-range order - in that case of the ground state of an Ising model. States at higher temperature do not possess long range order and thus do show neither time crystalline behavior nor lifetime enhancements (except at the edges due to topological effects). Viewing the driven pair model of Chapter 8 through this lens, it becomes apparent that no true time crystal can be expected at this level: The lowest order of the pair model just does not feature any interaction terms among the pairs and so no long-range order can be generated. Whether pair-pair interactions can change this fundamentally is questionable because there is a crucial difference to the Ising model: All eigenstates of an Ising interaction, i.e. $\sum_{ij} J_{ij} S_z^{(i)} S_z^{(j)}$, written in the symmetric sector of its \mathbb{Z}_2 symmetry feature long-range order because they must be superpositions of the form $|\psi\rangle \pm X|\psi\rangle$, where X is the generator of the symmetry. In contrast, this is not true for eigenstates of the pair model because each H_{pair} has $|\pm\rangle \propto |\uparrow\downarrow\rangle \pm |\downarrow\uparrow\rangle$ as possible eigenstates which itself are symmetric under spin-flip. Thus, the eigenstates for the pair model can fulfill the symmetry in local patches destroying the global long-range order in the process.

A consequence of this interpretation is that one learns about the structure of the eigenstates from the measurement of the time crystal protocol. An interesting application of this could be to study whether we can restore the time crystal signature by using different parameter regimes. The flexibility of the Rydberg platform allow for tuning the strength of not only Ising interactions but also of random on-site potentials which are generated through van der Waals interactions of neighboring spins [161]. So one could use the existence of a time crystal as an indicator to probe the crossover between XXZ and Ising models and thus the transition between pair localization and traditional Ising-like MBL. While MBL is conjectured to be absent for long-range interaction $\alpha < 2d$ by resonance counting arguments [34, 36], these estimates used coefficients of the same magnitude for Ising and hopping terms and so the Ising limit of power-law XXZ models is not studied to our knowledge.

Part IV
S U M M A R Y

S U M M A R Y

In this thesis, we have studied how spatial inhomogeneities can prohibit a system's thermalization at least on short and intermediate timescales. In Part II, we studied closed quantum systems featuring power-law interactions and demonstrated the presence of an emergent integrability following the structure of MBL. This feature appeared to be robust using numerical finite size scaling and also experimental data showed clear signatures of its consequences even in a critical case where $\alpha = d = 3$. While the existence of MBL as a true thermodynamic phase is hotly debated, its core concept, i.e. the disorder-induced emergent integrability, proved to be a very useful tool to understand the behavior of real-world experiments. Whether or not this apparent localization persists to infinite times and infinite system size can perhaps be answered by generalizing the perturbative RSRG procedure to higher orders but this is beyond the scope of this work.

Then, in Part III, we considered periodically driven systems and discerned the intricate interplay of driving and non-trivial, quasi-conserved quantities caused by spatial inhomogeneity. The key signature of these conservation laws manifests as long-lived oscillations that have a frequency that is an integer multiple of the driving frequency. However, we have seen that the details of the conservation laws and the connected symmetries have a strong influence on the stability of the dynamics. Thus, the microscopic structure of the system imprints on its macroscopic dynamics allowing for novel physics out-of-equilibrium.

More generally, we have seen that the absence of thermalization often comes with additional structure. Hence, even though out-of-equilibrium states are, per definitionem, not amenable to a thermal description, all is it not lost. For the systems studied here, effective conservation laws could be identified and subsequently exploited to gain insight into the systems' dynamics.

Speaking in terms of coffee: In a latte, the milk and coffee always intermix quickly. However, if the milk is strongly disordered, i.e. frothy, then it will not mix well into the coffee even if stirred. However the resulting macchiato is not much harder to describe than the latte. It just features some additional structure. At least in this regard, quantum systems are akin to coffee.

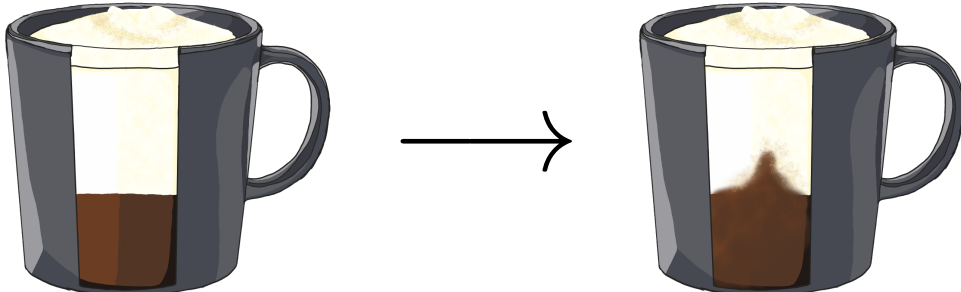


Figure 9.1: Localization exemplified by a macchiato.

B I B L I O G R A P H Y

- [1] J. M. Deutsch, “Quantum statistical mechanics in a closed system,” Physical Review A **43**, 2046–2049 (1991).
- [2] M. Srednicki, “Chaos and Quantum Thermalization,” Physical Review E **50**, 888–901 (1994).
- [3] J. M. Deutsch, “Eigenstate Thermalization Hypothesis,” Reports on Progress in Physics **81**, 082001 (2018).
- [4] P. W. Anderson, “Absence of Diffusion in Certain Random Lattices,” Physical Review **109**, 1492–1505 (1958).
- [5] M. Schreiber, S. S. Hodgman, P. Bordia, H. P. Lüschen, M. H. Fischer, R. Vosk, E. Altman, U. Schneider, and I. Bloch, “Observation of many-body localization of interacting fermions in a quasirandom optical lattice,” Science **349**, 842–845 (2015).
- [6] S. S. Kondov, W. R. McGehee, W. Xu, and B. DeMarco, “Disorder-Induced Localization in a Strongly Correlated Atomic Hubbard Gas,” Physical Review Letters **114**, 083002 (2015).
- [7] G. Kucsko, S. Choi, J. Choi, P. C. Maurer, H. Zhou, R. Landig, H. Sumiya, S. Onoda, J. Isoya, F. Jelezko, E. Demler, N. Y. Yao, and M. D. Lukin, “Critical Thermalization of a Disordered Dipolar Spin System in Diamond,” Physical Review Letters **121**, 023601 (2018).
- [8] L. S. Martin, H. Zhou, N. T. Leitao, N. Maskara, O. Makarova, H. Gao, Q.-Z. Zhu, M. Park, M. Tyler, H. Park, S. Choi, and M. D. Lukin, “Controlling Local Thermalization Dynamics in a Floquet-Engineered Dipolar Ensemble,” Physical Review Letters **130**, 210403 (2023).
- [9] K. X. Wei, C. Ramanathan, and P. Cappellaro, “Exploring Localization in Nuclear Spin Chains,” Physical Review Letters **120**, 070501 (2018).
- [10] D. M. Silevitch, C. Tang, G. Aeppli, and T. F. Rosenbaum, “Tuning high-Q nonlinear dynamics in a disordered quantum magnet,” Nature Communications **10**, 4001 (2019).
- [11] L. Fleishman and P. W. Anderson, “Interactions and the Anderson transition,” Physical Review B **21**, 2366–2377 (1980).
- [12] D. M. Basko, I. L. Aleiner, and B. L. Altshuler, “Metal-insulator transition in a weakly interacting many-electron system with localized single-particle states,” Annals of Physics **321**, 1126–1205 (2006).
- [13] I. V. Gornyi, A. D. Mirlin, and D. G. Polyakov, “Interacting Electrons in Disordered Wires: Anderson Localization and Low- T Transport,” Physical Review Letters **95**, 206603 (2005).
- [14] B. Bauer and C. Nayak, “Area laws in a many-body localized state and its implications for topological order,” Journal of Statistical Mechanics: Theory and Experiment **2013**, P09005 (2013).

- [15] M. Serbyn, Z. Papić, and D. A. Abanin, “Local Conservation Laws and the Structure of the Many-Body Localized States,” *Physical Review Letters* **111**, 127201 (2013).
- [16] D. A. Huse, R. Nandkishore, and V. Oganesyan, “Phenomenology of fully many-body-localized systems,” *Physical Review B* **90**, 174202 (2014).
- [17] J. Z. Imbrie, V. Ros, and A. Scardicchio, “Review: Local Integrals of Motion in Many-Body Localized systems,” *Annalen der Physik* **529**, 1600278 (2017).
- [18] A. Pal and D. A. Huse, “The many-body localization phase transition,” *Physical Review B* **82**, 174411 (2010).
- [19] S. Iyer, V. Oganesyan, G. Refael, and D. A. Huse, “Many-Body Localization in a Quasiperiodic System,” *Physical Review B* **87**, 134202 (2013).
- [20] D. J. Luitz, N. Laflorencie, and F. Alet, “Many-body localization edge in the random-field Heisenberg chain,” *Physical Review B* **91**, 081103(R) (2015).
- [21] S. Schiffer, J. Wang, X.-J. Liu, and H. Hu, “Many-body localization in X Y spin chains with long-range interactions: An exact-diagonalization study,” *Physical Review A* **100**, 063619 (2019).
- [22] T. Chanda, P. Sierant, and J. Zakrzewski, “Many-body localization transition in large quantum spin chains: The mobility edge,” *Physical Review Research* **2**, 032045(R) (2020).
- [23] S. Choi, J. Choi, R. Landig, G. Kucsko, H. Zhou, J. Isoya, F. Jelezko, S. Onoda, H. Sumiya, V. Khemani, C. Von Keyserlingk, N. Y. Yao, E. Demler, and M. D. Lukin, “Observation of discrete time-crystalline order in a disordered dipolar many-body system,” *Nature* **543**, 221–225 (2017).
- [24] A. Lukin, M. Rispoli, R. Schittko, M. E. Tai, A. M. Kaufman, S. Choi, V. Khemani, J. Léonard, and M. Greiner, “Probing entanglement in a many-body-localized system,” *Science* **364**, 256–260 (2019).
- [25] M. Rispoli, A. Lukin, R. Schittko, S. Kim, M. E. Tai, J. Léonard, and M. Greiner, “Quantum critical behaviour at the many-body localization transition,” *Nature* **573**, 385–389 (2019).
- [26] D. Abanin, J. Bardarson, G. De Tomasi, S. Gopalakrishnan, V. Khemani, S. Parameswaran, F. Pollmann, A. Potter, M. Serbyn, and R. Vasseur, “Distinguishing localization from chaos: Challenges in finite-size systems,” *Annals of Physics* **427**, 168415 (2021).
- [27] A. Morningstar, L. Colmenarez, V. Khemani, D. J. Luitz, and D. A. Huse, “Avalanches and many-body resonances in many-body localized systems,” *Physical Review B* **105**, 174205 (2022).
- [28] H. Ha, A. Morningstar, and D. A. Huse, “Many-Body Resonances in the Avalanche Instability of Many-Body Localization,” *Physical Review Letters* **130**, 250405 (2023).
- [29] A. Scocco, G. Passarelli, M. Collura, P. Lucignano, and A. Russomanno, *Thermalization propagation front and robustness against avalanches in localized systems*, July 2024.

- [30] P. Ponte, C. R. Laumann, D. A. Huse, and A. Chandran, “Thermal inclusions: how one spin can destroy a many-body localized phase,” Philosophical Transactions of the Royal Society A: Mathematical, Physical and Engineering Sciences **375**, 20160428 (2017).
- [31] T. Thiery, F. Huveneers, M. Müller, and W. De Roeck, “Many-Body Delocalization as a Quantum Avalanche,” Physical Review Letters **121**, 140601 (2018).
- [32] P. J. D. Crowley and A. Chandran, “Avalanche induced coexisting localized and thermal regions in disordered chains,” Physical Review Research **2**, 033262 (2020).
- [33] A. L. Burin, *Energy delocalization in strongly disordered systems induced by the long-range many-body interaction*, Nov. 2006.
- [34] N. Y. Yao, C. R. Laumann, S. Gopalakrishnan, M. Knap, M. Müller, E. A. Demler, and M. D. Lukin, “Many-Body Localization in Dipolar Systems,” Physical Review Letters **113**, 243002 (2014).
- [35] A. L. Burin, “Many-body delocalization in a strongly disordered system with long-range interactions: Finite-size scaling,” Physical Review B **91**, 094202 (2015).
- [36] A. L. Burin, “Localization in a random XY model with long-range interactions: Intermediate case between single-particle and many-body problems,” Physical Review B **92**, 104428 (2015).
- [37] S. Gopalakrishnan and D. A. Huse, “Instability of many-body localized systems as a phase transition in a nonstandard thermodynamic limit,” Physical Review B **99**, 134305 (2019).
- [38] R. Nandkishore, “Critical localization with van der Waals interactions,” Physical Review B **106**, L060306 (2022).
- [39] D. M. Long, P. J. D. Crowley, V. Khemani, and A. Chandran, “Phenomenology of the Prethermal Many-Body Localized Regime,” Physical Review Letters **131**, 106301 (2023).
- [40] F. Igloi and C. Monthus, “Strong disorder RG approach of random systems,” Physics Reports **412**, 277–431 (2005).
- [41] S. A. Parameswaran, A. C. Potter, and R. Vasseur, “Eigenstate phase transitions and the emergence of universal dynamics in highly excited states,” Annalen der Physik **529**, 1600302 (2017).
- [42] F. Igloi and C. Monthus, “Strong disorder RG approach – a short review of recent developments,” The European Physical Journal B **91**, 290 (2018).
- [43] C. Monthus, “Strong disorder renormalization for the dynamics of many-body-localized systems: iterative elimination of the fastest degree of freedom via the Floquet expansion,” Journal of Physics A: Mathematical and Theoretical **51**, 275302 (2018).
- [44] C. Dasgupta and S.-k. Ma, “Low-temperature properties of the random Heisenberg antiferromagnetic chain,” Physical Review B **22**, 1305–1319 (1980).
- [45] D. S. Fisher, “Random transverse field Ising spin chains,” Physical Review Letters **69**, 534–537 (1992).
- [46] R. Vosk and E. Altman, “Many-body localization in one dimension as a dynamical renormalization group fixed point,” Physical Review Letters **110**, 067204 (2013).

- [47] D. Pekker, G. Refael, E. Altman, E. Demler, and V. Oganesyan, “Hilbert-Glass Transition: New Universality of Temperature-Tuned Many-Body Dynamical Quantum Criticality,” *Physical Review X* **4**, 011052 (2014).
- [48] N. Moure, S. Haas, and S. Kettemann, “Many-Body Localization Transition in Random Quantum Spin Chains with Long-Range Interactions,” *EPL (Europhysics Letters)* **111**, 27003 (2015).
- [49] N. Moure, H.-Y. Lee, S. Haas, R. N. Bhatt, and S. Kettemann, “Disordered quantum spin chains with long-range antiferromagnetic interactions,” *Physical Review B* **97**, 014206 (2018).
- [50] Y. Mohdeb, J. Vahedi, N. Moure, A. Roshani, H.-Y. Lee, R. N. Bhatt, S. Kettemann, and S. Haas, “Entanglement properties of disordered quantum spin chains with long-range antiferromagnetic interactions,” *Physical Review B* **102**, 214201 (2020).
- [51] Y. Mohdeb, J. Vahedi, and S. Kettemann, “Excited-Eigenstate Entanglement Properties of XX Spin Chains with Random Long-Range Interactions,” *Physical Review B* **106**, 104201 (2022).
- [52] Y. Mohdeb, J. Vahedi, R. N. Bhatt, S. Haas, and S. Kettemann, “Global quench dynamics and the growth of entanglement entropy in disordered spin chains with tunable range interactions,” *Physical Review B* **108**, L140203 (2023).
- [53] D. A. Abanin, W. De Roeck, and F. Huveneers, “Theory of many-body localization in periodically driven systems,” *Annals of Physics* **372**, 1–11 (2016).
- [54] D. V. Else, B. Bauer, and C. Nayak, “Prethermal Phases of Matter Protected by Time-Translation Symmetry,” *Physical Review X* **7**, 011026 (2017).
- [55] P. Bordia, H. Lüschen, U. Schneider, M. Knap, and I. Bloch, “Periodically Driving a Many-Body Localized Quantum System,” *Nature Physics* **13**, 460–464 (2017).
- [56] D. V. Else, C. Monroe, C. Nayak, and N. Y. Yao, “Discrete Time Crystals,” *Annual Review of Condensed Matter Physics* **11**, 467–499 (2020).
- [57] H. Watanabe and M. Oshikawa, “Absence of Quantum Time Crystals,” *Physical Review Letters* **114**, 251603 (2015).
- [58] C. Gogolin and J. Eisert, “Equilibration, thermalisation, and the emergence of statistical mechanics in closed quantum systems,” *Reports on Progress in Physics* **79**, 056001 (2016).
- [59] L. D’Alessio, Y. Kafri, A. Polkovnikov, and M. Rigol, “From quantum chaos and eigenstate thermalization to statistical mechanics and thermodynamics,” *Advances in Physics* **65**, 239–362 (2016).
- [60] T. Mori, T. N. Ikeda, E. Kaminishi, and M. Ueda, “Thermalization and prethermalization in isolated quantum systems: a theoretical overview,” *Journal of Physics B: Atomic, Molecular and Optical Physics* **51**, 112001 (2018).
- [61] P. Reimann, “Foundation of Statistical Mechanics under Experimentally Realistic Conditions,” *Physical Review Letters* **101**, 190403 (2008).
- [62] N. Linden, S. Popescu, A. J. Short, and A. Winter, “Quantum mechanical evolution towards thermal equilibrium,” *Physical Review E* **79**, 061103 (2009).
- [63] J. Dziarmaga, “Dynamics of a quantum phase transition and relaxation to a steady state,” *Advances in Physics* **59**, 1063–1189 (2010).

- [64] A. Polkovnikov, K. Sengupta, A. Silva, and M. Vengalattore, “*Colloquium* : Nonequilibrium dynamics of closed interacting quantum systems,” *Reviews of Modern Physics* **83**, 863–883 (2011).
- [65] M. Rigol, V. Dunjko, and M. Olshanii, “Thermalization and its mechanism for generic isolated quantum systems,” *Nature* **452**, 854–858 (2008).
- [66] D. A. Abanin and Z. Papić, “Recent progress in many-body localization,” *Annalen der Physik* **529**, 1700169 (2017).
- [67] D. A. Abanin, E. Altman, I. Bloch, and M. Serbyn, “Many-body localization, thermalization, and entanglement,” *Reviews of Modern Physics* **91**, 021001 (2019).
- [68] N. Laflorencie, “Entanglement entropy and localization in disordered quantum chains,” in *Entanglement in spin chains: From theory to quantum technology applications*, edited by A. Bayat, S. Bose, and H. Johannesson (Springer International Publishing, Cham, 2022), pp. 61–87.
- [69] P. Sierant, M. Lewenstein, A. Scardicchio, L. Vidmar, and J. Zakrzewski, *Many-Body Localization in the Age of Classical Computing*, Apr. 2024.
- [70] V. Oganesyan and D. A. Huse, “Localization of interacting fermions at high temperature,” *Physical Review B* **75**, 155111 (2007).
- [71] T. C. Berkelbach and D. R. Reichman, “Conductivity of disordered quantum lattice models at infinite temperature: Many-body localization,” *Physical Review B* **81**, 224429 (2010).
- [72] A. De Luca and A. Scardicchio, “Ergodicity breaking in a model showing many-body localization,” *EPL (Europhysics Letters)* **101**, 37003 (2013).
- [73] A. Nanduri, H. Kim, and D. A. Huse, “Entanglement spreading in a many-body localized system,” *Physical Review B* **90**, 064201 (2014).
- [74] M. Serbyn, Z. Papić, and D. A. Abanin, “A criterion for many-body localization-delocalization phase transition,” *Physical Review X* **5**, 041047 (2015).
- [75] Y. Bar Lev, G. Cohen, and D. R. Reichman, “Absence of Diffusion in an Interacting System of Spinless Fermions on a One-Dimensional Disordered Lattice,” *Physical Review Letters* **114**, 100601 (2015).
- [76] T. Devakul and R. R. P. Singh, “Early Breakdown of Area-Law Entanglement at the Many-Body Delocalization Transition,” *Physical Review Letters* **115**, 187201 (2015).
- [77] D. J. Luitz, N. Laflorencie, and F. Alet, “Extended slow dynamical regime close to the many-body localization transition,” *Physical Review B* **93**, 060201 (2016).
- [78] N. Macé, F. Alet, and N. Laflorencie, “Multifractal Scalings Across the Many-Body Localization Transition,” *Physical Review Letters* **123**, 180601 (2019).
- [79] D. E. Logan and S. Welsh, “Many-body localization in Fock space: A local perspective,” *Physical Review B* **99**, 045131 (2019).
- [80] M. Tarzia, “Many-body localization transition in Hilbert space,” *Physical Review B* **102**, 014208 (2020).
- [81] P. Sierant, M. Lewenstein, and J. Zakrzewski, “Polynomially filtered exact diagonalization approach to many-body localization,” *Physical Review Letters* **125**, 156601 (2020).

- [82] M. Znidaric, T. Prosen, and P. Prelovsek, “Many body localization in Heisenberg XXZ magnet in a random field,” *Physical Review B* **77**, 064426 (2008).
- [83] J. H. Bardarson, F. Pollmann, and J. E. Moore, “Unbounded Growth of Entanglement in Models of Many-Body Localization,” *Physical Review Letters* **109**, 017202 (2012).
- [84] M. Kiefer-Emmanouilidis, R. Unanyan, M. Fleischhauer, and J. Sirker, “Evidence for Unbounded Growth of the Number Entropy in Many-Body Localized Phases,” *Physical Review Letters* **124**, 243601 (2020).
- [85] D. J. Luitz and Y. B. Lev, “Is there slow particle transport in the MBL phase?” *Physical Review B* **102**, 100202 (2020).
- [86] Y. Huang, *Extensive Entropy from Unitary Evolution*, Preprint (PHYSICAL SCIENCES, Apr. 2021).
- [87] D. A. Chávez, C. Artiaco, T. K. Kvorning, L. Herviou, and J. H. Bardarson, *Ultraslow Growth of Number Entropy in an l-bit Model of Many-Body Localization*, Dec. 2023.
- [88] H. Kim, T. N. Ikeda, and D. A. Huse, “Testing whether all eigenstates obey the Eigenstate Thermalization Hypothesis,” *Physical Review E* **90**, 052105 (2014).
- [89] V. Alba, “Eigenstate thermalization hypothesis (ETH) and integrability in quantum spin chains,” *Physical Review B* **91**, 155123 (2015).
- [90] R. Mondaini, K. R. Fratus, M. Srednicki, and M. Rigol, “Eigenstate thermalization in the two-dimensional transverse field Ising model,” *Physical Review E* **93**, 032104 (2016).
- [91] M. Mierzejewski and L. Vidmar, “Eigenstate thermalization hypothesis and integrals of motion,” *Physical Review Letters* **124**, 040603 (2020).
- [92] S. D. Geraedts, R. Nandkishore, and N. Regnault, “Many-body localization and thermalization: Insights from the entanglement spectrum,” *Physical Review B* **93**, 174202 (2016).
- [93] B. Swingle, *A simple model of many-body localization*, July 2013.
- [94] S. Adami, M. Amini, and M. Soltani, “Structural properties of local integrals of motion across the many-body localization transition via a fast and efficient method for their construction,” *Physical Review B* **106**, 054202 (2022).
- [95] A. Chandran, I. H. Kim, G. Vidal, and D. A. Abanin, “Constructing local integrals of motion in the many-body localized phase,” *Physical Review B* **91**, 085425 (2015).
- [96] M. Mierzejewski, P. Prelovšek, and T. Prosen, “Identifying Local and Quasilocal Conserved Quantities in Integrable Systems,” *Physical Review Letters* **114**, 140601 (2015).
- [97] M. Mierzejewski, T. Prosen, and P. Prelovšek, “Approximate conservation laws in perturbed integrable lattice models,” PHYSICAL REVIEW B, 8 (2015).
- [98] S. J. Thomson and M. Schiró, *Local Integrals of Motion in Quasiperiodic Many-Body Localized Systems*, Oct. 2021.
- [99] D. S. Fisher, “Random antiferromagnetic quantum spin chains,” *Physical Review B* **50**, 3799–3821 (1994).
- [100] R. Vosk, D. A. Huse, and E. Altman, “Theory of the Many-Body Localization Transition in One-Dimensional Systems,” *Physical Review X* **5**, 031032 (2015).

- [101] D. B. Gutman, I. V. Protopopov, A. L. Burin, I. V. Gornyi, R. A. Santos, and A. D. Mirlin, “Energy transport in the Anderson insulator,” *Physical Review B* **93**, 245427 (2016).
- [102] A. Safavi-Naini, M. L. Wall, O. L. Acevedo, A. M. Rey, and R. M. Nandkishore, “Quantum dynamics of disordered spin chains with power-law interactions,” *Physical Review A* **99**, 033610 (2019).
- [103] R. Yousefjani and A. Bayat, “Mobility edge in long-range interacting many-body localized systems,” *Physical Review B* **107**, 045108 (2023).
- [104] R. Vasseur, A. J. Friedman, S. A. Parameswaran, and A. C. Potter, “Particle-hole symmetry, many-body localization, and topological edge modes,” *Physical Review B* **93**, 134207 (2016).
- [105] R. N. Bhatt and P. A. Lee, “Scaling Studies of Highly Disordered Spin- $\frac{1}{2}$ Antiferromagnetic Systems,” *Physical Review Letters* **48**, 344–347 (1982).
- [106] D. S. Fisher, “Critical behavior of random transverse-field Ising spin chains,” *Physical Review B* **51**, 6411–6461 (1995).
- [107] R. Vosk and E. Altman, “Dynamical quantum phase transitions in random spin chains,” *Physical Review Letters* **112**, 217204 (2014).
- [108] P. Mason, A. Zagoskin, and J. Betouras, “Time-dependent Real-space Renormalization-Group Approach: application to an adiabatic random quantum Ising model,” *Journal of Physics A: Mathematical and Theoretical* **52**, 045004 (2019).
- [109] P. Ruggiero and X. Turkeshi, “Quantum information spreading in random spin chains,” *Physical Review B* **106**, 134205 (2022).
- [110] R. Vasseur, A. C. Potter, and S. A. Parameswaran, “Quantum Criticality of Hot Random Spin Chains,” *Physical Review Letters* **114**, 217201 (2015).
- [111] A. Kutlin and I. Khaymovich, “Renormalization to localization without a small parameter,” *SciPost Physics* **8**, 049 (2020).
- [112] S. Whitlock, A. W. Glaetzle, and P. Hannaford, “Simulating quantum spin models using Rydberg-excited atomic ensembles in magnetic microtrap arrays,” *Journal of Physics B: Atomic, Molecular and Optical Physics* **50**, 074001 (2017).
- [113] N. Šibalić and C. S. Adams, *Rydberg physics*, 2399-2891 (IOP Publishing, 2018).
- [114] A. Browaeys and T. Lahaye, “Many-body physics with individually controlled Rydberg atoms,” *Nature Physics* **16**, 132–142 (2020).
- [115] P. Scholl, M. Schuler, H. J. Williams, A. A. Eberharter, D. Barredo, K.-N. Schymik, V. Lienhard, L.-P. Henry, T. C. Lang, T. Lahaye, A. M. Läuchli, and A. Browaeys, “Quantum simulation of 2D antiferromagnets with hundreds of Rydberg atoms,” *Nature* **595**, 233–238 (2021).
- [116] A. Piñeiro Orioli, A. Signoles, H. Wildhagen, G. Günter, J. Berges, S. Whitlock, and M. Weidemüller, “Relaxation of an Isolated Dipolar-Interacting Rydberg Quantum Spin System,” *Physical Review Letters* **120**, 063601 (2018).
- [117] A. Signoles, T. Franz, R. F. Alves, M. Gärttner, S. Whitlock, G. Zürn, and M. Weidemüller, “Glassy dynamics in a disordered Heisenberg quantum spin system,” *Physical Review X* **11**, 011011 (2021).

- [118] M. D. Lukin, M. Fleischhauer, R. Cote, L. M. Duan, D. Jaksch, J. I. Cirac, and P. Zoller, “Dipole Blockade and Quantum Information Processing in Mesoscopic Atomic Ensembles,” *Physical Review Letters* **87**, 037901 (2001).
- [119] J. Wurtz, A. Polkovnikov, and D. Sels, “Cluster truncated Wigner approximation in strongly interacting systems,” *Annals of Physics* **395**, 341–365 (2018).
- [120] J. Brey and A. Prados, “Stretched exponential decay at intermediate times in the one-dimensional Ising model at low temperatures,” *Physica A: Statistical Mechanics and its Applications* **197**, 569–582 (1993).
- [121] P. Schultzen, T. Franz, S. Geier, A. Salzinger, A. Tebben, C. Hainaut, G. Zürn, M. Weidemüller, and M. Gärtnner, “Glassy quantum dynamics of disordered Ising spins,” *Physical Review B* **105**, L020201 (2022).
- [122] P. Schultzen, T. Franz, C. Hainaut, S. Geier, A. Salzinger, A. Tebben, G. Zürn, M. Gärtnner, and M. Weidemüller, “Semiclassical simulations predict glassy dynamics for disordered Heisenberg models,” *Physical Review B* **105**, L100201 (2022).
- [123] A. Haldar, *Slow Dynamics and Kohlrausch Relaxation in Isolated Disordered Many-Body Systems*, Feb. 2023.
- [124] S. Chandrasekhar, “Stochastic Problems in Physics and Astronomy,” *Reviews of Modern Physics* **15**, 1–89 (1943).
- [125] P. Kaposvári, *Describing the dynamics of disordered heisenberg xxz model with real space renormalisation group methods*, Master’s thesis, Heidelberg, Germany, Feb. 2021.
- [126] R. Nandkishore and S. Gopalakrishnan, “Many body localized systems weakly coupled to baths: Many body localized systems weakly coupled to baths,” *Annalen der Physik* **529**, 1600181 (2017).
- [127] W. De Roeck and F. Huveneers, “Stability and instability towards delocalization in many-body localization systems,” *Physical Review B* **95**, 155129 (2017).
- [128] K. Mukherjee, G. W. Biedermann, and R. J. Lewis-Swan, *Influence of disordered and anisotropic interactions on relaxation dynamics and propagation of correlations in tweezer arrays of Rydberg dipoles*, Aug. 2024.
- [129] X. Chen, T. Zhou, D. A. Huse, and E. Fradkin, “Out-of-time-order correlations in many-body localized and thermal phases,” *Annalen der Physik* **529**, 1600332 (2017).
- [130] B. Swingle, “Unscrambling the physics of out-of-time-order correlators,” *Nature Physics* **14**, 988–990 (2018).
- [131] D. J. Luitz and Y. B. Lev, “Emergent locality in systems with power-law interactions,” *Physical Review A* **99**, 010105 (2019).
- [132] S. Xu and B. Swingle, “Scrambling Dynamics and Out-of-Time-Ordered Correlators in Quantum Many-Body Systems,” *PRX Quantum* **5**, 010201 (2024).
- [133] F. S. Lozano-Negro, C. M. Sánchez, A. K. Chattah, G. A. Álvarez, and H. M. Pastawski, *Global Out of Time Order Correlators as a Signature of Scrambling Dynamics of Local Observables*, July 2024.
- [134] E. Davis, G. Bentsen, and M. Schleier-Smith, “Approaching the Heisenberg Limit without Single-Particle Detection,” *Physical Review Letters* **116**, 053601 (2016).

- [135] D. Linnemann, H. Strobel, W. Muessel, J. Schulz, R. J. Lewis-Swan, K. V. Kheruntsyan, and M. K. Oberthaler, “Quantum-Enhanced Sensing Based on Time Reversal of Nonlinear Dynamics,” *Physical Review Letters* **117**, 013001 (2016).
- [136] S. Colombo, E. Pedrozo-Peñaflor, A. F. Adiyatullin, Z. Li, E. Mendez, C. Shu, and V. Vuletić, “Time-reversal-based quantum metrology with many-body entangled states,” *Nature Physics* **18**, 925–930 (2022).
- [137] G. De Tomasi, D. Hetterich, P. Sala, and F. Pollmann, “Dynamics of strongly interacting systems: From Fock-space fragmentation to many-body localization,” *Physical Review B* **100**, 214313 (2019).
- [138] P. Sala, T. Rakovszky, R. Verresen, M. Knap, and F. Pollmann, “Ergodicity Breaking Arising from Hilbert Space Fragmentation in Dipole-Conserving Hamiltonians,” *Physical Review X* **10**, 011047 (2020).
- [139] Y. Han, X. Chen, and E. Lake, *Exponentially slow thermalization and the robustness of Hilbert space fragmentation*, Jan. 2024.
- [140] F. Yang, H. Yarloo, H.-C. Zhang, K. Mølmer, and A. E. B. Nielsen, *Probing Hilbert Space Fragmentation with Strongly Interacting Rydberg Atoms*, Mar. 2024.
- [141] C. M. Kropf, C. Gneiting, and A. Buchleitner, “Effective Dynamics of Disordered Quantum Systems,” *Physical Review X* **6**, 031023 (2016).
- [142] C. Gneiting, F. R. Anger, and A. Buchleitner, “Incoherent ensemble dynamics in disordered systems,” *Physical Review A* **93**, 032139 (2016).
- [143] H.-B. Chen, C. Gneiting, P.-Y. Lo, Y.-N. Chen, and F. Nori, “Simulating Open Quantum Systems with Hamiltonian Ensembles and the Nonclassicality of the Dynamics,” *Physical Review Letters* **120**, 030403 (2018).
- [144] C. Gneiting, “Disorder-dressed quantum evolution,” *Physical Review B* **101**, 214203 (2020).
- [145] A. Eckardt, “Colloquium: Atomic quantum gases in periodically driven optical lattices,” *Reviews of Modern Physics* **89**, 011004 (2017).
- [146] D. V. Else, B. Bauer, and C. Nayak, “Floquet Time Crystals,” *Physical Review Letters* **117**, 090402 (2016).
- [147] V. Khemani, R. Moessner, and S. L. Sondhi, *A Brief History of Time Crystals*, Oct. 2019.
- [148] S. Blanes, F. Casas, J. A. Oteo, and J. Ros, “The Magnus expansion and some of its applications,” *Physics Reports* **470**, 151–238 (2009).
- [149] S. Vajna, K. Klobas, T. Prosen, and A. Polkovnikov, “Replica resummation of the Baker-Campbell-Hausdorff series,” *Physical Review Letters* **120**, 200607 (2018).
- [150] L. D’Alessio and M. Rigol, “Long-time Behavior of Isolated Periodically Driven Interacting Lattice Systems,” *Physical Review X* **4**, 041048 (2014).
- [151] M. Bukov, L. D’Alessio, and A. Polkovnikov, “Universal high-frequency behavior of periodically driven systems: from dynamical stabilization to Floquet engineering,” *Advances in Physics* **64**, 139–226 (2015).
- [152] T. Kuwahara, T. Mori, and K. Saito, “Floquet–Magnus theory and generic transient dynamics in periodically driven many-body quantum systems,” *Annals of Physics* **367**, 96–124 (2016).

- [153] D. Abanin, W. De Roeck, W. W. Ho, and F. Huvveneers, “A Rigorous Theory of Many-Body Prethermalization for Periodically Driven and Closed Quantum Systems,” *Communications in Mathematical Physics* **354**, 809–827 (2017).
- [154] H. Burau, M. Heyl, and G. De Tomasi, “Fate of algebraic many-body localization under driving,” *Physical Review B* **104**, 224201 (2021).
- [155] P. Sierant, M. Lewenstein, A. Scardicchio, and J. Zakrzewski, “Stability of many-body localization in Floquet systems,” *Physical Review B* **107**, 115132 (2023).
- [156] C. W. Von Keyserlingk, V. Khemani, and S. L. Sondhi, “Absolute stability and spatiotemporal long-range order in Floquet systems,” *Physical Review B* **94**, 085112 (2016).
- [157] X. Mi et al., “Time-Crystalline Eigenstate Order on a Quantum Processor,” *Nature*, [10.1038/s41586-021-04257-w](https://doi.org/10.1038/s41586-021-04257-w) (2021).
- [158] M. Ippoliti, K. Kechedzhi, R. Moessner, S. L. Sondhi, and V. Khemani, “Many-body physics in the NISQ era: quantum programming a discrete time crystal,” *PRX Quantum* **2**, 030346 (2021).
- [159] J. Randall, C. E. Bradley, F. V. van der Gronden, A. Galicia, M. H. Abobeih, M. Markham, D. J. Twitchen, F. Machado, N. Y. Yao, and T. H. Taminiau, “Many-body-localized discrete time crystal with a programmable spin-based quantum simulator,” *Science* **374**, 1474–1478 (2021).
- [160] S. J. Geier, “Shaping the Hamiltonian of many-body spin systems on a Rydberg-atom quantum simulator,” [10.11588/heidok.00034235](https://doi.org/10.11588/heidok.00034235).
- [161] H.-K. Wu, T. Suzuki, N. Kawashima, and W.-L. Tu, “Programmable order by disorder effect and underlying phases through dipolar quantum simulators,” *Physical Review Research* **6**, 023297 (2024).
- [162] J. Bezanson, A. Edelman, S. Karpinski, and V. B. Shah, “Julia: a fresh approach to numerical computing,” *SIAM Review* **59**, 65–98 (2017).
- [163] G. Datseris, J. Isensee, S. Pech, and T. Gál, “DrWatson: the perfect sidekick for your scientific inquiries,” *Journal of Open Source Software* **5**, 2673 (2020).
- [164] Fons van der Plas et al., *Pluto.jl*, Zenodo, May 2024.
- [165] C. Rackauckas and Q. Nie, “Differentialequations.jl—a performant and feature-rich ecosystem for solving differential equations in Julia,” *Journal of Open Research Software* **5**, 15 (2017).
- [166] S. Danisch and J. Krumbiegel, “Makie.jl: flexible high-performance data visualization for Julia,” *Journal of Open Source Software* **6**, 3349 (2021).
- [167] M. Bouchet-Valat and B. Kamiński, “Dataframes.jl: Flexible and fast tabular data in Julia,” *Journal of Statistical Software* **107**, 1–32 (2023).

ACKNOWLEDGMENTS

First, I would like to thank my supervisor *Martin Gärttner* for the great time I was allowed to spend within his group. Well, in the beginning when I started (for my master project), there did not exist much of a group but it steadily grew over time into its current size. Throughout the whole time, the atmosphere was always open, engaged and welcoming, which really is a reflection of your mentality. I really appreciate that I could seek your advice at any time and you always expressed excitement about my/our work. I will always remember my time spent with you and the group fondly.

Secondly, I want to thank my co-advisor *Matthias Weidemüller* for the opportunity to work in so close collaboration with experiment. To me this was an ideal environment, where I could solve puzzles that actually have a counterpart in the real world.

I also thank *Tilman Enss* for reviewing this thesis and the further members of my committee *Selim Jochim* and *Werner Aeschbach*.

Although briefly mentioned above, I want to express my appreciation for all of my colleagues and friends from the MBQD group. You all (and this includes past members in HD as well as the new crew in Jena) contributed to make this a enjoyable time - be it on our retreats or just during normal work. I want to make a couple special shout-outs. Starting with *Niklas Euler*, with whom I had the pleasure of sharing my office and from whom I learned the secrets of cooking with Seitan. Further, I want to shout-out my norse namesake *Adrian Åsen* with whom I went on an epic quest to see the northern lights and experience the darkness of the polar night. *Javad Vahedi*, I really enjoyed our discussions about numerics and programming. And last but not least, *Mirco Erpelding* who made the last year 112% more enjoyable.

Another big source of joy and motivation were the frequent discussions with the Rydberg team. Especially I want to thank *Titus Franz* for easing my way into this project by sharing his knowledge about numerical simulations of the system. Towards the later part of my journey, *Sebastian Geier* was a great partner for discussions as well. I want to express my gratitude to you both and also include *Gerhard Zürn*. Thank you for your general excitement about the experiment, which made me always looking forward to our discussions, and for your patience in explaining more details about atomic physics or the experiment whenever my theorist's perspective was a bit too simplistic.

For the numerical work, I exclusively used the Julia programming language [162], which has been a constant source of joy. It certainly was a cornerstone of this thesis together with many excellent libraries/tools that also deserve acknowledging: `DrWatson.jl` [163] (reproducible scientific projects), `Pluto.jl` [164] (notebooks), `DifferentialEquations.jl` [165], `Makie.jl` [166] (plots) and `DataFrames.jl` [167].

Finally, I am very grateful for the continuous support of my friends and family. First and foremost, I want to express my heartfelt gratitude for my parents, *Petra* and *Achim*, who always encouraged my curiosity and supported me on every step of my way, and also for my sister *Lucy*, who always believed in me and cheered me up in times of doubt. Extra special love goes out to my wonderful partner *Brini*, who always was there for me when I needed her. Especially in times where this thesis filled my mind you were very understanding, supportive and even drew those coffee cups for me (see Figure 1 and Figure 9.1). I am very grateful to have you in my life and I very much look forward to less stressful times to enjoy together with you.